University holding the administrative responsability: Università degli Studi di Padova
Dipartimento di Scienze Chimiche

DOCTORAL COURSE: Scienze molecolari
CURRICOLO: Scienze Chimiche
CICLO XXIX°
Coordinatore: Prof. Antonino Polimeno

Hosting University: Johannes Gutenberg-Universtät Mainz
Department of Biologie

DOCTORAL COURSE: Biologie School

PHOTOPROTECTIVE MECHANISMS IN CHLOROPHYLL-BINDING PROTEINS STUDIED BY MEANS OF ELECTRON PARAMAGNETIC SPECTROSCOPIES

Supervisor: Prof.ssa Donatella Carbonera
Supervisor: Prof. Dr. Harald Paulsen

PhD candidate : Alessandro Agostini

PHOTOPROTECTIVE MECHANISMS IN CHLOROPHYLL-BINDING PROTEINS STUDIED BY MEANS OF ELECTRON PARAMAGNETIC SPECTROSCOPIES

Dissertation

zur Erlangung des Akademischen Grades
Doktor der Naturwissenschaften,

am Fachbereich 10, Biologie
der Johannes Gutenberg-Universität
Mainz

von

Alessandro Agostini
geb. am 26. Oktober 1989 in Camposampiero (Padova)

Mainz
2017

Dekan: Prof. Dr. Hans Zischler

1. Prüferin: Prof. Dr. D. Carbonera

2. Prüfer: Prof. Dr. Harald Paulsen

Tag der mündlichen Prüfung:

Table of contents

Summary ...1

Sommario ...3

Zusammenfassung ...5

Part I: Introduction

1. Photosynthesis and Photoprotection ...9

1.1 Overview of the oxygenic photosynthetic process ...9

1.2 Photosynthetic pigments ...10

1.2.1 Chlorophylls ...11

1.2.2 Carotenoids ...14

1.3 Structure of the photosynthetic apparatus ...16

1.4 Photoprotection ...19

1.4.1 WSCP ...23

1.5 References ...24

2. The triplet state ...29

2.1 The physic of the triplet state ...29

2.2 Electron-Exchange Interaction ...31

2.3 Electron-Electron Dipole Interaction ...32

2.3.1 Magnetic Resonance Transition at Zero Field ...35

2.4 The Hyperfine Coupling ...36

2.5 Zeeman Interaction ...37

2.5.1 Magnetic Resonance Transition in High-Field ...38

2.6 Optical polarization of electronic spin ...39

2.6.1 InterSystem Crossing ...39

2.6.2 Triplet-Triplet Energy Transfer ...41

2.7 References ...43

3. Optically Detected Magnetic Resonance ...45

3.1 Photo-induced steady-state ...45

3.2 Saturation of a transition ...47

3.3 ADMR and FDMR experiments ...48

3.3.1 FDMR of non-fluorescent species ...49

3.4 MIA experiments ...49

3.5 Experimental conditions ...50

3.5.1 Cryostat ...51

3.5.2 Microwave circuit ...51

3.5.3 Optical system ...52

3.5.4 Registration ...52

3.6 References ...52

4. Electron Paramagnetic Resonance ...53

4.1 CW-EPR ...53

4.2 TR-EPR ...54

4.2.1 Triplet state TR-EPR spectroscopy ...55

4.2 Pulse EPR ...56

4.2.1 Pulse ENDOR ...57

4.4 References ...59

Part II: Reaction Centers

Carotenoid triplet states in photosystem II: Coupling with low-energy states of the core complex **...63**

Supporting Information ...77

Differential Roles of Carotenes and Xanthophylls in Photosystem I Photoprotection **...91**

Supporting Information ...105

Triplet Charge Recombination in Heliobacterial Reaction Centers Does Not Produce a Spin-Polarized EPR Spectrum **...115**

Part III: Water Soluble Chlorophyll-binding Proteins

Water-Soluble Chlorophyll Protein (WSCP) Stably Binds 2 or 4 Chlorophylls **...133**

Supporting Information ...161

An unusual role for the phytyl chains in the photoprotection of the chlorophylls bound to Water-Soluble Chlorophyll-binding Proteins. **...167**

Supporting Information ...191

Appendix

Author contributions ...199

Statuary Declaration ...201

CV ...203

Acknowledgments ...207

Summary

Light is essential for photosynthesis, and hence in supporting life on earth, but all the steps of the light reactions may lead to the formation of dangerous oxidative species. Chlorophyll *a*, the green heart of oxygenic photosynthesis, is also its main Achilles' heel, due to a high intersystem crossing (ISC) probability that leads to the production of excited triplet state, an efficient singlet oxygen sensitizer. Photosynthetic organisms have consequently developed several photoprotective mechanisms aimed to avoid photo-oxidative stress originated from the excess of absorbed light, that otherwise would ultimately lead to cell death.

Photoprotection is pivotal for life on Earth, however a full comprehension of the molecular mechanisms is still lacking for several of the processes that photosynthetic organisms employ. The knowledge of the diverse adaptations of the photoprotective response to the various natural conditions in which photosynthetic organisms have evolved promises to highlight the essential characteristics that an efficient mechanism has to display. This understanding of the key molecular requirements for an efficient photoprotection may be exploited for the design of bio-mimetic molecular systems in the fields of artificial photosynthesis, photodynamic therapies and photocatalysis, to make them more durable in virtue of specifically tailored photoprotective mechanisms.

The quickest of the photoprotective processes taking place in natural photosystems relies on the capability of carotenoids to photoprotect the system, either by directly quenching the triplet state of chlorophyll through triplet-triplet energy transfer, or by deactivation of the photosensitized singlet oxygen once it is formed. With the aim of studying this pivotal trait of photosynthetic organisms, in the course of my graduate research I characterized the role of carotenoids in the photoprotection of the two major components of the oxygenic photosynthetic machinery, namely Photosystem I and Photosystem II. Due to the high complexity of the studied samples, consisting of multi-subunit complexes formed by the assembly of Reaction Centers with numerous bound antenna complexes, an Optically Detected Magnetic Resonance (ODMR) approach has been utilized. ODMR, being a double resonance technique, makes possible to disentangle the different triplet state contributions and extract the information regarding the triplet states populated upon illumination in the multi-chromophore complex of interest. A comparative approach, involving either differences in the size of the complexes or mutations, allowed to get insight into the energy transfer pathways and into the differential role that β-carotene and xanthophylls play in the photoprotection of the two photosystems.

With the aim to extend the study of natural photoprotective mechanisms and understand them at a molecular level, we started to work on an unusual chlorophyll binding protein, the Water-Soluble Chlorophyll-binding Protein (WSCP). This research has been conduct in the framework of a joint project between the university of Padova and the university of Mainz. WSCP remarkably differs from the other known chlorophyll-binding proteins, being not involved in the photosynthetic process. WSCP has been shown to be an incredibly stable complex, being able to protect its chlorophylls towards photodamage. Interestingly this protein does not contain carotenoids, in contrast to every other known chlorophyll-binding protein. By

combining biochemical and spectroscopic methodologies, we discovered a mechanism for the photoprotection of chlorophylls in WSCP completely new in the landscape of photoprotection We demonstrated that the observed resistance of the WSCP-bound chlorophylls to singlet oxygen damage depends on the localization of the phytyls moieties between the chlorophylls forming a tight dimer in WSCP. We were able to propose a photoprotective mechanism based on the capability of the phytyls to limit the singlet oxygen accessibility to the oxidizable sites of the chlorophylls.

Sommario

La luce è essenziale nel sostenere il processo fotosintetico, e con esso la vita sulla terra, ma la fase luminosa della fotosintesi è anche piagata dalla formazione di pericolose specie ossidanti. La clorofilla *a*, molecola su cui si basa la fotosintesi ossigenica, ne è anche il principale tallone d'Achille, a causa della sua elevate probabilità di *intersystem crossing* (ISC) con la conseguente alta resa di tripletto, uno stato elettronico che può efficacemente foto-sensibilizzare l'ossigeno allo stato di singoletto. Gli organismi fotosintetici di conseguenza hanno sviluppato svariati meccanismi fotoprotettivi finalizzati a ridurre lo stress ossidativo causato dall'eccessivo assorbimento luminoso, che altrimenti ne causerebbe la morte.

La fotoprotezione è essenziale per la vita sulla terra, ma è ancora incompleta la comprensione ad un livello molecolare per molti dei processi fotoprotettivi impiegati dagli organismi fotosintetici. La conoscenza dei diversi adattamenti della risposta foto-protettiva alle diverse condizioni ambientali nelle quali gli organismi fotosintetici si sono evoluti dovrebbe permettere di evidenziare le caratteristiche essenziali che un efficiente meccanismo foto-protettivo deve possedere. Questa comprensione delle caratteristiche molecolari necessarie per un'efficiente foto-protezione promette di essere sfruttabile nella progettazione di sistemi molecolari bio-mimetici nei campi della fotosintesi artificiale, della terapia fotodinamica e della fotocatalisi, di modo da rendere le molecole foto-attive più stabili in virtù di meccanismi fotoprotettivi specificatamene progettati.

I più rapidi di questi processi fotoprotettivi nei sistemi fotosintetici naturali sfruttano i carotenoidi per foto-proteggere il sistema, sia tramite una diretta diseccitazione dello stato di tripletto della clorofilla tramite un trasferimento di energia tripletto-tripletto, che tramite una diretta diseccitazione dell'ossigeno di singoletto foto-prodotto. Con l'intento di studiare questi importanti processi fotoprotettivi, nel corso del mio dottorato abbiamo studiato il ruolo fotoprotettivo dei carotenoidi nei due principali macchinari fotosintetici, ovvero il Fotosistema I e il Fotosistema II. A causa della loro elevata complessità, essendo complessi multimerici formati dall'assemblaggio dei centri di reazione con numerose antenne, nella loro caratterizzazione abbiamo impiegato la Risonanza Magnetica Rilevata Otticamente (ODMR). Questa metodologia, essendo una tecnica di doppia risonanza, rende possibile lavorare su complessi sistemi multicromoforici permettendo di isolare i contributi dei singoli stati di tripletto presenti nei campioni d'interesse. Un approccio comparativo, basato in un caso sulla differente dimensione dei complessi e nell'altro su opportune mutazioni di enzimi coinvolti nella funzionalizzazione dei carotenoidi, ha permesso di ottenere nuove informazioni riguardanti i cammini di trasferimento energetico e i differenti ruoli che il β-carotene e le xantofille svolgono nella fotoprotezione dei due fotosistemi.

Per accrescere la varietà di meccanismi fotoprotettivi caratterizzati con un livello di dettaglio molecolare, abbiamo iniziato a studiare un'inusuale proteina che lega la clorofilla, la *Water-Soluble Chlorophyll-binding Protein* (WSCP). Questo filone di ricerca è stato condotto nel contesto di un progetto congiunto tra le università di Padova e di Mainz. WSCP differisce significativamente dalle altre proteine che legano la clorofilla non essendo coinvolta nel processo fotosintetico. Questa proteina si è dimostrata essere un complesso incredibilmente

stabile, capace di foto-proteggere efficacemente le clorofille che lega. Sorprendentemente questa foto-stabilità è raggiunta senza l'impiego di carotenoidi, contrariamente ad ogni altra proteina contente clorofilla nota. Combinando metodologie di indagine biochimiche e spettroscopiche, abbiamo caratterizzato in WSCP un nuovo meccanismo di fotoprotezione delle clorofille. Abbiamo infatti dimostrato che la resistenza delle clorofille legate da WSCP al danneggiamento foto-indotto dipende dalla localizzazione delle catene fittoliche tra le clorofille che formano un dimero in WSCP. Abbiamo quindi proposto un meccanismo foto-protettivo basato sulla capacità dei fittoli di limitare l'accesso dell'ossigeno di singoletto ai siti ossidabili delle clorofille.

Zusammenfassung

Licht ist essentiell für die Photosynthese und damit für das Leben auf der Erde. Allerdings können alle Schritte der Lichtreaktion zur Bildung gefährlicher oxidativer Spezies führen. Chlorophyll *a* ist nicht nur das grüne Herz sondern gleichzeitig die Achillesferse der Photosynthese. Wegen seiner hohen ISC (*inter system crossing*)-Wahrscheinlichkeit gerät Chlorophyll *a* leicht in einen Triplett-Anregungszustand, aus welchem es effizient die Entstehung von Singulett-Sauerstoff begünstigt. Infolge dessen, haben photosynthetisch aktive Organismen verschiedene Lichtschutzmechanismen entwickelt, um photooxidativen Stress zu verhindern, welcher durch die überschüssige Absorption von Licht entsteht und der sonst zum ultimativen Zelltod führen würde.

Der Schutz vor überschüssigem Licht ist grundlegend für das Leben auf der Erde; dennoch fehlt ein molekulares Verständnis der Mechanismen vieler solcher Prozesse in photosynthetisierenden Organismen. Das Wissen um die verschiedenen Anpassungen der Schutzantwort auf überschüssiges Licht in unterschiedlichen natürlichen Umgebungen, in denen die Evolution Photosynthese betreibender Organismen stattgefunden hat, verspricht die grundlegenden Charakteristika, die einen effizienten Schutzmechanismus ausmachen, zu beleuchten. Ein solches Verständnis der molekularen Schlüsselanforderungen eines effektiven Schutzmechanismus könnte genutzt werden für das Entwerfen biomimetischer Systeme auf molekularer Ebene in den Bereichen artifizieller Photosynthese, photodynamischer Therapie und Photokatalyse, um diese durch speziell zugeschnittene Schutzmechanismen langlebiger und beständiger zu machen.

Der schnellste dieser Lichtschutzprozesse basiert auf der Fähigkeit der Carotinoide, entweder direkt den Triplett-Zustand der Chlorophylle mittels Triplett-Triplett Energietransfer zu löschen, oder aber den Singulett-Sauerstoff nach seiner lichtinduzierten Entstehung zu entschärfen. Mit dem Ziel, dieses grundlegende Merkmal photosynthetisch aktiver Organismen zu untersuchen, habe ich im Verlauf meiner Forschungen die Rolle der Carotinoide beim Schutz von Photosystem I und Photosystem II, den beiden Hauptbestandteilen des oxygenen Photosynthese-Apparates, vor überschüssigem Licht charakterisiert. Wegen der hohen Komplexität der untersuchten Beispiele, aufgebaut aus mehreren Untereinheiten, die durch Assemblierung von Reaktionszentren mit einer Vielzahl an assoziierten Antennenkomplexen gebildet werden, wurde die „Optically Detected Magnetic Resonance“ (ODMR) als Messmethode gewählt. ODMR stellt eine sogenannte Doppel-Resonanz Technik dar, die die Entschlüsselung der zahlreichen detektierbaren Triplett-Zustände in den Multi-Chromophor-Komplexen erlaubt und somit zu interessanten Informationen über diese Triplett-Zustände führt. Eine vergleichende Studie mit Komplexen entweder unterschiedlicher Größe oder mit eingeführten Mutationen erlaubte Einblicke in die Energietransferwege sowie in die unterschiedlichen Rollen, welche β-Carotin und Xanthophylle beim Schutz vor photodynamischer Degregation beider Photosysteme spielen.

Mit dem Ziel, mehr Lichtschutzmechanismen auf molekularer Ebene zu verstehen, begannen wir die Arbeit an einem ungewöhnlichen Chlorophyll-bindenden Protein, dem Wasserlöslichen Chlorophyll Protein (WSCP). Diese Untersuchungen wurden im Rahmen eines

gemeinsamen Projektes zwischen der Universität Padua und der Universität Mainz durchgeführt. WSCP unterscheidet sich deutlich von anderen bekannten Chlorophyll-bindenden Proteinen, da es nicht in den Prozess der Photosynthese involviert ist. Es konnte gezeigt werden, dass WSCP einen überaus stabilen Komplex bildet, welcher in der Lage ist, seine Chlorophylle gegenüber photodynamischer Schädigung zu schützen. Interessanterweise und im Gegensatz zu allen anderen bekannten Chlorophyll-bindenden Proteinen besitzt das WSCP keinerlei Carotinoide. Durch die Kombination von biochemischen und spektroskopischen Methoden konnten wir einen neuen Schutzmechanismus für Chlorophylle im WSCP aufdecken. Wir konnten zeigen, dass die beobachtete Widerstandsfähigkeit der WSCP-gebundenen Chlorophylle gegenüber Schädigung durch Singulett-Sauerstoff abhängig ist von der Anordnung der Phytolreste zwischen den Chlorophyllen, welche im WSCP als stark gekoppeltes Dimer vorliegen. Wir konnten somit als Schutzmechanismus vorschlagen, dass die Phytole den Zugang von Singulett-Sauerstoff zu den oxidierbaren Regionen der Chlorophyll-Moleküle beschränken.

Part I

Introduction

Photosynthesis and Photoprotection

The answer to the question "What is life?" is a major challenge in natural sciences. A comprehensive definition can be found in the work of Harold,(Harold 2001) where he defined life as the *"property of autopoietic systems capable of evolving by variation and natural selection"*, that invoke the central concept of autopoiesis,(Maturana & Varela 1980) that Harold stated as the property of: *"self-constructing, self-maintaining, energy transducing autocatalytic entities"*.(Harold 2001) The concept of *energy transduction* is pivotal, because organisms must consume energy in order to maintain themselves in a state away from equilibrium, since thermodynamic equilibrium can be seen as the true definition of death. This is true from the smallest cell to the whole biosphere, that affects deeply Earth's chemical composition keeping it far away from chemical equilibrium,(Kleidon 2010) a peculiarity that urged Vernadsky to define the biosphere as a geological force.(Vernadski 1926)

The persistence and proliferation of living beings require a noteworthy and continuous influx of energy in the trophic cycle that is accomplished by organisms relying on autotrophic metabolic processes to fuel themselves. From its emergence very early in the Earth's history,(Rosing 1999; Cardona 2016) photosynthesis is doubtlessly the most important biological process on Earth,(Raven 2009) whereby organisms trap the energy contained in photons by breaking and making chemical bonds against the thermodynamic equilibrium. All the steps of the photosynthetic process, from the absorption of photons to the oxidation of water and the production of reduced species, lead to the potential production of dangerous oxidative species. Consequently the large variety of photosynthetic organisms including bacteria, algae, and plants, have diversified both their photosynthetic and photoprotective apparatuses in order to adapt to the different light conditions in their specific ecological niches. From a comparison of the adaptations of the photoprotective response to the evolution pressure that the various organisms have experimented in their evolutionary history, it is expected that should arise a comprehension of the essential features that an efficient photoprotective mechanism has to display in order to function. This is only the first, but necessary, step in the design of artificial bio-mimetic photoprotective strategies, that promise to be necessary in all the fields of synthetic chemistry that aspire to employ the light to conduct a chemical work.

1.1 Overview of the photosynthetic process

The photosynthetic process relies on pigment-containing proteins that use light-driven electron transfer processes to produce energy rich chemical species (ATP) and reductive power (NADH or NADPH). These molecules are then used to supply anabolic processes like the Calvin–Benson-Bassham cycle and the nitrogen fixation. The photosynthetic process is usually divided in light-dependent (or "light") reactions that end with the production of ATP and NADPH, and

light-independent (or "dark") reactions in which the above mentioned energetic compounds are used to fuel the anabolic processes. The overall photosynthetic reaction can be expressed generally as:

$$n \cdot H_2D + n \cdot CO_2 \xrightarrow{h\nu} C_n(H_2O)_n + 2n \cdot D$$

Where H_2D is a electron donor like water or sulfuric acid and $C_n(H_2O)_n$ represents a carbohydrate. Of particular relevance is the photosynthetic process that involves H_2O as electrons source, in which O_2 evolves as oxidized byproduct: the oxygenic photosynthesis. This reaction has a fundamental importance in the history of the life on earth, because beyond its prevailing contribution to the global primary production,(Raven 2009) oxygenic photosynthesis made Earth congenial for us. In fact early oxygen-producing photoautotrophs pumped up atmospheric oxygen concentrations,(Van Valen 1971; Kasting 1993) allowing the development of oxygen-dependent complex multicellular life and afterward the colonization of the land, since the oxygen in stratosphere bred the ozone layer that shields against the solar ultraviolet radiation.

1.2 Photosynthetic pigments

To efficiently absorb the solar radiation, that after the travel thorough the atmosphere is mainly composed by wavelengths between 400 and 1000 nm, the photosynthetic organisms employ organic molecules, like chlorophylls (Chls), bacteriochlorophylls (BChls), carotenoids (Cars) and phycobilins with widely delocalized π systems that absorb in this spectral range. The types of pigments that occur in the different species and the ratio between them extensively vary in order to maximize the fitness of the organisms in different ecological niches, conferring to them the different colorations that are one of the most striking diversity in their phenotypes. This is reflected in the taxonomy of the photosynthetic organisms that is dominated by chromatic mentions. This great variation in the pigments applies to those dedicated to harvest the solar energy in the spectral region available in the habitat.

The collected energy, transiently stored as excitonic energy, is then funneled through energy transfer to a special pigment (or a couple of excitonically coupled pigments): the primary donor, which converts the energy of absorbed photons to electrochemical energy with a charge transfer event. The special pair, besides having an absorption strong enough to efficiently receive the excitation from the coupled light harvesting pigments, has to be capable to photochemically lose or gain electrons, providing a redox potential that for oxygenic photosynthesis has to be strong enough to oxidize water. In anoxygenic bacteria this role is consigned to different BChls, whereas almost all the oxygenic photosynthetic organisms use Chl *a*.

1.2.1 Chlorophylls

The structure of Chls and BChls is based on a porphyrinic ring with a fifth condensed ring, called the isocyclic ring. The five rings in Chls and BChls are lettered A through E, as reported in figure 1. Both Chls and BChls have a long hydrocarbon tail esterified to an acidic group of the D ring and coordinate a magnesium ion by means of the four pyrrolic nitrogens. Differences regarding the degree of unsaturation of the porphyrinic rings and their substituents distinguish between chlorophylls (*a, b, c1, c2, d, e* and *f*) and bacteriochlorophylls (*a, b, c,* c_s*, d, e, f* and *g*). The main difference is the number of the π electrons of the porphyrin ring, in particular all the Chls and BChls *c, d, e* and *g* are chlorins, meaning that their molecules have a 20-electron π system due to the reduction of D ring, whereas the remaining BChls belong to the bacteriochlorins due to the further reduction of B ring that leads to a 18-electron π system. Closely related classes of molecules involved in photosynthesis are pheophytins (Ph) and bacteriopheophytins (BPh), which are respectively Chls and BChls lacking the central Mg^{2+} ion.

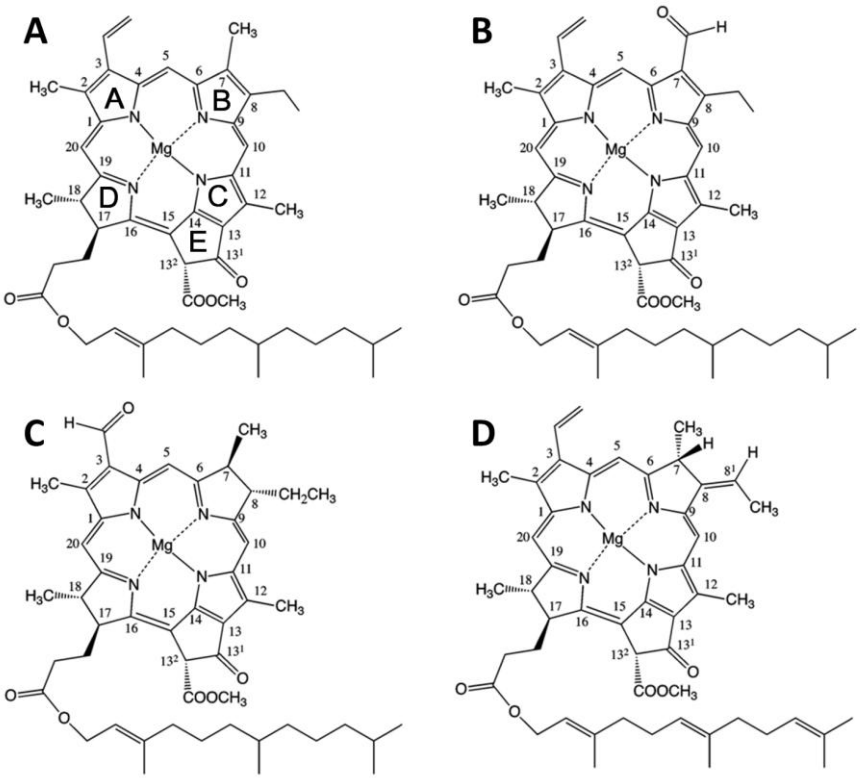

Figure 1: Molecular structure of Chl a ***(A)****, Chl b* ***(B)****, BChl a* ***(C)*** *and BChl g* ***(D)****, according to the IUPAC Numbering System.*

In photosynthetic organisms Ph has a function of intermediary electron acceptor and Chls are the pivotal pigments in light reactions, in which these molecules perform the essential tasks of harvesting the light and transforming the initial excitation in a more utilizable charge

separation that is successively exploited to synthesize high energy molecules. Among the chlorophylls, Chl *a* has a prominent role,(Björn et al. 2009) due to the fact that it is the only pigment capable to perform the challenging photo-reductive role required by oxygenic photosynthesis, due to its ability to generate a radical cation at +1 V in PS II, a radical anion at -1 V in PS I and to be completely redox silent in antennas. The only exception to his omnipresence is Chl *d*, which is found in some cyanobacteria that live in muddy water enriched in wavelengths longer than 700 nm, which are unusable by Chl *a* based photosynthetic organisms.(Hu et al. 1998)

Depending on their evolutionary ancestry, the various *taxa* of photosynthetic organisms contain different sets of light harvesting (bacterio)chlorophylls, specifically designed to adapt to the extremely different intensity and spectral profile of the available light in the different ecological niches in which photosynthetic organisms have evolved. The absorption spectra of Chls and BChls, have in common the two major absorption bands: one in the blue or near UV region and one in the red or near IR region. The lack of a significant absorption in the green region gives to chlorophylls their characteristic green or blue–green colour. These absorption bands are π→π* transitions that involve the electrons in the conjugated π system of the (bacterio)chlorin macrocycle. The absorption and fluorescence spectra of chlorophyll *a* in diethyl ether are shown in figure 2.

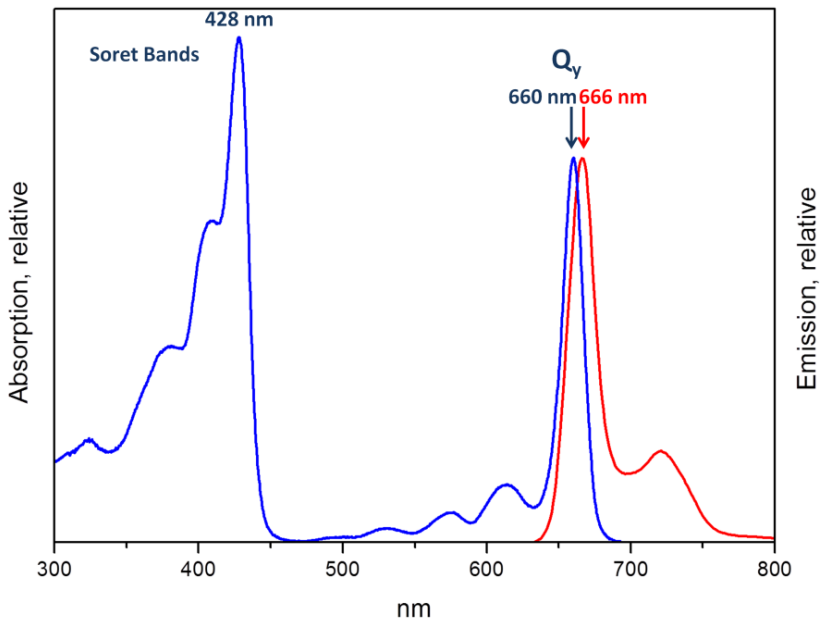

Figure 2: Absorption (blue line) and fluorescence (red line) spectra of Chl a in diethyl ether. The two spectra are normalized at their Q_y maxima.

The absorption spectrum can be described theoretically using a "four orbital" model, originally proposed by Gouterman in 1961.(Gouterman 1961) This model (depicted in figure 3) describes the system by means of only four π molecular orbitals, the two HOMOs (Ψ_1 and Ψ_2)

and the two LUMOs (Ψ_3 and Ψ_4), with the transition observable in the spectrum simply described as the promotion of an electron from one of the HOMOs to one of the LUMOs.

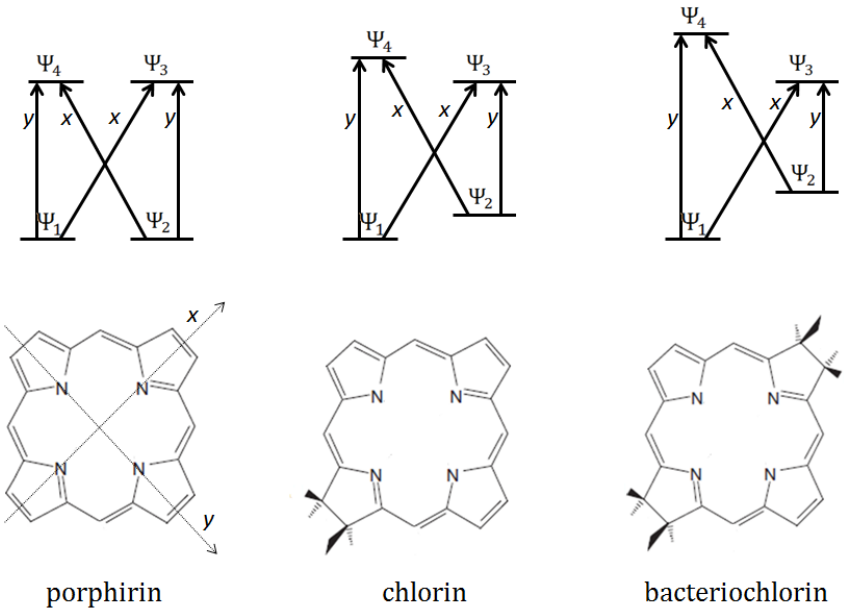

Figure 3: Energy diagrams, excitation and structures of porphyrin, chorine and bacteriochlorophyll.

The model starts the description from the symmetric porphyrin, described by two nearly isoenergetic HOMOs and two roughly degenerate LUMOs, that give rise to four excited states referred to as Q_y, Q_x, B_y and B_x. In this description *x* and *y* correspond to the molecular axes reported in figure 3, and convey the symmetry of the product of the initial and final wavefunction for each transition. The transitions with the same symmetry can interact, leading to the final excited states grouped in the low energy Q_y and Q_x and the more energetic B_y and B_x (also known as Soret bands). In chlorin, the reduction of one of the pyrrole rings perturbs the symmetry of the system, stabilizing some orbitals and destabilizing others, as is reported in figure 3. As a result, the lowest energy Q_y band moves to lower energy and gains dipole strength, while the opposite happens to B_y. The further reduction of another pyrrole, leading to a bacteriochlorin, maintains this trend with a further red-shift of the Q_y.

Upon optical excitation and subsequent internal conversion, Chls are promoted into their first singlet excited state ($\text{Chl} \xrightarrow{hv} {}^1\text{Chl}^*$). In solution the decay of this excited state involves, with a high quantum yield (more than 60% for Chl *a*)(Bowers & Porter 1967) the intersystem crossing (ISC) process that gives rise to the long-lived excited triplet state (${}^1\text{Chl}^* \xrightarrow{ISC} {}^3\text{Chl}^*$) and, as secondary contribution, the fluorescence that accounts for about 30% for Chl *a*.(Latimer et al. 1956) The ${}^3\text{Chl}^*$ is known to transfer its energy to O_2 in its triplet ground state (${}^3\text{Chl}^* + {}^3O_2 \rightarrow {}^1\text{Chl} + {}^1O_2^*$)(Küpper et al. 2002; Krasnovskii jr. & Kovalev 2014) due to the higher energy of its triplet state (10800 cm^{-1} for ${}^3\text{Chl}^*$(Krasnovskiĭ et al. 1974; Hartzler et al. 2014) in comparison to 7900 cm^{-1} for ${}^1O_2^*$(Krasnovskii jr. 1979; Hartzler et al. 2014)), generating the excited singlet

state $^1O_2$* which is a highly reactive oxygen species responsible, in natural systems, for damage of proteins, pigments and lipids of the photosynthetic machinery.(Triantaphylidès et al. 2008)

In antenna complexes the excitation is mainly transferred through Förster resonance energy transfer (FRET),(Förster 1939) a mechanism based on the interaction of the transition dipole moments of acceptors and donors. The process proceeds through a hopping among the Chls following the energetic gradient, reaching the reaction center (RC) on a 10-100 picosecond timescale.(Freiberg 2004) The transfer of the excitation reduces the time that the excitation spends on every Chl with a consequent reduction of the triplet production, which still remains constitutively present with a yield that has been estimated between 5% and 25% depending on the system and the light conditions.(Foyer & Harbinson 1999) In typical chlorophyll-containing proteins, the formation of singlet oxygen is prevented by carotenoids positioned close to the Chls, because these molecules effectively quench the ^{3}Chl* through triplet-triplet energy transfer (TTET).(Foote 1976; Siefermann-Harms 1987)

1.2.2 Carotenoids

Carotenoids (Car) are extended molecules with a delocalized π electron system. They are composed of a hydrocarbon backbone that contains a series of conjugated double bonds.(Young & Britton 1993) Two major groups of carotenoids are synthesized by photosynthetic organisms: *carotenes,* which are hydrocarbon polyenes either linear or cyclized at one or both ends of the molecule, and *xanthophylls,* which are oxygenated derivatives of carotenes. These molecules perform several critical functions in the photosynthetic apparatus including their acting as structural components of photosynthetic proteins, as accessory pigments for light harvesting, and as components of the photoprotection processes devoted to dissipate excess energy and scavenge singlet oxygen and chlorophyll triplets. In figure 4 the molecular structures of the main carotenoids presents in oxygenic photosynthetic organisms are reported.

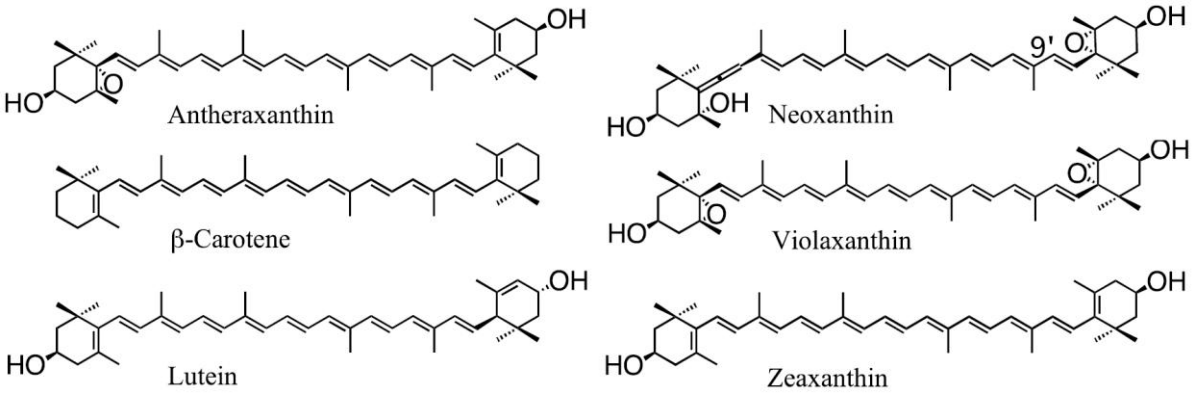

Figure 4: Structures of β-Carotene, Antheraxanthin, Lutein (Lut), Neoxanthin (Neo), Violaxanthin (Vio) and Zeaxanthin (Zea).

Traditionally, even for non linear polyenes and carotenoids, it is customary to assume that their electronic states follow those expected for an idealized C_{2h} symmetry; because the excited states of the non-linear molecules retain many of the characteristics of the linear systems.(Christensen 1999) The detailed spectroscopic information available for model polyenes leads to a simple, three-level energy scheme:

$$S_2(1^1B_u^+) > S_1(2^1A_g^-) > S_0(1^1A_g^-)$$

The optical properties of Cars are characterized by the fact that the $S_0 \rightarrow S_1$ transition is symmetry forbidden and the light is absorbed mainly by the $1^1B_u^+$ state. This $S_0 \rightarrow S_2$ transition is very strong and increases in intensity with the extent of π electron conjugation. After excitation, the S_2 state rapidly decays in a few hundred femtoseconds to the "dark" S_1 state, which then decays back to the ground state on a picosecond time scale with radiationless transition, due to the fact that also the $S_1 \rightarrow S_0$ is symmetry forbidden (the fluorescence quantum yield is less than 10^{-5}(Andersson et al. 1995)). The electronic spectra of naturally occurring carotenoids tend to be significantly broadened, and characterized by the fact that the $S_0 \rightarrow S_2$ transition undergoes a pronounced bathochromic shift when the polarisability of the solvent increases. The yellow-orange coloration of carotenoids is due to their strong $S_0 \rightarrow S_2$ absorption that falls in the greenish part of the spectrum, a portion which is not very well covered by any of the types of chlorophylls. At water depths of more than a few tens of meters, most of the available light happens to be in this middle region of the visible spectrum, due to the fact that the red light has been absorbed and the blue light scattered, making carotenoids crucial in the light harvesting of many aquatic photosynthetic organisms.(Larkum & Barrett 1996) In fact carotenoids in excited singlet states can transfer their energy to nearby chlorophylls, contributing in the light harvesting as accessory pigments (see figure 5).

The direct ISC process $S_1 \rightarrow T_1$ for carotenoids is not very probable due to the fast radiationless $S_1 \rightarrow S_0$ decay, nevertheless the triplet state of carotenoids has a crucial physiological role in photosynthetic organisms, because it can be populated from ^{3}Chl* and $^1O_2$*, lying at less energy (6800 cm^{-1} for β-carotene)(Lambert & Redmond 1994) compared to them. The resulting ^{3}Car* is an innocuous species that relaxes in microseconds to the ground state.(Land et al. 1970) This quenching mechanism is pivotal in photoprotection, explaining the ubiquitous presence of carotenoids in the photosynthetic apparatus of photosynthetic organisms. The relative energetic levels of chlorophyll, oxygen and carotenoid and the energy transfer (ET) pathways are summarized in the following figure.

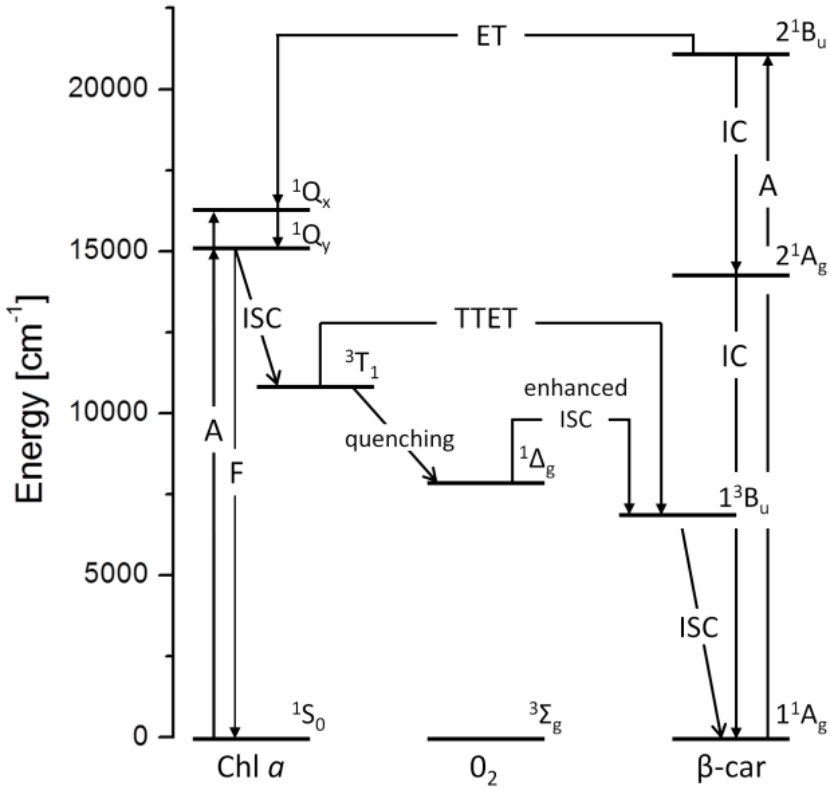

Figure 5: Scheme of the electronic states of Chl a, oxygen and β-carotene and the energy transfer pathways between them. The most allowed absorptions (A), fluorescence (F), internal conversions (IC), intersystem crossings (ISC), energy transfer are indicated.

1.3 Structure of the photosynthetic apparatus

The marvelous process of photosynthesis is carried out by supramolecular assemblies containing hundreds of cooperating protein subunits that, despite a great variation in the architecture among the different organisms, show many common features. This reflects the physical constrains determining the way in which the evolutionary pressure has shaped the development of photosynthesis.

During the early events of photosynthesis the light quanta are harvested from the pigments of the "antenna" proteins and converted into excited electronic energy, which is then funneled to the reaction center (RC), where a charge separation between the primary donor and acceptor takes place.(Ort & Yocum 1996) To stabilize the first photo-induced charge separation, the electron is further transferred from the primary acceptor to subsequent acceptors in the so called electron transport chain:

$$D_1^* A_1 A_2 \xRightarrow{\substack{charge \\ separation}} D_1^+ A_1^- A_2 \xRightarrow{\substack{first \\ electron \\ transfer}} D_1^+ A_1 A_2^- \overset{\cdots}{\Rightarrow}$$

while concomitantly the primary donor is reduced.

Two types of RC have been recognized in photosynthetic organisms: type I reaction centers are found in green filamentous bacteria, Heliobacteria, cyanobacteria and eukaryotes; type II reaction centers are found in purple bacteria, green sulfur bacteria, cyanobacteria and eukaryotes. Only oxygenic photosynthetic organisms (cyanobacteria and eukaryotes) possess both types of reaction centers, which act in series to couple the absorption of solar radiation with the transfer of electrons from water to $NADP^+$ and the generation of a transmembrane protonic gradient. In figure 6 the "Z scheme",(Hill & Bendall 1960) which describes the two coupled processes, is reported.

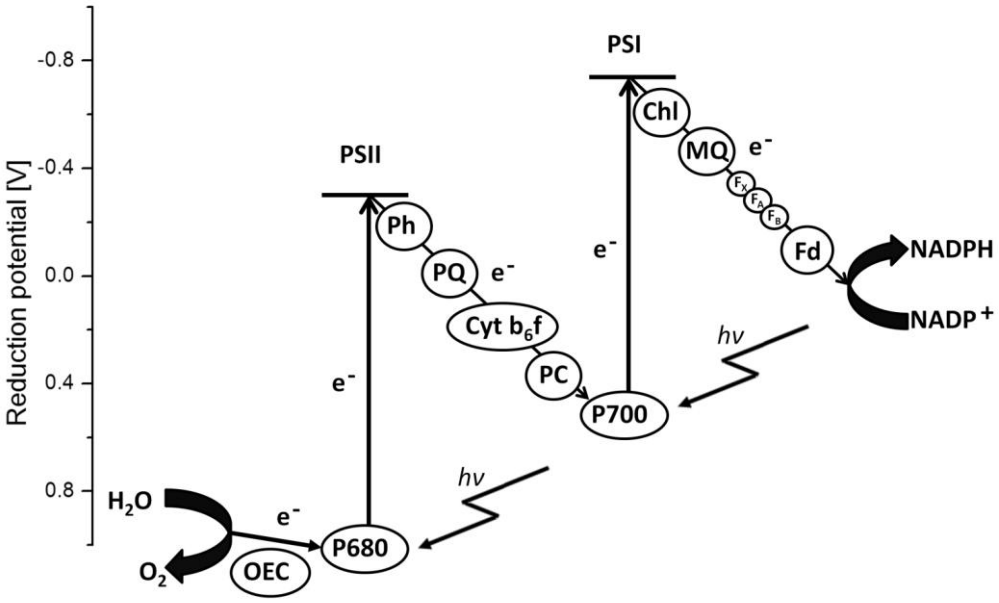

Figure 6: Z scheme of oxygenic photosynthesis.

In oxygenic organisms the primary donor is a dimer of Chl *a* (P680 for the PS II and P700 for the PS I), whereas the primary acceptor is Ph *a* in PS II and Chl *a* in PS I. The oxidized primary donor is then reduced in PS II by electrons provided by water, meanwhile in PS I $P700^+$ is reduced by plastocyanin (PC). In PS II the electrons deriving from water are used to reduce plastoquinone (PQ) to plastoquinol that diffuses in the membrane from the PS II to the Cytochrome b_6f complex (Cyt b_6f), an oxide-reductase enzyme that transfers electrons between the two RCs, from PS II to PS I. Indeed Cyt b_6f uses electrons to reduce plastocyanin (PC), which as mentioned above after having approached the PS I, is oxidized by $P700^+$.

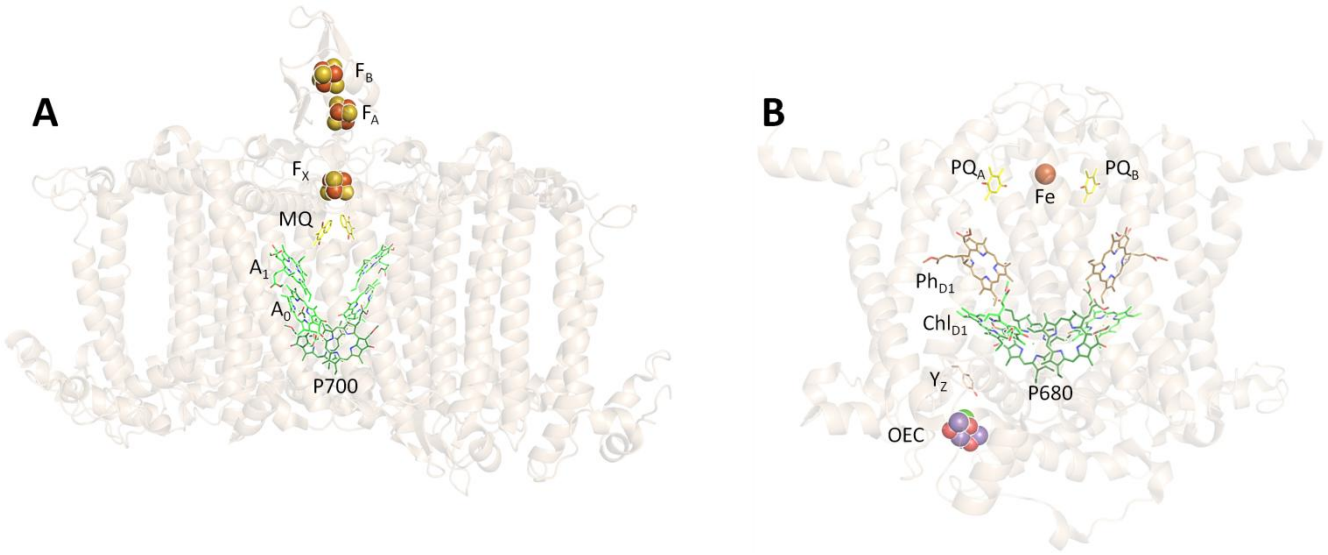

Figure 7: Side view of the structure Photosystem I (Umena et al. 2011) ***(A)*** *and Photosystem II* (Jordan et al. 2001) ***(B)*** *from Thermosynechococcus vulcanus. Only the cofactors involved in light-induced electron transport, i.e., P700, A_0, A_1, MQ, F_X, F_A, and F_B, for PSI and OEC, P680, Chl_{D1}, Ph_{D1}, PQ_A, PQ_B , and Fe for PSII are shown along with the backbones.*

The electron deriving from the photo-oxidation of P700, after absorption of light, is transferred via a Chl *a* acceptor molecule to a menaquinone (MQ) and three iron-sulfur centers (F_X, F_A and F_B) to be used to reduce another electron shuttle, the ferredoxin (Fd). Finally Fd:$NADP^+$ oxidoreductase (FNR) uses electrons from Fd to reduce NADP+ to NADPH. Concomitantly a transmembrane proton gradient is generated due to the quinone shuttle, that is reduced on the stromal side by both PS II and Cyt b_6f, whereas is oxidized back on the luminal side by Cyt b_6f. The overall electron transport chain is depicted in figure 8.

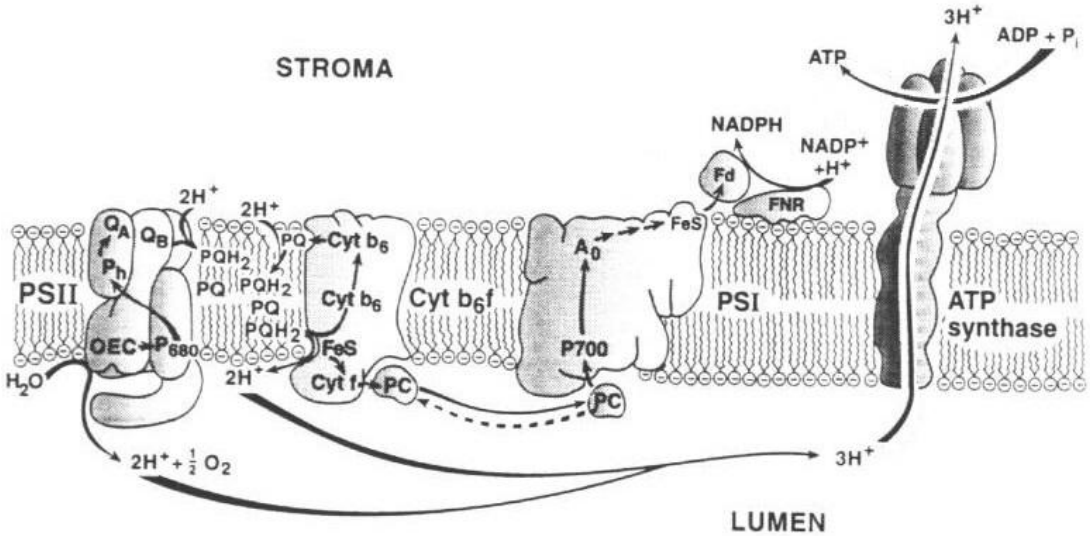

Figure 8: Schematic diagram of the oxygenic electrons transport chain in eukaryotic thylakoid membrane.(Ort & Yocum 1996)

To absorb efficiently the solar radiation, photosynthetic organisms could not rely upon RCs alone and have evolved a wide variety of light harvesting complexes, known as antenna complexes. If on one hand RCs have been highly conserved over millions of years and probably have been invented only once,(Xiong & Bauer 2002; Giacometti & Giacometti 2010; Cardona 2016) on the other hand light-harvesting complexes are present with striking differences between different photosynthetic organisms. Different kinds of antenna complexes have independent evolutionary origins specifically designed to adapt to the extremely different intensity and spectral profile of the available light in the different ecological niches in which photosynthetic organisms have evolved.

Usually the pigments are coordinated by proteins, which accomplish the dual task of properly orienting the pigments to obtain efficient energy transfer, and modulating their optical properties to improve the proficiency of absorption and transfer of the excitation energy.(Croce & van Amerongen 2014) The antennas can be either water soluble or integral membrane proteins. The main examples of the first kind are the Fenna-Matthews-Olson(Fenna & Matthews 1975) complex of *Chlorobiaceae*, the Peridinin-Chlorophyll-Protein(Hofmann et al. 1996) of *Dinoflagellates* and the phycobilisomes(Glazer 1985) of cyanobacteria, red algae and glaucophytes. Integral membrane proteins are common to both bacteria and eukaryotes, and are all structurally based on membrane-spanning α-helixes moieties that harbor (B)Chls and Cars. The antenna proteins in eukaryotes, which share high homology in the sequence, leading to transmembrane proteins that possess three α-helical transmembrane regions, are known as light-harvesting complexes (LHC).(Green & Durnford 1996)

Plants and algae carry out oxygenic photosynthesis in chloroplasts, special semi-autonomous organelles that enfold in their interior an aqueous matrix known as stroma and an internal membrane called thylakoids. All the light harvesting and energy transducing functions are located in the thylakoids, which form a continuous membrane system that encloses an aqueous compartment called lumen. These structures form the grana, that in green algae and plants are highly staked and connected by lamellae. Phylogenentic studies have demonstrated that photosynthetic eukaryotes acquired photosynthetic properties from endosymbiosis with cyanobacteria,(Gray 1992) which are the most ancient photosynthetic organisms able to produce oxygen.(Schopf 1993)

1.4 Photoprotection

Light is of course essential for photosynthesis and supports most life on earth, but light may be defined as excessive when it exceeds the capacity of photosynthesis to use it for fuels photochemical processes. When this happens, light induces damage via the generation of high levels of reactive oxygen species (ROS). In chloroplasts, two major pathways of ROS formation exist: 1) electron transfer to molecular oxygen at the acceptor side of PS I(Mehler 1951) or at PS II,(Ananyev et al. 1994) leading to the formation of the superoxide radical (O_2^-) and, in subsequent reactions, hydrogen peroxide (H_2O_2) or hydroxyl radicals ($\cdot OH$);(Apel & Hirt 2004)

2) energy transfer from triplet chlorophyll ($^3Chl^*$) to molecular oxygen, leading to the formation of singlet oxygen ($^1O_2$).(Krieger-Liszkay 2005; Triantaphylidès & Havaux 2009) These species are powerful oxidizing agents, and eventually lead to photo-bleaching and cell death.

Under natural conditions, nearly all photosynthetic organisms are exposed to changing light intensities which may vary over three orders of magnitude in both the short-term (seconds to minutes) and the long-term (hours to seasons).(Demmig-Adams et al. 2012) In addition to that, also other stress conditions, as cold, drought and depletion of key metabolites as nitrogen or iron can contribute to enhance the effects of the light variability on the photosynthetic apparatus. This means that the existence of dynamic photoprotection mechanisms is required, which allows to modulate the efficiency of light harvesting and utilization in response to the environmental conditions. This has resulted in the evolution of a remarkable variety of processes needed to bear the fluctuations, by regulation of the absorption of light and managing of the excess light absorbed, at a molecular level. In fact, these regulatory mechanisms are tightly integrated with photosynthesis itself, and there is emerging evidence that when these processes are altered, the ability of plants to assimilate carbon over long time periods and to produce biomass is affected.(Külheim et al. 2002; Murchie & Niyogi 2011)

To prevent the excessive absorption of light and respond to long-term fluctuations, the size and quantity of the light harvesting complexes are regulated through changes in gene expression and/or proteolysis, whereas faster variations are managed by photorelocation of the chloroplasts within the cells and through leaf movements in plants. Fast responses to excess light include the photoprotection mechanism described above as triplet-triplet energy transfer (TTET), which involves the triplet state of carotenoids, and other mechanisms in which the excited singlet states of chlorophyll are deactivated, as reported in the following figure.

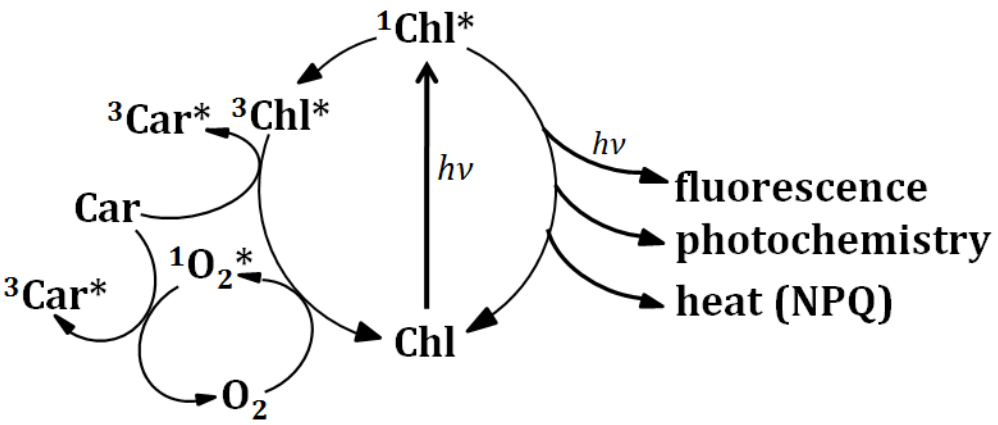

Figure 9: Possible fates of excited Chls.(Müller et al. 2001)

The photoprotective mechanisms that act in the light-harvesting complexes before the charge separation event, through the thermal dissipation of the excess light energy, are collectively called non-photochemical-quenching (NPQ). This class of mechanisms quench $^1Chl^*$ and harmlessly dissipate excess excitation energy as heat via enhanced internal conversion to

the ground state. These NPQ processes occur in almost all photosynthetic eukaryotes and they help to regulate and protect photosynthesis. NPQ can be divided into at least three different components according to their relaxation kinetics in darkness following a period of illumination, as well as their response to different inhibitors. The major and most rapid component in most algae and plants is the energy-dependent component, qE. This mechanism relaxes within seconds to minutes, and is stimulated by a combination of transmembrane proton gradient, the PsbS subunit of PS II and the enzymatic inter-conversion of violaxanthin and zeaxanthin (i.e. the xanthophyll cycle(Demmig-Adams 1990)). This cycle in plants, green algae, brown algae and *Eustigmatophyceae* consists on a pH-dependent conversion from violaxanthin, a xanthophyll with two epoxide groups, first to antheraxanthin (one epoxide group) and then to zeaxanthin (no epoxide group).

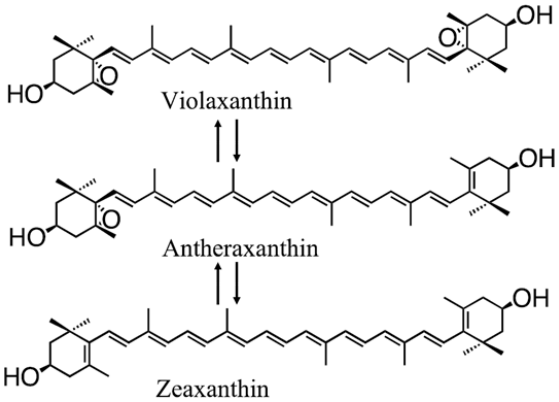

Figure 11: The violaxanthin cycle consisting of the de-epoxidation of violaxanthin in high light to first antheraxanthin and then zeaxanthin, catalyzed by violaxanthin de-epoxidase; zeaxanthin epoxidase catalyzes the reverse reaction.

A second component, qT, relaxes within ten of minutes. This component is due to the phenomenon of state transition, the uncoupling of LHCs from PS II regulated by the phosphorylation of the antenna proteins. The third component of NPQ shows the slowest relaxation (in the range of hours) and is related to photoinhibition of photosynthesis and is therefore called qI. This sustained mechanism is ascribable to a mix of long-term photoprotection and photodamage.

Moreover, in addition to the linear electron flow described previously (i.e. the electron transport chain described in paragraph 1.3) there are other electron transport systems that include cyclic electron transfer and water-water cycle(Asada 2000) that contribute to the photochemical utilization of the light energy in excess. This flexibility in the electron transport with multiple possible pathways contributes, when the linear electron flow is not fast enough in its turnover, to avoid the stagnation of the excitation that would lead to the production of dangerous species. The water-water cycle consists in the photo-reduction of dioxygen to water in PS I by electrons generated in PS II from water, whereas in cyclic electron transfer, as reported in figure 10, the electrons from ferredoxin are transferred back to quinone through different pathways.(Shikanai 2007) Although the contribution of the alternative electron sinks

appear to be limited in long term adaptations, they are especially important to respond to fast fluctuations.(Müller et al. 2001)

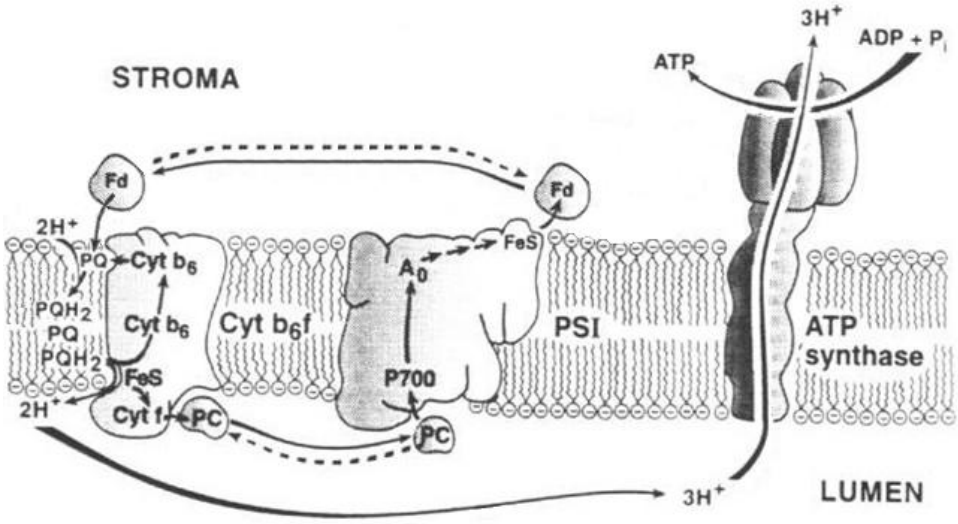

Figure 11: Schematic diagram of the cyclic transport chain in eukaryotic thylakoid membrane. (Ort & Yocum 1996)

In virtue of this complex and multifunctional array of safety valves,(Niyogi 2000) plants and algae are able to maintain a low steady-state ^{3}Chl* yield in a wide range of light intensities due to a combination of charge separation and NPQ. The formation of ^{3}Chl* and $^1O_2$ is particularly severe in the onset of the light-stress conditions. In this scenario the constitutive mechanism of TTET played by carotenoids represents the fastest way of response taking place before the onset of the long term adaptation mechanisms

Other mechanisms to avoid $^1O_2$ either sensitization or damage in (B)Chl containing proteins have been reported concerning both photosynthetic and non-photosynthetic proteins. It has been shown that the formation of the triplet excitons in the BChl aggregates can be sufficient to lower the triplet excited state energy below that of singlet oxygen, resulting in an effective photoprotection as suggested for BChl c aggregates of chlorosomes.(Kim et al. 2007) Also pigment-solvent interactions, similarly to the mentioned pigment-pigment interactions, may shift the triplet state energies of several chlorin-type molecules by up to 0.11 eV,(Hartzler et al. 2014) possibly below the energy of $^1O_2$, which would inhibit the energy transfer from the (B)Chl triplet state to O_2. This is likely the mechanism underlying the photostability of the Fenna-Matthews-Olson (FMO) complex, which contains several BChl a molecules but no carotenoids.(Kihara et al. 2015) Another photoprotective mechanism involving the protein matrix have been identified in the Cytochrome b6f complex. This complex binds a single Chl *a*, that has been shown to have its singlet excited state lifetime reduced by a factor of 20–25 due to electron transfer with a nearby tyrosine residue,(Dashdorj et al. 2005) with a consequent strong reduction of the formation of ^{3}Chl*.

In the framework of these diverse photoprotective strategies, an intriguing and still unresolved case is represented by the Water Soluble Chlorophyll Proteins (WSCPs) and its remarkable photostability.

1.4.1 WSCP

In the landscape of the chlorophyll-binding proteins, the Water Soluble Chlorophyll Proteins (WSCPs), a class of proteins found in plants belonging to the *Brassicaceae* family (flowering plants comprising among others cabbages, horseradish, and thale cress), are unique. These tetrameric proteins, despite binding chlorophylls, are non-photosynthetic proteins.(Horigome et al. 2007) In these complexes the bound Chls are organized in "open sandwich" dimers, characterized by a distribution of the oscillator strength between the excitonic bands with the main excitonic band at higher energies,(Renger et al. 2011) contrarily from the behavior typical of special pairs in photosynthetic reaction centers.

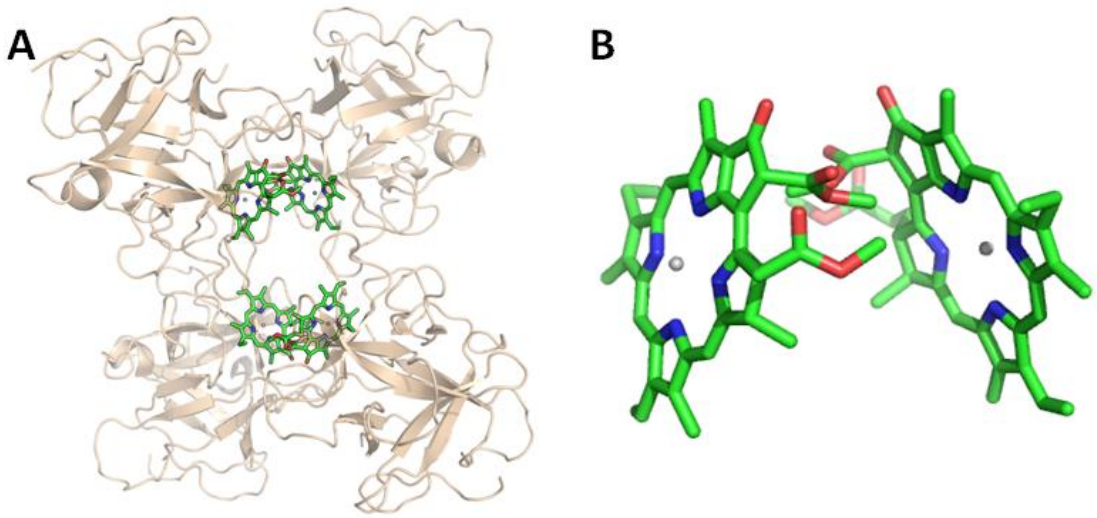

Figure 10: ***A*** *Structure of Lepidium virginicum WSCP*(Horigome et al. 2007) *with the chlorophylls a in green and the polypeptide chains in wheat.* ***B*** *Structure of one of the two "open sandwich" dimers. The phytols chains have been omitted for clarity.*

The physiological function of WSCPs is still unknown, however a possible role of these proteins in the scavenging of free Chls has been proposed,(Takahashi et al. 2012) due to their capability to bind Chls granting them a remarkably high photostability.(Schmidt et al. 2003) Alternatively, a role in herbivore resistance activation during greening and in programmed cell death. at least during flower development, has been proposed.(Boex-fontvieille, Rustgi, Wettstein, et al. 2015; Boex-fontvieille, Rustgi, Reinbothe, et al. 2015)

The photostability of this protein(Schmidt et al. 2003) still needs to be elucidated in its molecular mechanism. In fact, due to the absence of any bound carotenoid, it can not be attributed to the capability of these polyenes to operate as ^{3}Chl quenchers.

1.5 References

Ananyev, G. *et al.,* 1994. The photoproduction of superoxide radicals and the superoxide dismutase activity of Photosystem II. The possible involvement of cytochrome b559. *Photosynthesis Research*, 41(2), pp.327–338.

Andersson, P.O. *et al.,* 1995. Solvent and Temperature Effects on Dual Fluorescence in a Series of Carotenes. Energy Gap Dependence of the Internal Conversion Rate. *Journal of Physical Chemistry*, 99, pp.16199–16209.

Apel, K. & Hirt, H., 2004. REACTIVE OXYGEN SPECIES: Metabolism, Oxidative Stress, and Signal Transduction. *Annual Review of Plant Biology*, 55, pp.379–399.

Asada, K., 2000. The water-water cycle as alternative photon and electron sinks. *Philosophical transactions of the Royal Society of London Series B-Biological Sciences*, 355, pp.1419–1431.

Björn, L.O. et al., 2009. A viewpoint : Why chlorophyll a ? *Photosynthesis Research*, 99, pp.85–98.

Boex-fontvieille, E., Rustgi, S., Reinbothe, S., and Reinbothe, C. 2015. A Kunitz-Type Protease Inhibitor Regulates Programmed Cell Death during Flower Development in Arabidopsis Thaliana. *Journal of Experimental Botany*, 66, pp.6119–6135.

Boex-fontvieille, E., Rustgi, S., Von Wettstein, D., *et al.,* 2015. Water-Soluble Chlorophyll Protein Is Involved in Herbivore Resistance Activation during Greening of Arabidopsis Thaliana. *Proceedings of the National Academy of Sciences,* 112, pp.7303–7308.

Bowers, P.G. & Poter, G., 1967. Quantum Yields of Triplet Formation in Solutions of Chlorophyll. *Proceedings of the Royal Society of London. Series A, Mathematical and Physical Sciences*, 296(1447), pp.435–441.

Cardona, T., 2016. Reconstructing the Origin of Oxygenic Photosynthesis : Do Assembly and Photoactivation Recapitulate Evolution? *Frontiers in Plant Science*, 7, pp.1–16.

Christensen, J., 1999. *The Electronic States of Carotenoids*. In H. A. Frank et al., eds. The photochemistry of Carotenoids. Kluwer Academic Press.

Croce, R. & van Amerongen, H., 2014. Natural strategies for photosynthetic light harvesting. *Nature Chemical Biology*, 10(7), pp.492–501.

Dashdorj, N., Zhang, H., Kim, H. *et al.,* 2005. The Single Chlorophyll *a* Molecule in the Cytochrome b_6f Complex: Unusual Optical Properties Protect the Complex against Singlet Oxygen. *Biophysical Journal,* 88, pp.4178-4187

Demmig-Adams, B., 1990. Carotenoids and photoprotection in plants: A role for the xanthophyll zeaxanthin. *Biochimica et biophysica acta*, 1020, pp.1–24.

Demmig-Adams, B., *et al.*, 2012. Modulation of photosynthetic energy conversion efficiency in nature: From seconds to seasons. *Photosynthesis Research*, 113, pp.75–88.

Fenna, R.E. & Matthews, B.W., 1975. Chlorophyll arrangement in a bacteriochlorophyll protein from Chlorobium limicola. *Nature*, 258(5536), pp.573–577.

Foote, C.S., 1976. *Photosensitized oxidation and singlet oxygen: consequences in biological systems*. In W. A. Pryor, ed. Free radicals in biology vol. 2. Academic Press.

Förster, T., 1939. Zwischenmolekulare Energiewanderung und Fluoreszenz. *Annalen der physik*, 437,

pp.55–75.

Foyer, C.H. & Harbinson, J., 1999. *Relationships between antioxidant metabolism and carotenoids in the regulation of photosynthesis*. In H. A. Frank et al., eds. The photochemistry of Carotenoids. Kluwer Academic Press.

Freiberg, A., 2004. *Coupling of antennas to reaction centers*. In R. E. Blankenship, M. T. Madigan, & C. E. Bauer, eds. Advances in photosynthesis and respiration vol. 2. Kluwer Academic Press.

Giacometti, G. & Giacometti, G.M., 2010. Evolution of Photosynthesis and Respiration: Which Came First? *Applied Magnetic Resonance*, 37, pp.13–25.

Glazer, A.N., 1985. Light Harvesting by Phycobilisomes. *Annual Review of Biophysics and Biophysical Chemistry*, 14, pp.47–77.

Gouterman, M., 1961. Spectra of Porphyrins. *Journal of Molecular Spectroscopy*, 6, pp.138–163.

Gray, M.W., 1992. The Endosymbiont Hypothesis Revisited. *International Review of Cytology*, 141, pp.233–357.

Green, B.R. & Durnford, D.G., 1996. The Chlorophyll-Carotenoid Proteins of Oxygenic Photosynthesis. Annual review of plant physiology and plant molecular biology, 47, pp.685–714.

Harold, F.M., 2001. The Way of the Cell: Molecules, Organisms, and the Order of Life, New York: Oxford University Press.

Hartzler, D.A. et al., 2014. Triplet Excited State Energies and Phosphorescence Spectra of (Bacterio)Chlorophylls. *The Journal of Physical Chemistry* B, 118, pp.7221–7232.

Hill, R. & Bendall, F., 1960. Function of the Two Cytochrome Components in Chloroplasts: A Working Hypothesis. *Nature*, 186, pp.136–137.

Hofmann, E. et al., 1996. Structural Basis of Light Harvesting by Carotenoids : Peridinin-Chlorophyll-Protein from Amphidinium carterae. *Science*, 272(5269), pp.1788–1791.

Horigome, D. et al., 2007. Structural mechanism and photoprotective function of water-soluble chlorophyll-binding protein. *Journal of Biological Chemistry*, 282(9), pp.6525–6531.

Hu, Q. et al., 1998. A photosystem I reaction center driven by chlorophyll d in oxygenic photosynthesis. *Proceedings of the National Academy of Sciences*, 95(22), pp.13319–13323.

Jordan, P. et al., 2001. Three-dimensional structure of cyanobacterial photosystem I at 2.5 Å resolution. *Nature*, 411, pp.909–917.

Kasting, J.F., 1993. Earth's Early Atmosphere. *Science*, 259, pp.920–926.

Kihara, S., Hartzler, D. A., Orf, G. S., *et al.*, 2015. The Fate of the Triplet Excitations in the Fenna–Matthews–Olson Complex. *Journal Physical Chemistry B*, 119(18), pp.5765-5772

Kleidon, A., 2010. Life, hierarchy, and the thermodynamic machinery of planet Earth. *Physics of Life Reviews*, 7(4), pp.424–460.

Krasnovskiĭ, A.A., Lebedev, N.N. & Litvin, F.F., 1974. Spectral characteristics of chlorophyll and pheophytin a and b phosphorescence. *Proceedings of the USSR Academy of Sciences*, 216(6), pp.1406–1409.

Krasnovskii jr., A.A., 1979. Photoluminescence of singlet oxygen in pigment solutions. *Photochemistry and Photobiology,* 29, pp.29–36.

Krasnovskii jr., A.A. & Kovalev, Y. V, 2014. Spectral and Kinetic Parameters of Phosphorescence of Triplet Chlorophyll a in the Photosynthetic Apparatus of Plants. *Biochemistry (Moscow)*, 79(4), pp.349–361.

Krieger-Liszkay, A., 2005. Singlet oxygen production in photosynthesis. *Journal of Experimental Botany*, 56(411), pp.337–346.

Külheim, C., Agren, J. & Jansson, S., 2002. Rapid regulation of light harvesting and plant fitness in the field. *Science*, 297(2002), pp.91–93.

Küpper, H. et al., 2002. Kinetics and efficiency of excitation energy transfer from chlorophylls , their heavy metal-substituted derivatives , and pheophytins to singlet oxygen. *Biochimica et Biophysica Acta (BBA) - General Subjects*, 1572(1), pp.107–113.

Lambert, C. & Redmond, R.W., 1994. Triplet energy level of p-carotene. *Chemical Physics Letters*, 228, pp.495–498.

Land, E.J., Sykes, A. & Truscott, T.G., 1970. The in vitro photochemistry of biological molecules - II. The triplet states of β-carotene and lycopene excited by pulse radiolyisis. *Photochemistry and Photobiology*, 13, pp.311–320.

Larkum, A.W.D. & Barrett, J., 1996. *Light harvesting processes in algae*. In H. W. Woolhouse, ed. Advances in Botanical Research vol. 10. Academic Press.

Latimer, P., Bannister, T.T. & Rabinowitch, E., 1956. Quantum Yields of Fluorescence of Plant Pigments. *Science*, 124(3222), pp.585–586.

Maturana, H.R. & Varela, F.J., 1980. *Autopoiesis and Cognition: The Realization of the Living*,

Mehler, A.H., 1951. Studies on reactions of illuminated chloroplasts: I. Mechanism of the reduction of oxygen and other hill reagents*. Archives of Biochemistry and Biophysics*, 33(1), pp.65–77.

Müller, P., Li, X.P. & Niyogi, K.K., 2001. Non-photochemical quenching. A response to excess light energy. *Plant physiology*, 125, pp.1558–1566.

Murchie, E.H. & Niyogi, K.K., 2011. Manipulation of photoprotection to improve plant photosynthesis. *Plant physiology*, 155, pp.86–92.

Niyogi, K.K., 2000. Safety valves for photosynthesis. *Current Opinion in Plant Biology*, 3, pp.455–460.

Ort, D.R. & Yocum, C.K., 1996. *Oxygenic Photosynthesis: the light reaction*. In Govindjee, ed. Advances in Photosynthesis vol. 4. Kluwer Academic Press.

Raven, J.A., 2009. Contributions of anoxygenic and oxygenic phototrophy and chemolithotrophy to carbon and oxygen fluxes in aquatic environments. *Aquatic Microbial Ecology*, 56(2), pp.177–192.

Renger, G. et al., 2011. Water soluble chlorophyll binding protein of higher plants: A most suitable model system for basic analyses of pigment-pigment and pigment-protein interactions in chlorophyll protein complexes. *Journal of Plant Physiology*, 168(12), pp.1462–1472.

Rosing, M.T., 1999. 13C-Depleted Carbon Microparticles in > 3700-Ma Sea-Floor Sedimentary Rocks from West Greenland. *Nature*, 283, pp.674–676.

Schmidt, K. et al., 2003. Recombinant water-soluble chlorophyll protein from Brassica oleracea var. Botrys binds various chlorophyll derivatives. *Biochemistry*, 42, pp.7427–7433.

Schopf, J.W., 1993. Microfossils of the Early Archean Apex Chert: New Evidence of the Antiquity of Life. *Science*, 260(5108), pp.640–646.

Shikanai, T., 2007. Cyclic Electron Transport Around Photosystem I: Genetic Approaches. *Annual Review of Plant Biology*, 58, pp.199–217.

Siefermann-Harms, D., 1987. The light-harvesting and protective functions of carotenoids in photosynthetic membranes. *Physiologia Plantarum*, 69(3), pp.561–568.

Takahashi, S. et al., 2012. Molecular cloning, characterization and analysis of the intracellular localization of a water-soluble chl-binding protein from brussels sprouts (brassica oleracea var. gemmifera). *Plant and Cell Physiology*, 53(5), pp.879–891.

Triantaphylidès, C. et al., 2008. Singlet Oxygen Is the Major Reactive Oxygen Species Involved in Photooxidative Damage to Plants. *Plant physiology*, 148, pp.960–968.

Triantaphylidès, C. & Havaux, M., 2009. Singlet oxygen in plants: production, detoxification and signaling. *Trends in Plant Science*, 14, pp.219–228.

Umena, Y. et al., 2011. Crystal structure of oxygen-evolving photosystem II at a resolution of 1.9 Å. *Nature*, 473, pp.55–60.

Van Valen, L., 1971. The Hystory and Stability of Atmospheric Oxygen. *Science*, 171(3970), pp.439–443.

Vernadski, V., 1926. *Biosfera*, Leningrad: Nauka.

Vrieze, J. & Hoff, A.J., 1995. The orientation of the triplet axes with respect to the optical transition moments in (bacterio) chlorophylls. *Chemical Physics Letters*, 237, pp.493–501.

Xiong, J. & Bauer, C.E., 2002. A cytochrome b origin of photosynthetic reaction centers: an evolutionary link between respiration and photosynthesis. *Journal of molecular biology*, 322(5), pp.1025–1037.

Young, A. & Britton, G., 1993. *Carotenoids in photosynthesis,* Chapman & Hall.

The triplet state

In biological systems, with the remarkable exception of the molecular oxygen, the triplet states usually encountered are metastable excited states of unsatured organic molecules. This kind of molecules is ubiquitous in biological materials, ranging from aromatic moieties in amino acids and nucleotides to essential redox cofactor as nicotinamide, hemes and flavins and holochromes as carotenes, chlorins and bacteriochlorins. The triplet generation is often viewed as a weak perturbation of the molecular system that allows the study of its structure and environment in a very selective way due to the availability of dedicated spectroscopical techniques.

2.1 The physics of the triplet state

The vast majority of the organic molecules in the ground state possess an even number of electrons all coupled to give a total electron spin magnetic momentum $S = 0$, which, due to its spin multiplicity $2S + 1 = 1$, is called singlet state. For these molecules the triplet state is an excited electronic states thermally or optically populated from the fundamental state, so called due to its $S = 1$ that leads to a spin multiplicity equal to 3. Only the optical populating mechanism of triplet state will be considered because is relevant for the triplet states studied in this thesis.

The system of interest, an orbitally nondegenerate state with weak spin-orbit coupling, can be treated in good approximation as a two-electron system whose wavefunction can be expressed as

$$\Psi(1,2) = \Phi(1,2) \cdot \Sigma(1,2)$$

where Φ is the spatial part of the overall wavefunction Ψ that depends only on the spatial coordinates of the two electrons, whereas Σ is the spin part that depends solely on the spin coordinates. The two-electron approximation is justified by the fact that in the description of the populating and decaying mechanisms of the triplet state only the singlet fundamental state (S_0) and the first singlet and triplet excited levels (respectively S_1 and T_1) both generated by the promotion of a single electron from the highest occupied molecular orbital (HOMO) to the lowest unoccupied molecular orbital (LUMO), are involved. The factorization in spatial and spin wavefunctions is valid under the assumption that the spin-orbit coupling interaction is weak enough to be neglected.

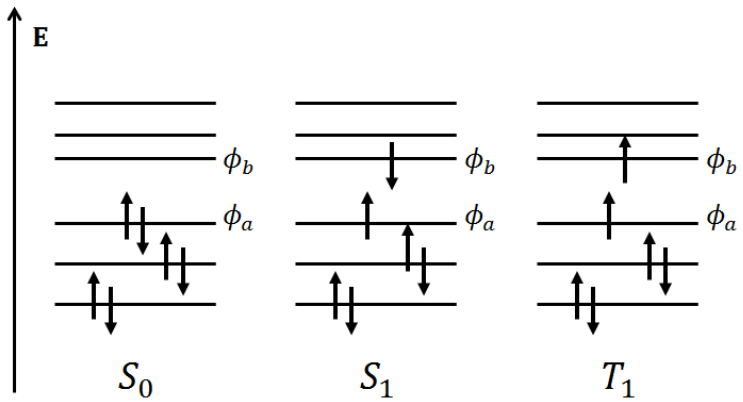

Figure 12: Electronic distribution in the molecular orbitals for the three different states S_0, S_1 and T_1.

For a system composed by two electrons occupying two nondegenerate molecular orbital ϕ_a and ϕ_b (HOMO and LUMO respectively as reported in figure 12), there are four possible spin states. One way of representing these states is the uncoupled representation, in which each state is constructed by the simple product of the individual spin states:

$$\alpha(1)\alpha(2)\ \alpha(1)\beta(2)\ \beta(1)\alpha(2)\ \beta(1)\beta(2)$$

This representation is optimal to describe a system with low interactions between the two spins, for which the spin quantum number s_i and the magnetic quantum numbers $m_{s,i}$ of the single electrons are good quantum numbers.

Conversely, when the two electrons interact appreciably, as in our molecular system, it is necessary to merge these configurations into combination of states because, due to the interactions between the spins, the system is better described by the total spin quantum number $S = \sum s_i$ and the total magnetic quantum numbers $M_s = \sum m_{s,i}$ of the single electrons. This coupled representation, comprises spin functions that are eigenfunctions of the operators $\hat{S}^2 = (\hat{s}_1 + \hat{s}_2)^2$ and $\hat{S}_z = \hat{s}_{z,1} + \hat{s}_{z,2}$, which are grouped in accord to the total spin quantum number: three triplet states (τ) and the remaining singlet state (σ). The triplet functions are discerned by their $\hat{S}_z$ eigenvalue, which can be equal to +1, 0 or -1.

$$\tau_{+1} = \alpha(1)\alpha(2)$$
$$\tau_0 = \frac{1}{\sqrt{2}}[\alpha(1)\beta(2) + \beta(1)\alpha(2)]$$
$$\tau_{-1} = \beta(1)\beta(2)$$

$$\sigma_0 = \frac{1}{\sqrt{2}}[\alpha(1)\beta(2) - \beta(1)\alpha(2)]$$

The spin part of the wavefunctions of the triplet state is all symmetric with respect to the exchange of the electrons. Due to that, the fermionic nature of the electrons implies that the spatial part of the total wavefunction has to be antisymmetric with respect to the exchange of the couple of electrons to guarantee an antisymmetric overall wavefunction. On the contrary, the antisymmetry of the spin part of the singlet wavefunction implies that the spatial part has to be symmetric. From all these considerations, it is possible to write the four wavefunctions for the first excited state:

$$\Psi_{1,S} = \frac{1}{2}[\phi_a(1)\phi_b(2) + \phi_b(1)\phi_a(2)][\alpha(1)\beta(2) - \beta(1)\alpha(2)]$$

$$\Psi_{1,T_{+1}} = \frac{1}{\sqrt{2}}[\phi_a(1)\phi_b(2) - \phi_b(1)\phi_a(2)][\alpha(1)\alpha(2)]$$

$$\Psi_{1,T_0} = \frac{1}{2}[\phi_a(1)\phi_b(2) - \phi_b(1)\phi_a(2)][\alpha(1)\beta(2) + \beta(1)\alpha(2)]$$

$$\Psi_{1,T_{-1}} = \frac{1}{\sqrt{2}}[\phi_a(1)\phi_b(2) - \phi_b(1)\phi_a(2)][\beta(1)\beta(2)]$$

where $\Psi_{1,S}$ is the wavefunction S_1 and the remaining three are the wavefunctions of the three sublevels of the T_1, discernible by their value of total magnetic quantum number.

2.2 Electron-Exchange Interaction

The difference in the spatial part between singlet and triplet levels leads to different averaged Coulombic interactions between the two electrons, because states with different spin multiplicity are not isoenergetic. In the present case the energy difference is equal twice the exchange integral value:

$$J_0 = -2\left\langle \phi_a(1)\phi_b(2) \middle| \frac{e^2}{4\pi\varepsilon_0 r_{12}} \middle| \phi_b(1)\phi_a(2) \right\rangle$$

where ε_0 is the vacuum permittivity, r_{12} is the inter-electronic distance and the bra-ket formalism indicate an integration over all the space of the variables x, y and z of ϕ_a and ϕ_b.

Working only on the spatial part of the wavefunction, the exchange interaction differentiates the triplet and the singlet states, leaving a three-fold degenerate triplet state. Whether the singlet or the triplet state lies lower depends on the sign of J_0. If $J_0 > 0$ the singlet state lies lowest, if, on the contrary, $J_0 < 0$ the reverse is observed.

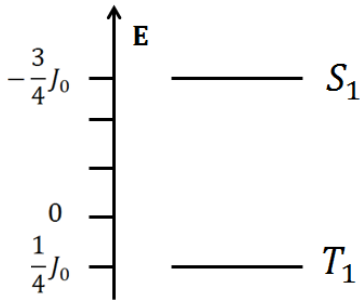

Figure 13: The state energies for a bi-electronic system with $J_0 < 0$.

2.3 Electron-Electron Dipole Interaction

In addition to the electron exchange, which splits the states into singlet and triplet, another important interaction is always present: the anisotropic magnetic dipole-dipole interaction. This removes the three-fold degeneracy of the triplet state independently from the presence of a magnetic field; an effect called zero-field splitting (ZFS).

The magnetic dipole-dipole interaction is given by the Hamiltonian term:

$$\hat{\mathcal{H}}_{ss} = \frac{\mu_0}{4\pi}(g\beta_e)^2\left[\frac{\hat{\mathbf{s}}_1 \cdot \hat{\mathbf{s}}_2}{r^3} - \frac{3(\hat{\mathbf{s}}_1 \cdot \mathbf{r})(\hat{\mathbf{s}}_2 \cdot \mathbf{r})}{r^5}\right]$$

where g is the electron g-factor, taken here to be isotropic, a good approximation for organic molecules; β_e is the Bohr magneton, $\hat{\mathbf{s}}_1$ and $\hat{\mathbf{s}}_2$ are the spins of the two electrons, $\mathbf{r}$ is the inter-electronic distance and μ_0 the vacuum permittivity.

Since the two electrons are coupled, it is more convenient to express $\hat{\mathcal{H}}_{ss}$ in terms of the total spin operator $\hat{\mathbf{S}}$ (defined as $\hat{\mathbf{S}} = \hat{\mathbf{s}}_1 + \hat{\mathbf{s}}_2$) and of the ZFS tensor $\tilde{\mathbf{D}}$ which is constituted by matrix elements of appropriate special components of $\hat{\mathcal{H}}_{ss}$ mediated over the spatial part of the wavefunction:

$$\tilde{\mathbf{D}} = \frac{(g\beta_e)^2\mu_0}{8\pi}\begin{pmatrix} \langle\frac{r^2-3x^2}{r^5}\rangle & \langle\frac{-3xy}{r^5}\rangle & \langle\frac{-3xz}{r^5}\rangle \\ \langle\frac{-3xy}{r^5}\rangle & \langle\frac{r^2-3y^2}{r^5}\rangle & \langle\frac{-3yz}{r^5}\rangle \\ \langle\frac{-3xz}{r^5}\rangle & \langle\frac{-3yz}{r^5}\rangle & \langle\frac{r^2-3z^2}{r^5}\rangle \end{pmatrix}$$

where the bra-ket notation expresses the average over the electronic spatial wavefunction. This treatment leads to the effective spin Hamiltonian:

$$\hat{\mathcal{H}}_0 = \hat{\mathbf{S}} \cdot \tilde{\mathbf{D}} \cdot \hat{\mathbf{S}}$$

The tensor $\widetilde{\mathbf{D}}$ always may be always expressed in diagonal form through the proper choice of a coordinate system, with the principal axes ***x, y*** and ***z*** corresponding to the molecular symmetry axes if the point group of the molecule contains C_{2v} as a subgroup. The diagonal elements of the diagonalized matrix are X, Y and Z. By convention, Z is taken to be the principal value with the largest absolute magnitude and Y has the smallest absolute magnitude when X ≠ Y. In this special coordinate frame, generally called the "principal axes system", $\widehat{\mathcal{H}}_d$ takes the simple form

$$\widehat{\mathcal{H}}_d = -\mathrm{X}\hat{\mathrm{S}}_\mathrm{x} - \mathrm{Y}\hat{\mathrm{S}}_\mathrm{y} - \mathrm{Z}\hat{\mathrm{S}}_\mathrm{z}$$

where $\hat{\mathrm{S}}_\mathrm{u}$ (with $u = x, y$ and z) are the components of $\hat{\mathbf{S}}$ along the principal axes of $\widetilde{\mathbf{D}}$ and X, Y and Z the tensor principal values:

$$\mathrm{X} = -\frac{(\mathrm{g}\beta_e)^2\mu_0}{8\pi}\langle\frac{r^2 - 3x^2}{r^5}\rangle$$

$$\mathrm{Y} = -\frac{(\mathrm{g}\beta_e)^2\mu_0}{8\pi}\langle\frac{r^2 - 3y^2}{r^5}\rangle$$

$$\mathrm{Z} = -\frac{(\mathrm{g}\beta_e)^2\mu_0}{8\pi}\langle\frac{r^2 - 3z^2}{r^5}\rangle$$

These values represent the energy associated with the three sublevels. Due to the fact that the dipolar tensor is traceless ($\mathrm{X} + \mathrm{Y} + \mathrm{Z} = 0$), only two of the three principal values are independent. So the eigenvalue can be expressed more conveniently in function of the two parameters D and E, known as ZFS parameters, definied as:

$$D = -\frac{3}{2}\mathrm{Z} = \frac{3}{4}\frac{(\mathrm{g}\beta_e)^2\mu_0}{4\pi}\langle\frac{r^2 - 3z^2}{r^5}\rangle$$

$$E = \frac{1}{2}(\mathrm{Y} - \mathrm{X}) = \frac{3}{4}\frac{(\mathrm{g}\beta_e)^2\mu_0}{4\pi}\langle\frac{x^2 - y^2}{r^5}\rangle$$

Thus, the diagonalized dipolar tensor can be rewritten as:

$$\widehat{\mathcal{H}}_d = D\left(\hat{\mathrm{S}}_\mathrm{z}^2 - \frac{\hat{\mathbf{S}}^2}{3}\right) + E\left(\hat{\mathrm{S}}_\mathrm{x}^2 - \hat{\mathrm{S}}_\mathrm{y}^2\right)$$

The ZFS parameters strongly depend on the averaged distance between the two unpaired electrons: E is a measurement of the deviation from the axial symmetry with respect to the ***z*** axis, while D depends on the extension of the electronic delocalization along the ***z*** axis.

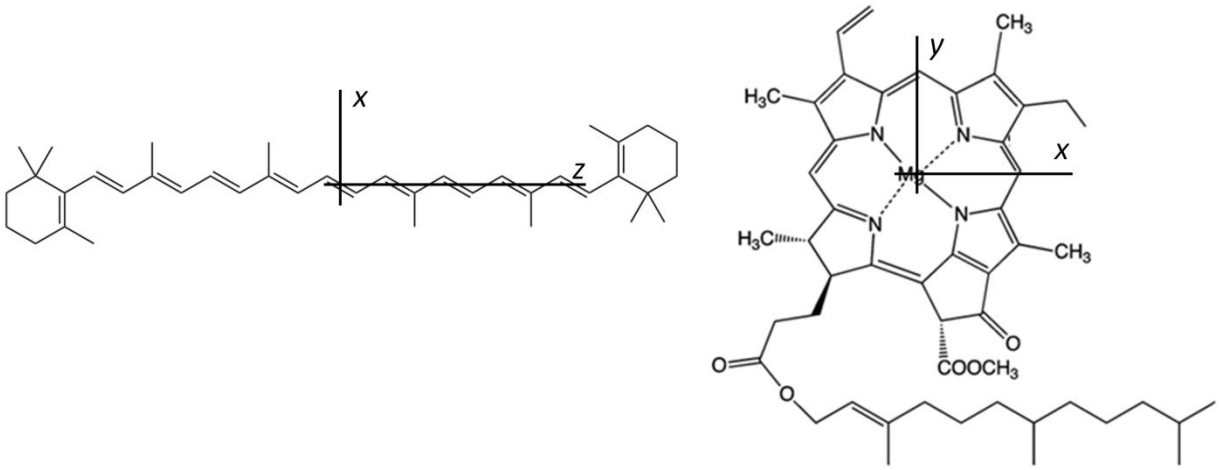

Figure 14: Molecular structures of β-carotene (at left) and chlorophyll a (at right) with the directions of the ZFS axes.

For the systems under study, reported in figure 14, it is useful to consider planar molecules, like chlorophylls, for which D is positive and $\boldsymbol{z}$ is perpendicular to the molecular plane,(Vrieze & Hoff 1995) whereas for a linear molecule, as carotenes, D is negative and $\boldsymbol{z}$ is along the molecular long axis.(Frick et al. 1990)

The obtained Hamiltonian contains only spin operators and can be verified that is not diagonal if it is applied on the high-field spin functions τ_{+1}, τ_0 and τ_{-1}. The following orthonormal linear combinations of the high-field spin functions provide a basis in which $\hat{\mathcal{H}}_d$ is diagonal.

$$\tau_x = \frac{1}{\sqrt{2}}[\tau_{-1} - \tau_{+1}] = \frac{1}{\sqrt{2}}[\beta(1)\beta(2) - \alpha(1)\alpha(2)]$$
$$\tau_y = \frac{i}{\sqrt{2}}[\tau_{-1} + \tau_{+1}] = \frac{i}{\sqrt{2}}[\beta(1)\beta(2) + \alpha(1)\alpha(2)]$$
$$\tau_z = \tau_0 = \frac{1}{\sqrt{2}}[\alpha(1)\beta(2) + \beta(1)\alpha(2)]$$

These functions have the following properties:

$$\hat{\mathrm{S}}_u|\tau_u\rangle = 0$$
$$\hat{\mathrm{S}}_u|\tau_v\rangle = \pm i|\tau_w\rangle$$

where $(u, v, w) = (x, y, z)$ and in the latter equation the sign is positive if x, y and z are in cyclic order. In zero magnetic field, it follows that:

$$\mu_u = \mathrm{g}\beta_e\langle T_u|\hat{\mathrm{S}}_u|T_u\rangle = 0$$

So there is no net magnetic dipole component along the axis associated with a triplet substate. Using the latter expression, it is easy to demonstrate that the energetic contributions due to the dipolar interaction for the triplet sublevels T_x, T_y and T_z ($T_u = \frac{1}{\sqrt{2}}[\phi_a(1)\phi_b(2) - \phi_b(1)\phi_a(2)] \cdot \tau_u$) are X, Y and Z, respectively.

Reformulating these energies in function of the ZFS parameters, the following values are obtained:

$$X = \frac{1}{3}|D| - |E|$$

$$Y = \frac{1}{3}|D| + |E|$$

$$Z = -\frac{2}{3}|D|$$

leading to the splitting reported in figure 15, guaranteed that $|D|/3 > |E|$ from the convention already stated that |Z|>|X|>|Y|.

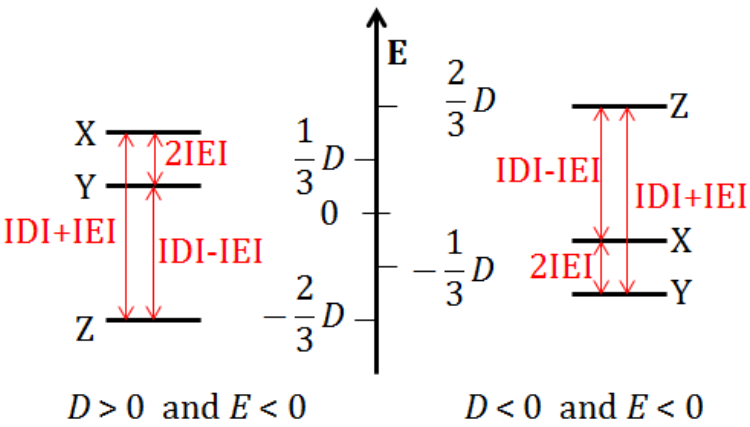

Figure 15: Splitting of the triplet sublevels in ZFS conditions for a chlorophyll a (D > 0 and E < 0, on the left) and for a carotenoid (D < 0 and E < 0, on the right).

2.3.1 Magnetic Resonance Transition at Zero Field

For an oscillating electromagnetic field $\boldsymbol{B}_1(t) = \boldsymbol{B}_1 cos(\omega t)$ aligned along an arbitrary axis $\boldsymbol{u}$, if the interaction is small enough to be treated as a perturbation, the corresponding Hamiltonian can be expressed as

$$\widehat{\mathcal{H}}_u' = -\mathrm{g}\beta_e B_1 \left(\boldsymbol{u} \cdot \hat{\mathbf{S}}\right) cos(\omega t)$$

where B_1 is the oscillating electromagnetic field amplitude and $\boldsymbol{u}$ is a unit vector that defines the polarization of the field of frequency ω. The time-dependent perturbation between two spin sublevels, say T_z and T_y, gives nonzero matrix elements

$$\langle T_z | \widehat{\mathcal{H}}_u' | T_y \rangle = -\langle T_y | \widehat{\mathcal{H}}_u' | T_z \rangle$$

only if it has a component $\widehat{\mathcal{H}}_x'$ perpendicular to both of them, otherwise

$$\langle T_z | \widehat{\mathcal{H}}_z' | T_y \rangle = \langle T_z | \widehat{\mathcal{H}}_y' | T_y \rangle = 0$$

So near the resonance, when $\omega \sim \omega_0 = \frac{|Y-Z|}{\hbar}$, transitions $\boldsymbol{x}$-polarized are induced between T_y and T_z with a transition probability proportional to $(\mathrm{g}\beta_e B_1)^2$. The ZFS resulting from $\widehat{\mathcal{H}}_d$ have the order of magnitude of the dipolar magnetic interaction between a pair of electrons at a separation comparable to the molecular dimensions, so the frequencies of this kind of resonant transitions lie in the range of 0.1-10 GHz. Consequently, the zero field (ZF) magnetic resonance transitions are to be found in the microwave spectral region, and are named $2|E|$, $|D|$-$|E|$ and $|D|$+$|E|$ as reported in figure 15.

2.4 The Hyperfine Coupling

Another interaction that is independent from the presence of a magnetic field is the hyperfine coupling. This interaction is originated from the coupling of the magnetic moment of the unpaired electrons with that of the surrounding nuclei. It is a great source of structural information since it holds a well-defined dependence on the distance and orientations of the interacting dipoles. The Hamiltonian describing the interaction can be formulated in an expression similar to the effective spin Hamiltonian used to describe the electron-electron dipole interaction:

$$\widehat{\mathcal{H}}_{HF} = \hat{\mathbf{S}} \cdot \widetilde{\mathbf{A}} \cdot \hat{\mathbf{I}}$$

with the $\widetilde{\mathbf{A}}$ term representing the 3x3 hyperfine coupling tensor, which holds all the information about the distance and the orientation of the interaction. The $\widetilde{\mathbf{A}}$ tensor itself is formulated as the sum of two individual contributions: an isotropic component a_{iso}, deriving from the quantum mechanical properties of the electron wavefunction, and an anisotropic, tensorial component $\widehat{\mathcal{H}}_{dip}$ describing the classical electron-nuclear dipole-dipole coupling. The a_{iso} term is also known as the Fermi Contact term(Fermi 1930) and it is given by:

$$a_{iso} = \frac{2}{3}\mu_0 g_e \beta_e \beta_n |\psi_0(0)|^2$$

The term $|\psi_0(0)|^2$ accounts for the dependence of a_{iso} to the probability of finding the unpaired electrons at the nucleus position, a feature that only s-orbital electrons possess. This type of electrons are the root of the Fermi contact interaction and their spherical symmetry ensures the isotropic nature of this interaction. A non zero a_{iso} can also be observed in π-type electrons radicals, even if they are characterized of a null probability of finding the electron at the nucleus position since the nuclei lie on a nodal plane of the π orbital. In this subtle case the π-type unpaired electron induce a polarization on the σ-type electrons bonding the two atoms, causing a net spin polarization at the hydrogen nucleus position, which results in an isotropic hyperfine interaction being observed.

The anisotropic component $\widehat{\mathcal{H}}_{dip}$ originates from the classical, orientation dependent, coupling of magnetic dipoles, in analogy to the electron-electron dipole interaction discussed in the 2.3 section. Hence for an electron spin magnetic dipole, $\boldsymbol{\mu}_{\mathrm{e}}$, with the nuclear spin magnetic dipole, $\boldsymbol{\mu}_{\mathrm{n}}$, of a surrounding nucleus placed at a distance r:

$$\widehat{\mathcal{H}}_H = \frac{\mu_0}{4\pi}(\mathrm{g}\beta_e)^2\left[\frac{\boldsymbol{\mu}_{\mathrm{e}}\cdot\boldsymbol{\mu}_{\mathrm{n}}}{\mathrm{r}^3} - \frac{3(\boldsymbol{\mu}_{\mathrm{e}}\cdot\mathbf{r})(\boldsymbol{\mu}_{\mathrm{n}}\cdot\mathbf{r})}{\mathrm{r}^5}\right]$$

Ignoring g_e and g_n anisotropy and substituting the classical magnetic dipoles with their corresponding quantum mechanical expressions, the Hamiltonian describing the anisotropic hyperfine interaction is obtained:

$$\widehat{\mathcal{H}}_{dip} = \frac{\mu_0}{4\pi}g_n g_e \beta_e \beta_n\left[\frac{\hat{\mathbf{S}}\cdot\hat{\mathbf{I}}}{\mathrm{r}^3} - \frac{3(\hat{\mathbf{S}}\cdot\mathbf{r})(\hat{\mathbf{I}}\cdot\mathbf{r})}{\mathrm{r}^5}\right]$$

2.5 Zeeman Interaction

In the presence of an external static magnetic field the Zeeman interaction has to be added to the spin Hamiltonian to properly describe the system. This field-induced interaction can be represented by the term:

$$\widehat{\mathcal{H}}_z = -\mathrm{g}\beta_e \boldsymbol{B}_0\cdot\hat{\mathbf{S}}$$

for which τ_x, τ_y and τ_z are not eigenfunctions, so the magnetic field $\boldsymbol{B}_0$ perturbs the energy levels and induces mixing of the zero field (ZF) spin eigenfunctions τ_x, τ_y and τ_z.

In the limit $\widehat{\mathcal{H}}_z \gg \widehat{\mathcal{H}}_d$, the spin eigenfunctions approach the high-field basis set τ_{+1}, τ_0 and $\tau_{-1}$and the spin angular momentum becomes quantized along the axis of the applied magnetic field. In this condition, the high-field eigenfunctions are obtained as linear combination of the ZF eigenfunctions and the high-field eigenvalues are obtained from the application of the Zeeman Hamiltonian to its eigenfunctions adding as first-order correction the dipolar interaction.

In this conditions there are simple solutions to the eigenvalue equation only if the static magnetic field is parallel to one of the ZFS axis, for example when $\boldsymbol{B}_0$ is parallel to $\boldsymbol{z}$:

$$T_{+1} = \frac{\sqrt{2}}{2i}\left(T_y - T_x\right) \qquad E_{+1} = g_e^2\beta^2 S H_{\mathbf{0}} + \frac{1}{2}(X + Y)$$

$$T_0 = T_z \qquad E_0 = Z$$

$$T_{-1} = \frac{\sqrt{2}}{2i}\left(T_y + iT_x\right) \qquad E_{-1} = -g_e^2\beta^2 S H_{\mathbf{0}} + \frac{1}{2}(X + Y)$$

with T_{M_S} the three triplet sublevels labeled with the eigenvalues of $\hat{S}_z$ and E_{M_S} their relative energy. Analogous results are obtained when the applied magnetic field is parallel to the $\boldsymbol{x}$ or the $\boldsymbol{y}$ axis.

From the expression reported above clearly appears that the dependence of the Hamiltonian's eigenvalues from the ZFS parameters D and E remains even in high field conditions. For example in figure 16 is reported the behavior of the sublevels energies with the growth of the magnetic field for a D>0 E<0 system.

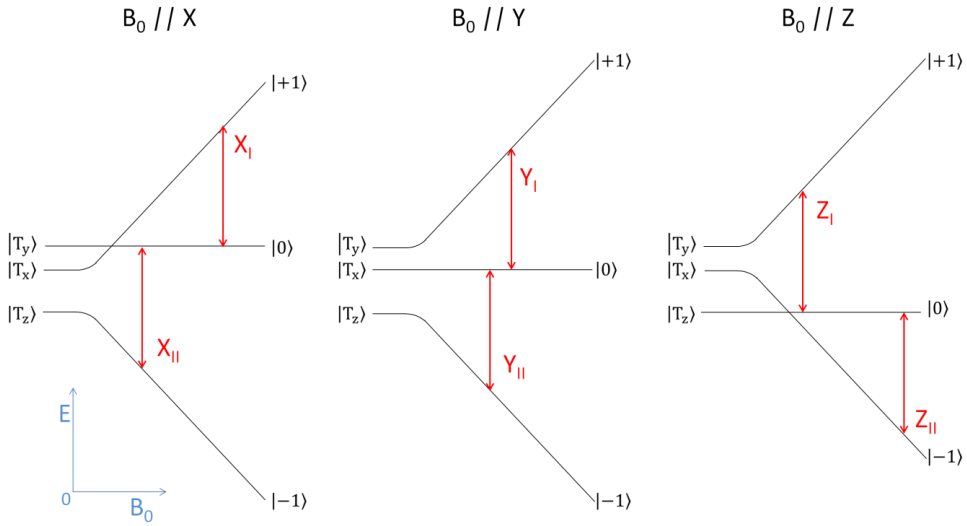

Figure 16: Dependence of the triplet sublevel energy from the applied magnetic field $\boldsymbol{B_0}$ *for a D > 0 and E < 0 system.*

2.5.1 Magnetic Resonance Transition in High-Field

In high-field conditions, the selection rule $\Delta M_S = \pm 1$ allows only the transitions $T_{\pm 1} \leftarrow T_0$ and $T_0 \leftarrow T_{\pm 1}$, giving rise to two possible transitions for every orientation of the magnetic field with respect to the molecular frame. Additionally the oscillating magnetic field must have a nonzero component perpendicular to the static magnetic field.

The three pairs of allowed transitions in the three special cases in which the molecules have one of the ZFS axes parallel to the static magnetic field are labeled $X_{|}$, $X_{||}$, $Y_{|}$, $Y_{||}$, $Z_{|}$, and $Z_{||}$ in

relation to the particular ZFS axis and to the transition ($T_{+1} \leftarrow T_0$ and $T_0 \leftarrow T_{-1}$), as reported in figure 16.

2.6 Optical polarization of electronic spin

As seen in the previous two paragraphs, both in the presence or in the absence of an external magnetic field the degeneracy of the three triplet sublevels is removed. The populating mechanisms that lead to the generation of the triplets are anisotropic with a distribution of the population between the three sublevels which is different from that expected by Boltzmann statistic. Therefore a polarized system is obtained. In Chls and BChls, the intersystem crossing (ISC) allows the spin-forbidden transition $T_1 \leftarrow S_1$; In carotenoids, the ISC has very low probability to occur, and they populate their triplet state by a triplet-triplet energy transfer (TTET) mechanism from triplet donors (for instance ^{3}(B)Chl).

2.6.1 Inter System Crossing

ISC is an isoenergetic transition between a triplet state and a singlet state: ($S_1 \xrightarrow{ISC} T_1$) and $\left(T_1 \xrightarrow{ISC} S_0\right)$. The spin-orbit coupling removes the spin-forbiddance of this kind of transitions, allowing coupling the change in electron spin with a change in orbital angular momentum, conserving the total angular momentum.

The value of this coupling can only be obtained from Dirac's relativistic equations and it is generalized for *n* electrons in the following form:

$$\hat{\mathcal{H}}_{SO} = \sum_{i=1}^{n} \xi(\boldsymbol{r}_i)\hat{\mathbf{l}}_i \cdot \hat{\mathbf{s}}_i$$

where $\hat{\mathbf{l}}_i$ is the angular momentum of the *i*-th electron and $\xi(\boldsymbol{r}_i)$ is the proportionality constant of the spin-orbit coupling for the *i*-th electron. It is important to underline that the latter term depends from the fourth power of the atomic number of the nuclei that contribute to this interaction.

The ISC matrix elements that describe the interaction between a singlet state, either the first excited or the fundamental, and the three triplet sublevels are different due to the differences in their symmetry properties:

$$\langle S_n|\hat{\mathcal{H}}_{\mathrm{SO}}|T_x\rangle \neq \langle S_n|\hat{\mathcal{H}}_{\mathrm{SO}}|T_y\rangle \neq \langle S_n|\hat{\mathcal{H}}_{\mathrm{SO}}|T_z\rangle$$

Without an external magnetic field the population (p_u) and depopulation (k_u) rates of the three sublevels of T_1 (with $u = x, y, z$) linearly depend on the square of the corresponding matrix elements:

$$p_u \propto \left|\langle S_1|\hat{\mathcal{H}}_{\mathrm{SO}}|T_u\rangle\right|^2$$

$$k_u \propto \left|\langle T_u|\hat{\mathcal{H}}_{\mathrm{SO}}|S_0\rangle\right|^2$$

In the presence of a static magnetic field the population (P_i) and depopulation (k_i) rates of the three sublevels (with $i = +1, 0, -1$) can be expressed as functions of the ZF rates

$$P_i = \sum_u |c_{iu}|^2\, p_u$$

$$K_i = \sum_u |c_{iu}|^2\, k_u$$

Where c_{iu} is the coefficient of the high field i-th function expressed as combination of the ZF functions. If $g\beta_e B_0 \gg$ D and E, for example, for the molecules which have u parallel to the static magnetic field, the populating and decaying rates of the high-field triplet sublevels can be easily correlated to those at ZF:

$$P_0 = P_u$$
$$P_{+1} = P_{-1} = \frac{1}{2}(P_v + P_w)$$

$$k_0 = k_u$$
$$k_{+1} = k_{-1} = \frac{1}{2}(k_v + k_w)$$

In every spectroscopy the intensity of the signal is proportional to the difference in population between the two levels in resonance, so a great anisotropy in the populating mechanism will give an intense spectrum.

In electron paramagnetic resonance (EPR) spectroscopy the transitions between the triplet sublevels are detected. For example the transition between T_0 and T_{+1} for a molecule with the molecular $\boldsymbol{x}$ axis parallel to the static magnetic field (i.e. the X_l transition as seen paragraph 2.5.1), has an intensity I which is proportional to the difference between P_0 and P_{+1}:

$$I_{0\to 1} \propto P_0 - P_{+1} \propto P_x - \frac{1}{2}\left(P_y + P_z\right)$$

Thus if P_0 is greater than P_{+1} the intensities will be positive and the line in absorption, otherwise it will be in emission. It is clear that the related X^- transition (i.e. between T_0 and T_{-1}) will have intensity:

$$I_{-1\to 0} \propto P_{-1} - P_0 = -I_{0\to 1}$$

equal in modulus and opposite in sign to the X_l transition, leading to the characteristic antisymmetric shape of the EPR spectrum of polarized triplets, that will be better described in the fourth chapter.

2.6.2 Triplet-Triplet Energy Transfer

Carotenoids have negligible ISC from S_1 to T_1 and their triplet states is predominantly populated, in photosynthetic systems, by means of the TTET mechanism, from ^{3}Chls (^{3}Chl + ^{1}Car $\xrightarrow{ISC}$ ^{1}Chl + ^{3}Car). This process implies the concurrent exchange of two electrons between a pair of interacting molecules, with the conservation of the total angular momentum guaranteed by the concomitant ^{3}D→ ^{1}D and ^{1}A→ ^{3}A transitions of the two species (with *A*=acceptor and *D*=donor).

This process, based on the Dexter mechanism(Dexter 1953) is permitted through the overlap of the molecular orbital of the interacting molecules and requires proximity of the donor-acceptor pair (figure 17).

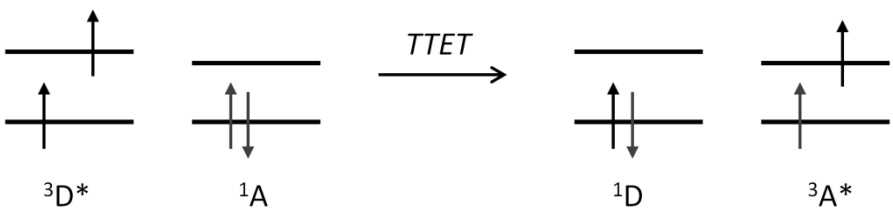

Figure 17: Scheme of the $^3D + {}^1A \xrightarrow{TTET} {}^1D + {}^3A$ *Dexter transfer.*

The probability ($W_{h\to k}$) of electron transfer from the *h*-th ZFS sublevel of the triplet state of the donor (T_h) to the *k*-th ZFS sublevel (T_k) of the acceptor with the concomitant transfer of another electron from the HOMO of the acceptor to that of the donor is proportional to the square of the electronic exchange integral:

$$W_{h\to k} \propto \left| \left\langle \Phi_D^{(3)}(1) T_{h,D}^{(3)}(1) \Phi_A^{(1)}(2) S_A^{(1)}(2) \left| \frac{e^2}{\kappa \mathbf{r}_{12}} \right| \Phi_A^{(3)}(2) T_{k,A}^{(3)}(2) \Phi_D^{(1)}(1) S_D^{(1)}(1) \right\rangle \right|^2$$

where D refers to the donor and A to the acceptor, 1 and 2 are the labels of the two exchanged electrons and the apexes (3) and (1) refer respectively to the triplet excited state and the singlet fundamental state. The wavefunctions are separated in their spatial (Φ) and spin (T for the

triplet and S for the singlet) components. Due to the fact that the operator $1/\mathbf{r}_{12}$ does not operate over the spin functions, during the transfer the total spin quantum number S and the total magnetic quantum numbers M_s are conserved,(El-Sayed et al. 1969; Imamura et al. 1984; Murai et al. 1988) and the integral can be rearranged giving:

$$W_{h\to k} \propto \left|\left\langle T_{h,D}^{(1)}(1)\middle|T_{k,A}^{(1)}(2)\right\rangle\right|^2 \left|\left\langle S_A^{(0)}(2)\middle|S_D^{(0)}(1)\right\rangle\right|^2 \left|\left\langle \varphi_D^{(1)}(1)\varphi_A^{(0)}(2)\middle|\frac{e^2}{\kappa \mathbf{r}_{12}}\middle|\varphi_D^{(0)}(1)\varphi_A^{(1)}(2)\right\rangle\right|^2$$

Considering that for a fixed configuration of the two molecules the second and third terms do not depend on the couple of triplet sublevels involved in the transition, the anisotropy of this process can be ascribed only to the remaining term:

$$W_{h\to k} \propto \left|\left\langle T_{h,D}^{(1)}(1)\middle|T_{k,A}^{(1)}(2)\right\rangle\right|^2$$

This square matrix element can be approximated to the square cosine of the angle comprised between the ZFS axes of the triplet sublevel h of the donor and k of the acceptor (θ_{hk}), due to the fact that the overlap of two triplet sublevels of different molecules is maximum when they have the axes parallel and goes to zero if perpendicular, leading to:

$$W_{h\to k} \sim \cos^2(\theta_{hk})$$

Hence the population of every triplet sublevel of the acceptor is determined from the sum of the three contributions from the triplet sublevels of the donor:

$$P_k^A = \sum_h \cos^2(\theta_{hk}) P_h^D$$

where P_k^A is the population of the k-th ZFS sublevel of the acceptor and P_h^D is the population of the h-th ZFS sublevel of the donor, with the summation carried over the three triplet sublevels of the donor. From this expression clearly appears that the polarization of the triplet state of the acceptor depends on the polarization of the triplet state of the donor (usually deriving from an ISC) and on the relative geometry of the acceptor-donor pair, therefore it can be used to obtain structural information about the system.

The treatment has been carried out in a ZF frame, but it can be easily extended to the high-field case by expressing the populations of the high-field triplet sublevels as combination of the ZF sublevels.

2.7 References

Dexter, D.L., 1953. A Theory of Sensitized Luminescence in Solids. *The Journal of Chemical Physics*, 21(5), pp.836–850.

El-Sayed, M.A., Tinti, D.S. & Yee, E.M., 1969. Conservation of Spin Direction and Production of Spin Alignment in Triplet – Triplet Energy Transfer Conservation of Spin Direction and Production of Spin Alignment in. *The Journal of Chemical Physics*, 51, pp.5721–5723.

Fermi, E., 1930. Über die magnetischen Momente der Atomkerne. *Zeitschrift für Physik*, 60, pp.320–333.

Frick, J. et al., 1990. First Detection of the (Nonphosphorescent) Triplet State in Single Crystals of β-Carotene*. Molecular Crystals and Liquid Crystals*, 183, pp.269–272.

Imamura, T. et al., 1984. Conservation of Spin Polarization during Triplet-Triplet Energy Transfer in Low-Temperature Matrices. *Journal of Physical Chemistry*, 88, pp.4028–4031.

Murai, H. et al., 1988. Intermolecular energy transfer of the spin-polarized triplet state in a γ-cyclodextrin cavity. *Chemical Physics Letters*, 144(4), pp.417–420.

Vrieze, J. & Hoff, A.J., 1995. The orientation of the triplet axes with respect to the optical transition moments in (bacterio) chlorophylls. Chemical Physics Letters, 237, pp.493–501.

Optically Detected Magnetic Resonance

Optically Detected Magnetic Resonance (ODMR) is a double resonance technique that consists in the optical detection of a resonant magnetic transition between electronic spin sublevels of a molecular system. This technique is often advantageous because it pairs the frequency resolution of magnetic resonance with the sensitivity of optical spectroscopy. It is primarily used for magnetic resonance of the triplet state, as the resonant transfer of population between the triplet sublevels generally gives rise to a concomitant change in the optical properties (phosphorescence, fluorescence and absorption) of the sample, because of the different decay rates of the sublevels. It is preferentially carried out in zero magnetic field, where the triplet wave functions are not mixed by the Zeeman interaction and the triplet sublevels are split mainly by the dipolar interaction. The optical detection enhances considerably sensitivity for disordered systems, as protein solutions.

In this chapter the theory of ODMR is summarized,(Clarke 1982; Hoff 1982) adopting the notation of Maki.(Maki 1984)

3.1 Photo-induced steady-state

The technique is performed with continuous illumination of the sample, which causes a dynamically coupling of the three electronic levels S_0, S_1 and T_1. This leads to a photo-induced steady state characterized by a redistribution of the population among the levels. If the spin-lattice relaxation processes are slow or removed, by working at sufficiently low temperature, it is possible to consider the sublevels of T_1 as independent states, which are characterized by different populations.

This dynamic equilibrium between the involved states can be described by the following system of kinetic differential equations:

$$\dot{N}_0(t) = -k_0\big(N_0(t) - N_1(t)\big) + k_1 N_1(t) + \sum_u k_u\, N_u(t)$$

$$\dot{N}_1(t) = k_0\big(N_0(t) - N_1(t)\big) - (k_1 + k_2) N_1(t)$$

$$\dot{N}_u(t) = k_2 p_u N_1(t) - \left(k_u + \sum_v W_{uv}\right) N_u(t) + \sum_v W_{vu}\, N_v(t)$$

in which N_0 is the population of the fundamental singlet state S_0, N_1 the corresponding term relative to the first excited singlet state S_1 and N_u (with $u = x, y$ and z) the populations of the three sublevels of the triplet state T_1. The kinetic constants involved in the description of the five-level system are reported in the following figure:

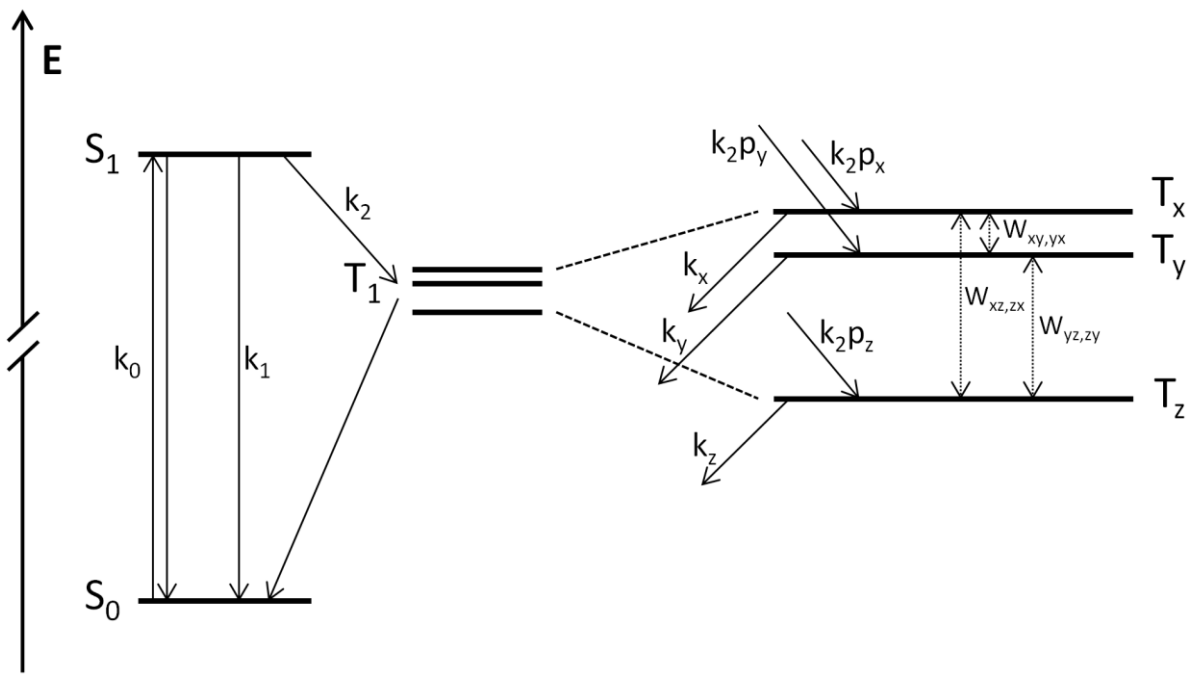

Figure 18: Scheme illustrating the populating and decaying constants of the five-level system.

in which k_0 describes the stimulated absorption $S_0 \rightarrow S_1$ and emission $S_1 \rightarrow S_0$ whereas k_1 accounts for the spontaneous emission $S_1 \rightarrow S_0$. k_2 is the constant related to the overall process of ISC $S_1 \rightarrow T_1$, p_u is the probability to transit through ISC from the singlet excited state to the u-th triplet sublevel (with $\sum_u p_u = 1$), k_u is the decay rate that governs de-excitation from the u-th sublevel back to the singlet ground state and the two terms W_{uv} and W_{vu} represent the relaxation process between the couple of sublevels T_u and T_v. Both p_u and k_u are determinated by molecular symmetry.

Under continuous illumination a steady state achieved and it is possible to consider $\dot{N}_0(t) = \dot{N}_1(t) = \dot{N}_u(t) = 0$, and, working at a very low temperature (below 4.2 K), the relaxation processes can be considered negligible ($W_{uv} = W_{uv} = 0$). Furthermore the mass conservation constrain $N_0 + N_1 + N_T = N$ (in which $\sum_u N_u = N_T$ and N is the overall number of photoexcitable molecules) can be simplified to $N_0 + N_T \approx N$ due to the fact that $N_0, N_T \gg N_1$.

The considerations reported above allow to analytically solve the kinetic equations, obtaining the populations N_0^0, N_1^0 and N_u^0 that characterize the five-level system in absence of resonant microwaves:

$$N_1^0 = \frac{k_0}{k_0 + k_1 + k_2}(N - N_T^0) = \frac{K}{k_2}(N - N_T^0)$$

$$N_u^0 = K\frac{p_u}{k_u}(N - N_T^0) = \frac{KN\frac{p_u}{k_u}}{1 + K\sum_u \frac{p_u}{k_u}}$$

where $K = \frac{k_0 k_2}{(k_0+k_1+k_2)}$ is the kinetic constant of the process $S_0 \rightarrow S_1 \rightarrow T_1$. This constant is linearly dependent on the intensity of the incident radiation and in the case of low intensity, verified in our experimental condition, allows to consider $1 \gg K\sum_u \frac{p_u}{k_u}$ and to obtain the final form of the expression:

$$N_u^0 = NK\frac{p_u}{k_u}$$

From the expression reported clearly emerges that while the fraction of molecules in the triplet states N_T^0/N depends on K, and so from the light intensity, on the contrary the relative steady-state sublevel population N_u^0/N_T^0 does not.

3.2 Saturation of a transition

In presence of a saturating electromagnetic field, in resonance with the transition $T_u \leftrightarrow T_v$, there will be a transfer of population between the two sublevels until they are equalized. In these conditions the populations of the sublevels of the triplet stare are:

$$N_u^{uv} = N_v^{uv} = NK\frac{p_{uv}}{k_{uv}}$$

where $p_{uv} = \frac{1}{2}(p_u + p_v)$ and $k_{uv} = \frac{1}{2}(k_u + k_v)$.

The remaining triplet sublevel T_w, for which there is no direct resonant transfer of population, is affected in its population only to a second order, due to the variation of the populations of the other two states to which it is linked via the photogeneration cycle. This term can be considered negligible. Subtracting the expression found in presence of the saturating microwaves from the corresponding expressions in absence of microwaves (or in off-resonance conditions) it is possible to obtain the variations in the populations of the sublevels induced by the resonant field:

$$\Delta N_u = N_u^{uv} - N_u^0 = NK\frac{(k_u p_v - k_v p_u)}{2k_u k_{uv}}$$
$$\Delta N_v = N_v^{uv} - N_u^0 = NK\frac{(k_v p_u - k_u p_v)}{2k_v k_{uv}}$$
$$\Delta N_w = 0$$

The resulting overall variation of the population of the triplet state is given by:

$$\Delta N_T = \Delta N_u + \Delta N_v + \Delta N_w = NK\frac{(k_u - k_v)}{2k_{uv}}\left(\frac{p_u}{k_u} - \frac{p_v}{k_v}\right)$$

This induced variation in the population of T_1 is reflected also in the populations of S_0 and S_1, being:

$$\Delta N_0 = -\Delta N_T$$

$$\Delta N_1 = -\frac{K}{k_2}\Delta N_T$$

if the condition $N_0, N_T \gg N_1$ is valid.

The fluorescence detected magnetic resonance (FDMR) is sensitive to the variation of population of S_1 and so its intensity will be proportional to ΔN_1:

$$I_{FDMR} \propto k_F \cdot \Delta N_1$$

with k_F the rate constant for fluorescence.

The absorbance detected magnetic resonance (ADMR) is governed by the perturbation of the populations of S_0 and T_1 and depends on ΔN_0 and on ΔN_T. Note that the microwave-induced change in the singlet fundamental absorption and in the triplet state absorption is opposite in sign.

The intensity of the signals is influenced by the overall variation in the population of the triplet state. To have a detectable signal the equilibrium populations $N_{u,v}^0$ and the decaying constants $k_{u,v}$ have to be different, being:

$$\Delta N_T = \frac{(k_u - k_v)}{2k_{uv}}(N_u^0 - N_v^0)$$

From the preceding expressions is also clear that the sign of ΔN_T, ΔN_0 and ΔN_1, and consequently the sign of the ODMR signal, depends on the relative values of the constants p_u and k_u.

3.3 ADMR and FDMR experiments

As implicitly said above, the ODMR experiments are conducted on a system under continuous illumination in absence of external magnetic field, at cryogenic temperature, sampling the fluorescence or the absorption of the sample at a fixed significant wavelength, while the microwaves are slowly scanned. If the resonance transitions between a couple of triplet sublevels is induced by the microwave field, a Gaussian contribution will appear in the spectrum. The non-lorentzian shape of the contribution is ascribable to the inhomogenous

distribution of the values of the ZFS parameters in the ensemble due to slight variation in energy and geometry of the sites.

From these kinds of experiments the resonance frequencies of the triplets present in a sample can be determined, from which the absolute values of the ZFS parameters (D and E) can be obtained. These parameters give information on the electronic distribution on the triplet, and hence on the structure of the molecule and its surrounding. The resolution with which these parameters can be determined by means of ODMR is higher in comparison to the more conventional electron paramagnetic resonance (EPR), due to the absence in the former technique, conducted in zero field, of the inhomogeneity introduced by the static magnetic field that have to be applied to measure EPR spectra.(Schmidt and van der Waals 1968) Moreover hyperfine splittings contribute only to the second order of the spectra. Additionally, since the modes of excitation and detection are uncoupled in ODMR, one is insensitive to noise source due to microwaves and the sensitivity is strongly enhanced relying on the more energetic optical quanta.

If different molecules in triplet state have similar ZFS parameters, the frequency spectra will be strongly overlapping. To disentangle the individual contributions of the spectra, it is possible to take advantage of the double-resonance nature of the ODMR, repeating the measurements at different detection wavelengths, because the different optical spectra (fluorescence and absorption spectra) of the different species giving the triplet states allow relative selection of the different components. This in turn allows to extract the different contributions by means of a global fitting of the collected dataset. An additional advantage is that it is possible in this way to correlate the optical and magnetic properties of the chromophores, leading to a complete electronic description of the species carrying the triplet state in the system.

3.3.1 FDMR of non-fluorescent species

Carotenoids are not fluorescent molecules, hence it is impossible to detect the FDMR spectra of their triplet state by monitoring their own emission.

However, in photosynthetic systems, FDMR of carotenoid triplet states can be obtained by detecting the Chl emission. This is possible only if in the system under investigation Car and Chl are connected via energy transfer.(Carbonera et al. 1992). Therefore this experimental approach is particularly informative in the characterization of photosynthetic complexes, in virtue of the fact that allows to directly assess the triplet-triplet energy transfer pathways in which the carotenoids are involved, being able to correlate carotenoid carrying triplet states to the specific chlorophylls that they are photoprotecting.

3.4 MIA experiments

The microwave-induced absorption (MIA) spectra are collected by scanning the detection wavelength with a monochromator, keeping fixed the frequency of the microwaves at a value

corresponding to a resonant transition (commonly individuated from preliminary ADMR or FDMR spectra).

These spectra are known also as T-S spectra (triplet minus singlet) because the singlet and the triplet absorptions of the species carrying the triplet states appear with opposite sign. The T-S spectra are invaluable in the assignation of the triplets individuated with FDMR or ADMR to specific chromophores due to the possibility to link their ZFS parameters to their optical absorption profile. These microwave-induced T-S spectra are more selective than the more conventional flash-induced technique, allowing to record the T-S spectra of individual triplet states in complexes multi-chromophore proteins. Additionally, if the electronic distribution of the triplet-carrier differs enough between the singlet and the triplet state to give rise to different interactions with the nearby molecules, then the T-S spectrum may also display the contribution of the molecules that interact with the molecule carrying the triplet state. This is another feature that allows to obtain information about the surrounding of the molecules carrying the triplet state.

3.5 Experimental conditions

The experiments presented in this thesis have been performed in the ODMR laboratory in the Department of Chemical Sciences of the University of Padova. The homemade ODMR apparatus, schematized in figure 19, is constituted by three main parts: the cryostat, the microwaves circuit and the optical excitation and detection system.(Hoff 1996)

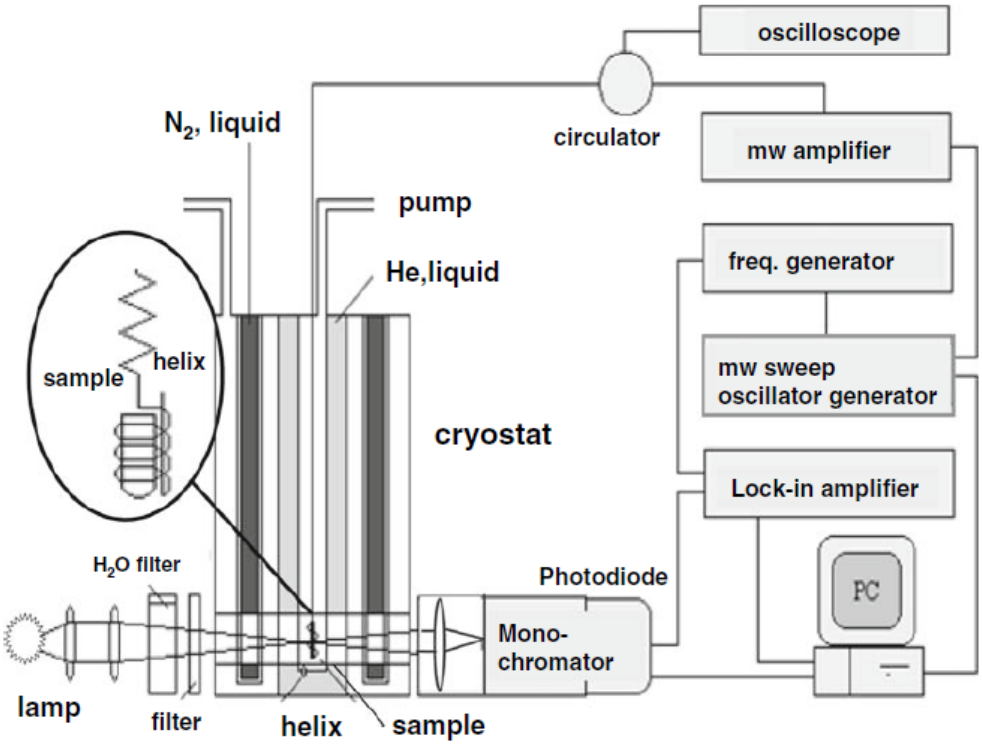

Figure 19: Scheme illustrating the ODMR instrumentation.(Carbonera 2009)

3.5.1 Cryostat

To be analyzable with ODMR instrumentation, a triplet state have to be polarized even at zero field, hence the spin-lattice relaxation process have to become negligible. For the organic molecules studied in this thesis, this condition is fulfilled at cryogenic temperature and therefore a liquid helium cryostat has to be employed. The cryostat (Spectromag 4 of the Oxford Instruments) has been modified to allow the ingress of a coaxial wire necessary to transmit the microwaves. The sample chamber is separated from the liquid helium reservoir with a connection between them that is regulated by a spill valve which modulates the quantity of the helium that comes into contact with the sample, allowing to hold the sample chamber at a controlled temperature between 1.7 and 200 K with a concomitant regulation of the helium flux and of a controllable heating system. The temperature in the chamber can be maintained below the λ-point of helium (2.1 K), by lowering the pressure above the liquid helium until the superfluid state is achieved. This is particularly important because under illumination the liquid helium boils and the bubbles generated by this process scatter the light prohibiting the measurements, whereas in the superfluid state no boiling process is observed. The sample chamber is equipped with four optical accesses, which allow the ingress of the excitation light and the detection of the absorbance and the fluorescence (at 90°).

3.5.2 Microwave circuit

The microwave generator utilized is an HP8350B with a plug-in devices H 83522A that works in the microwave range 0.01-2.4 GHz and has a maximal output power of 20 mW. The microwaves are amplified using two amplifiers working in different intervals, characterized by a maximal output power of 10 W: a LogMetrics A210/L in the range 1-2 GHz and a Sco-Nucleotudes ALP150 for the range 0.01-1 GHz. From the amplifier, the microwaves are sent through a semirigid coaxial cable to a copper helix that surrounds the flat cell that contains the sample in the sample chamber of the cryostat. To avoid dangerous reflection of the amplified microwaves back to the amplifier, a set of circulators is utilized, characterized by the different ranges of microwaves in which they operate.

The helix has been handmade coiling a copper wire around a plexiglass flat cell with a step of 2 mm. The helix is a broad-band resonator, which allows performing microwave scan experiments with almost constant power. The slim shape of the helix, enables to obtain a good irradiance and absorption of the microwave during the experiments, whereas its high step allows a good optical accessibility. In FDMR experiments the flat cell is oriented at 45° respect to the incident beam, whereas in the ADMR the flat cell is perpendicular to the beam.

To obtain a good signal to noise ratio, a phase-sensitive detection is employed. The microwaves are amplitude modulated, for this purpose a signal generator Wavetek is employed, which generates a square waveform amplitude modulation (on-off) of the microwaves. Then the photodetector signal is demodulated and amplified with a phase sensitive amplifier (lock-in EG&5210) before the registration.

3.5.3 Optical system

The sample is continuously irradiated with a tungsten lamp (Philips 250 W supplied by an Agilent 6653A power supply), focused on the sample in a spot 0.5 cm wide and 1 cm high, which invests the majority of the flat cell.

In the FDMR experiments reported in this thesis, the excitation light has been filtered with infrared cut-off filters and a solution of $CuSO_4$ (0.1 M, 5 cm) that is characterized by a band pass between 400 and 600 nm. The fluorescence, filtered with a cut-off filter at 645 nm to minimize the scatter, has been selected with interferential filters centered at different wavelengths and characterized by 10 nm of full width at half maximum (FWHM).

The ADMR spectra have been obtained filtering the excitation light with a water filter (5 cm) and infrared cut-off filters and fixing the detection wavelength using a monochromator (ISA employed Jobin Yvon HR250), with a resolution that has been varied in dependence of the intensity of the signal observed. In the microwave induced T-S spectra the monochromator wavelength is scanned while the microwave frequency is fixed at the resonant transition of interest.

The selected light is revealed by a photodiode (OSI 5KM Centronic) in both the experimental setups.

3.5.4 Registration

The instrumentation is interfaced to a PC that controls the scans of the oscillator and of the monochromator and the acquisition and handling of the data by means of programs written in the laboratory.

3.6 References

Carbonera, D., 2009. Optically detected magnetic resonance (ODMR) of photoexcited triplet states. *Photosynthesis Research*, 102, pp.403–414.

Carbonera, D., Giacometti, G. & Agostini, G., 1992. FDMR of carotenoid and chlorophyll triplets in Light-harvesting complex LHCII of spinach. *Applied Magnetic Resonance*, 3, pp.361–368.

Clarke, R. H., 1982 *Triplet state ODMR spectroscopy*. John Wiley and Sons.

Hoff, A. J. 1982 *ODMR spectroscopy in photosynthesis II*. In R. H. Clarke, ed. Triplet state ODMR spectroscopy. John Wiley and Sons.

Hoff, A. J., 1996 *Optically detected magnetic resonance (ODMR) of triplet states.* In: J. Amesz, A. J. Hoff, eds. *Advances in photosynthesis, vol 3 Biophysical techniques in photosynthesis*. Kluwer Academic Publishers.

Maki, A.H., 1984. *Techniques, theory, and biological applications of Optically Detected Magnetic Resonance (ODMR)*. In L. J. Berliner & J. Reuben, eds. Biological Magnetic Resonance vol. 6. Plenum Press.

Schmidt, J., van der Waals, J. H., 1968. Optical detection of Zero-Field transitions in phosphorescent triplet states. *Chemical Physics Letters*, 2, pp.640-642

Electron Paramagnetic Resonance

The electron paramagnetic resonance (EPR) is a spectroscopic technique that allows the study of the response of a chemical species with at least one unpaired electron, in the presence of a static magnetic field, to the magnetic part of an electromagnetic radiation, typically in the microwave region. The biological applications of this technique are wide because paramagnetic species like radicals, triplets and transition metal ions are present in many key metabolic steps as crucial intermediates, cofactors and toxic byproducts.

The frequency band most commonly used is comprised between 9-10 GHz, the so-called X band, but commercial EPR spectrometers which work in different bands in the range 1-95 GHz are available.

4.1 CW EPR

The simplest technique is the CW-EPR (continuous wave EPR), in which the sample is irradiated with a monochromatic microwave beam while a slow scan (slow respect to the decay/relaxation rates of the paramagnetic species under study) of the static magnetic field is performed. The observable transitions, which give rise to the signal, must fulfill the magnetic spectroscopy selection rule $\Delta M_S = \pm 1$ and are visible when the resonance condition is reached.(Weil & Bolton 2007)

To maximize the intensity of the magnetic component B_1 of the microwaves, the samples are allocated in opportunely designed resonant cavities. The particular geometry produces a standing wave with a maximum of B_1 and a node of E on the sample. When the scanned magnetic field brings one magnetic transition of the system in resonance with the monochromatic radiation, the variation of the magnetic properties of the sample-cavity system leads to a variation in the reflection of the microwaves, which are detected by a diode and constitute the EPR signal.

Low-frequencies noise reduction is achieved by phase-sensitive detection, by means of a fast modulation of the external magnetic field coupled with a lock-in detection. The modulation is usually realized at 100 KHz at the small amplitude of few Gauss by specific modulation coils. The current intensity detected by the diode is then proportional to the slope of the absorption, resulting in the first derivative lineshape.

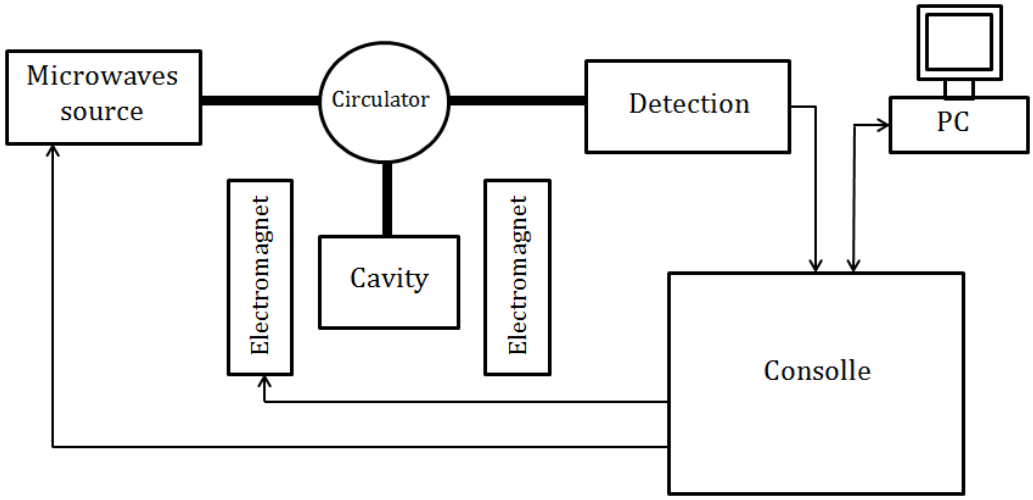

Figure 20. Schematic description of a CW-EPR instrument. In black the waveguide through which the microwaves are transmitted.

This steady state technique is suitable for stable paramagnetic species, like transition metal ions, nitroxides and other radicals,(Brustolon & Giamello 2009) but for the study of transient paramagnetic species, like photoexcited triplets and short-living radicals, a time resolved or pulsed approach is mandatory.

4.2 TR-EPR

As in the CW experiments, in time resolved EPR (TR-EPR) the microwave frequency is kept constant and the magnetic field is scanned. The striking difference is that in TR-EPR a third time dimension is introduced, with the consequence that this kind of spectra contains information about the time evolution of the paramagnetic species and appears as three-dimensional surfaces.

In the photoexcited TR-EPR experiments the sample, in a resonant cavity, is continuously irradiated with monochromatic microwaves, and after the laser pulse, the time evolution of the EPR signal is monitored, at a fixed value of the magnetic field. The procedure is repeated varying the magnetic field position. A series of time traces gives the final surface representing the evolution of the spectrum in time.

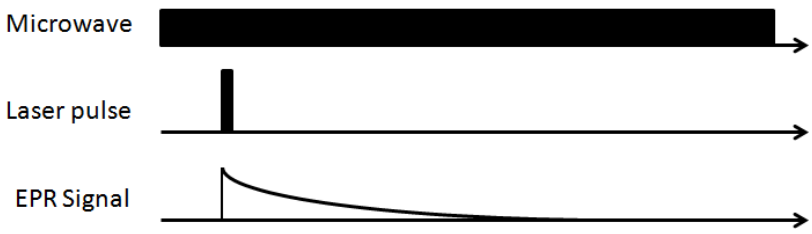

Figure 21. Schematic description of a TR-EPR experiment. The reported sequence is repeated at every field position.

The instrumentation involved in the acquisition of a TR-EPR spectrum is based on a common CW-EPR spectrometer; a laser beam is focused into the cavity to generate the photo-excited species. The signal is directly revealed by the diode without modulation and lock-in detection. Then detection is synchronized with the laser excitation through a trigger signal. The analogical signal of the diode is pre-amplified and collected by a digitalizer that must have a time-resolution high enough to follow the time-evolution of the signal.

4.2.1 Triplet state TR-EPR

The EPR spectrum of a molecule in the triplet state is substantially determined by the contributions of the Zeeman and electron dipolar interactions. The solution of the Hamiltonian, hence the determination of the eigenfunctions and the eigenvalues, have been already presented in the second chapter. The magnetic resonance selection rule $\Delta M_S = \pm 1$ imposes that for every orientation of the molecules with respect to the external magnetic field two transitions are allowed. This means that for a crystalline sample the spectrum will be composed by a pair of lines for every molecule in the crystal unity cell, with a splitting that depends on the orientation of the molecule in the crystal relatively to the magnetic field.

In a disordered matrix, like a glass or a polycrystalline powder, every possible orientation is present and contributes to the overall spectrum. This situation is common for solutions of proteins measured at low temperature after a fast freezing process, like the sample analyzed in this thesis. In this situation it is possible to identify in the spectrum six characteristic points, called "turning points", which are generated in couple by the molecules oriented with the magnetic field parallel to one of the ZFS axes. In figure 23 the simulated spectrum of a Chl *a* triplet, in which the turning points, corresponding to $Z_{|}$, $X_{||}$, $Y_{||}$, $X_{|}$, $Y_{|}$, and $Z_{||}$ are clearly visible, is reported as example.

The shape of the spectrum is also determined by the spin polarization, because, as explained in paragraph 2.5.1, the intensity and the sign of a couple of canonical transitions, for example $Z_{|}$ and $Z_{||}$, depend on the difference in population between p_0 (that for this orientation of the molecules is equal to p_z) and $p_{\pm 1}$ (that in this case are equal to $\frac{p_x+p_y}{2}$). For every orientation the populations $p_{\pm 1}$ and p_{-1} are equal, so the high field and low field transitions have the same intensity and are opposite in sign, generating the characteristic symmetric shape of the triplet spectra. The signs of the features of the spectra are commonly reported as *A* and *E* for absorption and emission respectively, for example the spectrum in figure 22 has an *EEEAAA* polarization pattern.

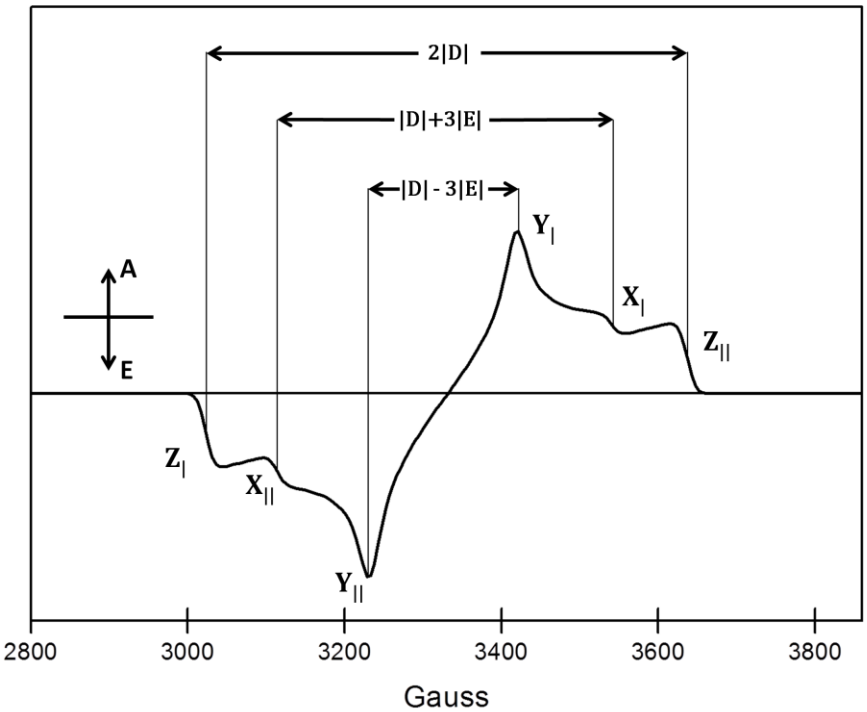

Figure 22: Simulated TR-EPR spectrum of a Chl a triplet, with the canonical transitions marked and the distance between every couple of them reported.

The great advantage of the TR-EPR technique, in the study of triplet states, is the possibility to record the initial spin-polarization of the triplets at a short time delay from their photo-generation, before contributing of the decay and relaxation processes. The initial polarization pattern in the case of carotenoid triplet states populated starting from chlorophyll triplet states via TTET, (see 2.5.2), depends on the geometry of the donor-acceptor pair and gives information about the structure and functionality of the photoprotection sites of the multichromophoric systems under study.

4.3 Pulse EPR

Alternatively, the time resolution required to study transient photoexcited species can be also achieved with a pulse EPR approach. Contrarily to the CW EPR methodologies described above, in which the sample is continuously irradiated with microwaves, in pulse EPR the spin ensemble is perturbed with microwave pulses (with lengths in the ns time range), and the signal is the result of the dynamic of the spin-system state prepared by the pulses.(Schweiger & Jeschke 2001) These methodologies are commonly employed in the investigation of the interaction of the electron spins with their direct nuclear surrounding, as well as in the measurement of the magnetic-dipolar interaction between unpaired electrons, from which is possible to extract information about their distance distribution. These experimental methodologies require the detection of an electron spin echo (ESE) signal, which limits their application to systems with a sufficiently large transverse relaxation time (more than 100

ns).(Kulik 2009) This makes pulse EPR not suitable for studies of liquid samples and generally requires low-temperature experiments in glassy matrices.

4.3.1 Pulse ENDOR

Among the several applications of pulse EPR, pulse electron–nuclear double resonance (ENDOR) has been widely employed in the study of paramagnetic states of photosynthetic cofactors. This is a double resonance technique, in which both microwave and radiofrequency (RF) pulses are employed to manipulate electron and nuclear spins, respectively. The technique allows to measure the nuclear hyperfine structure, which is often unresolved in EPR spectra. From the isotropic hyperfine couplings a map of the unpaired electron spin distribution over the molecule can be obtained, from which the detailed electronic structure can be derived.

The principle of pulse ENDOR is based on the change of the intensity of an EPR transition following the application of a selective nuclear spin transition. During the pulse ENDOR experiment, the magnetic field and the frequency of the microwave pulses are fixed, and the frequency of the RF pulse is swept while monitoring the ESE signal. The RFs at which the echo-signal changes are detected give information about the size of the hyperfine interactions.

In case of photoexcited species, as in the case of triplet states, all the pulses are triggered from the initial laser pulse. The microwave pulses are employed to induce EPR transitions, that in high field conditions follow the selection rule $\Delta M_S = \pm 1$, as described for the TR-EPR experiments. Similarly the RF pulses induce nuclear transitions, which follow an analogous selection rule with $\Delta M_S = 0$ and $\Delta M_I = \pm 1$. The ENDOR spectra of triplet states in frozen solutions are commonly collected at field positions corresponding to turning points of the EPR spectrum, in order to select only the molecules oriented with one of the ZFS axis parallel to the static field B_0. This methodology allows to obtain single crystal-like ENDOR spectra, from which it is possible to extract the projections of the hfc tensors on the ZFS axis system.

As shown in figure 23, for each EPR transition, only some of the nuclear transitions affect the population of the levels involved in the EPR transition. An ENDOR selection rule can be easily derived. For the case of the field parallel to the Z-axis of the ZFS tensor: $\nu_{ENDOR} = \nu_H - M_I A_Z$, where ν_H is the proton free Larmor frequencies at the particular B_0, and A_z is the projections of the hfc tensors on the Z-axis of the ZFS tensor. From this selection rule, it follows that for each EPR transition ($T_{+1} \leftarrow T_0$ and $T_0 \leftarrow T_{-1}$) there are two ENDOR resonance frequencies:

$$\nu_{ENDOR}(0) = \nu_H$$
$$\nu_{ENDOR}(\pm 1) = \nu_H \mp A_{ZZ}$$

From these expressions, it is clear that the ENDOR spectra of triplet states are asymmetric, with a transition common to all the nuclei (at the ν_H frequency), and two transitions at a frequency dependent from the hfc of the specific nucleus. In order to ease the analysis of the data, usually they are plotted as deviations from the ν_H frequency.

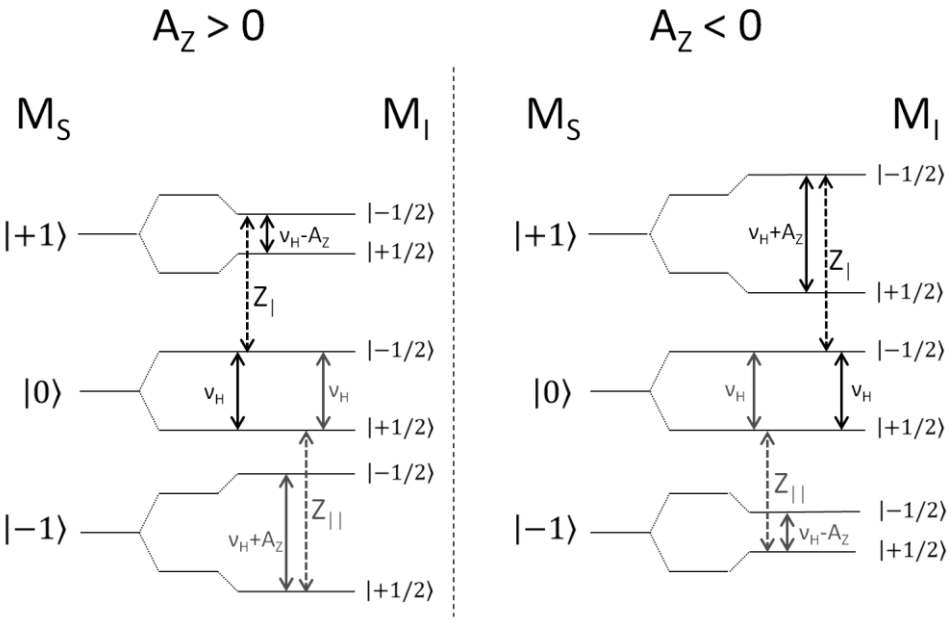

Figure 23: Spin energy levels of a triplet state showing positive and negative hyperfine splitting A_Z from one nucleus with spin I = 1/2 for the field parallel to the Z-axis of the ZFS tensor. Black dashed arrows: Z_I EPR transition; black thick arrows: ENDOR transitions for Z_I. Gray dashed arrows: Z_{II} EPR transition; gray thick arrows: ENDOR transitions for Z_{II}.

The mostly used pulse ENDOR schemes, namely the Davies (Davies 1974) and Mims (Mims 1965) sequences, are schematically described in the following figure.

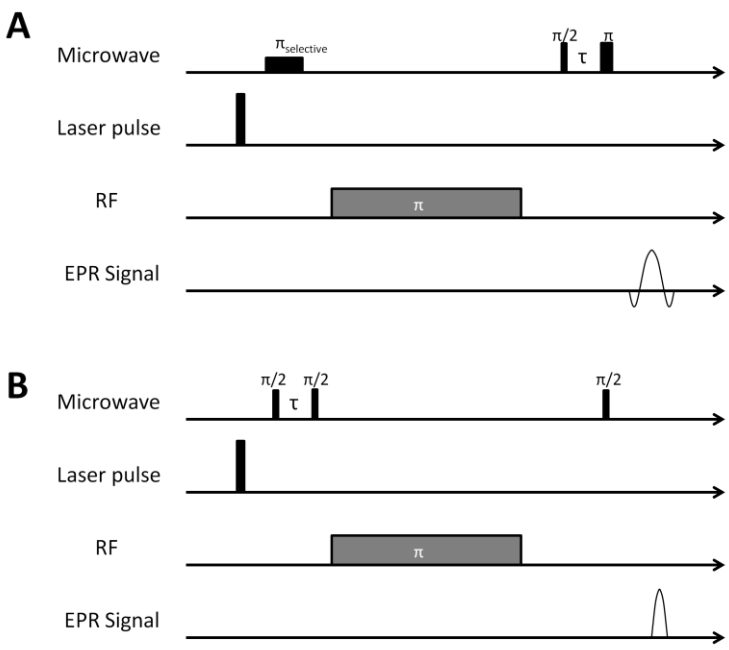

*Figure 24: Schematic description of the pulse scheme for **A)** Davies and **B)** Mims ENDOR experiments. The reported sequence is repeated varying the RF frequency, at a fixed field position.*

The two pulse schemes are complementary in the information that can be derived from the experiments. Davies ENDOR is suitable for measuring large hfcs but does not allow resolving signals with small hfcs. On the other hand, Mims ENDOR is powerful for the detection of small hfcs, but, since the spectra are intrinsically affected by blind spots, averaging at different τ values is required, making the experiment time consuming. Therefore, the best approach is to employ both the techniques, performing Mims experiments only in a narrow frequency interval around ν_H sufficient to obtain a complete set of the smaller hfcs.

4.4 References

Brustolon, M, Giamello, E., 2009. *Electron Paramagnetic Resonance: A Practitioners Toolkit.* Wiley.

Davies, E. R., 1974. A new pulse ENDOR technique. *Physics Letters*, 47(1), pp.1-2

Kulik, L., Lubitz, W., 2009. Electron-nuclear double resonance. *Photosynthetic research*, 102, pp.391-401

Mims, W. B., 1965. Pulsed ENDOR experiments. *Proceedings of the Royal Society of London. Series A, Mathematical and Physical Sciences*, 283(1395), pp.452-457

Schweiger, A., Jeschke, G., 2001 *Principles of pulse electron paramagnetic resonance*. Oxford University Press.

Weil, J. A., Bolton, J. R., 2007 *Electron paramagnetic resonance – elementary theory and practical applications II edition*. Wiley.

Part II

Reaction Centers

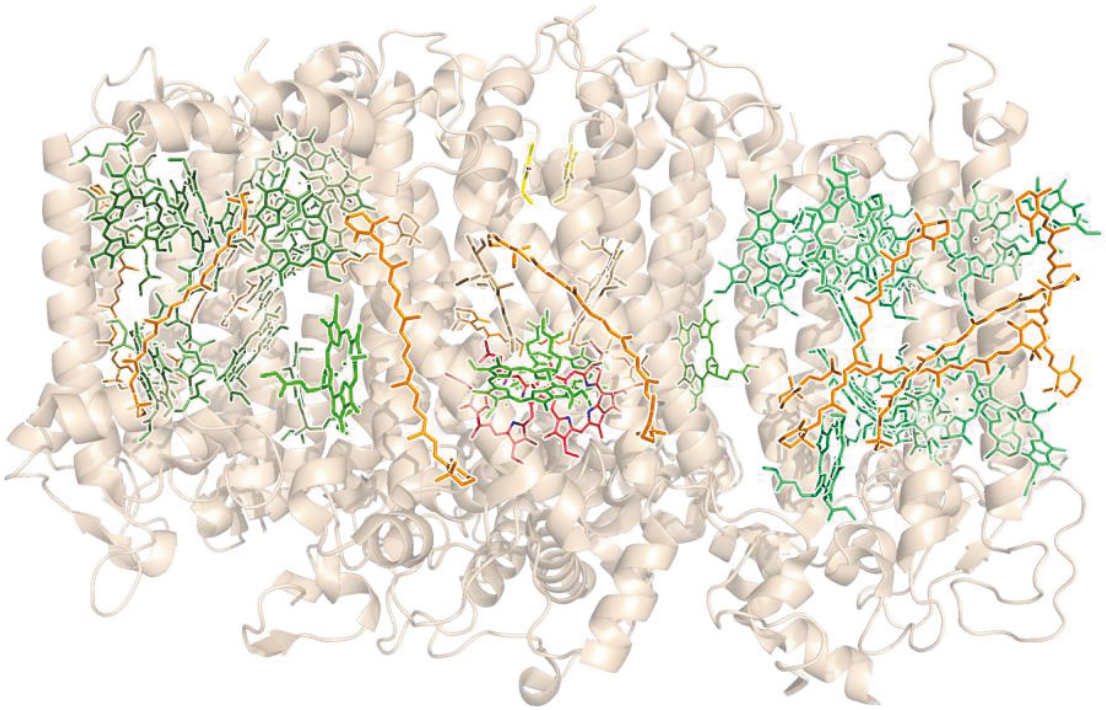

Biochimica et Biophysica Acta 1847 (2015) 262–275

Contents lists available at ScienceDirect

Biochimica et Biophysica Acta

journal homepage: www.elsevier.com/locate/bbabio

Carotenoid triplet states in photosystem II: Coupling with low-energy states of the core complex

Stefano Santabarbara [a,*], Alessandro Agostini [b], Anna Paola Casazza [c], Giuseppe Zucchelli [a], Donatella Carbonera [b,**]

[a] Istituto di Biofisica, Consiglio Nazionale delle Ricerche, Via Celoria 26, 20133 Milan, Italy
[b] Department of Chemical Sciences, Università di Padova, Via Marzolo 1, 35131 Padova, Italy
[c] Istituto di Biologia e Biotecnologia Agraria, Consiglio Nazionale delle Ricerche, Via Bassini 15a, 20133 Milano, Italy

ARTICLE INFO

Article history:
Received 25 September 2014
Received in revised form 19 November 2014
Accepted 21 November 2014
Available online 3 December 2014

Keywords:
Photosystem II
Photosystem II core complex
Carotenoid
Triplet state
Triplet state quenching
Optically Detected Magnetic Resonance

ABSTRACT

The photo-excited triplet states of carotenoids, sensitised by triplet–triplet energy transfer from the chlorophyll triplet states, have been investigated in the isolated Photosystem II (PSII) core complex and PSII–LHCII (Light Harvesting Complex II) supercomplex by Optically Detected Magnetic Resonance techniques, using both fluorescence (FDMR) and absorption (ADMR) detection. The absence of Photosystem I allows us to reach the full assignment of the carotenoid triplet states populated in PSII under steady state illumination at low temperature. Five carotenoid triplet (^{3}Car) populations were identified in PSII–LHCII, and four in the PSII core complex. Thus, four ^{3}Car populations are attributed to β-carotene molecules bound to the core complex. All of them show associated fluorescence emission maxima which are relatively red-shifted with respect to the bulk emission of both the PSII–LHCII and the isolated core complexes. In particular the two populations characterised by Zero Field Splitting parameters $|D| = 0.0370–0.0373\ cm^{-1}/|E| = 0.00373–0.00375\ cm^{-1}$ and $|D| = 0.0381–0.0385\ cm^{-1}/|E| = 0.00393–0.00389\ cm^{-1}$, are coupled by singlet energy transfer with chlorophylls which have a red-shifted emission peaking at 705 nm. This observation supports previous suggestions that pointed towards the presence of long-wavelength chlorophyll spectral forms in the PSII core complex. The fifth ^{3}Car component is observed only in the PSII–LHCII supercomplex and is then assigned to the peripheral light harvesting system.
© 2014 Elsevier B.V. All rights reserved.

1. Introduction

Photosystem II (PSII) is a macromolecular light-dependent oxido-reductase which catalyses the oxidation of water to molecular oxygen and protons, and the reduction of plastoquinone to plastoquinol e.g. [1–3]. From a structural point of view PSII can be seen as composed of two moieties: i) the *core* that serves both as photo-catalytic centre and proximal light harvesting antenna to the reaction centre (RC), and appears to be substantially conserved throughout evolution e.g. [4,5], and ii) an external antenna, whose function is only that of light harvesting, and which varies greatly amongst species as an adaptation to the spectral quality of incident radiation in different ecological environments e.g. [6,7].

The core complex is composed of over 20 subunits [1–5], binds about 40 chlorophyll (Chl) *a* and 10 β-carotene (β-Car) molecules, together with the other cofactors required for electron transfer, including two pheophytin and two plastoquinone molecules, a cytochrome (Cyt b_{559}), a Fe atom and a 4Mn–1Ca cluster, which is the site of water splitting e.g. [8,9]. Four subunits bind the vast majority of the pigments: the CP43 and CP47 complexes that compose the proximal antenna and the D1D2Cytb_{559} complex, which harbours all of the electron transfer cofactors [1–5,8,9].

In the green lineage, the external antenna is composed of Chl *a*/*b*-binding complexes [3,11–14], which are the product of the nuclear gene family known as *lhcb* [6,7]. The PSII external antenna contains several components. The principal component, called Light Harvesting Complex II (LHCII), is a trimer and is bound with a stoichiometry of 2–4 trimers per core complex [3,15,16]. Each monomeric unit binds 8 Chl *a*, and 6 Chl *b* as well as four oxygenated carotenoids (xanthophylls), two lutein, one neoxanthin and one violaxanthin molecules [3,11–14]. The latter can be exchanged with zeaxanthin depending on the growth conditions [17–19]. The other PSII antenna complexes, CP24, CP26 and CP29, are all isolated as monomers and bind with 1:1 stoichiometry to

Abbreviations: PSII(I), Photosystem II(I); LHC, Light Harvesting Complex; RC, reaction centre; Chl, chlorophyll; Car, carotenoid; Xan, xanthophyll; ODMR, Optically Detected Magnetic Resonance; FDMR/ADMR, Fluorescence/Absorption Detected Magnetic Resonance; ZFS, Zero Field Splitting; MIF, microwave-induced fluorescence spectrum; T − S, Triplet minus Singlet; NPQ, Non-Photochemical Quenching; TTET, triplet–triplet energy transfer

* Corresponding author. Tel.: +39 0250314857; fax: +39 0250314812.
** Corresponding author. Tel.: +39 498275144; fax: +39 498275161.
E-mail addresses: stefano.santabarbara@cnr.it (S. Santabarbara), donatella.carbonera@unipd.it (D. Carbonera).

http://dx.doi.org/10.1016/j.bbabio.2014.11.008
0005-2728/© 2014 Elsevier B.V. All rights reserved.

the core complex [3,15,16]. Like LHCII, albeit with a different stoichiometric ratio, the monomeric antennae bind, on average, 10–14 pigments per protein, both Chl *a* and Chl *b*, with ratios going from 1.2 to 2.2 and xanthophylls with ratios of 2–3 molecules per complex [3,11–14].

The carotenoids that are bound both to the core and to the external antenna of higher plants play several roles in the photosynthetic apparatus, particularly in PSII. They are involved in light harvesting of the portion of the incident solar spectrum in the blue-green region [19,20]. However, the spectral overlap with the so-called Soret band of Chl *a* and Chl *b* is significant and the increase in the antenna bandwidth is therefore limited overall [21]. Xanthophylls (Xan) are also involved in processes that regulate the efficiency of light harvesting in response to the increase in intensity of the incident radiation, such as Non-Photochemical Quenching (NPQ) (reviewed in Refs. [17–19]). One clear evidence is the enzymatic conversion of violaxanthin to zeaxanthin when the system is exposed to high irradiance regimes, concomitantly with the acidification of the thylakoid lumen [17–19,22]. Moreover, xanthophylls, either lutein or zeaxanthin, have been proposed to play a direct role in NPQ, representing the effective quenching site either through a singlet–singlet (Xan–Chl) energy transfer mechanism e.g. [23–25], or being partner in the formation of a Chl–Xan charge–transfer complex e.g. [26,27]. It has been also suggested that the carotenoid conformation (cis–trans isomerisation, bond twisting) can affect the chromophores binding within the LHC complexes and hence the chromophore–chromophore interactions, leading to the formation of singlet excited state quenchers (reviewed in Ref. [23]). Their involvement in controlling the fine "packing" of the antenna, mediating different interactions between adjacent complexes, has also been discussed [28]. Therefore, independently from the mechanism, which is much debated, the involvement of carotenoids in the NPQ process is generally accepted.

Carotenoids also have an important structural role, stabilising the folding of pigment binding proteins e.g. [29–33]. This has been demonstrated both in vitro by reconstitution experiments of LHC complexes [29,30], as well as in vivo in mutants affected in the carotenoid biosynthesis [31–33].

Certainly, a central role of carotenoids in the photosynthetic apparatus is the quenching of the Chl triplet state (^{3}Chl) through the triplet–triplet energy transfer (TTET) mechanism (reviewed in Refs. [20,34,35]). The direct population of the carotenoid triplet state (^{3}Car) by intersystem crossing (ISC) is a low probability event, due to the very short lifetime of the excited state of these molecules, that is dominated by internal conversion [20,34,35]. Energy transfer from the ^{3}Chl, which is populated with a yield of ~0.6 in the absence of other quenching mechanisms [36,37], is efficient in photosynthetic systems [38–40] because of the short average inter-pigment distances and because the ^{3}Car lays at an energy level which is below that of ^{3}Chl. It is established that the ^{3}Chl is an efficient sensitiser of singlet oxygen ($^1O_2$), which is an highly reactive species and one of the principal actors in photo-oxidative stress [41,42]. On the other hand, the energy level of the ^{3}Car present in photosynthetic complexes is too low to interact with molecular oxygen. Therefore, the quenching of the ^{3}Chl state by TTET to the ^{3}Car is of fundamental importance under physiological perspective. Indeed, the population of ^{3}Car under illumination is well documented both in relatively intact preparations, such as thylakoid membranes e.g. [38–40,43,44], as well as in isolated pigment–protein complexes where it has been investigated intensively e.g. [45–57].

However, the determination of specific Chl–Car interactions and the identification of the molecules involved in TTET are usually cumbersome due to the severe spectral "congestion" determined by the overlap in the absorption spectrum of different Chl forms, as well as different carotenoids, bound to oxygenic photosystems. Such difficulties can be in part overcome by the use of time-resolved magnetic resonance techniques, since the signal arising from the ^{3}Car is strongly polarized and the polarisation is extremely sensitive to the orientation of donor and acceptor molecules in the pair [58]. This allows the identification of the chromophores involved in the energy transfer process, provided that a structural model of the complex is known which sufficient accuracy. The approach has been successfully applied to the study of isolated LHCII and other antenna complexes e.g. [59–62].

An alternative approach is that of using techniques that allow the correlation of parameters characterising the electron spin of the chromophore with the optical properties of either the chromophore itself (i.e. ^{3}Car) or the sensitiser molecule (^{3}Chl). One such technique is Optically Detected Magnetic Resonance (ODMR), which is extremely selective for the detection of photo-excited triplet states (reviewed in Refs. [63–65]; a description of the basic principles of the ODMR technique is presented in Supporting information, Appendix 1). ODMR allows precise estimation of the zero-field splitting (ZFS) parameters that determine the energy split between the triplet sublevels and depend on the unpaired spin distribution with respect to the chromophore molecular frame. In recent years, the use of this technique has allowed the investigation of both ^{3}Car and ^{3}Chl in intact systems, such as the thylakoid membranes [65–69]. Using this spectroscopic method, particularly by fluorescence detection (FDMR), it was possible to identify the ^{3}Chl states populated in both Photosystem I (PSI) and PSII under ambient redox conditions [66–68]. These ^{3}Chl states were suggested to be involved in photo-oxidative stress [70]. It was also possible to detect a ^{3}Chl associated with the reaction centre of PSII under non-reducing conditions [66,67,71]. This ^{3}Chl shows a remarkably fast relaxation [66,67,71] with respect to the ^{3}Chl observed under reducing conditions typically employed to induce charge recombination e.g. [67,72–74].

Although the fluorescence yield of carotenoids is extremely low and therefore almost undetectable, especially in crowded chromophore–protein complexes, it is still possible to monitor ^{3}Car by FDMR, detecting the fluorescence emission of Chl molecules [45–48,65]. This is because the change in the mean rate of the ^{3}Car decay, induced by resonance conditions, affects the steady-state population of the singlet excited states of the Chl fluorescent molecules to which Cars are coupled by energy transfer (Fig. 1). Employing the FDMR technique it was then possible to observe, for the first time, that the ^{3}Car associated with the external antenna of PSI embedded in the thylakoid membranes [69]. The assignment was later confirmed in isolated LHCI complexes [75]. The ^{3}Car associated with PSII have also been investigated by FDMR in thylakoids [76]. However, due to the significant overlap of PSII and PSI

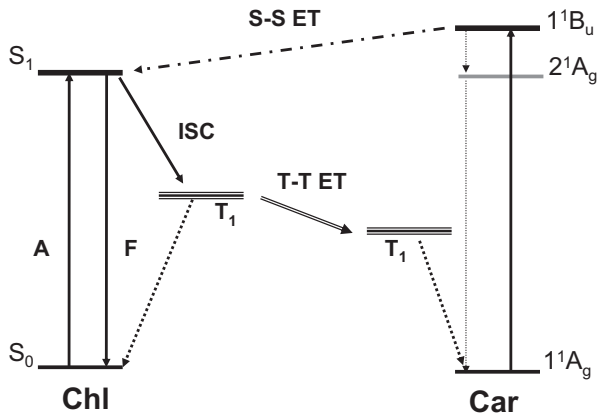

Fig. 1. Scheme describing the principle of FDMR detection of ^{3}Car by monitoring Chl fluorescence emission in photosynthetic systems. On the left it is shown the energy diagram for a Chl molecule, considering its ground (S_0), first singlet excited (S_1) and triplet excited (T_1) states. The Chl T_1 state is populated by intersystem crossing (ISC). On the right, the energy diagram for a Car molecule, considering its ground (1^1A_g), first (2^1A_g) and second (1^1B_u) singlet excited and triplet excited (T_1) states. The Car T_1 state is populated by triplet–triplet energy transfer (TTET) from the Chl triplet. The 1^1B_u singlet excited state of Car is coupled by singlet–singlet energy transfer (SSET) to the S_1 state of Chl. FDMR measurements are possible because the applied microwave field in resonance with a pair of sublevels of the Car T_1 alters the population of the Car ground and singlet excited state. Because of SSET between the Car and Chl molecules, the Chl excited state population is also affected and monitored on its fluorescence emission.

emission above 700 nm, the analysis was limited to a relatively narrow spectral window and led only to a partial characterisation of species belonging to PSII. Nevertheless, it was shown that several ^{3}Car populations are present in PSII: at least one was suggested to be associated to the external antenna and three to the core complex [76].

Here we present an extended and detailed analysis of the ^{3}Car in PSII–LHCII supercomplexes (BBY membranes) and core complexes of PSII isolated from spinach with the aim of identifying the carotenoid molecules involved in the protective quenching of the ^{3}Chl state, in photochemically active particles. The ^{3}Car were characterised employing both the FDMR and the microwave-induced Triplet minus Singlet (T − S) techniques. On the basis of the ZFS parameters and the associated microwave-induced fluorescence spectra (MIF), five ^{3}Car populations were identified in PSII–LHCII and four in the PSII core complex. Thus, four ^{3}Car populations are attributed to β-carotene molecules bound to the core complex. All of them show microwave-induced fluorescence emission maxima which are relatively red-shifted with respect to the bulk emission of both the PSII–LHCII and the isolated core complex.

2. Experimental procedures

2.1. Isolation of PSII–LHCII and PSII core complexes

PSII–LHCII was purified from spinach according to Berthold et al. [77] with the modification described by Dunahay et al. [78] by Triton X-100 fractionation of thylakoids (so-called BBY membranes). Thylakoid membranes were isolated from fresh spinach leaves as described in Ref. [79]. The Chl *a*/*b* ratio determined from water/acetone (20:80) extraction of the purified BBY membranes, using the extinction coefficients given by Lichtenthaler [80], was 2.0 ± 0.1 corresponding to a stoichiometry of approximately 3 LHCII trimers per core complex [3,15,16]. The purity of the preparation was checked by SDS-PAGE, using 15% polyacrylamide gels in 6 M urea (Laemmli discontinuous buffer system [81]) and Western-blot analysis indicating that PSI contamination, as judged by the presence of the high molecular weight subunits PsaA/PsaB, is less than 2%.

The PSII core complex was extracted from the isolated BBY membranes by solubilisation with octyl-β-D-glucopyranoside and successive dialysis, as described by Ghanotakis et al. [82]. After acetone/water extraction Chl *b* was below the level of detection, indicating that the preparation is virtually free of external antenna. The purity of the preparation was confirmed also by SDS-PAGE analysis.

2.2. Optically Detected Magnetic Resonance

FDMR, ADMR and T − S spectra were acquired in a laboratory assembled set-up which has been previously described in detail [46]. In brief, the light from a halogen lamp, powered by a stabilised driver unit, is directed to the sample, immersed in a bath helium cryostat (Oxford Instruments, mod. Spectromag 4), by a system of lenses, filtered through a heat filter and either a 5 cm $CuSO_4$ solution (FDRM) or a water filter (ADMR/T − S), depending on the experiment. The emission is collected by a Si-photodiode (OSI-Centronix) at 45° geometry, through bandpass filters (FWHM ~10 nm) and cut-on filters when necessary to remove the excitation stray light. The absorption is detected with standard geometry though a monochromator (Jobin Yvon, mod. HR250) and the same detector used for fluorescence measurements. The resonator consists of a slow pitch helix. The microwaves source is a HP8559b sweep oscillator equipped with a HP83522s plug-in, amplified by TWT amplifiers (Sco-Nucletudes mod 10-46-30 in the 0.01–1 GHz region, LogMetrics A210/L in the 1–2 GHz region). The microwaves, whose CW power was equivalent to ~1 W, were amplitude-modulated using a laboratory built function generator. The signal from the detector was sent to a Lock-In amplifier (EG&G, mod 5210), whose output was connected to a computer-controlled analogue-to-digital converter. The temperature was 1.8 K in all measurements. Immediately before the insertion into the cryostat, degassed glycerol was added to the samples to a final concentration of 60% v/v, in order to obtain homogeneous and transparent matrices upon freezing. After the dilution, the final Chl concentration of the samples was 150 μg/ml for FDMR experiments and 100 μg/ml for ADMR experiments.

2.3. Data analysis

ODMR is a double resonance technique, which correlates the optical properties of a chromophore with the magnetic resonance transition of its photo-excited triplet state. The resonance frequency depends on the energy separation amongst the triplet sublevel manifolds which, in the absence of an externally applied magnetic field, are determined by the triplet ZFS parameters |D| and |E|. Transitions are observed at energy equivalent to 2|E|, |D| − |E| and |D| + |E|, which in the case of ^{3}Car are all observable. A collection of FDMR records measured at discrete emission wavelengths constitutes, therefore, a data matrix that has one "optical" and one "magnetic" axis. The magnetic axis can be seen as be divided in three sub-sets, each associated with a particular magnetic resonance transition. Because of the correlation between the three magnetic resonance transitions on the "magnetic" axis and the optical properties of the chromophore on the "optical" axis, FDMR data are suitable to be analysed by global fitting procedures.

In the present study the data matrix constituted by the FDMR spectra (acquired in all three 2|E|, |D| − |E| and |D| + |E| transitions and at multiple emission wavelengths) is fitted using a "global constrained" strategy that has been already successfully applied to the investigation of both Chl [66,68] and Car [69,76] triplet states. The global model function is a linear combination of Gaussian functions. The details of the methods are described in Refs. [66,69,70]. A brief account of constrains imposed to the global fit can be summarised as:

i) for each triplet state population, described by a Gaussian sub-band, the peak position describing the 2|E| and the |D| + |E| transitions is common in the simultaneous description of measured spectra at different emission wavelengths. The number of sub-bands and their peak positions are, then, global "free running" fit parameters. The peak position of the |D| − |E| transition is determined from the values of the 2|E| and the |D| + |E| peak transitions; hence they are common to all emission wavelengths but they are not fit parameters [69,76].
ii) ii) for each triplet state population, instead, both the amplitudes and widths of the sub-band sets are "constrained" global fit parameters. The constraint consists in binding the sets of both amplitudes and widths of the sub-bands describing the 2|E| spectrum to those of the associated |D| − |E| and |D| + |E| spectra by scaling constants. Thus, the width and amplitudes of the Gaussian sub-bands describing the 2|E| transition are "free running" global fit and so are the values of the scaling constants.

The imposed constraints are based on the fact that the Gaussian width, dominated by site heterogeneity (inhomogeneous broadening) at 1.8 K, scale proportionally in the different transitions. The constraint on the amplitude is based on the rationale that each sub-band on the "magnetic axis", being associated with a specific chromophore triplet state on the "optical" axis, has an associated microwave induced fluorescence emission (MIF) spectrum whose band shape is expected to be invariant, when observed in the 2|E|, |D| − |E| and |D| + |E| "magnetic" transitions, but for an intensity factor. Moreover, in the measured |D| − |E| transition spectra a sharp negative peak is present that has no counterpart in the other spectral regions. One more sub-band is then necessary to describe the |D| − |E| transition region. This Gaussian sub-band has its frequency position, bandwidth and amplitude as free fit parameters.

The results of the fit analysis are, for each sub-band, the transition energy, from which the ZFS parameters are determined, and the MIF spectrum, which is the plot of the sub-band amplitudes as a function of the detection wavelength.

The number of Gaussian sub-bands required to fit the set of experimental spectra, measured at different emission wavelengths, is estimated as minimal number of fit parameters (i.e. sub-bands) required to yield a good value of the statistical estimators of the fit. To this end, the fitting routine minimises, for n experimental spectra, the "global" estimator χ_g^2 by a two-step sequential minimisation employing the Simplex (initial search) and Levenberg–Marquardt (refined search) algorithms. The "local" χ_l^2 is estimated, for the i-th spectrum, as the sum of square residual weighted for the shot-noise in the off-resonance tail of the same transition used as an estimator of the variance σ^2, and $\chi_g^2 = \frac{N}{N-p}\left(\sum_{l=1}^{n}\chi_l^2\right)\Big/n$, where N is the total number of data points and p is the total number of fit parameters. The quality of the fit is determined by the minimised value of χ_g^2, the inspection of the residual plot and by the stability of the solutions upon their perturbation.

This fit strategy limits the number of free fitting parameters and, then, reduces the number of numerical acceptable solutions, from purely statistic point of view, to a few meaningful physical solutions

3. Results

3.1. Fluorescence Detected Magnetic Resonance of carotenoid triplets in PSII–LHCII

Fig. 2 shows the FDMR spectra detected in the microwave region corresponding to the 2|E|, |D| + |E| and |D| − |E| resonance transitions, monitored at a few representative emission wavelengths across the

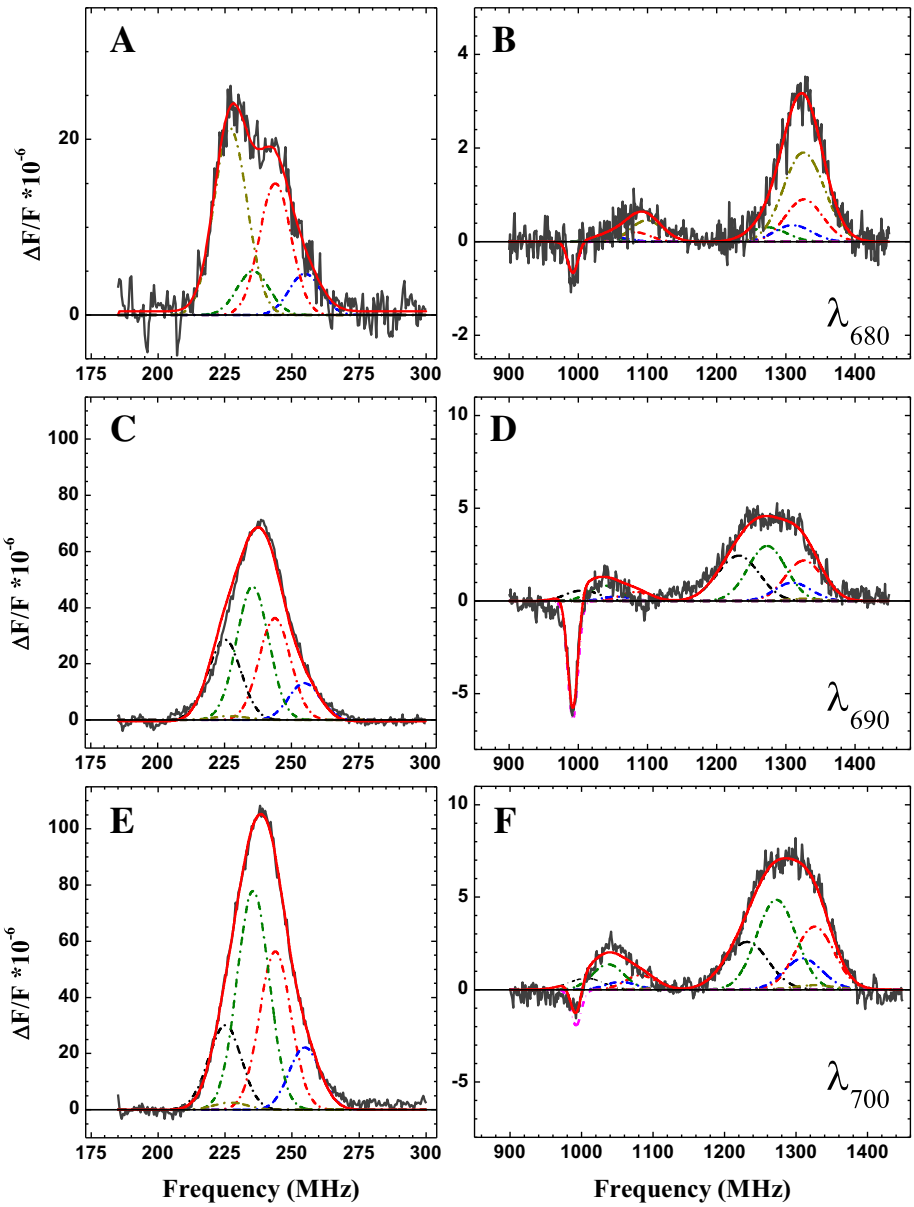

Fig. 2. FDMR spectra of carotenoid triplet states in the PSII–LHCII supercomplex detected at 680 nm (A, B), 690 (C, D) and 700 nm (E, F). Panels A, C and E show the 2|E| transition, whereas panels B, D and F show the |D| + |E| and |D| − |E| transitions. Also shown are the global fits in terms of a linear combination of Gaussian functions. Solid black lines: experimental spectra; red lines: fits. The dash-dotted lines show the contribution of each Gaussian sub-band. Black: T_1^{car} (|D| = 0.0373/|E| = 0.00375 cm^{-1}); red: T_2^{car} (|D| = 0.0402/|E| = 0.00406 cm^{-1}); green: T_3^{car} (|D| = 0.0385/|E| = 0.00393 cm^{-1}); blue: T_4^{car} (|D| = 0.0394/|E| = 0.00425 cm^{-1}); golden: T_5^{car} (|D| = 0.0404/|E| = 0.00378 cm^{-1}); magenta: T^{chl} (992 MHz). Experimental conditions: T = 1.8 K; MW Power: 1 W; mod. Amplitude: 330 Hz; phase: $\varphi = +26°$; scan rate: 0.5 MHz sec^{-1}.

fluorescence emission band of the PSII–LHCII complex. The FDMR spectra are equivalent to the corresponding microwave absorption spectra of the triplet states populated under illumination. However, it is not the microwave power which is detected, rather the fluorescence emission since it changes when the steady state populations of the singlet and triplet states are perturbed by the presence of a resonant microwave field (see Supporting information, Appendix 1 for further details on the technique). The FDMR spectra were recorded at a microwave modulation amplitude and phase sensitive detection which is selective for lifetimes in the order of ~10 μs, as expected for ^{3}Car. The intensities of the different transitions (2|E| ≫ |D| + |E| > |D| − |E)|) are characteristic of sublevel populations and anisotropic decay rates of ^{3}Car e.g. [45–48] confirming that the observed FDMR signals arise from these species. Whereas the 2|E| transition (maximum at about 240 MHz) is relatively narrow and well separated from the others, the |D| − |E| (~900–1100 MHz) and |D| + |E| (~1100–1450 MHz) transitions are much broader and partially overlap, indicating the presence of different ^{3}Car populations. At all wavelengths of detection (Figs. 2 and 3), the signals maintain the same polarisation, i.e. positive for the detection settings used in this study. An exception is the presence of a relative sharp negative signal (FWHM ~14 MHz), in the low frequency wing of the |D| − |E| transition, peaking at 992 MHz. This signal has been previously observed in thylakoids from higher plants [66,67] and green algae [68]. It was assigned to a chlorophyll triplet state, probably located in the reaction centre of PSII [67], which is characterised by an unusual fast decay [67,71]. Since the focus of the present study concerns the ^{3}Car in PSII, this fast-decaying ^{3}Chl will be considered in the analysis, because it is necessary to reconstruct the FDMR spectra in region of the carotenoid |D| − |E| transition. Its detailed characterisation will be the subject of further independent investigations.

In order to distinguish the different ^{3}Car populations that contribute to the FDMR signals detected in PSII–LHCII, the data were fitted, globally, by a linear combination of Gaussian functions. As described in the section 2.3 of the Experimental Procedures as well as in previous studies [66,68,76], the global fit poses the constraint that the Gaussian components belonging to the same carotenoid triplet population have also the same microwave-induced fluorescence (MIF) spectrum. Moreover, only the centre position of the Gaussian bands describing the 2|E| and |D| + |E| transitions are free fit parameters, whereas the centre of the |D| − |E| transition is determined from the formers. A minimal number of five Gaussian representing distinct ^{3}Car populations is necessary to describe satisfactorily the FDMR spectra acquired across the whole PSII–LHCII emission. The best global fit parameters are reported in Table 1. Examples of the fit for the 2|E|, |D| + |E| and |D| − |E| transitions are also shown in Fig. 2, whereas the fits across a broader range of emission wavelengths are presented in Fig. 3 for the 2|E| transition. Fig. 4A shows the MIF spectra associated to each of the five carotene populations. The spectrum associated with the abovementioned fast decaying Chl triplet, centred at 992 MHz, is also shown for comparison. Each MIF spectrum derived from the data fitting, is equivalent to the spectrum which would be obtained by scanning the emission wavelengths in the presence of a fixed (amplitude modulated) microwave field, if such ^{3}Car component (in resonance with the microwave field) were the only one present in the complex.

Of the five carotenoid triplet populations resolved by the global fitting analysis, the one described by the ZFS parameters |D| = 0.0404 cm^{-1}, |E| = 0.00378 cm^{-1} (T_5^{car}) has a particularly blue-shifted MIF (Fig. 4A), characterised by a maximum at ~680 nm and relatively weak intensity at detection wavelengths above 690 nm. It should be noted that, the contribution of T_5^{car} to the sub-band decomposition across most of the emission band is almost negligible (Figs. 2 and 3). Nevertheless, its presence is necessary when a global fit analysis of the entire set of measured spectra is considered, due to a significant presence of this contribution in the FDMR spectra monitored in the

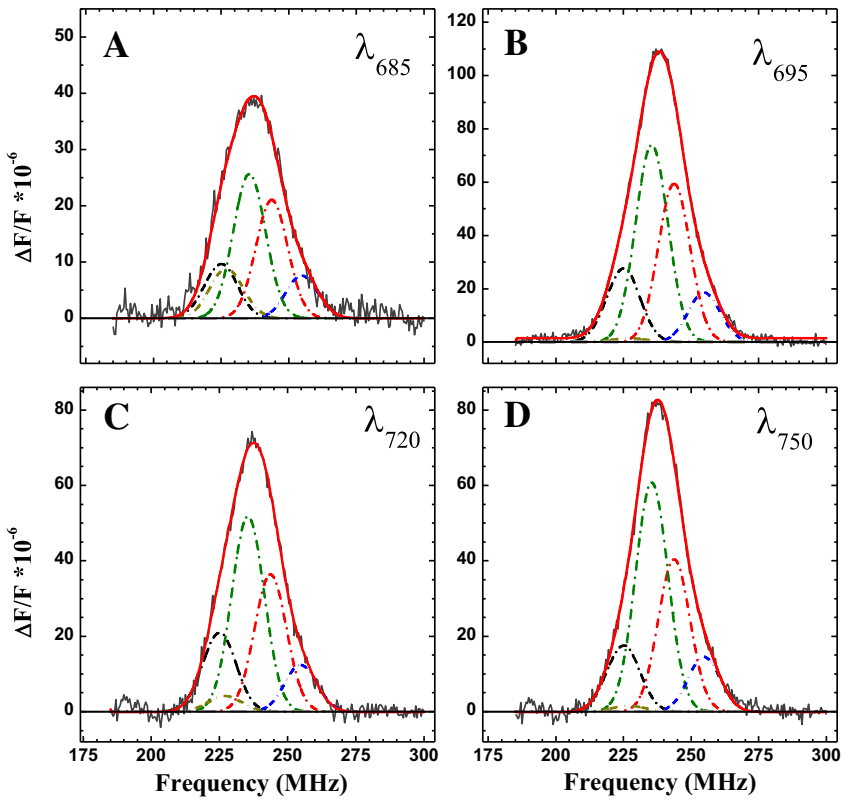

Fig. 3. 2|E| FDMR transition of carotenoid triplet states in the PSII–LHCII supercomplex, detected at 685 (A), 695 (B), 720 (C) and 750 nm (D). The black lines are the experimental spectra, the reds lines are the results of the global fit in terms of linear combinations of Gaussian functions. The dash-dotted lines show the contribution of each Gaussian sub-band. Black: T_1^{car} (|D| = 0.0373/|E| = 0.00375 cm^{-1}); red: T_2^{car} (|D| = 0.0402/|E| = 0.00406 cm^{-1}); green: T_3^{car} (|D| = 0.0385/|E| = 0.00393 cm^{-1}); blue: T_4^{car} (|D| = 0.0394/|E| = 0.00425 cm^{-1}); golden: T_5^{car} (|D| = 0.0404/|E| = 0.00378 cm^{-1}). Experimental conditions as in the legend of Fig. 2.

Table 1
Global fit of the FDMR spectra recorded in the PSII–LHCII supercomplex.

	2|E|		|D| − |E|		|D| + |E|		ZFS	
	Centre (MHz)	FWHM (MHz)	Centre (MHz)	FWHM (MHz)	Centre (MHz)	FWHM (MHz)	|D| (cm^{-1})	|E| (cm^{-1})
T_1^{car}	225 ± 3	14.4 ± 0.5	1233 ± 18	71 ± 9	1008 ± 18	57 ± 7	0.0373	0.00375
T_2^{car}	244 ± 6	13.8 ± 0.5	1326 ± 23	63 ± 7	1082 ± 24	51 ± 6	0.0402	0.00406
T_3^{car}	235 ± 6	14.0 ± 0.3	1272 ± 23	65 ± 8	1037 ± 24	52 ± 7	0.0385	0.00393
T_4^{car}	255 ± 6	13.9 ± 0.4	1309 ± 25	63 ± 7	1055 ± 26	50 ± 6	0.0394	0.00425
T_5^{car}	227 ± 5	14.5 ± 0.5	1325 ± 15	69 ± 10	1098 ± 16	55 ± 7	0.0404	0.00378

Fit parameters retrieved from the global analysis of the FDMR spectra in the 680–760 nm interval, decomposed in terms of a linear combination of Gaussian sub-bands.

680–685 nm emission window (Figs. 2–4). Whereas the 2|E| transition associated to the T_5^{car} population is substantially overlapped with that of another population (T_1^{car}, Fig. 2 and Table 1), the |D| + |E| and |D| − |E| transitions are more distinguished.

This is also apparent in the MIF spectrum retrieved from the fit (Fig. 4A). By comparison with low temperature fluorescence emission spectra of the isolated LHCII complex, that peaks in the 682–684 nm interval [83–89], it is possible to assign the ^{3}Car population associated with the most blue-shifted MIF, to a triplet state populated in PSII external antenna.

On the other hand, the MIF spectra of the remaining ^{3}Car populations have maximal intensity in the 690–710 nm window. In particular the two populations characterised by |D| = 0.0373 cm^{-1}, |E| = 0.00375 cm^{-1} (T_1^{car}) and |D| = 0.0385 cm^{-1}, |E| = 0.00393 cm^{-1} (T_3^{car}) have the most red-shifted maxima, peaking at about 705 nm. These MIF spectra also show a pronounced shoulder at 695 nm, which is more evident for the case of T_1^{car}, whereas for T_3^{car} it is more intense resulting in a relatively flat maximum between 695 and 705 nm (Fig. 4A). The MIF spectra associated with the populations characterised by the larger ZFS parameters |D| = 0.0402 cm^{-1}, |E| = 0.00406 cm^{-1} (T_2^{car}) and |D| = 0.0394 cm^{-1}, |E| = 0.00425 (T_4^{car}) have maxima at 695 and 700 nm, respectively. In the case of T_2^{car} the MIF also displays a shoulder in the 685–690 nm range and some residual intensity at shorter emission wavelengths, which is much weaker for the T_4^{car} population. An interesting feature that characterises all of the ^{3}Car MIF spectra (excluding the T_5^{car} population) is that they also display large intensities at wavelengths longer than 710 nm. This is a remarkable red-shift with respect to the maximum of the emission spectrum of the PSII enriched membranes [89–91], peaking at 695 nm also in our experimental conditions (data not shown). This feature is further highlighted by the comparison with the MIF spectrum of the fast-decaying Chl population that has a well defined maximum at about 690 nm, and significantly less intensity in the fluorescence emission tail.

The spectral window above 690 nm could be satisfactorily fitted considering only four Gaussian components, without significant differences either of the ZFS or of the associated MIF spectra (data not presented). This indicates that a fifth Gaussian component is only necessary when considering the short-wavelength emission in the 680–685 nm interval, providing further confirmation that the T_5^{car} is specifically coupled to blue-shifted Chl emission forms. Moreover, the red-shift of all the other ^{3}Car -associated MIF spectra is independent on the exact number of fitting components.

An increase in the relative intensity of the MIF spectra in the long wavelength emission tail is expected as they are measured as ΔF/F ratios (see Discussion). Nevertheless, in Fig. 4A the MIF spectra associated with the different ^{3}Car populations are compared with the MIF spectrum belonging to a ^{3}Chl likely associated with the reaction centre, which does not show remarkable intensity above 710 nm instead. Since this ^{3}Chl was detected in the same sample and experimental conditions as the ^{3}Car, it can be used as an internal reference, indicating that at least two ^{3}Car populations are indeed coupled by energy transfer to low-energy Chl *a* spectral forms, and that the increased intensity in the long-wavelength emission tail of the MIF spectra is not solely due to spectral distortion deriving from the representation in terms of ΔF/F ratios.

The lowest Chl *a* transition energies in PSII have often been suggested to be associated with chromophores bound to the proximal antenna complexes CP43 and CP47 e.g. [49,53,92–95]. Moreover, it has also been suggested that red-shifted transitions are present in the reaction centre complex [96–99]. To further investigate this issue we have conducted a parallel investigation in the isolated core complex of PSII.

3.2. Fluorescence Detected Magnetic Resonance of carotenoid triplets in the PSII core

Fig. 5 shows the FDMR spectra recorded in the isolated core complex of PSII, at characteristic emission wavelengths, under the same

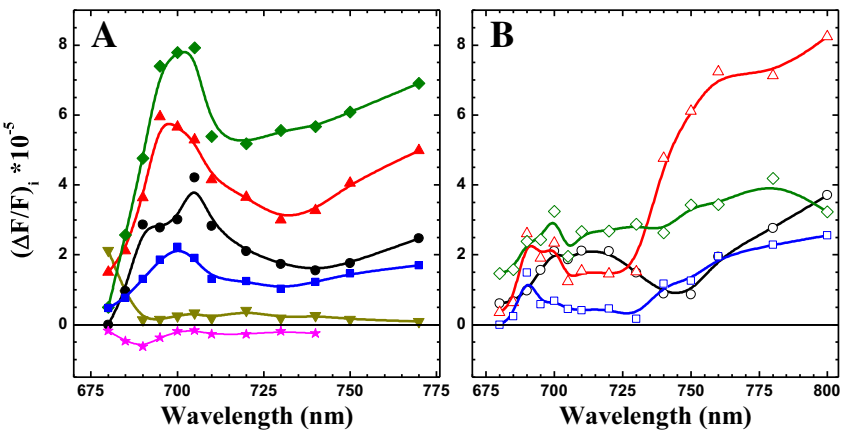

Fig. 4. Microwave-induced fluorescence emission spectra (MIF) derived from the global analysis of the FDMR spectra recorded in the PSII–LHCII supercomplex (A, solid symbols) and the PSII core complex (B, open symbols). Black lines and circles: $T_{1,(c)}^{car}$; red lines and triangles: $T_{2(c)}^{car}$; green lines and diamonds: $T_{3(c)}^{car}$; blue lines and squares: $T_{4(c)}^{car}$; golden lines and downward-triangles: T_5^{car} (PSII–LHCII only). In panel A the MIF of the fast-decaying ^{3}Chl (magenta and stars) detected at 992 MHz, is also shown for comparison; note the opposite sign of the signal. Intensities are scaled on the 2|E| transition.

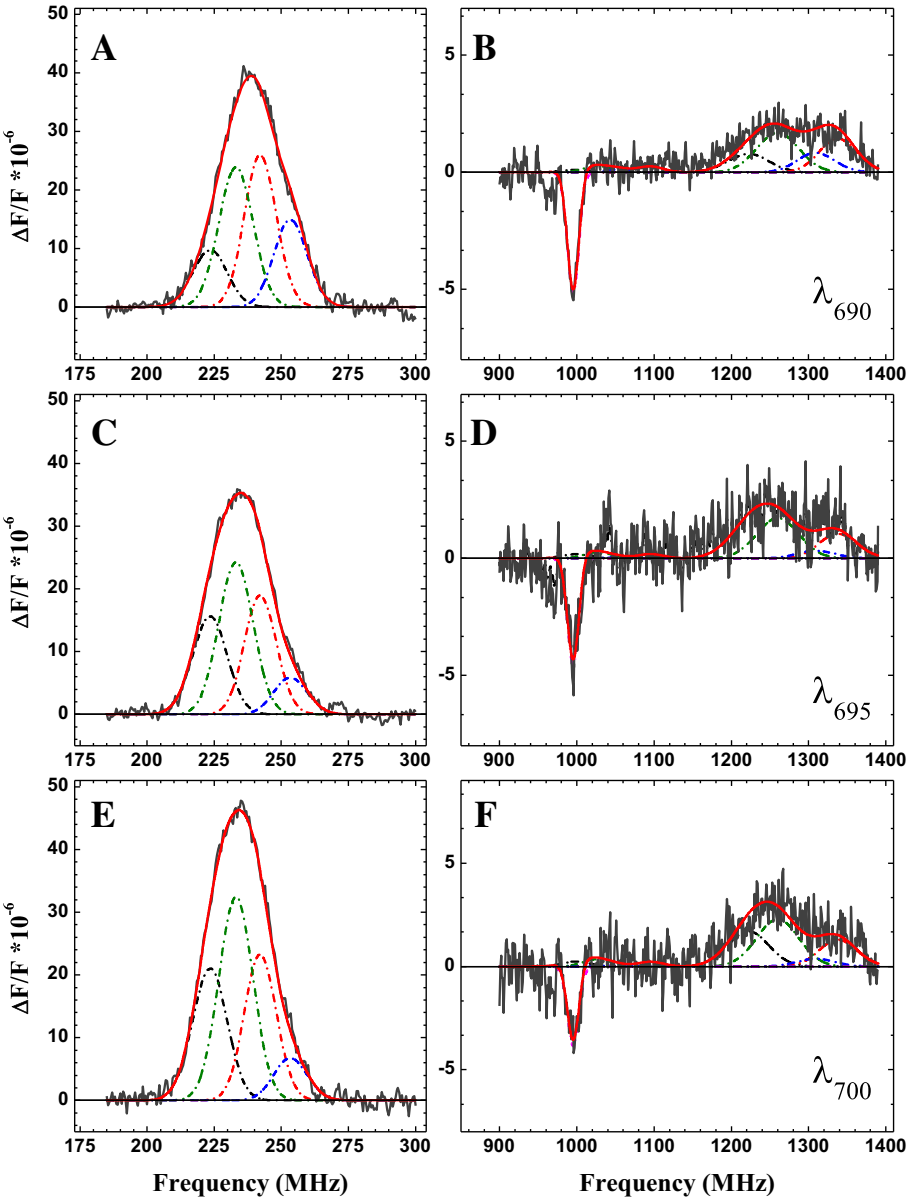

Fig. 5. FDMR spectra of carotenoid triplet states in the isolated PSII core complex detected at 690 (A, B), 695 (C, D) and 700 nm (E, F). Panels A, C and E show the 2|E| transition, whereas panels B, D and F show the |D| + |E| and |D| − |E| transitions. The black lines are the experimental spectra, the red lines are the results of the global fit in terms of linear combinations of Gaussian functions. The dash-dotted lines show the contribution of each Gaussian sub-band. Black: $T^{car}_{1,c}$ (|D| = 0.0370/|E| = 0.00373 cm^{-1}); red: $T^{car}_{2,c}$ (|D| = 0.0406/|E| = 0.00404 cm^{-1}); green: $T^{car}_{3,c}$ (|D| = 0.0381/|E| = 0.00389 cm^{-1}); blue: $T^{car}_{4,c}$ (|D| = 0.0394/|E| = 0.00422 cm^{-1}); magenta: T^{chl} (995 MHz). Experimental conditions as in the legend of Fig. 2.

experimental conditions employed for the PSII–LHCII supercomplex. The FDMR spectra recorded in the PSII core share some characteristics with those presented in Fig. 2, in terms of polarisation, peak positions and relative intensities of the 2|E|, |D| + |E| and |D| − |E| transitions. The presence of a sharp negative feature peaking at ~995 MHz is also observed, further supporting the previous assignment of this signal to a ^{3}Chl state associated to the PSII core complex [66,67,71]. In order to investigate the contribution of different ^{3}Car populations, the FDMR spectra have been globally decomposed by a linear combination of Gaussian functions. Four populations are sufficient to describe the data across the whole emission spectrum. The global fit parameters resulting from the fits are reported in Table 2. Representative fits for the 2|E|, |D| + |E|

Table 2
Global fit of the FDMR spectra recorded in the PSII core complex.

	2|E|		|D| − |E|		|D| + |E|		ZFS	
	Centre (MHz)	FWHM (MHz)	Centre (MHz)	FWHM (MHz)	Centre (MHz)	FWHM (MHz)	|D| (cm^{-1})	|E| (cm^{-1})
$T^{car}_{1,c}$	224 ± 5	15.2 ± 0.6	1222 ± 30	62 ± 8	998 ± 31	41 ± 5	0.0370	0.00373
$T^{car}_{2,c}$	242 ± 6	14.0 ± 0.5	1337 ± 34	57 ± 6	1095 ± 34	38 ± 4	0.0406	0.00404
$T^{car}_{3,c}$	233 ± 5	15.0 ± 0.5	1260 ± 36	64 ± 8	1027 ± 36	42 ± 5	0.0381	0.00389
$T^{car}_{4,c}$	253 ± 6	14.6 ± 0.5	1309 ± 36	57 ± 7	1056 ± 36	38 ± 5	0.0394	0.00422

Fit parameters retrieved from the global analysis of the FDMR spectra in the 680–800 nm interval, decomposed in terms of a linear combination of Gaussian sub-bands.

and |D| − |E| transitions are also presented in Fig. 5, and over a wider fluorescence emission wavelength interval (2|E| only) in Fig. 6.

The ^{3}Car population observed in the BBY membranes, characterised by |D| = 0.0404 cm^{-1}, |E| = 0.00378 cm^{-1} and blue-shifted MIF spectrum (Table 1, Fig. 4A), is absent in the core complex, confirming its assignment to a carotenoid triplet state populated in the external antenna.

The peak positions and hence the ZFS parameters associated to the four ^{3}Car detected in the PSII core complex do not differ significantly from those observed in PSII–LHCII (compare Tables 1 and 2). However, the MIF spectra appear more structured (Fig. 4B) in the bulk emission wavelength between 685 and 710 nm, and show substantial intensity at wavelength longer than 730 nm. Although this was also observed in the PSII–LHCII complex (Fig. 4A), the intensity of the tail above 710 nm is further increased in PSII core.

The MIF spectra associated with the populations having ZFS |D| = 0.0370 cm^{-1}, |E| = 0.00373 cm^{-1} ($T^{car}_{1,c}$) and |D| = 0.0381 cm^{-1}, |E| = 0.00389 cm^{-1} ($T^{car}_{3,c}$) have the most red-shifted maxima in the bulk emission, peaking at 700 nm (Fig. 4B). Based on the ZFS comparison, they can be correlated to the PSII–LHCII ^{3}Car populations that displayed the most red-shifted MIF spectra, although the maximum is ~5 nm blue-shifted in the PSII core complex. The broad shoulders observed at 690 nm for $T^{car}_{1,c}$ and at 685 nm for $T^{car}_{3,c}$ are also 5–10 nm blue-shifted with respect to what observed in the PSII–LHCII. On the other hand, the intensity of the MIF spectra at detection wavelength longer than 710 nm increases for both ^{3}Car populations.

The MIF spectra associated with the populations characterised by |D| = 0.0406 cm^{-1}, |E| = 0.00404 cm^{-1} ($T^{car}_{2,c}$) and |D| = 0.0394 cm^{-1}, |E| = 0.00422 ($T^{car}_{4,c}$), that have the largest values for the ZFS parameters, show maxima at 690 nm. In the case of $T^{car}_{2,c}$ the MIF also displays a secondary peak at 700 nm, which appears just as a weak shoulder for the $T^{car}_{4,c}$ population. In both cases, significant intensity is observed in the red emission tail above 730 nm; this is particularly remarkable for $T^{car}_{2,c}$.

Taken together, these results suggest that the four populations observed in the core complex correspond to those observed in the

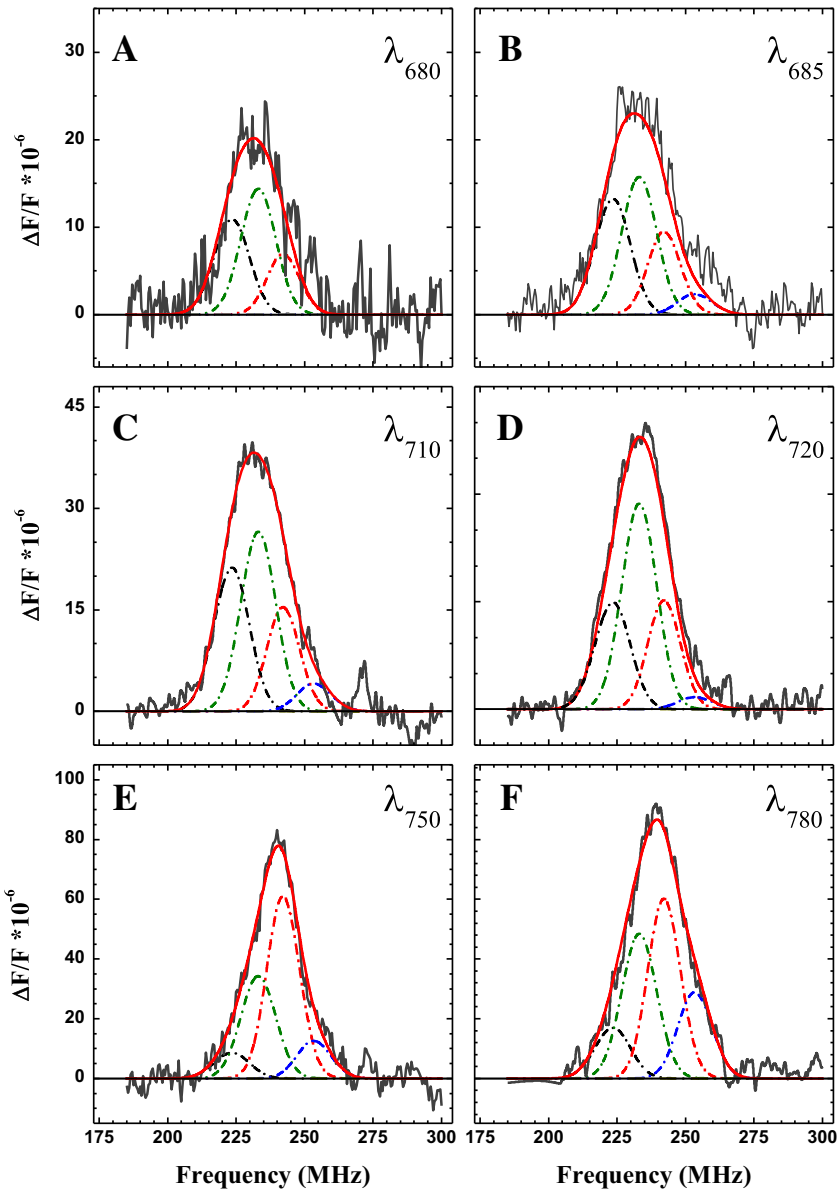

Fig. 6. 2|E| FDMR transition of carotenoid triplet states in the isolated PSII core complex detected at 680 (A), 685 (B), 710 (C), 720 (D), 750 (E) and 780 nm (F). The black lines are the experimental spectra, the red lines are the results of the global fit in terms of linear combinations of Gaussian functions. The dash-dotted lines show the contribution of each Gaussian sub-band. Black: $T^{car}_{1,c}$ (|D| = 0.0370/|E| = 0.00373 cm^{-1}); red: $T^{car}_{2,c}$ (|D| = 0.0406/|E| = 0.00404 cm^{-1}); green: $T^{car}_{3,c}$ (|D| = 0.0381/|E| = 0.00389 cm^{-1}); blue: $T^{car}_{4,c}$ (|D| = 0.0394/|E| = 0.00422 cm^{-1}). Experimental conditions as in the legend of Fig. 2.

PSII–LHCII membranes, with the exclusion of the one that can be assigned to a ^{3}Car belonging to the external antenna. Therefore the ^{3}Car populations observed in the core of PSII are assigned to triplet states sitting on β-Car molecules ($^3\beta$ - Car), since this is the only carotenoid present in the complex. The slight variation in the ZFS and the blue-shift of the MIF spectra (~5 nm on average within the spectra resolution of the technique) observed in the core complex point towards subtle re-arrangements of both the β-Car molecules and the emitting Chls, upon removal of the external antenna. This could be either an effect of the binding of the antenna complexes to the core, leading to fine structural rearrangements of the pigments, or an effect of the biochemical procedure employed in the purification of the core complex.

3.3. Triplet minus Singlet spectra of carotenoids in the core and PSII–LHCII complexes

In order to gain further insight into the nature of the ^{3}Car detected in PSII, these were further investigated, both in the core and in the PSII–LHCII complex, by microwave-induced Triplet minus Singlet (T − S) spectroscopy. These spectra are detected by scanning the transmission wavelength in the presence of an amplitude modulated microwave field at a given frequency, which in this case was set at values close to the maxima observed in the 2|E| transition by FDMR. In Fig. 7 the T − S spectra recorded in PSII–LHCII, upon microwave pumping in the 2|E| transition at 230 MHz, 237 MHz and 245 MHz are presented. The T − S spectra recorded in the PSII core complex upon microwave excitation at 224 MHz, 235 MHz and 245 MHz are shown in Fig. 8. In both samples a clear dependence of the T − S profile on the microwave excitation frequency is observed. This is the result of selective excitation of different triplet populations at the different microwave pump frequencies. In order to resolve the different $T_1 \rightarrow T_n$ transitions (and associated ground state bleaching), the T − S spectra recorded in the PSII core and PSII–LHCII complexes were fitted to a linear combination of Gaussian functions. The results of the fit analysis are reported in Table 3. The $T_1 \rightarrow T_n$ absorption is dominated, both in the PSII–LHCII and in the PSII core complexes by three species with maxima at 518, 527 and 538 nm. A weak component with a red-shifted maximum at 553 nm is obtained by the fit of the data only in PSII–LHCII. The most red-shifted $T_1 \rightarrow T_n$ absorption is observed preferentially by excitation at 230 MHz and with lower relative intensity by excitation at 237 MHz. This component seems to be associated to the T_5^{car} population detected in PSII–LHCII that has a maximum in the 2|E| at 227 MHz and is attributed to a ^{3}Xan populated in the external antenna. Previous studies performed on isolated LHCII showed the presence of $T_1 \rightarrow T_n$ transitions peaking at 505 and 525 nm [45,48,50,55,57]. The $T_1 \rightarrow T_n$ transition centred at 505 nm was not observed in our measurements, presumably because it is being masked by the singlet bleaching of the red-most carotenes ($^3\beta$ − Car). In view of these uncertainties and due to its very weak signal intensity it is not possible, at present, to give further information concerning the T_5^{car} triplet population.

\All the other transitions, also based on the FDMR results, are attributed to $^3\beta$ - Car in the core. Although they are observed upon excitation at all the microwave frequencies employed in this study, their relative contribution to the T − S spectra depends on the specific excitation. The shortest $T_1 \rightarrow T_n$ transition, peaking at 518 nm, is observed preferentially in the isolated PSII core and in PSII–LHCII upon 245 MHz excitation, hence upon preferential excitation of the triplet population with the larger |E| ZFS parameter. These correspond to the $T_{2(c)}^{car}$(that peaks at ~243 MHz in the 2|E| transition) and to a lesser extent to the $T_{4(c)}^{car}$ component, peaking at ~254 MHz (Tables 1 and 2). Interestingly the $T_{2(c)}^{car}$ and $T_{4(c)}^{car}$populations are also associated with the less red-shifted MIF spectra, peaking at 695/700 and 690 nm in PSII–LHCII and PSII core respectively. On the other hand, the more intense relative contribution of the most red-shifted $^3\beta$ - Car transition (538 nm) is observed upon excitation at 225–230 MHz, which selects preferentially the $T_{1(c)}^{car}$populations in the PSII–LHCII and the PSII core complexes. This is the ^{3}Car that shows the most red-shifted MIF. On the other hand, the maximal relative contribution of the $T_1 \rightarrow T_n$ transition peaking at 527 nm, is detected for excitation close to the maximum of the 2|E| transition (235–237 MHz). These pump frequencies excite preferentially the most intense ^{3}Car ($T_{3(c)}^{car}$) that displays a rather red-shifted MIF, peaking between 700 and 705 nm.

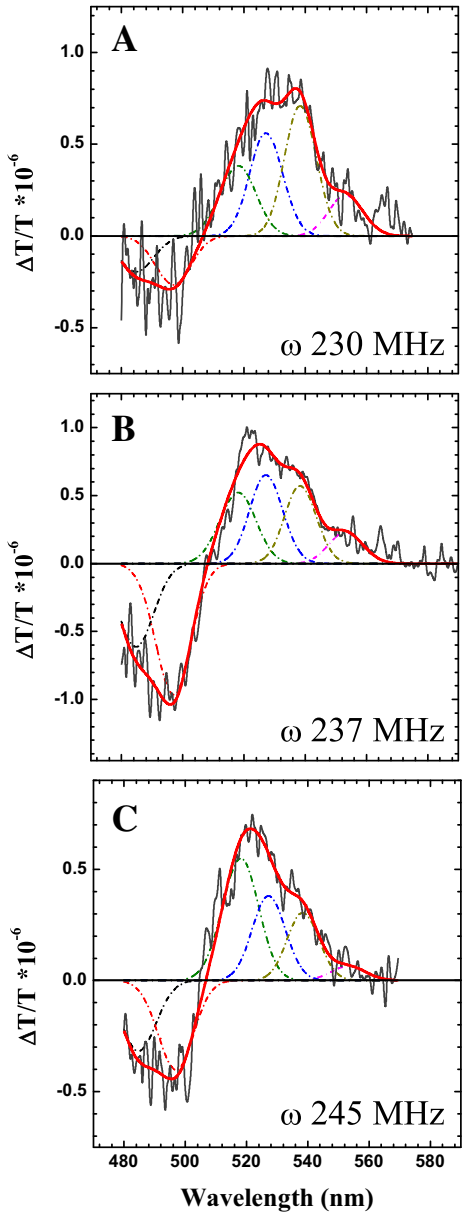

Fig. 7. Microwave-induced T − S spectra of carotenoid triplet states in the PSII–LHCII supercomplex upon selective excitation in the 2|E| transition: 230 MHz (A), 237 MHz (B) and 245 MHz (C). Black solid lines: experimental data; red solid lines: fits; dash-dotted lines: Gaussian sub-bands. Fit parameters are reported in Table 3. Experimental conditions: T = 1.8 K; MW Power: 1 W; mod. Amplitude: 330 Hz; phase: $\varphi = -154°$; time constant: 3 s; slit width: 1.0 nm.

4. Discussion

Quenching of the ^{3}Chl by carotenoids represents a fundamental photoprotective strategy in photosynthetic systems, as it prevents the sensitisation of $^1O_2$. Although the crucial physiological importance of this process is generally acknowledged (reviewed in Refs. [3,11–19, 22]), and several studies have been performed to gain insights into the nature of the ^{3}Car populated in isolated Chl/Car-binding complexes [45–57], the characterisation of these species in relatively intact systems,

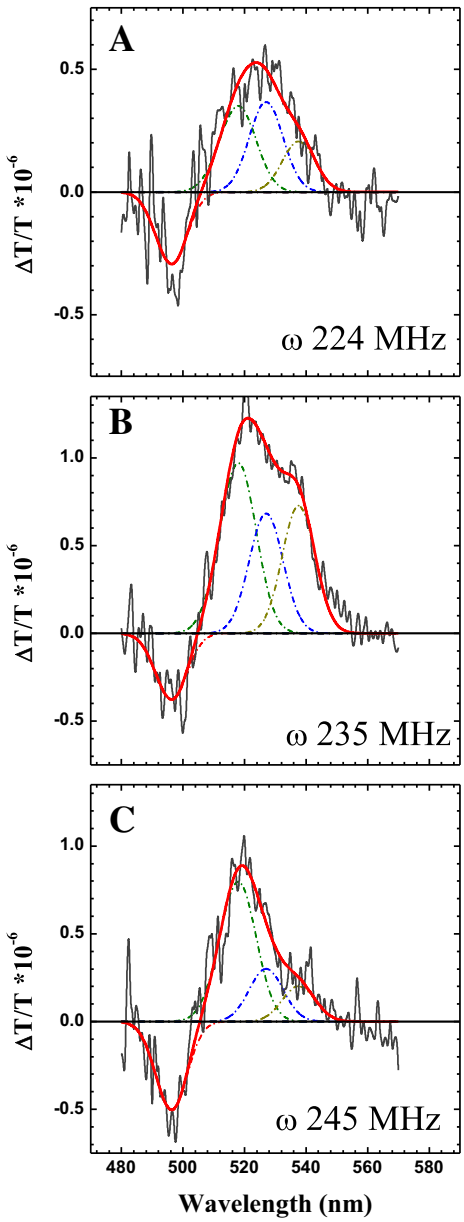

Fig. 8. Microwave-induced T − S spectra of carotenoid triplet states in the PSII core complex upon selective excitation in the 2|E| transition: 224 MHz (A), 235 MHz (B) and 245 MHz (C). Black solid lines: experimental data; red solid lines: fits; dash-dotted lines: Gaussian sub-bands. Fit parameters are reported in Table 3. Experimental conditions as in the legend of Fig. 7.

Table 3
Global fits of the T − S spectra in PSII–LHCII and PSII core.

PSII–LHCII				PSII core		
	Centre (nm)	FWHM (nm)	Assignment	Centre (nm)	FWHM (nm)	Assignment
Band 1	484 ± 2	13 ± 2	$S_0 \rightarrow S_1$	486 ± 3	13 ± 3	$S_0 \rightarrow S_1$
Band 2	497 ± 2	14 ± 2	$S_0 \rightarrow S_1$	496 ± 2	12 ± 3	$S_0 \rightarrow S_1$
Band 3	518 ± 1	14 ± 2	$T_1 \rightarrow T_n$	517 ± 4	14 ± 4	$T_1 \rightarrow T_n$
Band 4	527 ± 1	13 ± 2	$T_1 \rightarrow T_n$	527 ± 2	13 ± 3	$T_1 \rightarrow T_n$
Band 5	538 ± 1	12 ± 2	$T_1 \rightarrow T_n$	538 ± 3	13 ± 3	$T_1 \rightarrow T_n$
Band 6	553 ± 4	13 ± 3	$T_1 \rightarrow T_n$	–	–	–

Fit parameters retrieved from the global analysis of the T − S spectra in the PSII–LHCII and the PSII core complex, decomposed in terms of a linear combination of Gaussian sub-bands.

such as whole photosystems, remains rather incomplete due to spectral crowding. Because of the crucial photoprotective action of ^{3}Chl quenching by Cars through the TTET mechanism, the identification of ^{3}Car and ^{3}Chl in more intact, photochemically active, complexes represents a significant step in the understanding of the physiological role of these chromophores.

Therefore, in this study we have performed a comparative analysis of ^{3}Car in the PSII–LHCII supercomplex and the PSII core complex by ODMR, a technique that allows correlating the magnetic resonance frequencies between the triplet sublevel manifold with the optical properties of the chromophores carrying the triplet state. It was then possible to identify five ^{3}Car populations in the isolated PSII–LHCII and their associated MIF spectra and ZFS parameters. The latter are in substantial agreement with those retrieved from the FDMR analysis of isolated thylakoid membranes [76]. However, the analysis of PSII ^{3}Car in thylakoids was limited to the 680–695 nm fluorescence emission range because at longer wavelengths the PSI emission precludes their selective detection. The present improved analysis of ^{3}Car in the isolated PSII–LHCII and PSII core complexes allows the assignment of four of the detected populations to β-Car triplet states located in the core complex and one ^{3}Car populated in the external antenna of PSII. Since ODMR measurements are performed at cryogenic temperatures (1.8 K), the singlet excited state distribution is different from that encountered at room temperature, as it tends to be localised on the lowest energy Chl forms. It is therefore possible that more ^{3}Car than those observed in our current analysis are populated at physiological temperatures. Nonetheless, the ^{3}Car observed here, particularly those attributed to β-Car molecules of the core complex, are expected to be observed also at room temperature since, although less markedly, the low energy forms present in this complex are expected to carry (relatively) more excited state population than the "bulk" of the emission. On the other hand, at low temperature most of the excited states are localised in the core complex because of the presence of red-shifted transitions [83,84,88–90] with respect to outer antenna [85–87]. Therefore, the Car involved in triplet quenching in the external antenna bound to the core of PSII might largely escape detection in our measurements. In this respect, it is also interesting to note that the stoichiometry of Car binding is larger for the external antenna than the core complexes e.g. [3,10–13]. This issue will likely require further investigations by complementary techniques which allow measurements to be performed at, or near, room temperature.

In the following paragraphs we will discuss, separately, the characterisation of the ^{3}Xan and ^{3}Car associated with the external antenna and the core complex of PSII detected in this study.

4.1. Carotenoid triplet states in PSII external antenna

One ^{3}Car population ($|D| = 0.0404\ cm^{-1}$, $|E| = 0.00378\ cm^{-1}$) is observed in PSII–LHCII but not in the core complex, and it is therefore attributed to a ^{3}Xan populated in the external antenna. This assignment is consistent with the observation of a blue-shifted MIF spectrum associated to this triplet, displaying maximal intensity at 680 nm. In fact, it has been previously shown that at low temperatures the maximal emission of the isolated LHCII complex peaks at 683–685 nm e.g. [85–87], i.e. 5–10 nm to the blue with respect to those of CP43 and CP47 [51–54], the PSII core complex [49,88,90] and the whole photosystem [83,84,89]. It is however interesting to note that the previous FDMR analysis of thylakoid membranes [76] suggested the presence of two ^{3}Xan. The ZFS parameters of the population detected in PSII–LHCII closely agree with those of the most intense component attributed to ^{3}Xan in thylakoids [76]. The second ^{3}Xan detected in the membranes had a relative intensity of about one third of the dominating one. Since the intensity of the FDMR at the shortest emission wavelengths is weaker in the isolated PSII–LHCII compared to thylakoids, it is possible that the less intense ^{3}Xan either falls below the level of detection, or that it is not discerned by the fit analysis. Moreover, it has often been reported that part of

the LHCII antenna, on average one trimer per core complex, is lost during the isolation of PSII–LHCII e.g. [3,15,16]. Thus the weakening of the FDMR signals at 680–685 nm with respect to those detected at 690–695 nm could also be related to the decrease of the external antenna size during the purification of PSII.

The values of the ZFS parameters of the T_5^{car} population are in fairly good agreement with those determined in the isolated LHCII complex, even though, as for the analysis of thylakoids, at least two ^{3}Xan have been detected in the isolated complex by the ODMR techniques [45–47,55]. Still, some differences are observed, as previously noticed [76] in the analysis of the isolated thylakoids, that might be the result of either a perturbation of the carotenoids bound to LHCII upon biochemical isolation or subtle changes in the binding of the chromophores occurring when the antenna is bound to the photosystem, i.e. closer to its natural environment. Further investigations are required to gain more conclusive evidence on this matter.

4.2. Carotenoid triplet states in the core of PSII

The remaining four triplet populations are attributed to $^3\beta$ - Car species as they are characterised by the same set of ZFS parameters, within the confidence limits of the FDMR Gaussian decomposition analysis, in both PSII–LHCII and PSII core complexes. The improvement in the quality of MIF spectra (Fig. 4) obtained in the present study, compared to the previous analysis of thylakoids, shows that all the $^3\beta$ - Car are associated with relatively low-energy Chl forms present in the core, with emission maxima between 695 and 705 nm. The MIF spectra of the $^3\beta$ - Car characterised by $|D| = 0.0370/0.0373\ cm^{-1}$, $|E| = 0.00373/0.00375\ cm^{-1}$ ($T_{1(c)}^{car}$) and $|D| = 0.0381/0.0385\ cm^{-1}$, $|E| = 0.00389/0.00393\ cm^{-1}$ ($T_{3(c)}^{car}$), have maxima at about 705 nm in the PSII–LHCII supercomplex and 700 nm in the core. In both cases, shoulders in the 690–695 nm interval are also observed, although with different intensities.

The MIF spectra of the other two $^3\beta$ - Car populations characterised by $|D| = 0.0406/0.0402\ cm^{-1}$, $|E| = 0.00404/0.00406\ cm^{-1}$ ($T_{2(c)}^{car}$) and $|D| = 0.0394\ cm^{-1}$, $|E| = 0.00422/0.00425\ cm^{-1}$ ($T_{4(c)}^{car}$) are instead coupled to less red-shifted Chl forms having maximal emission at about 690–695 nm, being generally 5 nm red-shifted in PSII–LHCII with respect to the core complex. The MIF spectra also show shoulders at about 700–705 nm. Another interesting observation, that is common to all the $^3\beta$ - Car resolved in the analysis, is that the MIF spectra show pronounced intensity at wavelength longer than 710 nm, that is clearly outside the main fluorescence emission band.

The interpretation of MIF spectra requires some considerations. First, at the low temperature at which the measurements are performed (<2 K), the fluorescence emission from the system is expected to stem exclusively from the lowest energy transition within the pigment array, acting as a terminal emitter. Yet it is commonly reported, particularly for large particles such as whole photosystems or core complexes, that the emission derives from more than one spectral form e.g. [83,84,88–90]. These observations can be explained considering the presence of barriers for excited state equilibration in the energetic landscape of pigment system comprising about 40 Chls, in the case of the core complex, and 200–250 Chls, in the case of PSII–LHCII. These energy barriers tend to localise the excited states in more than one "local" energy minimum, representing local energy sinks. These forms can be either proper low-temperature terminal emitters, i.e. being completely energetically uncoupled from the others, or pre-equilibrated emitters, in the case that the energy transfer rates amongst the local emitters are comparable to the excited state lifetimes of the low energy chromophores.

Second, it should be noted that the MIF spectra are presented as $\Delta F/F$ ratios. For a single chromophore the $\Delta F/F$ ratio should assume the same value across the emission band, including the long wavelength tail that arise from vibrational modes strongly coupled to the $S_0 \rightarrow S_1$ transition. This explains, qualitatively, the long wavelength tail observed in the spectra of all the $^3\beta$ - Car populations. On the other hand, structured MIF spectra imply the overlapping emission of more than one chromophore, thereby rendering their interpretation less straightforward. Hence, we have performed simulations considering a simplified kinetic and spectral scheme which yields realistic (but not quantitative) information. The details of the MIF spectra simulations are presented in Appendix 2 of Supporting information. In the following we only discuss the principal outcomes derived from the calculations. Based on the qualitative simulations it is argued that in order to obtain MIF spectra having band shapes compatible to the experimental results, it is necessary that the $^3\beta$ - Car are populated by TTET energy transfer from ^{3}Chl representing local emitters, coupled by slow singlet–singlet ($S - S$) energy transfer to red Chls, acting as terminal emitters (see Fig. S5 of Supporting information). On the contrary, the direct population of $^3\beta$ - Car by a long wavelength Chl form, as well as the rapid energy transfer between the sensitising (local) Chl and the low energy (terminal) emitter results in calculated MIF spectra which are not in agreement with the experimental ones. Therefore, the analysis suggests that although the maximal MIF intensity is observed around 700–705 nm, resulting from the emission of relatively red-shifted Chl forms present in the core of PSII, the $^3\beta$ - Car is initially sensitised by Chl forms that are blue-shifted by 10–15 nm with respect to the lower energy states in the complex.

4.3. Comparison of MIF spectra attributed to β-carotene triplets with low energy states of the isolated core complexes

This study reveals the presence of Chl forms in the core of PSII having maximal emission at about 705 nm. In order to address their possible location within the complex, it is interesting to discuss previous literature reports concerning the lowest energy transitions in the core, and in the isolated core antenna complexes, CP43 and CP47. Whereas there is a general agreement concerning the lowest transition energies in the isolated core antenna complexes, their assignment to specific chromophores is still debated [51,91–94]. The lowest energy state in the isolated CP47 complex is identified as a Chl *a* form having maximal absorption at 690 nm and emission at 695 nm [51,91–94]. At least one other Chl *a* form having maximal absorption at 684–685 nm and emission at 686–688 nm is present in this complex [51,91–94,100]. In CP43 two degenerate states both characterised by maximal absorption around 683 nm, but having significant different bandwidths (one being almost tree time as broad as the other), have been identified [54,94–96]. The maximal emission of CP43 at low temperature peaks between 684 and 686 nm, even though an intense shoulder at ~690 nm is also observed [54,94–96,100]. However, in none of the isolated core antenna complexes, to our knowledge, Chl forms with emission maxima close to 700–710 nm, have been resolved.

On the other hand, the energy of the lowest energy state in the reaction centre (which is isolated as the D1D2Cytb_{559} complex) is more controversial. This is because there is a host of experimental evidences, particularly from the analysis of the T − S spectra associated with the recombination triplet state and hole-burning spectroscopy, that the site energies are perturbed upon biochemical isolation of the D1D2Cytb_{559} complex [74,96–98,101]. Thus, the most reliable information are retrieved from the study of the core complex which also harbours CP43 and CP47. In the core complex, as well as in the BBY particles, the bleaching associated with the population of the recombination triplet peaks in the 684–686 nm interval [74,96–98], and a further shift to 687 nm was observed in isolated thylakoids [66,67]. For an average Stokes' shift of 3–4 nm, as commonly observed for Chl *a* in photosynthetic complexes, the Chl carrying the recombination triplet, which at low temperatures is likely to be the so-called Chl_{D1} molecule, is expected to emit between 687 and 690 nm, i.e. almost iso-energetic to the CP43 lower energy states. However, Chl_{D1} appears to be, based on the structural models [8,9], too distant from the two β - Car molecules coordinated by the RC to allow triplet–triplet energy transfer. Intriguingly, the presence of a weak and broad emission

form, having a maximal absorption between 700 and 705 nm and a suggested emission extending above 780 nm, has also been reported [97–99]. The rate of singlet–singlet ($S-S$) energy transfer of this spectral form with the other chromophores in the system must, however, be particularly weak, otherwise it would represent by far the lowest energy state in PSII, from which all the emission, at low temperatures, is expected to stem from, as observed from the so-called red-forms of PSI e.g. [3,11,102,103]. Moreover, the emission of such "deep-red form" species is excessively red-shifted to be correlated to the 705 nm emission form observed in the FDMR measurements. Thus, the 700–705 nm emission form resolved in this study appears to be distinct from the deep-red form which has been previously reported [97–99]. As just discussed, this newly resolved emission form does not appear to correlate with any of the lowest emitters observed either in the isolated RC or in core antenna complexes, CP43/CP47. Since it is observed in the whole core complex (but also in the PSII–LHCII supercomplex), it is likely that this state is either strongly perturbed by the isolation procedure required to obtain the proximal antenna complexes, or that it represents a state generated by exciton coupling between chromophores at the interface of the proximal antenna and the RC complex.

4.4. Assignment of β-carotene triplets to specific sites of PSII core complex

The emission peaks detected in the core of PSII and in the BBY membranes at 685 and 695 nm at cryogenic temperatures have been suggested to be correlated with the emission of the low energy states of CP43 and CP47, respectively [88–90], acting as terminal emitters uncoupled in terms of energy transfer. The MIF spectra associated with $^3\beta$ - Car are all red-shifted with respect to the maximum of the emission spectrum of both complexes (due, as stated above, to the weak $S-S$ energy coupling with a red-shifted Chl emitting at about 705 nm). Still, in the 685–700 nm interval, the MIF spectra show features that overlap with the proximal antenna low energy states. Although the lowest energy forms present in the RC also fall in a similar range, those have been attributed to photochemically active pigments, which are essentially uncoupled to carotenoids. In fact, the MIF of the fast decaying Chl triplet (FDMR peaking at 992–995 MHz) has maximal (absolute) intensity at 690 nm and very weak intensity in all of the red-emission tail [66,67] and is therefore markedly blue-shifted with respect to those attributed to $^3\beta$ - Car (Fig. 4A).

On the basis of the previous discussion, we tentatively assign the most red-shifted $T^{car}_{1(c)}$ and $T^{car}_{3(c)}$ populations to $^3\beta$ - Car populated in the CP47 complex since it harbours the lowest energy Chl states of PSII proximal antenna. The observation of intense features at ~700 nm in the MIF of both these triplet populations is interpreted as a preferential singlet energy coupling of CP47 triplet sensitising Chl forms with the state emitting at 705 nm. The remaining populations ($T^{car}_{2(c)}$ and $T^{car}_{4(c)}$) are then assigned to states populated either in CP43 or in the peripheral pigments of the RC complex. These sensitising Chl forms appear more weakly coupled by $S-S$ energy transfer to the 705 nm emitting Chl form.

4.5. Tuning of the fine spectroscopic properties of β-carotene in the PSII core complex

Finally, it is interesting to note that the difference between the highest and the lowest $T_1 \rightarrow T_n$ β - Car transition, observed in the T − S spectra (Figs. 7 and 8, Table 3), is about 20 nm. Hence, the binding of the same chromophore (β - Car) to specific protein sites leads to rather remarkable tuning of its electronic transition energies. Such an effect is comparable to that expected for a progressive increase of the conjugation length of the chromophore e.g. [104–106]. Recently this protein fine-tuning of the electronic properties of carotenoids, in addition to their well known dependence from the polarisability of the surrounding [107], has been demonstrated to depend also on the alteration of the effective conjugation length, through steric hindrance acting on the conjugated end cycles [108]. This observation is in full agreement with the results presented here. Actually, amongst the triplet states assigned to core β-Car, the components $T^{car}_{2(c)}$ and $T^{car}_{4(c)}$, which have large |D| values, have a correspondent blue-shifted absorption (518 nm), as both properties depend on the number of conjugated double bonds [109]. On the contrary, the component $T^{car}_{1(c)}$, characterised by the smallest |D| value amongst the various components, concomitantly has the most red-shifted transition (528 nm). Hence, the modulation of the optical properties of the β-Cars in the different sites depends, at least in part, on their effective conjugation length. It is also worth noticing that the β-Car populations displaying the most blue-shifted $T_1 \rightarrow T_n$ transition also have the most blue-shifted MIF spectrum, and vice versa for the most red-shifted ones. This can be rationalized in terms of the fine tuning of the protein-mediated acceptor-donor pair properties, in order to optimise the efficiency of both singlet and triplet energy transfer.

5. Conclusions

The parallel investigation of Car triplet states in the PSII–LHCII supercomplex and the PSII core complex by ODMR techniques allowed us to resolve four $^3\beta$-Car populations in the core complex and one ^{3}Xan population in the external antenna.

Two of the detected ^{3}Car, $T^{car}_{1(c)}$ and $T^{car}_{3(c)}$, are populated by Chl forms coupled by weak singlet–singlet interactions to a low energy state having maximal emission at about 705 nm. These populations show a maximal $T_1 \rightarrow T_n$ transition between 527 and 538 nm, representing the most red-shifted absorption amongst PSII $^3\beta$ - Car. We tentatively localise these $^3\beta$ - Car components in the CP47 core antenna. The remaining populations ($T^{car}_{2(c)}$ and $T^{car}_{4(c)}$), which show a weaker $S-S$ energy coupling to the 705 nm emitter, are tentatively assigned to $^3\beta$-Car triplets populated in the CP43 complex.

Moreover, the results highlight the presence of Chl spectral forms in the core complex of PSII absorbing/emitting at longer wavelengths (10–15 nm red-shifted) than the photochemical reaction centre.

These triplets states, observed at low temperature when the excitation is localised on a few pre-equilibrated emitters, are expected to be populated also at physiological temperatures when the excitation is more delocalised over the entire array of antenna chromophores. Even though it is likely that other ^{3}Car will be populated at higher temperatures, particularly in the external antenna whose singlet excited state is depopulated at low temperature, the populations detected in the present study are still expected to be present and therefore play an important role in photo-protection. We consider that their identification represents a first, yet necessary, step to get a more in depth understanding of their physiological role.

Acknowledgements

This research was in part founded by the grant PRIN2010/2011 Prot. 2010FM738P awarded to D.C. from the Italian Ministry of Education, Universities and Research (MIUR). We thank Prof. Robert Jennings (University of Milan) for fruitful discussion.

Appendix A. Supplementary data

Appendix 1 described the basic principle of the ODMR technique. Appendix 2 describes in detail the kinetic and spectral model utilised for the simulations of the microwave-induced fluorescence emission spectra. Supplementary data to this article can be found online at http://dx.doi.org/10.1016/j.bbabio.2014.11.008.

References

[1] B.A. Diner, F. Rappaport, Structure, dynamics, and energetics of the primary photochemistry of photosystem II of oxygenic photosynthesis, Annu. Rev. Plant Biol. 53 (2002) 551–580.

[2] N. Nelson, C.F. Yocum, Structure and function of photosystems I and II, Annu. Rev. Plant Biol. 57 (2006) 521–565.
[3] S. Caffarri, T. Tibiletti, R.C. Jennings, S. Santabarbara, A comparison between plant Photosystem I and Photosystem II architecture and functioning, Curr. Protein Pept. Sci. 15 (2014) 296–331.
[4] T. Cardona, A. Sedoud, N. Cox, A.W. Rutherford, Charge separation in photosystem II: a comparative and evolutionary overview, Biochim. Biophys. Acta Bioenerg. 1817 (2012) 26–43.
[5] J.P. Allen, J.C. Williams, The evolutionary pathway from anoxygenic to oxygenic photosynthesis examined by comparison of the properties of photosystem II and bacterial reaction centers, Photosynth. Res. 107 (2011) 59–69.
[6] A.G. Koziol, T. Borza, K. Ishida, P. Keeling, R.W. Lee, D.G. Durnford, Tracing the evolution of the light-harvesting antennae in chlorophyll a/b-containing organisms, Plant Physiol. 143 (2007) 1802–1816.
[7] M. Ballottari, J. Girardon, L. Dall'osto, R. Bassi, Evolution and functional properties of photosystem II light harvesting complexes in eukaryotes, Biochim. Biophys. Acta Bioenerg. 1817 (2012) 143–157.
[8] A. Zouni, H.T. Witt, J. Kern, P. Fromme, N. Krauss, W. Saenger, P. Orth, Crystal structure of photosystem II from *Synechococcus elongatus* at 3.8 Å resolution, Nature 409 (2001) 739–743.
[9] Y. Umena, K. Kawamaki, N. Kamiya, Crystal structure of oxygen-evolving photoystem II at a resolution of 1.9 Å, Nature 473 (2011) 55–60.
[10] R. Bassi, B. Pineau, P. Dainese, J. Marquardt, Carotenoid-binding proteins of photosystem II, Eur. J. Biochem. 212 (1993) 297–303.
[11] R. Jennings, G. Zucchelli, R. Bassi, Antenna structure and energy transfer in higher plant photosystems, in: J. Mattay (Ed.), Topics in Current Chemistry, vol. 177, Spinger-Verlag, Berlin, Heidelberg, Germany, 1996, pp. 147–181.
[12] D. Sandonà, R. Croce, A. Pagano, M. Crimi, R. Bassi, Higher plants light harvesting proteins. Structure and function as revealed by mutation analysis of either protein or chromophore moieties, Biochim. Biophys. Acta Bioenerg. 1365 (1998) 207–214.
[13] H. van Amerongen, R. Croce, Light harvesting in photosystem II, Photosynth. Res. 116 (2013) 251–263.
[14] X. Pan, Z. Liu, M. Li, W. Chang, Architecture and function of plant light-harvesting complexes II, Curr. Opin. Struct. Biol. 23 (2013) 515–525.
[15] R. Kouřil, J.P. Dekker, E.J. Boekema, Supramolecular organization of photosystem II in green plants, Biochim. Biophys. Acta Bioenerg. 1817 (2012) 2–12.
[16] S. Caffarri, R. Kouřil, S. Kereïche, E.J. Boekema, R. Croce, Functional architecture of higher plant photosystem II supercomplexes, EMBO J. 28 (2009) 3052–3063.
[17] P. Horton, A.V. Ruban, R.G. Walters, Regulation of light harvesting in green plants, Annu. Rev. Plant Physiol. Plant Mol. Biol. 47 (1996) 655–684.
[18] A.V. Ruban, M.P. Johnson, Xanthophylls as modulators of membrane protein function, Arch. Biochem. Biophys. 504 (2010) 78–85.
[19] D. Siefermann-Harms, Carotenoids in photosynthesis. I. Location in photosynthetic membranes and light-harvesting function, Biochim. Biophys. Acta 811 (1985) 325–355.
[20] H.A. Frank, R. Cogdell, Photochemistry and function of carotenoids in photosynthesis, in: A. Young, G. Britton (Eds.), Carotenoids in Photosynthesis, Chapman and Hall, London, United Kingdom, 1993, pp. 253–326.
[21] A. Rivadossi, G. Zucchelli, F.M. Garlaschi, R.C. Jennings, Light absorption by the chlorophyll a/b complexes of photosystem II in a leaf with special reference to LHCII, Photochem. Photobiol. 80 (2004) 492–498.
[22] B. Demmig-Adams, Carotenoids and photoprotection in plants: a role for the xanthophyll zeaxanthin, Biochim. Biophys. Acta Bioenerg. 1020 (1990) 1–24.
[23] B. Robert, P. Horton, A.A. Pascal, A.V. Ruban, Insights into the molecular dynamics of plant light-harvesting proteins *in vivo*, Trends Plant Sci. 9 (2004) 385–390.
[24] A.A. Pascal, Z.F. Liu, K. Broess, B. van Oort, H. van Amerongen, C. Wang, P. Horton, B. Robert, W.R. Chang, A. Ruban, Molecular basis of photoprotection and control of photosynthetic light-harvesting, Nature 436 (2005) 134–137.
[25] A.V. Ruban, R. Berera, C. Ilioaia, I.H.M. van Stokkum, J.T.M. Kennis, A.A. Pascal, H. van Amerongen, B. Robert, P. Horton, R. van Grondelle, Identification of a mechanism of photoprotective energy dissipation in higher plants, Nature 450 (2007) 575–578.
[26] N.E. Holt, D. Zigmantas, L. Valkunas, X.P. Li, K.K. Niyogi, G.R. Fleming, Carotenoid cation formation and the regulation of photosynthetic light harvesting, Science 307 (2005) 433–436.
[27] T.K. Ahn, T.J. Avenson, M. Ballottari, Y.C. Cheng, K.K. Niyogi, R. Bassi, G.R. Fleming, Architecture of a charge-transfer state regulating light harvesting in a plant antenna protein, Science 320 (2008) 794–797.
[28] M. Zubik, R. Luchowski, W. Grudzinski, M. Gospodarek, I. Gryczynski, Z. Gryczynski, J.W. Dobrucki, W.I. Gruszecki, Light-induced isomerization of the LHCII-bound xanthophyll neoxanthin: possible implications for photoprotection in plants, Biochim. Biophys. Acta Bioenerg. 1807 (2013) 1237–1243.
[29] F.G. Plumley, G.W. Schmidt, Reconstitution of Chl a/b light-harvesting complexes. Xanthophyll-dependent reconstitution and energy transfer, Proc. Natl. Acad. Sci. U. S. A. 84 (1987) 145–150.
[30] E. Formaggio, G. Cinque, R. Bassi, Functional architecture of the major light-harvesting complex from higher plants, J. Mol. Biol. 314 (2001) 1157–1166.
[31] K. Humbeck, S. Romer, H. Senger, Evidence for an essential role of carotenoids in the assembly of an active photosystem II, Planta 179 (1989) 242–250.
[32] J.A. Bautista, F. Rappaport, M. Guergova-Kuras, R.O. Cohen, J.H. Golbeck, J.Y. Wang, D. Béal, B.A. Diner, Biochemical and biophysical characterization of photosystem I from phytoene desaturase and zeta-carotene desaturase deletion mutants of *Synechocystis* sp. PCC 6803: evidence for PsaA- and PsaB-side electron transport in cyanobacteria, J. Biol. Chem. 280 (2005) 20030–20041.
[33] S. Santabarbara, A.P. Casazza, K. Ali, C.K. Economou, T. Wannathong, F. Zito, K.E. Redding, F. Rappaport, S. Purton, The requirement for carotenoids in the assembly and function of the photosynthetic complexes in *Chlamydomonas reinhardtii*, Plant Physiol. 161 (2013) 535–546.
[34] T.G. Truscott, The photophysics and photochemistry of the carotenoids, J. Photochem. Photobiol. B 6 (1990) 359–371.
[35] H.A. Frank, R.J. Cogdell, Carotenoids in photosynthesis, Photochem. Photobiol. 63 (1996) 257–264.
[36] P.G. Bowers, G. Porter, Quantum yield of triplet formation in solutions of chlorophylls, Proc. R. Soc. A 296 (1967) 435–441.
[37] A.A. Krasnovsky, Delayed luminescence and phosphorescence of plant pigments, Photochem. Photobiol. 36 (1992) 733–741.
[38] H. Kramer, P. Mathis, Quantum yield and rate of formation of the carotenoid triplet state in photosynthetic structure, Biochim. Biophys. Acta Bioenerg. 593 (1980) 319–329.
[39] P. Mathis, W.L. Butler, K. Satoh, Carotenoid triplet state and chlorophyll fluorescence quenching in chloroplasts and subchloroplast particles, Photochem. Photobiol. 30 (1979) 603–614.
[40] C. Wolff, H.T. Witt, On metastable states of carotenoids in primary events of photosynthesis, Z. Naturforsch. 24b (1969) 1031–1037.
[41] A.A. Krasnovsky, Photoluminescence of singlet oxygen in pigment solutions, Photochem. Photobiol. 29 (1979) 29–36.
[42] A. Krieger-Liszkay, Singlet oxygen production in photosynthesis, J. Exp. Bot. 56 (2005) 337–346.
[43] T. Javorfi, G. Garab, K.R. Naqvi, Reinvestigation of the triplet-minus-singlet spectrum of chloroplasts, Spectrochim. Acta A 56 (2000) 211–214.
[44] A. Sonneveld, H. Rademaker, L.N.M. Duysens, Transfer and trapping of excitation energy ion photosystem II as studied by chlorophyll fluorescence quenching by dinitrobenzene and carotenoid triplet. The matrix model, Biochim. Biophys. Acta Bioenerg. 593 (1980) 272–289.
[45] R. Van der Vos, D. Carbonera, A.J. Hoff, Microwave and optical spectroscopy of carotenoid triplets in light-harvesting complex LHCII of spinach by absorbance-detected magnetic resonance, Appl. Magn. Reson. 2 (1991) 179–202.
[46] D. Carbonera, G. Giacometti, G. Agostini, FDMR of carotenoid and chlorophyll triplets in light-harvesting complex LHCII of spinach, Appl. Magn. Reson. 3 (1992) 361–368.
[47] D. Carbonera, G. Giacometti, G. Agostini, A. Angerhofer, V. Aust, ODMR of carotenoid and chlorophyll triplets in CP43 and CP47 complexes of spinach, Chem. Phys. Lett. 194 (1992) 275–281.
[48] R. Van der Vos, E.M. Franken, A.J. Hoff, ADMR study of the effect of oligomerisation on the carotenoid triplet and triplet–triplet energy transfer in light harvesting complex II (LHC II) of spinach, Biochim. Biophys. Acta Bioenerg. 1188 (1994) 243–250.
[49] M.-L. Groot, E.J. Peterman, I.H.M. van Stokkum, J.P. Dekker, R. van Grondelle, Temperature dependent triplet and fluorescence quantum yield of photosystem II described in a thermodynamic model, Biophys. J. 67 (1994) 318–330.
[50] E.J.G. Peterman, F.M. Dekker, R. van Grondelle, H. Van Amerongen, Chlorophyll a and carotenoid states in light harvesting complex II of higher plants, Biophys. J. 59 (1995) 2670–3678.
[51] M.-L. Groot, E.J. Peterman, I.H. van Stokkum, J.P. Dekker, R. van Grondelle, Triplet and fluorescing states of the CP47 antenna complex of photosystem II studied as a function of temperature, Biophys. J. 68 (1995) 281–290.
[52] V. Barzda, E.J.G. Peterman, R. van Grondelle, H. van Amerongen, The influence on triplet formation in light-harvesting chlorophyll a/b pigment–protein complex II of green plants, Biochemistry 37 (1998) 546–551.
[53] R. Schödel, K.-D. Irrgang, J. Voigt, G. Renger, Rate of carotenoid triplet formation in solubilised light-harvesting complex II (LHCII) from spinach, Biophys. J. 75 (1998) 3143–3153.
[54] M.-L. Groot, R.N. Frese, F. deWeerd, K. Bromek, Å. Petterson, E.J.G. Peterman, I.H.M. van Stokkum, R. van Grondelle, J.P. Dekker, Spectroscopic properties of the CP43 core antenna protein of photosystem II, Biophys. J. 77 (1999) 3328–3340.
[55] S.S. Lampoura, V. Barzda, G.M. Owen, A.J. Hoff, H. van Amerongen, Aggregation of LHCII leads to a redistribution of the triplets over the central xanthophylls in LHCII, Biochemistry 41 (2002) 9139–9144.
[56] R. Croce, M. Mozzo, T. Morosinotto, A. Romeo, R. Hienerwadel, R. Bassi, Singlet and triplet state transitions of carotenoids in the antenna complexes of higher-plant photosystem I, Biochemistry 46 (2007) 3846–3855.
[57] M. Mozzo, L. Dall'Osto, R. Hienerwadel, R. Bassi, R. Croce, Photoprotection in the antenna complexes of photosystem II: role of individual xanthophylls in chlorophyll triplet quenching, J. Biol. Chem. 283 (2008) 6184–6192.
[58] K. Akiyama, S. Terokubota, T. Ikoma, Y. Ikegami, Spin Polarization conservation during intramolecular triplet–triplet energy transfer studied by Time-Resolved EPR Spectroscopy, J. Am. Chem. Soc. 116 (1994) 5324–5327.
[59] R. Bittl, E. Schlodder, I. Geisenheimer, W. Lubitz, R.J. Cogdell, Transient EPR and absorption studies of carotenoid triplet formation in purple bacterial antenna complexes, J. Phys. Chem. B 105 (2001) 5525–5553.
[60] M. Di Valentin, F. Biasibetti, S. Ceola, D. Carbonera, Identification of the sites of chlorophyll triplet quenching in relation to the structure of LHC-II from higher plants. Evidence from EPR spectroscopy, J. Phys. Chem. B 113 (2009) 13071–13078.
[61] D. Carbonera, A. Agostini, M. Di Valentin, C. Gerotto, S. Basso, G.M. Giacometti, T. Morosinotto, Photoprotective sites in the violaxanthin–chlorophyll a binding Protein (VCP) from *Nannochloropsis gaditana*, Biochim. Biophys. Acta Bioenerg. 1837 (2014) 1235–1246.
[62] M. Di Valentin, E. Meneghin, A. Polimeno, C. Büchel, E. Salvadori, C.W.M. Kay, D. Carbonera, Triplet–triplet energy transfer in fucoxanthin-chlorophyll protein from diatom *Cyclotella meneghiniana*: insights into the structure of the complex, Biochim. Biophys. Acta Bioenerg. 1827 (2013) 1226–1234.

[63] R.H. Clarke, Triplet state ODMR spectroscopy, in: R.H. Clarke (Ed.), Techniques and Applications to Biophysical Systems, Wiley-Interscience, New York, U.S.A. 1982
[64] A.J. Hoff, Optically detected magnetic resonance of triplet states, in: A.J. Hoff (Ed.), Advanced EPR, Elsevier, Amsterdam, The Netherlands1989.
[65] D. Carbonera, Optically Detected Magnetic Resonance (ODMR) of photoexcited triplet states, Photosynth. Res. 102 (2009) 403–414.
[66] S. Santabarbara, E. Bordignon, R.C. Jennings, D. Carbonera, Chlorophyll triplet states associated with photosystem II of thylakoids, Biochemistry 41 (2002) 8184–8194.
[67] S. Santabarbara, R.C. Jennings, D. Carbonera, Analysis of photosystem II triplet states in thylakoids by fluorescence detected magnetic resonance as a function of the reduction state of the primary quinone acceptor Q_A, Chem. Phys. 294 (2003) 257–267.
[68] S. Santabarbara, G. Agostini, A.P. Casazza, C.D. Syme, P. Heathcote, F. Böhles, M.C.W. Evans, R.C. Jennings, D. Carbonera, Chlorophyll triplet states associated with Photosystem I and Photosystem II in thylakoids of the green alga *Chlamydomonas reinhardtii*, Biochim. Biophys. Acta Bioenerg. 1767 (2007) 88–105.
[69] S. Santabarbara, D. Carbonera, The carotenoid triplet state associated with the long wavelength emitting chlorophyll forms of Photosystem I in isolated thylakoid membranes, J. Phys. Chem. B 109 (2005) 986–991.
[70] S. Santabarbara, K.V. Neverov, F.M. Garlaschi, G. Zucchelli, R.C. Jennings, Involvement of uncoupled antenna chlorophylls in photoinhibition in thylakoids, FEBS Lett. 491 (2001) 109–113.
[71] W.O. Feikema, P. Gast, I.B. Klenina, I.I. Proskuryakov, EPR characterisation of the triplet state in photosystem II reaction centers with singly reduced primary acceptor Q_A, Biochim. Biophys. Acta Bioenerg. 1709 (2005) 105–112.
[72] H.J. Den Blanken, A.J. Hoff, A.P.J.M. Jongenelis, B.A. Diner, High-resolution triplet-minus singlet absorbance difference spectroscopy of photosystem II particles, FEBS Lett. 157 (1983) 21–27.
[73] F. VanMiegem, W. Nitschke, P. Mathis, A.W. Rutherford, The influence of the quinone–iron electron acceptor complex on the reaction centre photochemistry of Photosystem II, Biochim. Biophys. Acta 977 (1989) 207–214.
[74] D. Carbonera, G. Giacometti, G. Agostini, A well resolved ODMR triplet minus singlet spectrum of P680 from PSII particles, FEBS Lett. 343 (1994) 200–204.
[75] D. Carbonera, G. Agostini, T. Morosinotto, R. Bassi, Quenching of chlorophyll triplet states by carotenoids in reconstituted Lhca4 subunit of peripheral light-harvesting complex of photosystem I, Biochemistry 44 (2005) 8337–8346.
[76] S. Santabarbara, G. Agostini, P. Heathcote, D. Carbonera, A fluorescence detected magnetic resonance investigation of the carotenoid triplet states associated with photosystem II of isolated spinach thylakoid membranes, Photosynth. Res. 86 (2005) 283–296.
[77] D.A. Berthold, G.T. Babcock, C.F. Yocum, A highly resolved, oxygen-evolving photosystem II preparation from spinach thylakoid membranes, FEBS Lett. 134 (1981) 231–234.
[78] T.G. Dunahay, L.A. Stahelin, M. Seibert, P.G. Ogilvie, S.P. Berg, Structural, biochemical, and biophysical characterisation of four oxygen-evolving photosystem II preparation from spinach, Biochim. Biophys. Acta Bioenerg. 764 (1984) 179–193.
[79] R.C. Jennings, F.M. Garlaschi, P.D. Gerola, R. Etzion-Katz, G. Forti, Proton-induced grana formation in chloroplast. Distribution of chlorophyll–protein complexes and photosytem II photochemistry, Biochim. Biophys. Acta Bioenerg. 638 (1981) 100–107.
[80] H.K. Lichtenthaler, Chlorophyll and carotenoids: pigments of photosynthetic membranes, Methods Enzymol. 148 (1987) 350–382.
[81] U.K. Laemmli, Cleavage of structural proteins during the assembly of the head of bacteriophage T4, Nature 227 (1970) 680–685.
[82] D.F. Ghanotakis, D.M. Demetriou, C.M. Yocum, Isolation and characterization of an oxygen-evolving photosystem II reaction center core preparation and a 28 kDa chl-binding protein, Biochim. Biophys. Acta Bioenerg. 891 (1987) 15–21.
[83] R. Strasser, W.L. Butler, Fluorescence emission spectra of photosystem I, photosystem II and the light-harvesting chlorophyll a/b complex of higher plants, Biochim. Biophys. Acta Bioenerg. 462 (1977) 307–313.
[84] C.P. Rijgersberg, J. Amesz, A.P. Thielen, J.A. Swager, Fluorescence emission spectra of chloroplasts and subchloroplast preparations at low temperature, Biochim. Biophys. Acta Bioenerg. 637 (1981) 272–277.
[85] E.J.G. Peterman, S.F. Hobe, F. Calkoen, R. van Grondelle, H. Paulsen, H. van Amerongen, Low temperature spectroscopy of monomeric and trimeric form of reconstituted light-harvesting chlorophyll a/b complex, Biochim. Biophys. Acta Bioenerg. 1273 (1996) 171–174.
[86] A.V. Ruban, J.P. Dekker, P. Horton, R. van Grondelle, Temperature dependence of chlorophyll fluorescence from the light harvesting complex II of higher plants, Photochem. Photobiol. 61 (1995) 216–221.
[87] G. Zucchelli, F.M. Garlaschi, R.C. Jennings, Thermal broadening analysis of the light harvesting complex II absorption spectrum, Biochemistry 35 (1996) 16247–16254.
[88] E. Krausz, J.L. Hughes, P.J. Smith, R.J. Pace, S.P. Arsköld, Assignment of the low-temperature fluorescence in oxygen-evolving photosystem II, Photosynth. Res. 84 (2005) 193–199.
[89] E.G. Andrizhiyevskaya, A. Chojnicka, J.A. Bautista, B.A. Diner, R. van Grondelle, J.P. Dekker, Origin of the F685 and F695 fluorescence in photosystem II, Photosynth. Res. 84 (2005) 173–180.
[90] M. Mimuro, S. Akimoto, T. Tomo, M. Yokono, H. Miyashita, T. Tsuchiya, Delayed fluorescence observed in the nanosecond time region at 77 K originates directly from the photosystem II reaction center, Biochim. Biophys. Acta Bioenerg. 1767 (2007) 327–334.
[91] M. Reppert, K. Acharya, B. Neupane, R. Jankowiak, Lowest electronic states of the CP47 antenna protein complex of photosystem II: simulation of optical spectra and revised structural assignments, J. Phys. Chem. B 114 (2010) 11884–11898.
[92] B. Neupane, N.C. Dang, K. Acharya, M. Reppert, V. Zazubovich, R. Picorel, M. Seibert, R. Jankowiak, Insight into the electronic structure of the CP47 antenna protein complex of photosystem II: hole burning and fluorescence study, J. Am. Chem. Soc. 132 (2010) 4214–4219.
[93] M. Reppert, V. Zazubovich, N.C. Dang, M. Seibert, R. Jankowiak, Low-energy chlorophyll states in the CP43 antenna protein complex: simulation of various optical spectra. II, J. Phys. Chem. B 112 (2008) 9934–9947.
[94] A.P. Casazza, M. Szczepaniak, M.G. Müller, G. Zucchelli, A.R. Holzwarth, Energy transfer processes in the isolated core antenna complexes CP43 and CP47 of photosystem II, Biochim. Biophys. Acta Bioenerg. 1797 (2010) 1606–1616.
[95] N.C. Dang, V. Zazubovich, M. Reppert, B. Neupane, R. Picorel, M. Seibert, R. Jankowiak, The CP43 proximal antenna complex of higher plant photosystem II revisited: modelling and hole burning study, J. Phys. Chem. B 112 (2008) 9921–9933.
[96] P.J. Smith, S. Peterson, V.M. Masters, T. Wydrzynski, S. Styring, E. Krausz, R.J. Pace, Magneto-optical measurements of the pigments in fully active photosystem II core complexes from plants, Biochemistry 41 (2002) 1981–1989.
[97] S.P. Arsköld, V.M. Masters, B.J. Prince, P.J. Smith, R.J. Pace, E. Krausz, Optical spectra of synechocystis and spinach photosystem II preparations at 1.7 K: identification of the D1-pheophytin energies and stark shifts, J. Am. Chem. Soc. 125 (2003) 13063–13074.
[98] E. Krausz, N. Cox, S.P. Arsköld, Spectral characteristics of PS II reaction centres: as isolated preparations and when integral to PS II core complexes, Photosynth. Res. 98 (2008) 207–217.
[99] J. Morton, J. Hall, P. Smith, F. Akita, F.H. Koua, J.R. Shen, E. Krausz, Determination of the PS I content of PS II core preparations using selective emission: a new emission of PS II at 780 nm, Biochim. Biophys. Acta Bioenerg. 1837 (2014) 167–177.
[100] G. Raszewski, T. Renger, Light harvesting in photosystem II core complexes is limited by the transfer to the trap: can the core complex turn into a photoprotective mode? J. Am. Chem. Soc. 130 (2008) 4431–4446.
[101] K. Acharya, V. Zazubovich, M. Reppert, R. Jankowiak, Primary electron donor(s) in isolated reaction center of photosystem II from *Chlamydomonas reinhardtii*, J. Phys. Chem. B 116 (2012) 4860–4870.
[102] R. Croce, G. Zucchelli, F.M. Garlaschi, R.C. Jennings, A thermal broadening study of the antenna chlorophylls in PSI-200, LHCI, and PSI core, Biochemistry 37 (1998) 17355–17360.
[103] R. Croce, H. van Amerongen, Light-harvesting in photosystem I, Photosynth. Res. 116 (2013) 153–166.
[104] H. Hashimoto, Y. Koyama, K. Ichimura, T. Kobayashi, Time resolved absorption spectroscopy of triplet states produced from the all-tran, 7-cis, 9-cis, 13-cis, 15-cis isomers of β-carotene, Chem. Phys. Lett. 162 (1989) 517–522.
[105] P. Mathis, J. Kleo, The triplet state of β-carotene and analog polyene of different length, Photochem. Photobiol. 18 (1973) 343–346.
[106] Y. Koyama, H. Hashimoto, Spectroscopy of carotenoids in carotenoids in photosynthesis, in: A. Young, G. Britton (Eds.), Chapman & Hall, London, UK1983.
[107] K. Hirayama, Absorption spectra and chemical structure. II. Solvent effect, J. Am. Chem. Soc. 77 (1955) 379–381.
[108] M.M. Mendes-Pinto, D. Galzerano, A. Telfer, A.A. Pascal, B. Robert, C. Ilioaia, Mechanisms underlying carotenoid absorption in oxygenic photosynthetic proteins, J. Biol. Chem. 288 (2013) 18758–19765.
[109] G. Araki, T. Murai, Molecular structure and absorption spectra of carotenoids, Progr. Theor. Phys. 8 (1952) 639–654.

Carotenoid Triplet States in Photosystem II: Coupling With Low-Energy States of the Core Complex.

Stefano Santabarbara[a*], Alessandro Agostini[b], Anna Paola Casazza[c], Giuseppe Zucchelli[a] and Donatella Carbonera[b*]

[a]Istituto di Biofisica, Consiglio Nazionale delle Ricerche, Via Celoria 26, 20133 Milan, Italy.
[b]Department of Chemical Sciences, Università di Padova, Via Marzolo 1, 35131 Padova, Italy.
[c]Istituto di Biologia e Biotecnologia Agraria, Consiglio Nazionale delle Ricerche, Via Bassini 15a, 20133, Milano, Italy.

Supplementary Information

Appendix 1. Basic Principle of Optically Detected Magnetic Resonance.

Optically Detected Magnetic Resonance (ODMR) is a double resonance technique, which allows the correlation between the optical properties of a chromophore with the energy splitting within the sublevels of a photo-excited triplet state manifold (Figure S1). The energy of three spin sub-levels of triplet states are non-degenerate even in absence of an applied magnetic field, because of dipolar interactions between the unpaired spins which give rise to zero-field splitting (ZFS). The strength of zero field splitting depends on the spin density distribution over the molecular frame of the chromophore and can be fully described by two terms, |D| and |E| which are called the axial and rhombic ZFS parameters respectively. The strength of the interaction determines the splitting of the triplet sublevels, which occurs at energy equal to 2|E|, |D|–|E|, |D|+|E|. For most molecules of chemical and biochemical interest the splitting amongst the triplet sublevels falls in the microwave region (MHz to GHz).

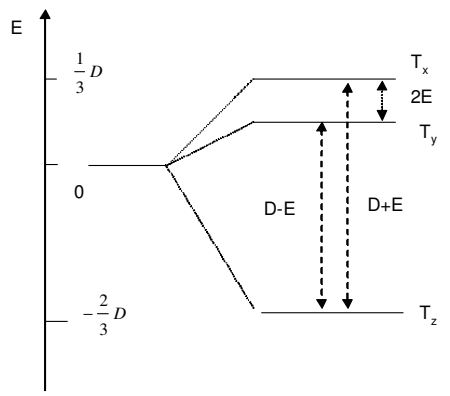

Figure S1. Splitting of the triplet state levels in Zero Field, for the case of D>0, E<0. Also shown (dashed line) are the possible resonance transitions.

ODMR allows determining the resonance frequency between the sublevels of a photo-excited triplet state in absence of an applied magnetic field (it is sometimes referred to zero-field Electron Paramagnetic Resonance), henceforth the accurate determination of the ZFS parameters, by monitoring the optical properties of chromophore.

The principle of the ODMR technique may be illustrated by considering the example, shown in Figure S2, in which the triplet state of a molecule is populated by photo-excitation. Under continuous illumination a steady state population of the three sublevels T_x, T_y and T_z (where x, y and z are the ZFS axes related to the molecular symmetry) is attained, which depend on the rate of population and depopulation of each sublevel. In the particular case considered, the population rates are taken to be the same ($p_x = p_y = p_z$) whereas the decay rate constants are assumed to be $k_x, k_y >> k_z$. In this scenario, the steady state populations of the three triplet sublevels will be: $n_z >> n_x$, n_y. Moreover, it is important to point out that, under steady state conditions, populations of the singlet ground and the singlet excited state of the chromophore also depends on the triplet population and depopulation rates.

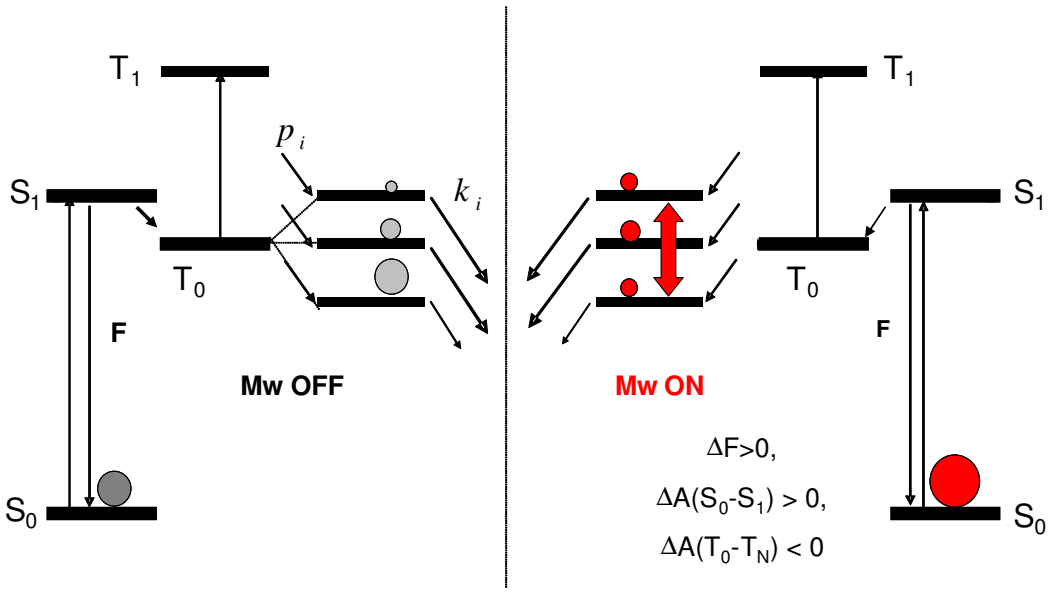

Figure S2. Schematic representation of the basic principle of ODMR spectroscopy. The symbols S_0, S_1, T_0 and T_1 are the ground singlet state, excited state singlet, lowest photo-excited triplet, and one higher-excited triplet state levels respectively. Also shown is the enlarged on energy scale, splitting of the T_0 triplet state in absence of applied magnetic field. The rates of population p_i and relaxation k_i give rise to different populations in the triplet sublevels (represented by the grey circles). The right part shows how, upon application of a resonant microwave field of appropriate frequency, population is transferred between two sublevels, and because of the anisotropic rate of depopulation, the state-state population level of S_0, S_1, as well as of T_0 and T_1 is perturbed, giving rise to a detectable difference in the singlet-singlet and triplet-triplet absorption as well as in the fluorescence emission.

When a resonant microwave field between a couple of sublevels is applied, it will lead to transfer of population between the levels. As a consequence their populations are redistributed and different steady-state population levels are attained in the presence of the microwave field. If, in the example of Figure S2, the microwave field of a frequency corresponding to a transition between the T_x and T_z levels is applied, it will transfer population from the more populated and slowly decaying T_z to the much less populated, fast decaying T_x level. This transferred population will quickly decay to the ground state leading to different steady-state, established by the presence of the resonant microwave field, in which the singlet ground state population is enhanced while the global triplet state population ($N_{\mathrm{T}}=n_z+n_x+n_y$) is decreased. This in turn, will induce an increase of fluorescence, an enhanced singlet ground state absorbance and a decrease of triplet-triplet absorbance.

The change in the population of singlet and triplet levels of a chromophore in presence of a resonant microwave field represent the basic principle of ODMR spectroscopy. The basic requirement for the triplet to be observed is an anisotropy of the triplet sublevel decay rates (k_i). Another important caveat is that enough population is transferred between a pair of levels to induce a detectable change in the steady-state. This is often difficult because the relaxation between the triplet sublevels, which is mediated by spin-lattice processes, is competitive with the resonance induced population transfer. To limit spin-lattice relaxation, experiments are often performed at very low temperature. In our experiments a temperature below 2 K is used, as it increase sensitivity and at this temperature He is super-fluid and perfectly transparent thereby reducing detection noise.

In general, two types of experiment experiments are performed:

i) the microwave frequency is varied by scanning while monitoring either the fluorescence emission (FDMR) or absorption (ADMR) of the sample

ii) the microwave frequency is held fixed (at a known value giving rise to resonance) and either the absorption (A) or the fluorescence emission (F) wavelength is scanned obtaining the microwave-induced absorption spectra (MIA or $T-S$) and microwave induced fluorescence spectra (MIF).

In FDMR/ADMR, when the microwave field is in resonance with two of the triplet sublevels an increase (or decrease) in the steady state level of the singlet state give rise to an either positive or negative ODMR signal. In this configuration the experiment is conceptually identical to a classic EPR measurements, but rather than monitoring the microwave absorption directly, it is the optical properties of the chromophore which are monitored instead. However, compared to conventional EPR, ODMR is a quite sensitive technique. This is due to the fact that the energies of

optical quanta (detected by ODMR) are much higher than the energies of microwaves quanta (detected by EPR) and this enhances the sensitivity of the detector (the quantum-up conversion factor is about 10^5). Furthermore, the lines are much narrower, because there is not the anisotropy associated with an applied magnetic field.

A unique feature of ODMR is the possibility to probe the resonance at different wavelengths, which may help on distinguish among different triplet states present in the sample, and to correlate optical and magnetic properties. This feature is better exploited in the type of experiment described at point (ii). The most common implementation is by scanning the transmission in presence of amplitude modulated resonant microwave field. The result is a Triplet-minus-Singlet ($T-S$) spectrum which is conceptually identical to that obtainable by time resolved transient absorption. For crowded molecular systems, however, *microwave-induced* $T-S$ might offer superior resolution since the triplet state is selected among several present under illumination in the sample by the resonant microwave field.

Appendix 2: Simulations of $\Delta F/F$ microwave-induced fluorescence (MIF) emission spectra.

Microwave–induced fluorescence (MIF) spectra are typically presented in terms of $\Delta F/F$ ratio, as this allows the compensation of differences in the relative transmission of band-pass filters utilised to monitor the emission, as well as different gains/sensitivity of the detectors, amplifiers and digitising apparatus. On the other hand, the interpretation of the MIF spectra requires some caution, since the $\Delta F/F$ ratio might lead to spectral distortion. These aspects are discussed in this appendix, where a simplified scheme for a qualitative approach to simulate the MIF spectra in a multi-chromophore system, such as the photosynthetic pigment-protein complexes, is presented.

The FDMR effect is based on the changes in the intensity of the steady-state fluorescence emission which can be observed, under resonance conditions between a couple of triplet state sublevels, because the population transfer within the triplet manifold determines a change in the steady-state population of the ground state and, as a consequence, of the singlet excited state (for a more detailed description, see the extended review by Carbonera [**1**]). The microwave-induced differences in the excited populations can be monitored either directly on the chromophore carrying the triplet state or indirectly because of energy transfer between a pair (or array) of chromophores. The latter is the case of the triplet state of carotenoids (^3Car) that have an intrinsically low fluorescence yield. However, their FDMR signals can be recorded by monitoring the fluorescence emission of the Chl to which the carotenoids are coupled via excited state energy transfer.

When the microwave-induced change in fluorescence intensity is measured on the emission of a single chromophore, it is expected that the whole emission band is affected in the same fashion,

so that $\Delta F(\lambda)/F(\lambda)$ assumes a constant, wavelength independent, value. On the other hand, when the resonance affects only one of the different emitting chromophores present in the system, the shape of the MIF spectrum (in the form of ΔF/F), will depend on the emission of all the fluorescent species and will be wavelength-dependent. For a simple case of two emitting chromophores only, characterised by the emission spectra $F_1(\lambda)$ and $F_2(\lambda)$, respectively (with $F_1(\lambda) \neq F_2(\lambda)$), and in the assumption that the resonant field affects only one of the chromophores, *e.g.* $F_1(\lambda)$, the MIF spectrum can be represented as $\Delta F(\lambda)/F(\lambda) = \Delta F_1(\lambda)/(F_1(\lambda) + F_2(\lambda))$. It is clear that the value of $\Delta F(\lambda)/F(\lambda)$ will assume a maximal value at wavelengths where the $F_2(\lambda)/F_1(\lambda)$ ratio is minimal, and minimal values when the $F_2(\lambda)/F_1(\lambda)$ ratio is maximal. The situation just described is applicable, for instance, to a mixture of non-interacting chromophores. Yet, such a simple scenario does not reflect the conditions encountered in a photosynthetic pigment-protein complex, where singlet–singlet ($S-S$) energy transfer amongst pigments occurs. Since ODMR measurements are generally performed at very low temperatures, typically below 4 K, the fluorescence emission from a non-isoenergetic pigment cluster is expected only from the lowest energy state. However, in whole photosystems, comprising the reaction centre as well as the core and the external antenna, more than one spectral form is observed instead. In the case of Photosystem II (PSII), the fluorescence emission spectrum displays peaks at around 685 nm and 695 nm. This can be explained considering a "rough" energetic landscape in the antenna matrix determining the presence of barriers for energy transfer that tend to localise the excited states in a few local minima, rather than in the lowest energy state of the system. These local emitters might either be i) uncoupled in terms of $S-S$ energy transfer, or ii) "weakly" coupled, in the sense that the excited state transfer rate is of the same order of magnitude, or slower, than the rate of the excited state relaxation. In this case fluorescence emission from the local emitter occurs before the (Boltzmann) equilibrium population is attained.

Due to the complexity of the system under investigation, we have performed qualitative simulations that aid in the interpretation of the experimental MIF expressed as $\Delta F(\lambda)/F(\lambda)$ ratios. The simulations need to consider kinetic schemes accounting for: i) the effect of the resonant microwave field, within the ^3Car state manifold, on the singlet state of the carotenoid itself, ii) $S-S$ energy transfer between ^1Car and ^1Chl, iii) $S-S$ energy transfer between Chls having different emission maxima. In Figure S3 is shown the kinetic scheme for a relatively simple scenario, which considers *only* two emitters, namely F_1^{695} with maximal emission at 695 nm and F_2^{705} with maximal emission at 705 nm. Both Chl emission forms are coupled (by Triplet-Triplet

($T-T$) as well as by $S-S$ energy transfer) to Cars, named Car_1 and Car_2 respectively. Because of the difference in the energy levels, at the temperature at which the measurements are performed, $S-S$ energy transfer between Car_1 and F_1^{695} as well as Car_2 and F_2^{705} can be considered as irreversible. The same holds also for $T-T$ energy transfer between ${}^3F_1^{695}$ and ${}^3Car_1$ and between ${}^3F_2^{705}$ and ${}^3Car_2$. Then, the effect of the microwave field can be simulated simply by an increase (or decrease, depending on the sublevels kinetics) in the initial singlet population of the carotenoid species sensing the resonance field.

The scheme of Figure S3 also considers explicitly $S-S$ energy transfer between F_1^{695} and F_2^{705}, that are coupled by the forward and backward transfer rate constants $k_{F_1 \to F_2}$ and $k_{F_2 \to F_1}$, respectively. The simulations were performed for i) uncoupled emitters, i.e. $k_{F_1 \to F_2} = k_{F_2 \to F_1}$ =0 and ii) for energy transfer rates, $k_{F_1 \to F_2}$, in the range of 0.25 to 8 times that of the excited state relaxation (k_d =0.25 ns^{-1}). The value of $k_{F_2 \to F_1}$ is given by the Boltzmann distribution factors.

The excited state populations are simulated by solving a system of linear differential equations (ODE), that has general solution of the form $F_j(t) = \sum_i A_{ji} \cdot \exp[-t/\tau_i]$ where $\tau_i = -\gamma_i$, γ_i being the eigenvalues and A_{ji} the eigenvectors of the rate matrix associated to the ODE system. The effect of the microwave resonance is accounted by changing the (boundary) conditions defining the initial population of the ${}^1Car_j$ levels. To simulate the off-resonance conditions, equal initial population in all the (singlet) excited states were considered. Changes in the initial populations of ${}^1Car_j$ coupled to the highest and lowest energy Chls, that mimic on-resonance conditions, were considered independently. The steady-state (SS) levels are computed by the integration of the population evolution of each of the states considered, i.e. $F_J^{SS} = \sum_i A_{ji} \cdot \tau_i$. However, only F_1^{695} and F_2^{705} attain significant population at steady-state. The calculations were performed for the boundary conditions mimicking the off- and on-resonance conditions, from which the values of ΔF_J^{SS} are determined. These ΔF_J^{SS} values represent only relative changes in the populations of the level considered, but do not contain any spectral information (but for the "mean" energy of the state).

In order to describe the wavelength dependence of the MIF spectra, the emission from the Chl forms $F_1^{695}(\lambda)$ and $F_2^{705}(\lambda)$ has to be considered. The spectral bandshape of each of these states is described by a sum of Gaussian functions dressing the principal $S_0 \to S_1$ transition and the associated vibronic progression (Figure S4A). The spectra of Figure S4A are a simplified

description that serves the purpose of qualitatively simulating the red tail of the emission. In Figure S4B are also shown the emission spectra of the two-chromophore system, as a result of increasing the value of the energy transfer rate $k_{F_1 \to F_2}$. These emission spectra have been calculated from the population retrieved by solving the ODE system (under non-resonant conditions) that weights the "area-normalised" bandshape ($\tilde{F}_j(\lambda)$) of each of the states considered, i.e. the emission spectra are computed as $F^{SS}(\lambda) = \sum_j F_j^{SS} \cdot \tilde{F}_j(\lambda)$. As expected, the increase of $k_{F_1 \to F_2}$ value leads to a progressive quenching of the $F_1^{695}(\lambda)$ emission with respect to that of $F_2^{705}(\lambda)$.

Figure S5 (A, B) shows the simulations of the $\Delta F(\lambda)/F(\lambda)$ MIF spectra considering only two chlorophyll spectral forms $F_1^{695}(\lambda)$ and $F_2^{705}(\lambda)$, for resonance affecting either Car_1 (i.e. direct coupling with $F_1^{695}(\lambda)$, Panel S5A) or Car_2 (i.e. direct coupling with $F_2^{705}(\lambda)$, Panel S5B). For both cases, the simulations obtained for increasing values of energy transfer rate between the two energy levels are also shown.

The simulated MIF spectra obtained considering only the emission from $F_1^{695}(\lambda)$ and $F_2^{705}(\lambda)$ yielded reasonable results, in terms of bandshape, when the resonance occurs in the *Car* coupled to the lowest energy form $F_2^{705}(\lambda)$. The simulated spectra of Figure S5B reproduce the increase in the value of $\Delta F / F$ at the long detection wavelengths. However, in the main emission band (see Figure S4 for the simulated emission) the spectra do not show any fine structure in the 680-690 nm interval, and are dominated by a spectral feature peaking at ~705 nm. On the other hand, when the triplet resonance is coupled to $F_1^{695}(\lambda)$ (Figure S5A), the simulated MIF bandshapes are clearly not comparable with the experimental spectra (Figure 3 of the main body). Particularly, excessive $\Delta F / F$ intensities are predicted in the high-energy wing of the emission.

The description of the PSII emission spectrum in terms of only two (weakly coupled or uncoupled) local emitting forms likely represents an oversimplification. Hence, in order to reproduce more realistically (but still under a qualitative point of view) the emission spectrum, we have performed simulations in which we considered also additional Chl forms, emitting in the 685-695 nm interval. These constitute the "bulk" emission, not influenced by the on-resonance conditions, that is used to "dress" the $F_1^{695}(\lambda)$ and $F_2^{705}(\lambda)$ spectra (Figure S4C). The "bulk" emission is assumed to be uncoupled from both $F_1^{695}(\lambda)$ and $F_2^{705}(\lambda)$, and the latter remains the lowest energy state in the systems. The simulated spectra considering the "bulk" as well as the

$F_1^{695}(\lambda)$ and $F_2^{705}(\lambda)$ emission are presented in Figure S4C, whereas the simulation of the MIF spectra are presented in Figure S5 (C, D).

Figure S5 shows clearly that in both cases when the ^3Car resonance is felt by the lowest energy chlorophyll form F_2^{705} (Figure S5B and D) a remarkable intensity in the red tail, which further increases at the very red edge of the spectrum, is predicted similarly to what observed in the experimental MIF spectra (Figure 3). Similar effects are also predicted when the ^3Car resonance affects the population of F_1^{695} and the latter is connected via $S-S$ energy transfer with F_2^{705} (depending on the energy transfer rate), when a more realistic emission bandshape for the whole chromophore system is considered (Figure S5C). However, when the ^3Car is coupled to F_1^{695} and this form is uncoupled from F_2^{705}, a decrease in intensity in the red edge of the MIF spectrum is predicted instead (Figure S5A). The relative intensity of the MIF on the "vibronic emission" tail depends on the overlap with the emitters that are unaffected by the resonance conditions, as well as on the overlap between the $F_1^{695}(\lambda)$ and $F_2^{705}(\lambda)$ emission bandshapes. The largest MIF intensity in the red tail results from the less significant overlap between the lowest triplet-sensing emitter and the "bulk" of the emission which is uninfluenced by the microwave field. This is because at long wavelengths, at least in the simulation, the emission is exclusively associated with the red-most vibrational band coupled to the lowest $S_0 \rightarrow S_1$ transition, so that the $\Delta F / F$ signal tends toward the maximal value that would be measured if it were the only emitting species present (i.e. $\Delta F_2^{(705)} / F_2^{(705)}$), whereas at shorter wavelengths the signal is "damped" by the contributions of all local emitters, (i.e. $\Delta F_2^{(705)} /(F_2^{(705)} + F_1^{(695)} + F_{bulk})$).

In the principal emission band (i.e. between 675 and 710 nm) the bandshape of the MIF simulated for coupling of the ^3Car with the lowest energy form F_2^{705}, that is also the red-most form of the whole simulated system, is, to a good approximation, independent from rate of the $S-S$ coupling with the higher energy form F_1^{695}, except for a slight broadening of the peak on the blue wing (Figure S5D). Hence, the bandshape of the MIF essentially reflects that of the chromophore that is directly coupled to the ^3Car, with minimal effect due to the chromophores whose emission is insensitive to the resonance. On other hand the MIF spectra simulated for the case in which the ^3Car is directly coupled to the F_1^{695} level depend significantly on the degree of coupling of this form with the lowest F_2^{705} (Figure S5C). Even for slow energy transfer rates between the two forms, a shoulder is predicted at the maximum of $F_2^{705}(\lambda)$, i.e. 705 nm. Increasing the rate of $S-S$ energy

transfer from F_1^{695} to F_2^{705}, the intensity of the feature peaking at 705 nm increases, and might becomes dominant. A parallel increase between the intensity of the 705 nm peak in the MIF and the intensity in the red-most tail on the vibrational emission is also predicted (Figure S5C).

Based on the MIF simulations and their comparison with the experimental results it is therefore possible to draw some qualitative conclusions:

i) the presence of spectral features in the experimental "main" emission band suggests that ^3Car are populated, predominantly, by local emitters having maximal transitions in the 685-695 nm interval, since these features fail to be simulated when ^3Car are populated only from the lowest energy state of the system (705 nm);

ii) the $\Delta F / F$ signal in the red-most tail of the emission indicates however that red Chls are coupled *via* $S-S$ energy transfer to those sensitizing the ^3Car;

iii) the different intensities between the 690-695 nm and 700-705 nm peaks/shoulders observed in the experimental MIF associated to different $^3\beta\text{-}Car$ populations indicate an heterogeneity in the rate of $S-S$ energy transfer between the sensitizing pigments and the lowest energy state, although confined to slow energy hopping rate comparable to the exited state relaxation (i.e. in the order of 0.1–2 ns^{-1}).

Considering the qualitative nature of the simulations, it is difficult to extract more accurate and quantitative information on these aspects. Nevertheless, these simulations are in reasonable qualitative accordance with the experimental findings.

Appendix 2, figures and legends:

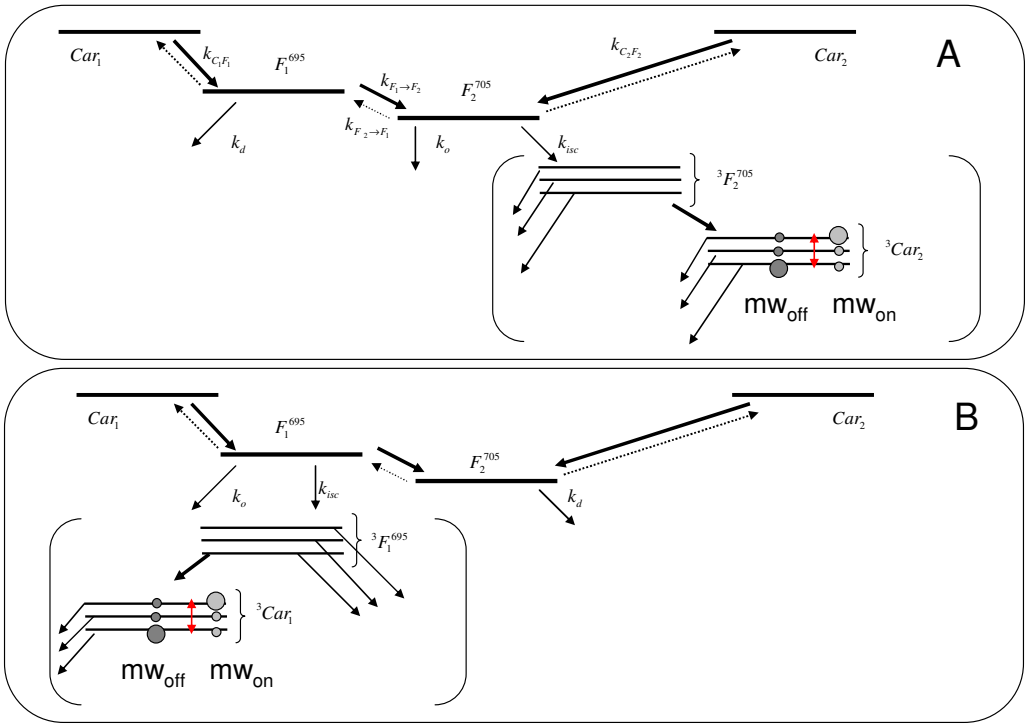

Figure S3. Kinetic scheme utilised to model the $\Delta F / F$ MIF spectra. The scheme considers two emitting states, F_1^{695} and F_2^{705}, each of which is coupled by $S-S$ energy transfer to a carotenoid state, Car_1 and Car_2, respectively, with the transfer rates $k_{C_1F_1} = k_{C_2F_2}$ =5*10^3 ns^{-1} (*e.g.* Refs. [**2-5**]). F_1^{695} and F_2^{705} populate their respective triplet states ($^3F_1^{695}$ and $^3F_2^{705}$) by intersystem crossing (k_{isc} =0.16 ns^{-1}) *e.g.* [**6-8**], and decay to the ground state by other relaxation processes with constant k_o =0.08 ns^{-1}; the effective excited state relaxation is $k_d = k_{isc} + k_o$ =0.24 ns^{-1}. The $^3F_i^{\lambda}$ state sensitizes the ^3Car by $T-T$ energy transfer. These are shown in brackets as these processes has not been included explicitly in the simulations: a decrease in the steady-state population of $^3Car_i$ induced by the resonant microwave field (also shown in the scheme) has been assumed instead (in agreement with the conclusions of van der Vos *et al* .[**9**] and Carbonera *et al.* [**10**]). Energy transfer between the Chl singlet excited states is accounted by the transfer rates $k_{F_1 \to F_2}$ and $k_{F_2 \to F_1}$. Simulations were performed for values of $k_{F_1 \to F_2}$ in the range of 0.2-8$\cdot k_d$.

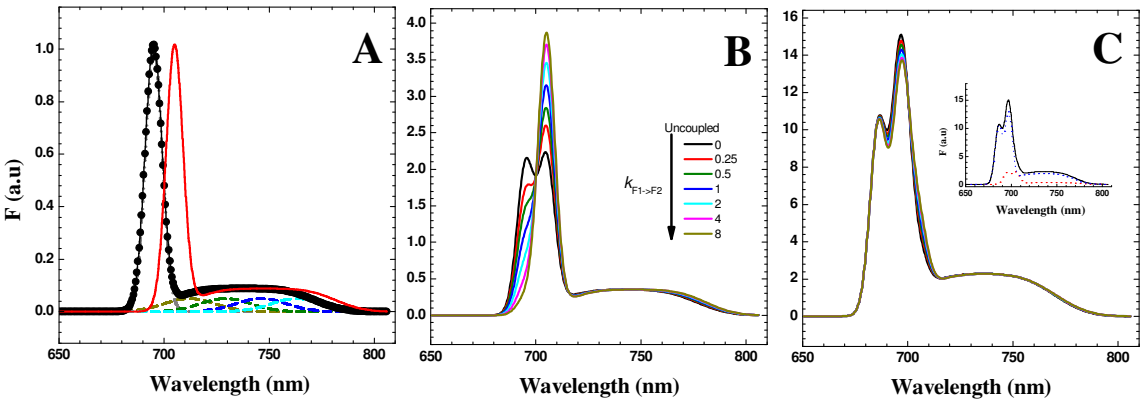

Figure S4. Simulations of the emission spectra. **A:** Emission spectra of the two spectral forms considered explicitly in the kinetic model. $F_1^{695}(\lambda)$ black line (and symbols) and $F_2^{705}(\lambda)$ red line. For $F_1^{695}(\lambda)$ the Gaussian functions used to describe the main and the vibrational transitions are also shown. Spectra are normalised on the maximal emission. **B:** Emission spectra of the "two-local-emitter" system ($F_1^{695}(\lambda)$ + $F_2^{705}(\lambda)$) for different values of the $S-S$ energy transfer rate ($k_{F_1 \to F_2}$). **C:** Emission spectra considering both the two-local-emitter system (treated explicitly) and an invariant "bulk" emission contribution. The ratio between the integrated emission of the non-resonant bulk and the terminal emitters was assumed to be 4, and it is shown in the insert of panel C: blue line, "bulk emission"; red line, sum of "resonant" local emitters under uncoupled conditions, i.e. as $k_{F_1 \to F_2}$=0 of Panel B. The spectra were simulated considering different values of $k_{F_1 \to F_2}$ (as in Panel B), whereas the emission of the bulk is the same in all simulations.

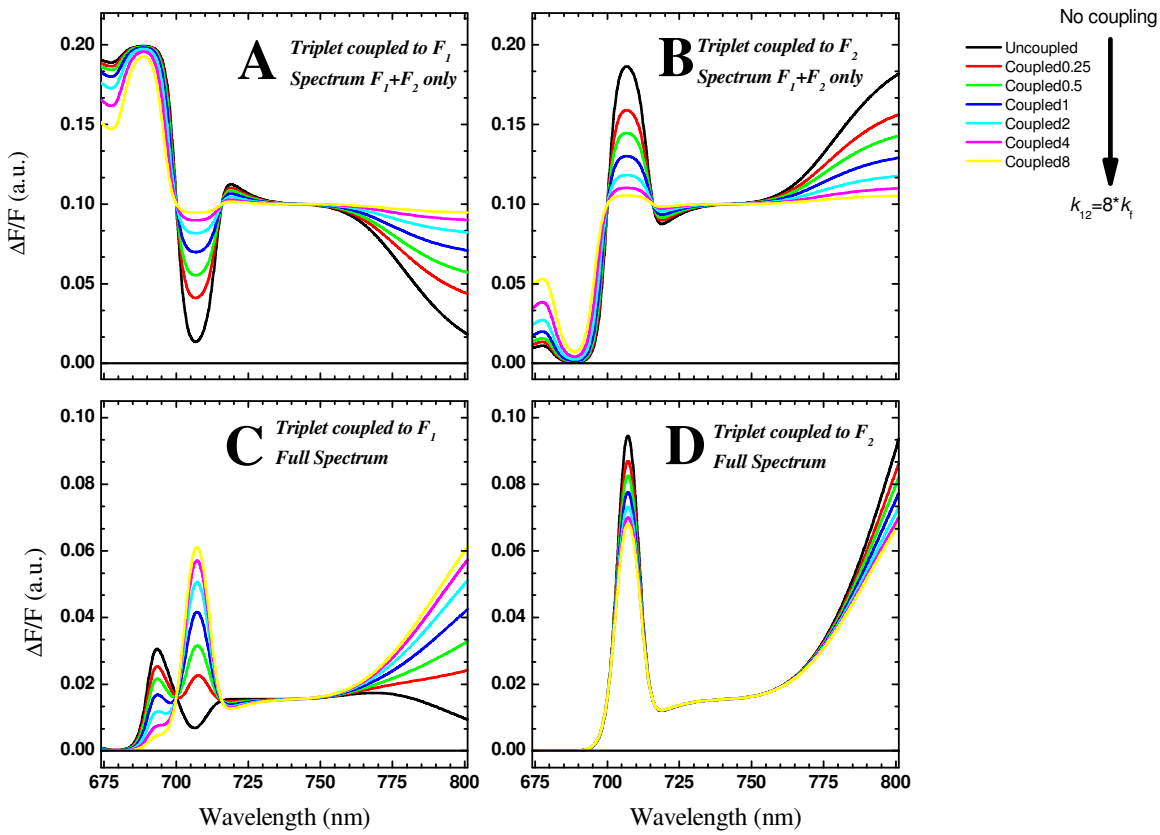

Figure S5. Simulations of the ^{3}Car MIF spectra. Two Chl forms $F_1^{695}(\lambda)$ and $F_2^{705}(\lambda)$ coupled to each other by weak $S-S$ energy transfer are considered with different rates of energy transfer, ranging form 0.25 to 8 folds the rate of radiative deactivation. Panel A and B show the results of simulations for a system considering only $F_1^{695}(\lambda)$ and $F_2^{705}(\lambda)$, whereas panel C and D show the results obtained when in addition a "dressing" spectral bandshape which is independent on the resonant microwave field is considered. Panels A and C show the simulated MIF for the case of the microwave field affecting the initial population of the carotene coupled to $F_1^{695}(\lambda)$. Panels B and D show the simulated MIF for the case of the microwave field affecting the initial population that coupled to $F_2^{705}(\lambda)$. See the appendix for further detail.

References:

[1] Carbonera, D. Optically Detected Magnetic Resonance (ODMR) of photoexcited triplet states. *Photosynth. Res.* 102 (2009) 403–414.

[2] Connelly, J.P.; Müller, M.G.; Bassi, R.; Croce, R.; Holzwarth, A.R. Femtosecond transient absorption study of carotenoid to chlorophyll energy transfer in the light-harvesting complex II of photosystem II. *Biochemistry* 36 (1997) 281–287.

[3] Petermanm, E.J.G.; Monshouwer, R.; van Stokkum, I.H.M.; van Grondelle, R.; Van Amerongen, H. Ultrafast singlet excitation transfer from carotenoids to chlorophylls via different pathways in light-harvesting complex II of higher plants *Chem. Phys. Lett*. 264 (1997) 279–284.

[4] Croce, R.; Müller, M.G.; Bassi, R.; Holzwarth, A.R. Carotenoid-to-chlorophyll energy transfer in recombinant major light-harvesting complex (LHCII) of higher plants. I. Femtosecond transient absorption measurements. *Biophys. J.* 80 (2001) 901–915.

[5] Gradinaru, C.C.; Pascal, A.A.; van Mourik, F.; Robert, B.; Horton, P.; van Grondelle, R.; van Amerongen, H. Ultrafast evolution of the excited states in the chlorophyll a/b complex CP29 from green plants studied by energy-selective pump-probe spectroscopy. *Biochemistry* 37 (1998) 1143–1149.

[6] Bowers, P.G.; Porter. G. Quantum yield of triplet formation in solutions of chlorophylls. *Proc. R. Soc. A.* 296 (1967) 435–441.

[7] Krasnovsky, A.A. Delayed luminescence and phosphorescence of plant pigments. *Photochem. Photobiol.* 36 (1992) 733–741.

[8] Kramer, H.; Mathis P. Quantum yield and rate of formation of the carotenoid triplet state in photosynthetic structure. *Biochim. Biophys. Acta-Bioenerg.* 593 (1980) 319–329.

[9] Van der Vos, R.; Carbonera, D.; Hoff A.J. Microwave and optical spectroscopy of carotenoid triplets in light-harvesting complex LHCII of spinach by absorbance-detected magnetic resonance. *Appl. Magn. Res.* 2 (1991) 179–202.

[10] Carbonera, D.; Giacometti, G.; Agostini, G. FDMR of carotenoid and chlorophyll triplets in light-harvesting complex LHCII of spinach. *Appl. Magn. Reson.* 3 (1992) 361-366.

BIOCHEMISTRY
including biophysical chemistry & molecular biology

Article

pubs.acs.org/biochemistry

Differential Roles of Carotenes and Xanthophylls in Photosystem I Photoprotection

Stefano Cazzaniga,[†] Mauro Bressan,[†] Donatella Carbonera,[‡] Alessandro Agostini,[‡] and Luca Dall'Osto*[,†]

[†]Dipartimento di Biotecnologie, Università di Verona, Strada Le Grazie 15, 37134 Verona, Italy

[‡]Dipartimento di Scienze Chimiche, Università di Padova, via Marzolo 1, 35100 Padova, Italy

Supporting Information

ABSTRACT: Carotenes and their oxygenated derivatives, xanthophylls, are structural elements of the photosynthetic apparatus and contribute to increasing both the light-harvesting and photoprotective capacity of the photosystems. *β*-Carotene is present in both the core complexes and light-harvesting system (LHCI) of Photosystem (PS) I, while xanthophylls lutein and violaxanthin bind exclusively to its antenna moiety; another xanthophyll, zeaxanthin, which protects chloroplasts against photooxidative damage, binds to the LHCI complexes under conditions of excess light. We functionally dissected various components of the xanthophyll- and carotene-dependent photoprotection mechanism of PSI by analyzing two *Arabidopsis* mutants: *szl1* plants, with a carotene content lower than that of the wild type, and *npq1*, with suppressed zeaxanthin formation. When exposed to excess light, the *szl1* genotype displayed PSI photoinhibition stronger than that of wild-type plants, while removing zeaxanthin had no such effect. The PSI−LHCI complex purified from *szl1* was more photosensitive than the corresponding wild-type and *npq1* complexes, as is evident from its faster photobleaching and increased rate of singlet oxygen release, suggesting that *β*-carotene is crucial in controlling chlorophyll triplet formation. Accordingly, fluorescence-detected magnetic resonance analysis showed an increase in the amplitude of signals assigned to chlorophyll triplets in *β*-carotene-depleted complexes. When PSI was fractioned into its functional moieties, it was revealed that the boost in the rate of singlet oxygen release caused by *β*-carotene depletion was greater in LHCI than in the core complex. We conclude that PSI−LHCI complex-bound *β*-carotene elicits a protective response, consisting of a reduction in the yield of harmful triplet excited states, while accumulation of zeaxanthin plays a minor role in restoring phototolerance.

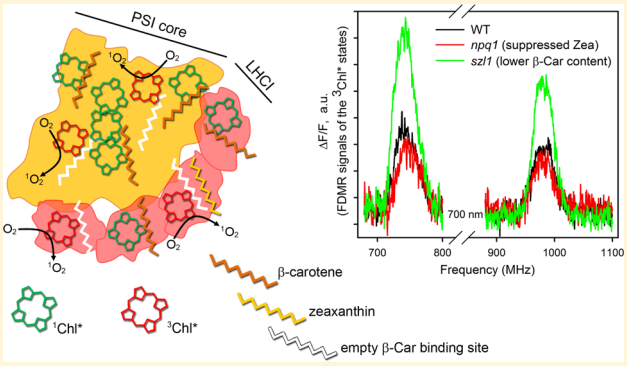

Multimeric pigment−protein complexes present on the thylakoid membrane catalyze light-driven electron transport from water to $NADP^+$, fuel ATP production, and lead to the assimilation of CO_2 into organic matter. Major components of the photosynthetic electron transport chain include Photosystems (PS) II and I, functionally connected by plastoquinone, the cytochrome b_6f complex, and plastocyanin.[1] In each PS, the first stage of solar energy conversion consists of photon absorption by an array of chlorophylls (Chl), which funnel excitation energy to the reaction center where charge separation occurs.[2,3]

Plants are highly effective at photosynthesis, and under steady-state conditions, the singlet excited states of the primary pigment chlorophyll (^{1}Chl*) are efficiently quenched by the photochemical reaction centers.[4] However, the photosynthetic apparatus can easily experience photooxidative damage: excess light (EL) shifts the balance of the captured to utilized energy ratio, increasing the probability of the intersystem crossing to the Chl triplet state (^{3}Chl*) and releasing the highly reactive oxygen species (ROS) singlet oxygen ($^1O_2$).[5,6] This ROS damages its local environment by destroying lipids and proteins, until a depression of the photosynthetic efficiency called photoinhibition occurs.[7] Within the photosynthetic apparatus, the PSII reaction center and its peripheral antenna system were observed to be the major sites of $^1O_2$ release and the main targets of photooxidative damage.[8]

Besides Chls, the major class of pigments present in the photosynthetic apparatus is carotenoids (Car).[9] These are either carotenes, bound to the core complex of both PSs and the light-harvesting complexes (LHC) of PSI,[10−12] or their oxygenated derivatives, xanthophylls (Xan), which are structural elements of the LHC subunits.[10,12,13] Cars are involved in a number of photoprotection mechanisms and are active in (i) preventing overexcitation of the reaction center by de-exciting ^{1}Chl* states,[14,15] (ii) quenching ^{3}Chl* through carotenoid triplet (^{3}Car*) formation,[16] and (iii) acting as antioxidants, thus preventing lipid peroxidation.[17]

Of particular interest for chloroplast photoprotection is xanthophyll zeaxanthin (Zea): absent under low-light conditions, it accumulates in EL only upon the reversible de-

Received: May 2, 2016
Revised: June 6, 2016
Published: June 13, 2016

ACS Publications © 2016 American Chemical Society

DOI: 10.1021/acs.biochem.6b00425
Biochemistry 2016, 55, 3636−3649

epoxidation of violaxanthin (Vio).[18,19] Once synthesized, Zea can either be freed into the thylakoids or bound to LHC; the latter process is termed xanthophyll exchange.[20−22] The role of the free Zea pool was investigated in *Arabidopsis thaliana*, where it was observed to possess a capacity to scavenge ROS greater than those of all other xanthophyll species.[23] Furthermore, the photoprotective effect of Zea is greatly enhanced by its binding to LHC subunits,[24,25] where it has been observed to increase the level of PSII photoprotection by (i) enhancing thermal dissipation of ^{1}Chl*[26,27] and (ii) downregulating the ^{3}Chl* yield, thus preventing the release of $^1O_2$.[28]

The role of carotenes in photoprotection has been mainly investigated in the PSII core complex, where most of the β-carotene (β-Car) molecules are in close contact with Chl headgroups, to facilitate ^{3}Chl* quenching. Only the two β-Car ligands in the PSII reaction center are distant from the special pair of Chls[29] and are likely to act as quenchers of $^1O_2$ produced during charge recombination.[30]

Unlike PSII, PSI has been considered to be less sensitive to photooxidative stress: its photoprotection mechanism is believed to rely mainly on ROS scavenging at its acceptor side,[31] because its photosensitivity *in vivo* increases under chilling conditions, which inhibit superoxide scavenging.[32] However, PSI can also be targeted by photoinhibition under conditions unbalancing linear versus cyclic electron transport,[33] or in mutants with a lower β-Car content.[34] Thus, the specific interaction between Chls and Cars in the LHCI antenna system of PSI might play a more relevant role in PSI photoprotection than is generally believed. Supporting this view is the fact that Cars bound to the LHCI system are effective in quenching ^{3}Chl*, thus suggesting that pigments bound to these complexes are well-protected from EL damage.[35,36] Only recently has the presence of a specific binding site for β-Car in LHCI subunits been confirmed,[12,37] whereas differences in the de-epoxidation of Vio in the LHCI subunits suggest different accessibility to the respective Car-binding sites.[38] Despite these observations, the Car-dependent contribution to PSI photoresistance is still rather unclear, and more detailed analyses are needed to understand it.

With this work, we addressed the question of what role both carotene and xanthophyll ligands of PSI play in the photoprotection of this complex. To this aim, we compared a panel of *Arabidopsis* mutants whose biosynthesis of either xanthophylls or carotenes was impaired and analyzed the effect of these depletions on photosensitivity both *in vivo* and *in vitro*. In particular, the *szl1* mutant has both a lower carotene content and an altered xanthophyll composition, whereas Zea does not accumulate in *npq1*. We observed that Zea binds to the peripheral antenna system of PSI; however, it neither enhances photoprotection of the supercomplex under EL conditions nor limits the release of $^1O_2$. On the other hand, however, *szl1* and *szl1 npq1* plants displayed a comparable photoinhibition of PSI but stronger than those of both WT and *npq1* plants, thus suggesting that β-Car ligands play a crucial role in the photoprotection of the supercomplex. Indeed, FDMR analyses of PSI−LHCI complexes from *szl1* plants revealed a greater level of ^{3}Chl*, suggesting a β-Car-specific effect in decreasing the yield of dangerous excited states. Fractionation of PSI supercomplexes from EL-treated plants into core and antenna moieties provided new insight into the photoprotective contribution of β-Car in the domains of PSI. We conclude that, in addition to the previously described effects of carotenes in preventing PSII photoinhibition, a crucial mechanism is mediated by β-Car bound to the peripheral antenna system of PSI, which is instrumental in reducing the yield of harmful ^{3}Chl*.

■ EXPERIMENTAL METHODS

Plant Material and Growth Conditions. Wild-type plants of *A. thaliana* ecotype Columbia and mutants *chy1chy2*, *lut5*, *szl1*, and *szl1 npq1* were obtained as previously reported.[39,40] T-DNA knockout lines are *chy1* (SAIL line 49A07), *chy2* (SAIL line 1242B12), and *lut5* (SALK line 116660).[39] Mutants *szl1* and *szl1 npq1* were kindly provided by K. K. Niyogi.[41] Plants were grown for 5 weeks on Sondermisch potting mix (Gramoflor) under controlled conditions (∼100 μmol of photons m^{-2} s^{-1}, 23 °C, 8 h light/16 h dark).

Stress Conditions. For EL treatments, light was provided by 150 W halogen lamps (Focus 3, Prisma). Short-term EL treatment was performed at 1000 μmol of photons m^{-2} s^{-1} and 20 °C for 1 h to measure the maximal accumulation of Zea on detached leaves. Samples for high-performance liquid chromatography (HPLC) analysis were rapidly frozen in liquid nitrogen prior to pigment extraction. Photooxidative stress was induced in either whole plants or detached leaves: plants were exposed to 550 μmol of photons m^{-2} s^{-1} at 8 °C for 2 days (16 light/8 h dark photoperiod); detached leaves were exposed to 800 μmol of photons m^{-2} s^{-1} at 8 °C for 14 h.

Isolation and Sample Preparation for Chloroplasts and Thylakoids. Chloroplasts and stacked thylakoid membranes were isolated from leaves as previously described.[42] To achieve the maximal de-epoxidation state, thylakoids isolated from dark-adapted leaves were incubated in 0.33 M sorbitol, 1 mM EDTA, 30 mM Hepes, 20 mM MES, and 40 mM ascorbate (pH 5.5) at 23 °C for 45 min.[43] Membranes corresponding to 750 μg of Chls were solubilized in 1% β-DM and then fractionated by ultracentrifugation in a 0.1 to 1 M sucrose gradient (40000 rpm, 22 h) to purify the PSI−LHCI complexes.[44] Once PSI−LHCI bands had been harvested, complexes were further purified by dilution in 5 mM Tricine (pH 7.8) and ultracentrifugation (70000 rpm, 3 h). Sodium dodecyl sulfate−polyacrylamide gel electrophoresis (SDS−PAGE) analysis was performed using the Tris-Glycine buffer system.[45] PSI core and LHCI moieties were dissociated through a further solubilization with 1% β-DM and 0.5% zwittergent.[46]

Pigment Analyses. Pigments were extracted from either leaves or complexes with 80% acetone, then separated, and quantified by HPLC.[47]

Spectroscopy. Steady-state spectra were recorded using samples in 10 mM Hepes (pH 7.5), 0.06% $\alpha(\beta)$-DM, and 0.2 M sucrose. Absorption measurements were performed using an SLM-Aminco DW-2000 spectrophotometer at room temperature (RT). Fluorescence emission spectra were recorded at RT using a Jobin-Yvon Fluoromax-3 spectrofluorometer. *In vivo* P700 absorption changes were sampled by weak monochromatic flashes (10 nm bandwidth, 705 nm) provided by LEDs (JTS10, Bio-Logic Science Instruments).

ROS Production. ROS production was measured on purified complexes using the Singlet Oxygen Sensor Green (SOSG), a fluorescent probe highly selective for $^1O_2$ that increases the intensity of its 530 nm emission band in the presence of this ROS.[48,49] Isolated complexes were illuminated with red light (600 nm < λ < 750 nm, 1600 μmol of photons m^{-2} s^{-1}, 10 °C), and the fluorescence yield of SOSG was

DOI: 10.1021/acs.biochem.6b00425
Biochemistry 2016, 55, 3636−3649

determined before and during light treatment, to quantify the $^1O_2$-dependent fluorescence increase.

Photobleaching Assay. The photobleaching kinetics of pigment−protein complexes were measured as described previously,[50] using actinic light intensities of 6500 μmol of photons m^{-2} s^{-1}; samples were cooled at 10 °C. The initial and maximal absorbance were set, so the same absorbance area (corresponding to ∼5 μg of Chls/mL) was used in the wavelength range of actinic light (600 nm < λ < 750 nm).

Determination of the Sensitivity to Photooxidative Stress. The decay kinetics of the maximal photochemical quantum yield of PSII (F_v/F_m)[51] and the maximal content of photooxidizable P700 (ΔA_{max} at 705 nm)[52] were recorded on leaves during EL treatment to assess the inhibition of PSII and PSI, respectively. ΔA_{max} was recorded during far-red light illumination (2500 μmol of photons m^{-2} s^{-1}; λ_{max} = 720 nm). To precisely evaluate the extent of PSI photoinhibition, leaves were vacuum infiltrated with 50 mM dibromothymoquinone and 1 mM methyl viologen upon EL, a treatment that restores the maximal oxidation level of P700.[32]

Measurement of Electron Transport in PSI Using Artificial Donors. Linear electron transport from artificial donor $TMPDH_2$ (*N,N,N,N*-tetramethyl-*p*-phenylenediamine, reduced form, 250 mM) to $NADP^+$ was measured in a dual-wavelength spectrophotometer (Unicam AA, Thermo scientific) under conditions of red light illumination (150 μmol of photons m^{-2} s^{-1}, RT) as described in ref 42. Thylakoids (15 μg of Chl/mL) were continuously stirred during illumination.

Fluorescence-Detected Magnetic Resonance. For all these experiments, the samples were dissolved in a buffer to a final concentration of 100 μg of Chl/mL. Degassed glycerol was added [60% (v/v)] just before the samples were frozen in a precooled cryostat at 40 K. All experiments were performed at 1.8 K. At this temperature, spin−lattice relaxation is inhibited and the FDMR signals reach maximal intensity. FDMR experiments were performed in a specific apparatus, details of which are described in refs 53−55. All spectra are presented as $\Delta F/F$ versus microwave frequency, where ΔF is the fluorescence change induced by the resonant microwave field and F is the steady-state fluorescence detected by the photodiode at the selected wavelength.

■ RESULTS

β-Carotene Depletion Enhances Photosensitivity under EL and Chilling Conditions. Because of a point mutation in the lycopene β-cyclase gene,[40] *szl1* plants have a lower carotene content and altered xanthophyll composition compared to those of WT plants when grown under low-light conditions (100 μmol of photons m^{-2} s^{-1}, 8 h light, 23 °C/16 h dark, 20 °C), while the *npq1* mutation[41] impairs only the plant's capacity to accumulate Zea without further affecting its carotene/xanthophyll ratio (Figure 1 and Table 1).

Pigment composition in plants both dark-adapted (a condition under which Vio accumulates in WT leaves) and transferred for 60 min to EL (1000 μmol of photons m^{-2} s^{-1}, to maximize de-epoxidation of Vio into Zea) was analyzed via HPLC on acetone extracts. Chl *a*/*b* ratios were essentially the same in the WT, *szl1*, *npq1*, and *szl1 npq1* genotypes, whereas the Chl/Car ratios were significantly reduced in *szl1*; because Chl content is not affected by the mutation of lycopene β-cyclase,[34] it means that the total Car content is slightly increased (∼10%) in the *szl1* genetic background. The 65% reduction in β-Car content in *szl1* and *szl1 npq1* versus WT

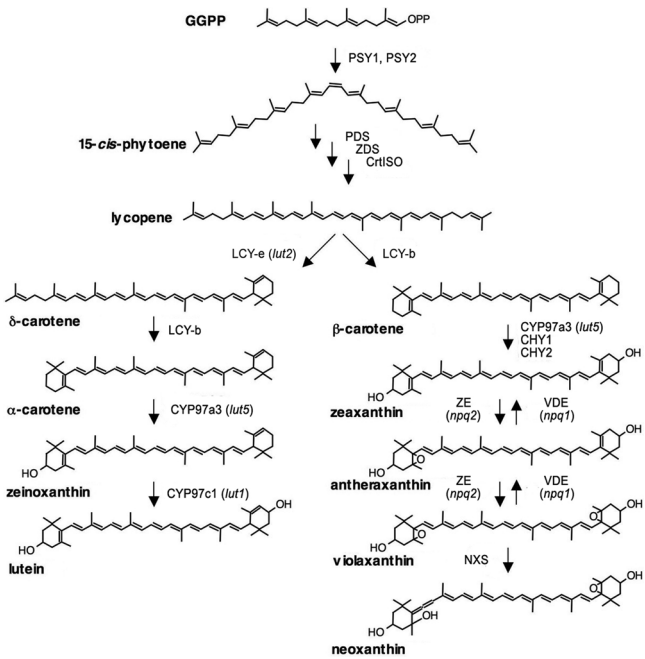

Figure 1. Biosynthetic pathway of carotenoids in *A. thaliana*, showing the enzymes controlling each step: lycopene β-cyclase (LCY-b), lycopene ε-cyclase (LCY-e), β-carotene hydroxylase (CYP97A3), ε−β-carotene hydroxylase (CYP97C1), β-carotene hydroxylase 1 and 2 (CHY1 and CHY2, respectively), Zea epoxidase (ZEP), Vio deepoxidase (VDE), and neoxanthin synthase (NXS). The names of *Arabidopsis* knockout mutants are given in brackets.

leaves (Table 1) was consistent with a previous report.[40] Moreover, both *szl1* genotypes showed an accumulation of the lutein precursor α-carotene (10 times that found in WT plants), a smaller amount of β,β-xanthophylls (Vio, Zea, and neoxanthin), and higher levels of lutein (ε,β-xanthophyll), and hence a $\beta,\beta/\varepsilon,\beta$ xanthophyll ratio far lower than that of the WT. When plants were exposed to EL, the level of accumulation of Zea was lower in *szl1* than in the WT [−78% (Table 1)]. The aim of this work was to address the photoprotective function of carotenoid molecules bound to PSI. Previous characterizations of Car biosynthesis mutants[49,56] revealed that changes in the xanthophyll composition of LHC did affect photoprotection. It is worth noting that *szl1* plants, besides having a lower carotene content, also have a $\beta,\beta/\varepsilon,\beta$ xanthophyll ratio lower than that of the WT, so it is necessary to distinguish the consequences of β-Car depletion from those of the increased relative amount of lutein versus β,β-xanthophylls in the antenna moiety of the PSI. For this reason, we included *chy1 chy2* and *lut5* genotypes in this characterization, which were used as controls: the *chy1 chy2* mutation affects the efficiency of conversion of β-Car into Vio, thus yielding the same $\beta,\beta/\varepsilon,\beta$ xanthophyll ratio seen for *szl1* plants (Figure 1 and Table 1). The *lut5* mutant was included as a control for α-carotene accumulation: the latter compound competes for the β-Car-binding sites,[49] but because it accumulates in both *szl1* and *lut5* (Table 1), it is possible to trace back their different contributions to photoprotection efficiency. The *chy1 chy2* and *lut5* genotypes had Chl *a*/*b* and Chl/Car ratios similar to those of WT plants, while the xanthophyll versus carotene content was significantly lower in both genotypes than in the WT (Table 1).

Conditions of EL cause photooxidative stress in plants, the severity of which is enhanced by low temperatures, due to a

DOI: 10.1021/acs.biochem.6b00425
Biochemistry 2016, 55, 3636−3649

Table 1. Photosynthetic Pigment Content of Wild-Type and Mutant Plants[a]

	genotype	Chl *a*/*b*	Chl/Car	mol of pigment/100 mol of Chl							
				neoxanthin	violaxanthin	antheraxanthin	zeaxanthin	lutein	α-carotene	β-carotene	$\beta_1\beta/\varepsilon_1\beta$ xanthophyll ratio
dark-adapted	WT	3.2 ± 0.1 a	3.7 ± 0.3 a	4.6 ± 0.6 a	2.9 ± 0.3 a	–	–	13.1 ± 0.7 a	0.1 ± 0.1 a	6.6 ± 0.7 a,c	0.6 ± 0.1 a
	npq1	3.2 ± 0.1 a	3.5 ± 0.2 a,b	4.8 ± 0.1 a	3.1 ± 0.2 a	–	–	14.7 ± 1.8 a	0.1 ± 0.1 a	6.2 ± 0.1 a	0.5 ± 0.1 a
	szl1	3.1 ± 0.1 a	3.3 ± 0.1 b	1.6 ± 0.4 b	0.8 ± 0.1 b	–	–	25.0 ± 1.4 b	1.1 ± 0.3 b	2.3 ± 0.1 b	0.1 ± 0.1 b
	szl1 npq1	3.4 ± 0.2 a	3.3 ± 0.3 b	1.8 ± 0.2 b	0.8 ± 0.1 b	–	–	24.4 ± 2.7 b	1.3 ± 0.2 b	2.3 ± 0.5 b	0.1 ± 0.1 b
	chy1 chy2	3.1 ± 0.1 a	3.9 ± 0.3 a	1.4 ± 0.1 b	0.7 ± 0.1 b	–	–	16.1 ± 1.1 a	0.1 ± 0.1 a	7.3 ± 0.6 c	0.1 ± 0.1 b
	lut5	3.1 ± 0.1 a	4.1 ± 0.2 a	3.4 ± 0.6 c	1.5 ± 0.1 c	–	–	11.2 ± 0.5 c	5.4 ± 0.2 c	2.6 ± 0.2 b	0.5 ± 0.1 a
HL	WT	3.1 ± 0.1 a	3.8 ± 0.1 a	4.7 ± 0.1 a	1.3 ± 0.1 a	0.2 ± 0.1 a	1.4 ± 0.1 a	12.3 ± 0.1 a	0.1 ± 0.1 a	6.1 ± 0.1 a	0.6 ± 0.1 a
	npq1	3.1 ± 0.1 a	3.5 ± 0.1 a,b	5.1 ± 0.4 a	2.7 ± 0.1 b	–	–	14.4 ± 0.4 b	0.2 ± 0.1 a	6.0 ± 0.1 a	0.5 ± 0.1 a
	szl1	3.0 ± 0.1 a	3.4 ± 0.1 b	1.7 ± 0.1 b	0.3 ± 0.1 c	0.1 ± 0.1 a	0.3 ± 0.1 b	22.7 ± 0.3 c	1.1 ± 0.1 b	3.1 ± 0.4 b	0.1 ± 0.1 b
	szl1 npq1	3.0 ± 0.1 a	3.4 ± 0.1 b	1.6 ± 0.1 b	0.7 ± 0.1 d	–	–	21.7 ± 0.3 c	1.2 ± 0.1 b	3.1 ± 0.1 b	0.1 ± 0.1 b
	chy1 chy2	3.0 ± 0.1 a	3.9 ± 0.1 a	1.5 ± 0.1 b	0.5 ± 0.1 c,d	0.1 ± 0.1 a	0.4 ± 0.1 b	15.8 ± 0.1 b	0.3 ± 0.1 a	7.3 ± 0.1 c	0.2 ± 0.1 b
	lut5	3.2 ± 0.1 a	3.9 ± 0.1 a	3.4 ± 0.6 c	1.0 ± 0.1 a	0.1 ± 0.1 a	0.6 ± 0.1 b	11.3 ± 0.3 c	6.2 ± 1.1 c	3.2 ± 0.1 b	0.5 ± 0.1 a

[a]Pigment content was determined before (dark-adapted) and after (HL) the leaves were exposed to 1000 μmol of photons m^{-2} s^{-1} for 30 min. Data are normalized to 100 Chl *a* + *b* molecules and are expressed as means ± SD (n = 3). Values within a given column and in a certain light regime that are marked with the same letters do not differ significantly (Student's *t* test; $P < 0.05$).

greater level of release of $^1O_2$ and the inhibition of scavenging enzymes.[32,57] To analyze the effect of missing Cars on the sensitivity to EL and to determine the primary target of photooxidation, the kinetics of both PSII and PSI photoinhibition were determined (Figure 2). WT and mutant plants were transferred from the control growth conditions to EL with cold stress (550 μmol og photons m^{-2} s^{-1}, 8 °C), and the maximal photochemical yield of PSII (F_v/F_m) was monitored for 30 h. F_v/F_m in WT plants gradually decreased from 0.8 to 0.4 during this interval (half-time for PSII photoinhibition of ∼30 h). The *szl1* plants were more photosensitive than the WT, because their F_v/F_m decreased to 0.16 at the end of the treatment, corresponding to a half-time for PSII photoinhibition of approximately 8 h (Figure 2A). F_v/F_m decay was the same in *chy1chy2* and *lut5* plants and followed a pattern that was roughly between those of WT and *szl1* plants (Figure 2B). Interestingly, the half-time of PSII photoinhibition was significantly shorter for *npq1* versus WT and for *szl1 npq1* versus *szl1* (Figure 2A), thus confirming a role for Zea in PSII photoprotection.[18]

The kinetics of PSI photoinhibition were assessed by quantifying the maximal content of photooxidizable P700 upon exposure of the plants to EL at chilling temperature. These stressing conditions had a much more dramatic effect on the photoinhibition of PSI than on that of PSII, with the photooxidizable P700 of the WT *Arabidopsis* plants gradually decreasing to 50% of its initial value in approximately 4.5 h (Figure 2C). The half-time for photoinhibition was the same as that of WT in *npq1* and *chy1 chy2*, shorter for *lut5* [being 50% inhibited in ∼2 h (Figure 2D)], and far shorter in *szl1* plants (approximately 0.8 h), thus confirming the great increase in photosensitivity caused by β-Car depletion.[34] To investigate the function of Zea in PSI photoprotection, we analyzed mutants lacking the ability to synthesize Zea (*npq1*) in a WT or *szl1* genetic background. The *npq1* mutation did not appear to affect in a significant manner PSI photoinhibition in either *npq1* or *szl1 npq1* (Figure 2C). These findings imply that, although Zea depletion impairs PSII photoprotection (Figure 2A), its role in limiting PSI photoinhibition is less important under the tested conditions.

Photobleaching Rate and $^1O_2$ Production in Purified PSI−LHCI Complexes. The results described above suggest a key role for β-Car in protecting the PSI−LHCI complex by photoinactivation, whereas a lack of Zea has a greater impact on the photoinhibition rate of PSII than on that of PSI.

Previous investigations show that under EL conditions, xanthophyll exchange occurs in the inner L2 site of LHCI,[38] and recent crystallographic data reveal that each LHCI subunit binds one β-Car molecule.[37] To shed more light on the functional role of these ligands, we measured the photosensitivity of isolated PSI−LHCI complexes. To prevent any damage to the complexes by the EL treatment targeted at Zea accumulation, thylakoids isolated from dark-adapted leaves were de-epoxidated in the dark by incubating them at pH 5.2, a treatment that pushes the de-epoxidation index over 50%. Subsequently, PSI−LHCI complexes were purified by sucrose gradient ultracentrifugation (Figure S1) and further characterized (Figure S2): photooxidizable P700 content (Figure S2A) and $NADP^+$ photoreduction rate (Figure S2B) were the same in all samples; SDS−PAGE analysis revealed no major difference in polypeptide composition between mutant and WT complexes (Figure S2C), and moreover, spectral deconvolution analysis of the Q_y absorption band into spectral forms of Chl

DOI: 10.1021/acs.biochem.6b00425
Biochemistry 2016, 55, 3636−3649

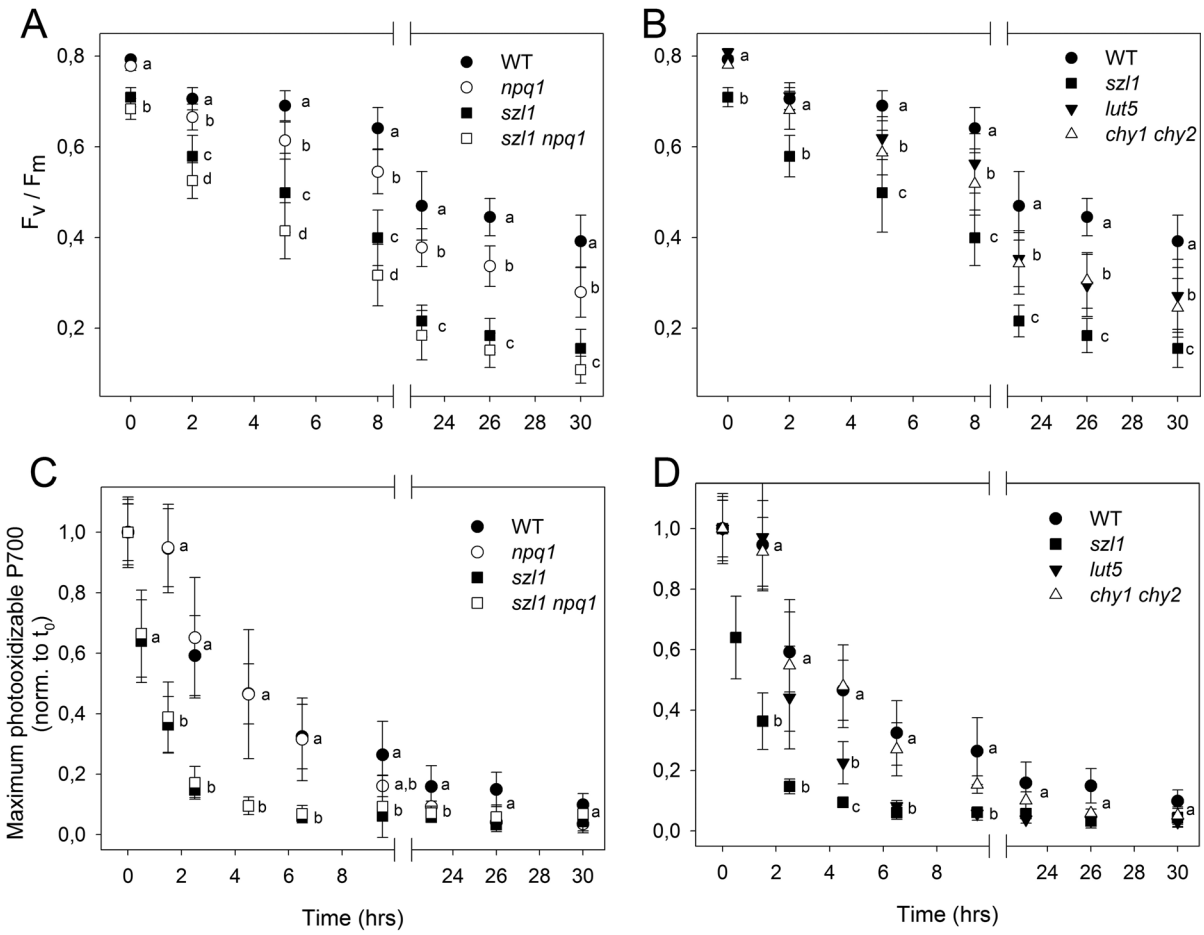

Figure 2. Photooxidation in wild-type and mutant *Arabidopsis* exposed to high light intensity at chilling temperatures. (A and B) F_v/F_m decay kinetics (PSII photoinhibition) was monitored in WT and mutant plants, exposed to 550 μmol of photons m^{-2} s^{-1} at 8 °C for 30 h with a 6 h period of dark between the 12 h of EL stress. (C and D) Decay kinetics of maximal photooxidizable P700 (PSI photoinhibition) were measured on leaves exposed to 500 μmol of photons m^{-2} s^{-1} at 8 °C for 30 h. Data are expressed as means ± SD ($n > 6$). t_0 indicates time zero. Values marked with the same letters are not significantly different from each other at the given time point (Student's *t* test; $P < 0.05$).

did not show any changes in the pigment organization (Figure S2D). Overall, these data confirm that the introduced mutation did not cause any structural or functional destabilization of the PSI−LHCI complexes in plants grown in low light.

The pigment composition of the complexes was determined by HPLC (Table 2). The Chl/Car ratio was essentially the same in WT, *npq1*, *chy1chy2*, and *lut5* genotypes but higher in *szl1* and *szl1 npq1* because of their lower carotene content (−23%). The relative abundance of *ε*,*β*- and *β*,*β*-xanthophylls was similar in the PSI−LHCI complexes from WT, *npq1*, and *lut5* plants, whereas complexes isolated from *szl1*, *szl1 npq1*, and *chy1 chy2* plants had much lower levels of *β*,*β*-xanthophylls and displayed a compensatory increase in the level of Lut. Only the complexes from WT and *lut5* plants showed signs of Vio−Zea exchange, while PSI−LHCI complexes from *chy1 chy2* and *szl1* plants did not bind any detectable level of Zea.

The hypothesis that the lack of either *β*-Car or Zea might prevent the activation of photoprotective mechanisms localized within the PSI−LHCI complex, thus enhancing ROS production, was further investigated by measuring photobleaching rates on purified complexes. Strong illumination of Chl proteins induces the formation of ^{3}Chl*, which in turn leads to $^1O_2$ release and Chl bleaching with kinetics that are inversely dependent on the efficiency of ^{3}Chl* quenching by bound Car. The results are illustrated in Figure 3. The greatest levels of resistance were found in WT complexes binding Zea and a full complement of *β*-Car molecules, while the PSI−LHCI complex from *npq1* plants was slightly more prone to photobleaching (Figure 3A). Mutations *lut5* and *chy1 chy2* did not affect the photosensitivity of complexes (Figure 3B). On the other hand, the *szl1* complex was far more sensitive to photobleaching than that from the WT, thus suggesting a major role for *β*-Car in photoprotecting PSI, presumably by limiting $^1O_2$ release.

We further compared the photoprotection capacity of the PSI−LHCI complexes by analyzing the amount of $^1O_2$ released. The $^1O_2$ yield was measured upon illumination of the complexes in the presence of fluorescent dye SOSG (see Materials and Methods for details), and the results are shown in Figure 4. *β*-Car depletion in *szl1* complexes significantly increases the amount of $^1O_2$ produced under EL conditions (Figure 4A). On the other hand, a lack of Zea (*npq1*), an altered xanthophyll/carotene ratio (*chy1 chy2*), or larger amounts of *α*-carotene (*lut5*) did not significantly enhance the yield of $^1O_2$ from the PSI−LHCI complexes (Figure 4B). These results suggest that the PSI−LHCI complexes binding a full complement of *β*-Car have a far stronger capacity for photoprotection than those lacking carotenes. No similar effect was observed in Zea-binding complexes; i.e., there was no

DOI: 10.1021/acs.biochem.6b00425
Biochemistry 2016, 55, 3636−3649

Table 2. Pigment Composition of PSI–LHCI Complexes Purified from the Various Genotypes[a]

genotype	Chl *a*/*b*	Chl/Car	mol of pigment/155 mol of Chl[37]								
			neoxanthin	violaxanthin	antheraxanthin	zeaxanthin	lutein	α-carotene	β-carotene	$\beta_N\beta/\varepsilon_N\beta$ xanthophyll ratio
WT	12.1 ± 0.2 a	4.6 ± 0.2 a	–	2.7 ± 0.1 a	–	1.7 ± 0.1 a	6.8 ± 0.1 a	–	22.6 ± 0.2 a	0.7 ± 0.1 a
npq1	11.7 ± 0.3 a	4.6 ± 0.1 a	–	4.5 ± 0.1 b	–	–	7.0 ± 0.1 a	–	22.2 ± 0.6 a	0.7 ± 0.1 a
szl1	12.2 ± 0.5 a	5.3 ± 0.2 b	–	0.7 ± 0.1 c,d	–	–	10.9 ± 0.4 b	2.4 ± 0.1 a	15.0 ± 0.6 b	0.1 ± 0.1 b
szl1 npq1	11.8 ± 0.3 a	5.3 ± 0.1 b	–	0.9 ± 0.1 c	–	–	10.7 ± 0.3 b	2.5 ± 0.1 a	15.2 ± 0.5 b	0.1 ± 0.1 b
chy1 chy2	7.6 ± 0.1 b	4.8 ± 0.1 a	–	0.6 ± 0.1 d	–	–	8.7 ± 0.1 c	–	23.2 ± 0.2 c	0.1 ± 0.1 b
lut5	8.9 ± 0.1 c	5.0 ± 0.2 a	–	1.9 ± 0.1 e	–	1.1 ± 0.1 b	6.1 ± 0.1 d	11.6 ± 0.1 b	10.3 ± 0.1 d	0.5 ± 0.1 a

[a]To maximize the accumulation of Zea, these complexes were purified from thylakoids that were de-epoxidized *in vitro*. See Materials and Methods for purification details. Data are normalized to 155 Chl *a* + *b* molecules (Chls bound to one PSI–LHCI complex) and are expressed as means ± SD ($n = 3$). Values within a given column that are marked with the same letter do not differ significantly (Student's *t* test; $P < 0.05$).

significant difference in the $^1O_2$ yield based on the Vio versus Zea content of PSI (Figure 4A).

Investigations of Chlorophyll to Carotenoid Triplet Transfer. The reason behind the greater rate of release of $^1O_2$ caused by β-Car depletion could be the lower efficiency of ^{3}Chl* quenching by the remaining Cars. To investigate this hypothesis, we assessed the ^{3}Chl* yield in plants lacking either β-Car or Zea by using FDMR. This is a double-resonance technique by which a triplet population is generated under conditions of steady-state illumination, and then a resonant electromagnetic field applied between a couple of spin sublevels of the triplet state induces a change in the steady-state triplet population itself, caused by anisotropy decay and population rates of the three spin sublevels. This event is detected as a corresponding change in the fluorescence emission of the system.[58,59] The samples were directly frozen by being placed in a precooled sample chamber; hence, the spectra obtained are representative of the conformational distribution present at RT. Moreover, thylakoids isolated from WT and mutant dark-adapted leaves were de-epoxidated in the dark by incubation at pH 5.2 to maximize Zea accumulation while avoiding any damage to the complexes by EL, which could affect the triplet population.

The low-temperature emission spectrum of PSI–LHCI complexes purified from WT and mutant *Arabidopsis* plants displayed the typical Chl *a* fluorescence bands peaking at 735 nm due to the antenna pools of PSI (not shown). The FDMR signals of PSI–LHCI complexes from WT plants, detected at wavelengths ranging between 700 and 740 nm, hence in the microwave frequency range expected for ^{3}Chl*,[54,55] are shown in Figure S3A. These signals suggest a dependence on wavelength detection, revealing the presence of at least four different triplet populations. Two ^{3}Chl* components peak at short wavelengths (700 nm) and may be assigned to a Chl belonging to antenna proteins, while the other two, previously assigned to ^{3}P700,[60] peak at 720–740 nm. Figure S4 shows the reconstructed spectra, while the fitting parameters are reported in Table 1S.

The three FDMR transitions recorded at setup settings selective for ^{3}Car* are shown in Figure S3B. Not surprisingly, the $2|E|$ transitions are the most intense, as often observed for ^{3}Car*.[60] The $|D| + |E|$ transition, which is usually ~3 times the $|D| - |E|$ for ^{3}Car*, is here underestimated because of the reduced microwave power used in this region. The linearity of FDMR transitions indicates the presence of different components contributing to the signals, as previously observed in thylakoid FDMR spectra detected at long emission wavelengths where the PSI contribution predominates.[60]

The FDMR spectra of the PSI–LHCI complexes isolated from *npq1* leaves were identical to those of samples from de-epoxidated WT over the entire detection range explored, indicating that the ^{3}Chl* population does not change (Figure 5A). When FDMR measurements were performed on PSI–LHCI complexes isolated from de-epoxidated *szl1* leaves, a significant increase (2 times) in the intensity of the FDMR components assigned to the ^{3}Chl* states was observed (Figure 5B and Figures S4 and S5 and Table 2S for details). Interestingly, a decrease in the intensity of the FDMR signals of the ^{3}Car* states was also observed in the PSI–LHCI complex from *szl1* plants (Figure 5C,D). These findings are consistent with the greater photosensitivity displayed by the mutant *in vivo* (Figure 2C).

DOI: 10.1021/acs.biochem.6b00425
Biochemistry 2016, 55, 3636–3649

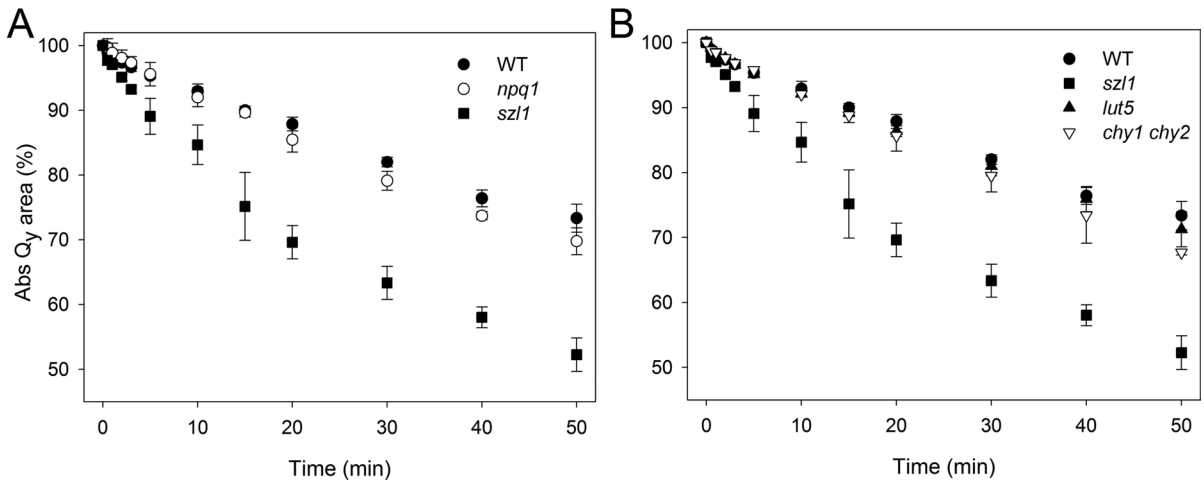

Figure 3. Photobleaching behavior of isolated PSI−LHCI complexes. (A) PSI−LHCI complexes isolated from de-epoxidized thylakoids of WT, *npq1*, and *szl1* plants were analyzed by monitoring the Q_y transition absorbance decay during a period of strong illumination, as described in Materials and Methods. Chl concentrations of complexes were set to 8 μg/mL. Samples were cooled to 10 °C during measurements. (B) Photobleaching kinetics of PSI−LHCI complexes from *lut5* and *chy1 chy2* thylakoids were compared with those of genotypes WT and *szl1*. Data are expressed as means ± SD ($n = 3$). At all time points, the complexes isolated from *szl1* were significantly more sensitive to photooxidation (Student's *t* test; $P < 0.05$) than the others.

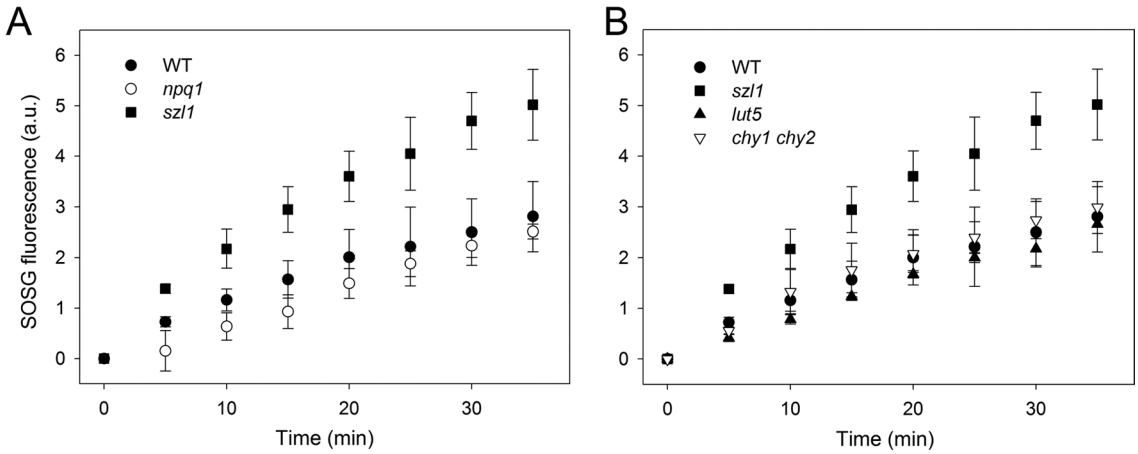

Figure 4. Production of singlet oxygen by PSI−LHCI complexes. (A) Kinetics of $^1O_2$ release was measured in PSI−LHCI complexes purified from de-epoxidated thylakoids of WT, *npq1*, and *szl1* plants. (B) Release of $^1O_2$ from *lut5* and *chy1 chy2* PSI−LHCI complexes was compared with that from the same complexes purified from WT and *szl1*. SOSG was used as an $^1O_2$-specific fluorogenic probe, because its fluorescence emission increases upon reaction with $^1O_2$ in solution. Symbols and error bars indicate means ± SD ($n = 3$). At all time points, the complexes isolated from *szl1* released significantly more $^1O_2$ (Student's *t* test; $P < 0.05$) than the others did.

$^1O_2$ Production in LHCI and PSI Core Complexes. The data presented so far indicate that β-Car makes a relevant contribution to protecting the PSI−LHCI complex from radiation damage *in vivo*. However, β-Car molecules are not uniformly distributed within the PSI−LHCI complex, because 85% of the total Car is bound to the core complex and only 15% to the antenna moiety.[37] To test the role of these subpopulations in photoprotection, we purified LHCI and PSI core particles from whole PSI−LHCI complexes of WT, *npq1*, and *szl1* plants (Figure S6) and analyzed the effect of either β-Car or Zea depletion on the $^1O_2$ yield under EL conditions.

Pigment composition analysis of these complexes (Table 3) revealed that the Chl/Car ratio was essentially the same in the LHCI from WT and *npq1*; it was however greater in *szl1* because of a lower carotene content (−20%, corresponding to ∼0.8 molecule of carotene per unit of LHCI); moreover, LHCI from *szl1* had Vio levels lower than and Lut levels higher than those of the *npq1* (−2.6 mol of Vio and +2.4 mol of Lut per unit of LHCI, respectively). These findings suggest that sites N1 (binding β-Car) are partially empty due to β-Car depletion, and that part of the missing Vio in sites L2 is replaced by Lut.[37] Only antenna complexes from WT bound a significant amount of Zea (de-epoxidation index of 24%, corresponding to ∼1 molecule of Zea per unit of LHCI). PSI core complexes from WT and *npq1* plants had the same pigment composition, whereas the corresponding *szl1* complex had a lower carotene content per unit of Chls (−18%, corresponding to ∼4 molecules of carotene per unit of PSI core).

The release of $^1O_2$ was monitored upon illumination of the complexes in the presence of the dye SOSG (Figure 6). β-Car depletion in the *szl1* PSI core significantly enhanced the amount of $^1O_2$ produced [+53% vs that of the WT complex (Figure 6A)], and the effect was even greater in LHCI from *szl1* [+65% (Figure 6B)]. Lack of Zea (*npq1*), on the other hand, did not significantly affect the $^1O_2$ yield of antenna complexes (Figure 6B).

DOI: 10.1021/acs.biochem.6b00425
Biochemistry 2016, 55, 3636−3649

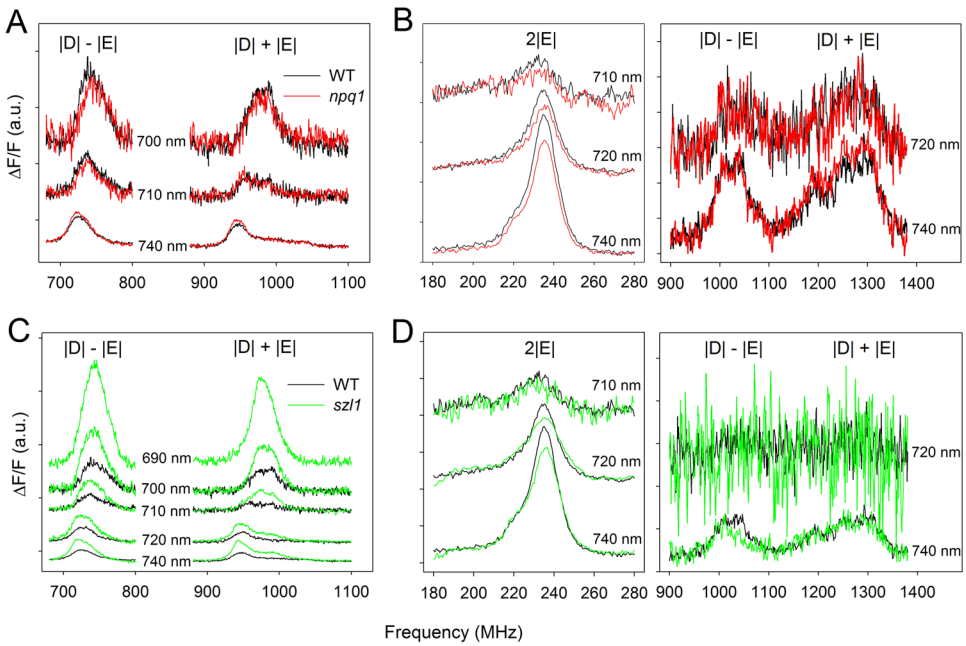

Figure 5. Fluorescence-detected magnetic resonance of the Chl and Car triplet states in purified PSI−LHCI complexes. FDMR signals of the ^{3}Chl* states (|*D*| − |*E*| and |*D*| + |*E*| transitions; panels A and B) and the ^{3}Car* states (2|*E*|, |*D*| − |*E*|, and |*D*| + |*E*| transitions; panels C and D) observed in the PSI−LHCI complex purified from high-light-treated leaves of WT (black), *npq1* (red), and *szl1* (green) plants. FDMR signals were detected at the various wavelengths indicated in each panel. Spectra were vertically shifted to simplify comparison. Amplitude modulation frequency of 33 Hz (^{3}Chl* states) or 325 Hz (^{3}Car* states), time constant of 600 ms, 20 scans, microwave power of 500 mW, temperature of 1.8 K.

Table 3. Pigment Composition of Lhca and PSI Core Complexes Purified from Thylakoids of WT, *npq1*, and *szl1*[a]

				mol of pigment/98 mol of Chl[37]					
sample	genotype	Chl *a*/*b*	Chl/Car	violaxanthin	zeaxanthin	lutein	*α*-carotene	*β*-carotene	*β*,*β*/*ε*,*β* xanthophyll ratio
PSI core	WT	–	5.5 ± 0.1 a	–	–	–	–	18.0 ± 0.4 a	–
	npq1	–	5.5 ± 0.1 a	–	–	–	–	17.9 ± 0.2 a	–
	szl1	–	6.7 ± 0.1 b	–	–	–	1.7 ± 0.1 a	13.0 ± 0.1 b	–
				mol of pigment/57 mol of Chl[37]					
sample	genotype	Chl *a*/*b*	Chl/Car	violaxanthin	zeaxanthin	lutein	*α*-carotene	*β*-carotene	*β*,*β*/*ε*,*β* xanthophyll ratio
Lhca	WT	3.8 ± 0.1 a	4.4 ± 0.1 a	2.5 ± 0.1 a	0.8 ± 0.1 a	5.6 ± 0.1 a	–	4.0 ± 0.1 a	0.6 ± 0.1 a
	npq1	3.9 ± 0.2 a	4.4 ± 0.1 a	3.2 ± 0.2 b	–	5.8 ± 0.2 a	–	4.0 ± 0.1 a	0.6 ± 0.1 a
	szl1	3.9 ± 0.1 a	4.8 ± 0.2 b	0.6 ± 0.1 c	–	8.2 ± 0.1 b	1.1 ± 0.1 a	2.1 ± 0.1 b	0.1 ± 0.1 b

[a]The complexes were purified from thylakoids de-epoxidized *in vitro*, to maximize the accumulation of Zea. See Materials and Methods for details of purification. Data are normalized to either 98 or 57 Chl molecules (Chls bound to one PSI core or LHCII, respectively) and are expressed as means ± SD (n = 3). Values within a given column that are marked with the same letter do not differ significantly (Student's t test; $P < 0.05$).

■ DISCUSSION

Binding of Zea to Lhcb proteins was observed to play a major role in enhancing photoprotection of PSII *in vivo* by modulating the yield of both the ^{1}Chl*[61,62] and ^{3}Chl* states.[28] The mechanism of Vio de-epoxidation has been described in LHCI,[38] but its importance in the photoprotection of PSI is not clear.[63] Moreover, recent results suggest that the xanthophyll and carotene composition are crucial for PSI stability.[64,65] The focus of this investigation was the relative contribution of carotene versus xanthophyll ligands of Photosystem I to its photoprotection. To this aim, mutants of *Arabidopsis* with altered carotenoid biosynthesis pathways were compared: *szl1*, containing fewer carotenes because of its reduced *β*-cyclase activity,[40] *npq1*, incapable of Zea accumulation,[41] and the double mutant *szl1 npq1*. Because carotenes are intermediate products of carotenoid biosynthesis (Figure 1), variations in carotene levels inevitably affect those of xanthophylls, which are downstream from this metabolic pathway. Moreover, the decrease in *β*-cyclase activity yields a larger amount of *α*-carotene, usually barely detectable in *A. thaliana*. Hence, genotypes *lut5* and *chy1 chy2* were included in the study and used as controls: a comparison with their photosynthetic phenotype helped determine whether photosensitivity could be ascribed to either changes in the xanthophyll/carotene ratio, which is very similar in *szl1* and *chy1 chy2*, or the presence of *α*-carotene, observed in both *szl1* and *lut5*.

Changes in Xanthophyll and Carotene Composition Have a Different Effect on the Photoprotection Capacity of PSII and PSI. Carotenoids mediate photoprotection through a number of mechanisms, which include quenching of ^{3}Chl*,[66,67] scavenging of ROS,[18,68] and quenching of ^{1}Chl*, which prevents ROS release.[69] The photosensitive phenotypes of *Arabidopsis* mutants with an altered xanthophyll composition[49,56,69] suggest that the relative abundance of these pigments is crucial for chloroplast photoprotection.

DOI: 10.1021/acs.biochem.6b00425
Biochemistry 2016, 55, 3636−3649

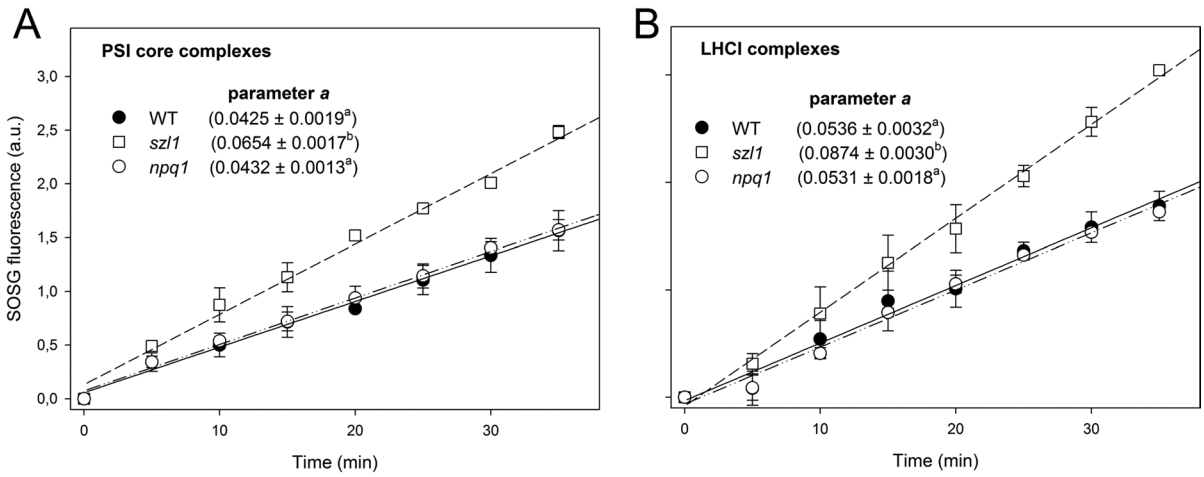

Figure 6. Production of singlet oxygen from the PSI core and LHCI complexes. Kinetics of $^1O_2$ release was measured on (B) PSI core and (C) LHCI complexes, purified from de-epoxidated PSI−LHCI complexes of WT, *npq1*, and *szl1* plants. SOSG was used as an $^1O_2$-specific fluorogenic probe. Symbols and error bars indicate means ± SD ($n = 3$). Each data set was fitted with a linear function $y = y_0 + ax$, and the kinetics of $^1O_2$ release was assessed in the various samples by comparing their parameter a, which describes the slope of the linear function. Values marked with the same letter are not significantly different (Student's t test).

The *npq1* mutant displayed a PSII photoinhibition rate significantly greater than that of WT plants (Figure 2A), which is consistent with the photoprotective role of Zea versus Vio in PSII.[18] *chy1 chy2* plants, whose $\beta,\beta/\varepsilon,\beta$ xanthophyll ratio is 6-fold lower than that of WT (Table 1) plants, are more prone to PSII photoinhibition (Figure 2B). Even *lut5* plants, containing smaller amounts of xanthophyll versus Chl than WT plants, possessed a greater PSII photosensitivity. This result is consistent with previous investigations, which reveal that optimal photoprotection of the PSII antennas occurs with balanced ^{3}Chl* quenching by Lut and ROS scavenging by β,β-xanthophylls.[49,70] *szl1* plants had the same $\beta,\beta/\varepsilon,\beta$ xanthophyll ratio as *chy1 chy2* plants and are able to synthesize Zea, even if to a lower extent than WT due to a limited Vio pool (Table 1); however, the F_v/F_m decrease was far greater than in *npq1* and *chy1 chy2* plants. These data indicate that (i) β-Car plays a role in PSII photoprotection, promoting the scavenging of $^1O_2$ produced by the PSII core,[30] and (ii) β-Car abundance had an additive effect on PSII photostability with respect to Zea accumulation and β,β-xanthophyll composition.

Interestingly, these changes in carotenoid composition affect PSI differently. HPLC analysis of the PSI−LHCI complex purified from either *chy1 chy2* or *szl1* revealed a similar xanthophyll composition, with a Vio decrease and an equivalent Lut increase (Table 2). Lut and Vio bind to sites L1 and L2, respectively, of each Lhca protein;[37] therefore, in *chy1 chy2* and *szl1*, a lack of Vio in site L2 is most likely compensated by the binding of additional Lut. Conversely, the binding of a xanthophyll in site N1, which is highly selective for β-Car, appears unlikely.

The P700 photoinhibition rate was essentially the same in WT, *npq1*, and *chy1 chy2* plants, whereas the *szl1* genotype revealed a greater degree of photodamage, losing all PSI activity in ∼4 h. Besides carotene depletion, a further feature of *szl1* plants is the presence of α-carotene in both PSI core and LHCI complexes, partially replacing β-Car (Table 3) and potentially being a cause of photosensitivity. However, *lut5* has an α/β-carotene ratio far greater than that of *szl1* (Tables 1 and 2), yet both the photobleaching kinetics and $^1O_2$ production in the PSI complexes isolated from this genotype did not differ significantly from those of WT plants (Figures 3 and 4), suggesting that α-carotene is not the main cause of photosensitivity.

These differences in photosensitivity did not arise from structural changes in the PSI−LHCI complex upon β-Car depletion. Both the maximal P700 and the PSI electron transport rate were identical to those in WT plants (Figure S3), indicating that the PSI of *szl1* plants is fully functional under the control lighting conditions. SDS−PAGE analysis revealed no major changes in either polypeptide composition or relative abundance of subunits in any complex (Figure S3), including the four Lhcas. Deconvolution analysis yielded a description of absorption spectra of all PSI−LHCI complexes with spectral forms very similar in terms of amplitude and λ_{max}. Overall, these data indicate that the greater photosensitivity of *szl1* is not a consequence of a pleiotropic, structural/functional destabilization of PSI−LHCI complexes.

Two conclusions can be drawn. The first is that the replacement of the majority of Vio with Lut within the LHCI system does not significantly affect PSI photosensitivity (Figures 2−4). Hence, PSI behaves differently compared to PSII: in the latter system, the binding of Lut as the only xanthophyll present renders LHCs unable to sustain $^1O_2$ scavenging and causes an extreme photosensitivity and rapid photobleaching of the LHC complexes.[49] The second observation is that while in PSII Lut content, Vio−Zea exchange and β-Car abundance have an additive effect on photoprotection, β-Car depletion is the main factor responsible for PSI phototolerance as shown by the extreme photosensitivity of P700 in *szl1* (Figure 2).

Zeaxanthin and PSI Photoprotection. Previous results indicated that Zea synthesis has multiple effects, such as enhancing energy dissipation[71,72] or scavenging ROS released by pigment-binding complexes.[23] Genetic dissection showed that the photoprotective effect of Zea depends on its binding to LHC proteins, which causes a downregulation of ^{3}Chl* yield in PSII.[28] Upon Vio−Zea exchange, a number of LHC undergo changes in their conformation,[73] which affect Chl−Chl/Chl−protein interactions and downregulate the probability of $^1O_2$ release. Although the molecular mechanism involved is still

DOI: 10.1021/acs.biochem.6b00425
Biochemistry 2016, 55, 3636−3649

unknown, the physiological effect on LHC is remarkable, resulting in an effective photoprotection of PSII.[28]

Xanthophyll exchange takes place in the L2 site of LHC, whose occupancy depends on the type of protein: Lut in trimeric LHCII and Vio in both monomeric Lhcb and LHCI.[37,74,75] With regard to the PSI−LHCI complex, *in vivo* studies reveal a stable binding of Zea upon EL treatment.[38] Previous results showed that, even in the absence of the xanthophyll cycle, PSI was resistant to chilling-induced photoinhibition,[63] while more recently, a Zea-dependent quenching action by ^{1}Chl* has been suggested to occur in LHCI.[76]

Our results indicate that, despite the high de-epoxidation level achieved in *Arabidopsis* thylakoids (Table 1), a small amount of Zea molecules (∼1 per unit of PSI−LHCI complex) was stably bound to the antenna moiety of the WT PSI−LHCI complex. This Zea pool was retained even after several purification steps and correlated to a corresponding decrease in the Vio content of the supercomplex (Table 3), thus supporting the idea of xanthophyll exchange rather than nonspecific binding.

In WT thylakoids, however, the binding of Zea to LHCI proteins is insufficient to alter the triplet-state properties of the complex (Figure 5A). This is unlike what was observed in PSII antennas, whose ^{3}Chl* yield is downregulated by Vio−Zea exchange[28] and correlates with a lower rate of $^1O_2$ evolution under EL conditions. Current FDMR data are consistent with the plants' photoprotection capacity *in vivo*: when plants were challenged with EL and cold stress, the level of P700 photoinhibition was no greater in *npq1* than in WT (Figure 2C), which suggests that Zea may not be crucial for PSI photoprotection, or at least not under the conditions tested. The same conclusion could be drawn from analyzing the purified PSI−LHCI complex (Figure 4) and LHCI (Figure 6), which gave the same $^1O_2$ yield, irrespective of the presence (WT sample) or absence (*npq1* sample) of bound Zea. The data also agree with the FDMR results, which show comparable triplet yields in de-epoxidated WT and *npq1* samples (Figure 5A).

We cannot exclude the possibility that the binding of Zea to the PSI−LHCI complex could be more pronounced in other plant species, under different stress conditions, or upon prolonged exposure to EL, thus becoming more important in PSI photoprotection. Alternatively, Zea bound to LHCI might be involved in the downregulation of ^{1}Chl*, as recently suggested by fluorescence decay kinetics of the PSI−LHCI supercomplex.[76]

No Zea was detected in the PSI−LHCI complex purified from *szl1* de-epoxidated thylakoids (Table 2), presumably because of the smaller xanthophyll cycle pigment pool size of the mutant, which limits the amount of Zea to $^1/_5$ of that present in WT plants (Table 1). *szl1* plants have a photosensitivity much greater than those of the WT and *npq1* genotypes both at whole plant (Figure 2) and isolated PSI−LHCI complex (Figures 3 and 4) levels. However, the effect of the *npq1* mutation in limiting PSI photoinhibition was not significant in the *szl1* genetic background (Figure 2C), suggesting that the lack of Zea is not the major cause of its strong photosensitivity.

β-Carotene and PSI Photoprotection. The PSI−LHCI complex of *szl1* plants has a carotene content lower than that of the corresponding WT complex: HPLC analyses (Table 3) reveal that approximately 20% of β-Car-binding sites in both the core complex and N1 sites are devoid of carotenes.[37] This greatly impairs the plant's photoprotection capacity, with PSI being far more affected than PSII.

In the PSII core complex, most β-Car molecules are in close contact with Chl, so that they can effectively quench ^{3}Chl*.[77] The exception is represented by the two β-Car ligands in the PSII reaction center, whose distance from the P680 special pair is too great to allow ^{3}P680* quenching.[29,30] PSII has been reported to be the primary target of EL stress,[5,78] because the D1 subunit is easily photo-oxidized and rapidly turned over. P700$^+$, on the other hand, has been observed to be an efficient quencher of excitation energy and, by removing excess reducing power, can protect PSI from photodamage.[32] However, charge recombination can give rise to ^{3}P700*, and its yield is increased under conditions of acceptor limitation.[79] Furthermore, PSI exposed to intense light generates ^{3}Car* mainly associated with LHCI,[60] and a selective bleaching of Lut bound to the peripheral antenna;[80] hence, the question of the role of carotene ligands arises.

While an efficient PSII repair machinery has been described,[5] no similar mechanism has been identified for PSI: after photooxidative damage, it takes several days to recover its functionality[32,81] because this process entails the degradation and resynthesis of the entire complex. Because its consequences are essentially irreversible, all efforts must be made to avoid PSI photoinhibition. There are a number of mechanisms ensuring effective photoprotection, which include activation of the stromal scavenging enzymes[31] and PGR5-dependent regulation of electron transfer.[33] In several plant species, including *Arabidopsis*, PSI photosensitivity is exacerbated at low temperatures, presumably because they slow these protective mechanisms and decrease the size of sink of reductants.[32] Under these conditions, hyper-reduction of the electron chain occurs, and the yield of both ^{3}P700* and $^1O_2$ increases; the iron−sulfur centers are the primary targets for PSI photo-oxidation by ROS.[82,83]

The results in Figure 2 show that our stressing conditions damaged PSI in the WT genotype, and the effect is even greater in *szl1* plants, as shown by its 4-fold faster PSI photoinhibition rate (Figure 2C). A plausible hypothesis regarding the molecular mechanism(s) behind the photosensitivity of PSI in *szl1* is that its carotene composition affects its photoprotection capacity. Unlike WT plants, *szl1* plants contain α-carotene in both PSI core and LHCI moieties of the mutant, partially replacing β-Car (Table 3). However, although the PSI−LHCI complex from the *lut5* genotype has an α-carotene content greater than that of the *szl1* genotype (Table 2), similar photobleaching rates (Figure 4B) and $^1O_2$ release (Figure 5B) were observed in PSI−LHCI complexes isolated from *lut5* and WT plants. These findings rule out the possibility that the main reason for PSI photosensitivity in *szl1* plants is the α-carotene present either in its core complex or in its LHCI.

Alternatively, PSI stability might be affected by the amount of carotene molecules available. Most β-Car molecules are coordinated by either different subunits or distant regions within PSI,[84] suggesting that these pigments may have a crucial role in preserving the structural integrity of PSI. In *szl1* plants, a weakened PSI−LHCI structure would make the complex more susceptible to ROS damage. However, electron transfer efficiency and Chl organization are comparable to those of the WT (Figure S2); moreover, harsh solubilization of whole complexes, aimed at promoting antenna detachment, gave the same migration rate of the different moieties on a sucrose

DOI: 10.1021/acs.biochem.6b00425
Biochemistry 2016, 55, 3636−3649

gradient, and similar LHCI detachment efficiency (Figure S6), thus suggesting that the PSI−LHCI complex from *szl1* plants is quite stable. The increased photosensitivity of the PSI core complex from *szl1* (Figure 6A) can therefore be ascribed to a lower carotene content, which leaves a portion of ^{3}Chl* unquenched.

Interestingly, LHCI complexes purified from *szl1* released amounts of $^1O_2$ greater than that released by the PSI core (Figure 6) despite a far lower *β*-Car depletion in LHCI versus the PSI core [9 and 22% increase in Chl/Car ratio, respectively (Table 3)], thus suggesting that binding of *β*-Car to PSI antennas is a key factor for PSI photoresistance. Recent investigations of the crystal structure of the PSI−LHCI complex confirm that each Lhca binds one *β*-Car at its N1 site.[37] Another report[85] reveals that preferential degradation of LHCI upon strong light treatment is effective in preserving P700 activity in isolated PSI−LHCI complexes. Because recovery from photoinhibition entails the degradation and resynthesis of the entire PSI complex, sacrificing the antennae might be a strategy for restricting photooxidative damage in the LHCI moiety, thus protecting Fe−S clusters. The role of LHCI as a safety fuse for PSI might be linked to the presence of red-absorbing forms of LHCI.[35,85,86] Given their low energy level, these "red Chls" concentrate the excitation energy before transferring it to the RC;[87] therefore, the probability of generating ^{3}Chl* is greater here than anywhere else within the PSI−LHCI complex. These triplet excited states are probably quenched by nearby Car, because the efficiency of the mechanism is impaired in LHCI isoforms devoid of red Chl.[35] However, it is unlikely that *β*-Car is involved in this process, because the cluster that includes red Chls is located too far from *β*-Car in site N1 for an efficient triplet transfer.[37] On the other hand, xanthophyll in site L2, located close to the Chls absorbing low-energy forms, presumably contributes to a much greater extent to the ^{3}Chl* quenching mechanism. At any rate, LHCI lacking fewer than one *β*-Car in sites N1 displays a ^{3}Chl* yield and an $^1O_2$ release greater than those of the corresponding WT complex. Moreover, FDMR analyses reveal that the ^{3}Chl* populations assigned to the antenna components are larger in the *szl1* PSI−LHCI complex than in WT ones. A comparison with the FDMR signals of isolated Lhca4 found in the literature[35] suggests that the increase we observed in the PSI−LHCI complex affects at least in part the ^{3}Chl* population of LHCI (Figure S5B). These findings highlight another striking difference between the LHCI and LHCII complexes: *β*-Car molecules in the N1 site of LHCI actively participate in ^{3}Chl* quenching, unlike the xanthophyll in site N1 of LHCII, which does not directly contribute to this process; the latter compound, however, has been reported to act as a barrier, limiting the access of O_2 to the inner domain of the LHCII and thereby contributing to its photostability.[67]

At the same time, the decrease in the carotenoid triplet states detected would also appear to be linked to certain ^{3}Car* components (Figure S5A) previously found in Lhca4.[35]

■ CONCLUSIONS

szl1 plants have a less active *β*-cyclase,[40] and consequently, their PSI−LHCI complex has a carotene content lower than that of the corresponding WT complex and their LHCI moiety an altered xanthophyll composition. In *npq1* plants, which have no functional Vio de-epoxidase, Zea formation is impaired. When challenged with EL and cold stress, the *szl1* genotype displayed PSI photoinhibition more severe than that of the WT plants, and a comparative analysis with the *chy1 chy2* and *lut5* mutants identified carotene depletion in both the PSI core and LHCI complexes as the major source of photodamage. On the other hand, the binding of Zea to the LHCI was far less important. The high levels of $^1O_2$ release in the LHCI complexes from *szl1* (Figure 6) and the presence of larger amounts of ^{3}Chl*, detected by FDMR (Figure 5), suggest that PSI antennas too, like LHCII, constitutively experience ^{3}Chl* formation and that carotenoid species bound to LHCI play a key role in ^{3}Chl* quenching. Consequently, it appears that regulation of the PSI Chl excited states under EL conditions is crucial for the effective protection of the photosynthetic apparatus.

■ ASSOCIATED CONTENT

Supporting Information

The Supporting Information is available free of charge on the ACS Publications website at DOI: 10.1021/acs.biochem.6b00425.

Purification of PSI−LHCI complexes (Figure S1), characterization of PSI−LHCI complexes purified from WT and mutant genotypes (Figure S2), fluorescence-detected magnetic resonance of the chlorophyll and carotenoid triplet states on PSI−LHCI complexes isolated from dark-adapted, WT plants (Figure S3), reconstruction of the FDMR spectra of the ^{3}Chl* states on purified PSI−LHCI complexes, with Gaussian components (Figure S4), fluorescence-detected magnetic resonance of ^{3}Car* and ^{3}Chl* on purified PSI−LHCI complexes (Figure S5), purification of PSI core and LHCI complexes (Figure S6), parameters of the Global Gaussian Deconvolution of ^{3}Chl* states on purified PSI−LHCI complexes, with Gaussians components (Table 1S), and amplitude of the Gaussian components of ^{3}Chl* states used in the reconstruction of the FDMR spectra on purified PSI−LHCI complexes at different wavelengths (Table 2S) (PDF)

■ AUTHOR INFORMATION

Corresponding Author

*Dipartimento di Biotecnologie, Università di Verona, Strada Le Grazie 15, 37134 Verona, Italy. E-mail: luca.dallosto@univr.it. Phone: +39 045 8027806. Fax: +39 045 8027929.

Author Contributions

S.C. and M.B. contributed equally to this work. S.C. and M.B. were involved in the photooxidative treatments of plants, measurements of stress-related factors, the purification of pigment−protein complexes, measurements of ROS production and photobleaching kinetics, and data analysis. A.A. and D.C. conducted FDMR analysis. L.D. conceived the study, took part in its design and coordination, and drafted the manuscript.

Funding

This work was supported by MIUR (PRIN2010−2011 prot. 2010FM38P_004).

Notes

The authors declare no competing financial interest.

■ ACKNOWLEDGMENTS

L.D. is grateful to Prof. K. K. Niyogi for his kind gift of the *szl1* and *szl1 npq1* genotypes.

■ ABBREVIATIONS

Chl, chlorophylls; Car, carotenoids; Crt, carotenes; EL, excess light; FDMR, fluorescence-detected magnetic resonance; LHCI and LHCII, Photosystem I and II light-harvesting systems, respectively; Lhca and Lhcb, Photosystem I and II light-harvesting complexes, respectively; LL, low light; PS, Photosystem; P680 and P700, PSII and PSI reaction centers, respectively; ROS, reactive oxygen species; RT, room temperature; SD, standard deviation; SOSG, singlet oxygen sensor green; Vio, violaxanthin; Xan, xanthophylls; WT, wild type; Zea, zeaxanthin; β-Car, β-carotene; ^{1}Chl* and ^{3}Chl*, singlet and triplet excited states of chlorophyll, respectively; $^1O_2$, singlet oxygen.

■ REFERENCES

(1) Nelson, N., and Ben Shem, A. (2004) The complex architecture of oxygenic photosynthesis. *Nat. Rev. Mol. Cell Biol. 5*, 1−12.

(2) Croce, R., and Van Amerongen, H. (2013) Light-harvesting in photosystem I. *Photosynth. Res. 116*, 153−166.

(3) Van Amerongen, H., and Croce, R. (2013) Light-harvesting in photosystem II. *Photosynth. Res. 116*, 251−263.

(4) Nelson, N., and Junge, W. (2015) Structure and Energy Transfer in Photosystems of Oxygenic Photosynthesis. *Annu. Rev. Biochem. 84*, 659−683.

(5) Aro, E.-M., Virgin, I., and Andersson, B. (1993) Photoinhibition of Photosystem II - inactivation, protein damage and turnover. *Biochim. Biophys. Acta, Bioenerg. 1143*, 113−134.

(6) Long, S. P., Humphries, S., and Falkowski, P. G. (1994) Photoinhibition of photosynthesis in nature. *Annu. Rev. Plant Physiol. Plant Mol. Biol. 45*, 633−662.

(7) Krieger-Liszkay, A. (2004) Singlet oxygen production in photosynthesis. *J. Exp. Bot. 56*, 337−346.

(8) Anderson, J. M., Park, Y. I., and Chow, W. S. (1997) Photoinactivation and photoprotection of photosystem II in nature. *Physiol. Plant. 100*, 214−223.

(9) Frank, H. A., and Cogdell, R. J. (1996) Carotenoids in photosynthesis. *Photochem. Photobiol. 63*, 257−264.

(10) Amunts, A., Toporik, H., Borovikova, A., and Nelson, N. (2010) Structure Determination and Improved Model of Plant Photosystem I. *J. Biol. Chem. 285*, 3478−3486.

(11) Umena, Y., Kawakami, K., Shen, J. R., and Kamiya, N. (2011) Crystal structure of oxygen-evolving photosystem II at a resolution of 1.9 A. *Nature 473*, 55−60.

(12) Mazor, Y., Borovikova, A., and Nelson, N. (2015) The structure of plant photosystem I super-complex at 2.8 Å resolution. *eLife 4*, e07433.

(13) Pan, X., Liu, Z., Li, M., and Chang, W. (2013) Architecture and function of plant light-harvesting complexes II. *Curr. Opin. Struct. Biol. 23*, 515−525.

(14) Ruban, A. V., Johnson, M. P., and Duffy, C. D. (2012) The photoprotective molecular switch in the photosystem II antenna. *Biochim. Biophys. Acta, Bioenerg. 1817*, 167−181.

(15) de Bianchi, S., Ballottari, M., Dall'Osto, L., and Bassi, R. (2010) Regulation of plant light harvesting by thermal dissipation of excess energy. *Biochem. Soc. Trans. 38*, 651−660.

(16) Mathis, P., Butler, W. L., and Satoh, K. (1979) Carotenoid triplet state and chlorophyll fluorescence quenching in chloroplasts and sub chloroplasts particles. *Photochem. Photobiol. 30*, 603−614.

(17) El Agamey, A., Lowe, G. M., McGarvey, D. J., Mortensen, A., Phillip, D. M., Truscott, T. G., and Young, A. J. (2004) Carotenoid radical chemistry and antioxidant/pro-oxidant properties. *Arch. Biochem. Biophys. 430*, 37−48.

(18) Havaux, M., and Niyogi, K. K. (1999) The violaxanthin cycle protects plants from photooxidative damage by more than one mechanism. *Proc. Natl. Acad. Sci. U. S. A. 96*, 8762−8767.

(19) Demmig-Adams, B. (1990) Carotenoids and photoprotection in plants: A role for the xanthophyll zeaxanthin. *Biochim. Biophys. Acta, Bioenerg. 1020*, 1−24.

(20) Jahns, P., Latowski, D., and Strzalka, K. (2009) Mechanism and regulation of the violaxanthin cycle: the role of antenna proteins and membrane lipids. *Biochim. Biophys. Acta, Bioenerg. 1787*, 3−14.

(21) Pinnola, A., Dall'Osto, L., Gerotto, C., Morosinotto, T., Bassi, R., and Alboresi, A. (2013) Zeaxanthin binds to light-harvesting complex stress-related protein to enhance nonphotochemical quenching in Physcomitrella patens. *Plant Cell 25*, 3519−3534.

(22) Betterle, N., Ballottari, M., Hienerwadel, R., Dall'Osto, L., and Bassi, R. (2010) Dynamics of zeaxanthin binding to the photosystem II monomeric antenna protein Lhcb6 (CP24) and modulation of its photoprotection properties. *Arch. Biochem. Biophys. 504*, 67−77.

(23) Havaux, M., Dall'Osto, L., and Bassi, R. (2007) Zeaxanthin has enhanced antioxidant capacity with respect to all other xanthophylls in Arabidopsis leaves and functions independent of binding to PSII antennae. *Plant Physiol. 145*, 1506−1520.

(24) Dall'Osto, L., Cazzaniga, S., Havaux, M., and Bassi, R. (2010) Enhanced photoprotection by protein-bound vs free xanthophyll pools: a comparative analysis of chlorophyll b and xanthophyll biosynthesis mutants. *Mol. Plant 3*, 576−593.

(25) Hartel, H., Lokstein, H., Grimm, B., and Rank, B. (1996) Kinetic studies on the xanthophyll cycle in barley leaves (influence of antenna size and relations to Nonphotochemical chlorophyll fluorescence quenching). *Plant Physiol 110*, 471−482.

(26) Ahn, T. K., Avenson, T. J., Ballottari, M., Cheng, Y. C., Niyogi, K. K., Bassi, R., and Fleming, G. R. (2008) Architecture of a charge-transfer state regulating light harvesting in a plant antenna protein. *Science 320*, 794−797.

(27) Polivka, T., Zigmantas, D., Sundström, V., Formaggio, E., Cinque, G., and Bassi, R. (2002) Carotenoid S-1 state in a recombinant light-harvesting complex of photosystem II. *Biochemistry 41*, 439−450.

(28) Dall'Osto, L., Holt, N. E., Kaligotla, S., Fuciman, M., Cazzaniga, S., Carbonera, D., Frank, H. A., Alric, J., and Bassi, R. (2012) Zeaxanthin protects plant photosynthesis by modulating chlorophyll triplet yield in specific light-harvesting antenna subunits. *J. Biol. Chem. 287*, 41820−41834.

(29) Telfer, A., De Las Rivas, J., and Barber, J. (1991) Beta-Carotene within the isolated photosystem II reaction centre: Photooxidation and irreversible bleaching of this chromophore by oxidised P680. *Biochim. Biophys. Acta, Bioenerg. 1060*, 106−114.

(30) Telfer, A., Dhami, S., Bishop, S. M., Phillips, D., and Barber, J. (1994) β-carotene quenches singlet oxygen formed by isolated photosystem II reaction centers. *Biochemistry 33*, 14469−14474.

(31) Asada, K. (1999) The water-water cycle in chloroplasts: scavenging of active oxygens and dissipation of excess photons. *Annu. Rev. Plant Physiol. Plant Mol. Biol. 50*, 601−639.

(32) Sonoike, K. (2011) Photoinhibition of Photosystem I. *Physiol. Plant. 142*, 56−64.

(33) Suorsa, M., Jarvi, S., Grieco, M., Nurmi, M., Pietrzykowska, M., Rantala, M., Kangasjarvi, S., Paakkarinen, V., Tikkanen, M., Jansson, S., and Aro, E. M. (2012) Proton Gradient Regulation5 Is Essential for Proper Acclimation of Arabidopsis Photosystem I to Naturally and Artificially Fluctuating Light Conditions. *Plant Cell 24*, 2934−2948.

(34) Cazzaniga, S., Li, Z., Niyogi, K. K., Bassi, R., and Dall'Osto, L. (2012) The Arabidopsis szl1 mutant reveals a critical role of β-carotene in photosystem I photoprotection. *Plant Physiol. 159*, 1745−1758.

(35) Carbonera, D., Agostini, G., Morosinotto, T., and Bassi, R. (2005) Quenching of chlorophyll triplet states by carotenoids in reconstituted Lhca4 subunit of peripheral light-harvesting complex of photosystem I. *Biochemistry 44*, 8337−8346.

(36) Croce, R., Mozzo, M., Morosinotto, T., Romeo, A., Hienerwadel, R., and Bassi, R. (2007) Singlet and triplet state transitions of carotenoids in the antenna complexes of higher-plant Photosystem I. *Biochemistry 46*, 3846−3855.

DOI: 10.1021/acs.biochem.6b00425
Biochemistry 2016, 55, 3636−3649

(37) Qin, X., Suga, M., Kuang, T., and Shen, J.-R. (2015) Structural basis for energy transfer pathways in the plant PSI-LHCI supercomplex. *Science 348*, 989−995.
(38) Wehner, A., Storf, S., Jahns, P., and Schmid, V. H. (2004) De-epoxidation of violaxanthin in light-harvesting complex I proteins. *J. Biol. Chem. 279*, 26823−26829.
(39) Fiore, A., Dall'Osto, L., Fraser, P. D., Bassi, R., and Giuliano, G. (2006) Elucidation of the beta-carotene hydroxylation pathway in Arabidopsis thaliana. *FEBS Lett. 580*, 4718−4722.
(40) Li, Z., Ahn, T. K., Avenson, T. J., Ballottari, M., Cruz, J. A., Kramer, D. M., Bassi, R., Fleming, G. R., Keasling, J. D., and Niyogi, K. K. (2009) Lutein accumulation in the absence of zeaxanthin restores nonphotochemical quenching in the Arabidopsis thaliana npq1 mutant. *Plant Cell 21*, 1798−1812.
(41) Niyogi, K. K., Grossman, A. R., and Björkman, O. (1998) Arabidopsis mutants define a central role for the xanthophyll cycle in the regulation of photosynthetic energy conversion. *Plant Cell 10*, 1121−1134.
(42) Casazza, A. P., Tarantino, D., and Soave, C. (2001) Preparation and functional characterization of thylakoids from Arabidopsis thaliana. *Photosynth. Res. 68*, 175−180.
(43) Ruban, A. V., Lee, P. J., Wentworth, M., Young, A. J., and Horton, P. (1999) Determination of the stoichiometry and strength of binding of xanthophylls to the photosystem II light harvesting complexes. *J. Biol. Chem. 274*, 10458−10465.
(44) Croce, R., and Bassi, R. (1998) in *Photosynthesis: Mechanisms and Effects* (Garab, G., Ed.) pp 421−424, Kluwer Academic Publisher, Dordrecht, The Netherlands.
(45) Laemmli, U. K. (1970) Cleavage of structural proteins during the assembly of the head of bacteriophage T4. *Nature 227*, 680−685.
(46) Croce, R., Zucchelli, G., Garlaschi, F. M., and Jennings, R. C. (1998) A thermal broadening study of the antenna chlorophylls in PSI- 200, LHCI, and PSI core. *Biochemistry 37*, 17355−17360.
(47) Lagarde, D., Beuf, L., and Vermaas, M. (2000) Increased production of zeaxanthin and other pigments by application of genetic engineering techniques to Synechocystis sp strain PCC 6803. *Appl. Environ. Microbiol. 66*, 64−72.
(48) Flors, C., Fryer, M. J., Waring, J., Reeder, B., Bechtold, U., Mullineaux, P. M., Nonell, S., Wilson, M. T., and Baker, N. R. (2006) Imaging the production of singlet oxygen in vivo using a new fluorescent sensor, Singlet Oxygen Sensor Green. *J. Exp. Bot. 57*, 1725−1734.
(49) Dall'Osto, L., Fiore, A., Cazzaniga, S., Giuliano, G., and Bassi, R. (2007) Different roles of α- and β-branch xanthophylls in photosystem assembly and photoprotection. *J. Biol. Chem. 282*, 35056−35068.
(50) Croce, R., Weiss, S., and Bassi, R. (1999) Carotenoid-binding sites of the major light-harvesting complex II of higher plants. *J. Biol. Chem. 274*, 29613−29623.
(51) Havaux, M., Dall'Osto, L., Cuine, S., Giuliano, G., and Bassi, R. (2004) The effect of zeaxanthin as the only xanthophyll on the structure and function of the photosynthetic apparatus in Arabidopsis thaliana. *J. Biol. Chem. 279*, 13878−13888.
(52) Yang, J.-S., Wang, R., Meng, J.-J., Bi, Y.-P., Xu, P.-L., Guo, F., Wan, S.-B., He, Q.-W., and Li, X. G. (2010) Overexpressionof Arabidopsis CBF1 gene in transgenic tobacco alleviates photoinhibition of PSII and PSI during chilling stress under low irradiance. *J. Plant Physiol. 167*, 534−539.
(53) Carbonera, D., Giacometti, G., and Agostini, G. (1992) FDMR of carotenoid and chlorophyll triplets in Light-harvesting complex LHCII of spinach. *Appl. Magn. Reson. 3*, 859−872.
(54) Santabarbara, S., Bordignon, E., Jennings, R. C., and Carbonera, D. (2002) Chlorophyll triplet states associated with photosystem II of thylakoids. *Biochemistry 41*, 8184−8194.
(55) Santabarbara, S., Agostini, G., Heathcote, P., and Carbonera, D. (2005) A fluorescence detected magnetic resonance investigation of the carotenoid triplet states associated with photosystem II of isolated spinach thylakoid membranes. *Photosynth. Res. 86*, 283−296.
(56) Kim, J., Smith, J. J., Tian, L., and DellaPenna, D. (2009) The evolution and function of carotenoid hydroxylases in Arabidopsis. *Plant Cell Physiol. 50*, 463−479.
(57) Zhang, S., and Scheller, H. V. (2004) Photoinhibition of Photosystem I at chilling temperature and subsequernt recovery in Arabidopsis thaliana. *Plant Cell Physiol. 45*, 1595−1602.
(58) Clarke, R. H. (1982) *Triplet State ODMR Spectroscopy. Techniques and Applications to Biophysical Systems*, New York.
(59) Hoff, A. J. (1989) *Optically detected magnetic resonance (ODMR) of triplet states in vivo*, Elsevier, Amsterdam.
(60) Santabarbara, S., and Carbonera, D. (2005) Carotenoid triplet states associated with the long-wavelength-emitting chlorophyll forms of Photosystem I in isolated thylakoid membranes. *J. Phys. Chem. B 109*, 986−991.
(61) Horton, P., Ruban, A., and Wentworth, M. (2000) Allosteric regulation of the light-harvesting system of photosystem II. *Philos. Trans. R. Soc., B 355*, 1361−1370.
(62) Avenson, T. J., Ahn, T. K., Zigmantas, D., Niyogi, K. K., Li, Z., Ballottari, M., Bassi, R., and Fleming, G. R. (2008) Zeaxanthin radical cation formation in minor light-harvesting complexes of higher plant antenna. *J. Biol. Chem. 283*, 3550−3558.
(63) Havaux, M., and Kloppstech, K. (2001) The protective functions of carotenoid and flavonoid pigments against excess visible radiations at chilling temperature investigated in Arabidopsis npq and tt mutants. *Planta 213*, 953−966.
(64) Dall'Osto, L., Piques, M., Ronzani, M., Molesini, B., Alboresi, A., Cazzaniga, S., and Bassi, R. (2013) The Arabidopsis nox mutant lacking carotene hydroxylase activity reveals a critical role for xanthophylls in photosystem I biogenesis. *Plant Cell 25*, 591−608.
(65) Toth, T. N., Chukhutsina, V., Domonkos, I., Knoppova, J., Komenda, J., Kis, M., Lenart, Z., Garab, G., Kovacs, L., Gombos, Z., and Van Amerongen, H. (2015) Carotenoids are essential for the assembly of cyanobacterial photosynthetic complexes. *Biochim. Biophys. Acta, Bioenerg. 1847*, 1153−1165.
(66) Peterman, E. J., Dukker, F. M., van Grondelle, R., and Van Amerongen, H. (1995) Chlorophyll a and carotenoid triplet states in light-harvesting complex II of higher plants. *Biophys. J. 69*, 2670−2678.
(67) Mozzo, M., Dall'Osto, L., Hienerwadel, R., Bassi, R., and Croce, R. (2008) Photoprotection in the antenna complexes of photosystem II: role of individual xanthophylls in chlorophyll triplet quenching. *J. Biol. Chem. 283*, 6184−6192.
(68) Trevithick-Sutton, C. C., Foote, C. S., Collins, M., and Trevithick, J. R. (2006) The retinal carotenoids zeaxanthin and lutein scavenge superoxide and hydroxyl radicals: a chemiluminescence and ESR study. *Mol. Vis. 12*, 1127−1135.
(69) Niyogi, K. K., Shih, C., Soon Chow, W., Pogson, B. J., DellaPenna, D., and Björkman, O. (2001) Photoprotection in a zeaxanthin- and lutein-deficient double mutant of Arabidopsis. *Photosynth. Res. 67*, 139−145.
(70) Dall'Osto, L., Lico, C., Alric, J., Giuliano, G., Havaux, M., and Bassi, R. (2006) Lutein is needed for efficient chlorophyll triplet quenching in the major LHCII antenna complex of higher plants and effective photoprotection in vivo under strong light. *BMC Plant Biol. 6*, 32.
(71) Demmig-Adams, B., Winter, K., Kruger, A., and Czygan, F.-C. (1989) in *Photosynthesis. Plant Biology Vol. 8* (Briggs, W. R., Ed.) pp 375−391, Alan R. Liss, New York.
(72) Nilkens, M., Kress, E., Lambrev, P., Miloslavina, Y., Muller, M., Holzwarth, A. R., and Jahns, P. (2010) Identification of a slowly inducible zeaxanthin-dependent component of non-photochemical quenching of chlorophyll fluorescence generated under steady-state conditions in Arabidopsis. *Biochim. Biophys. Acta, Bioenerg. 1797*, 466−475.
(73) Moya, I., Silvestri, M., Vallon, O., Cinque, G., and Bassi, R. (2001) Time-resolved fluorescence analysis of the Photosystem II antenna proteins in detergent micelles and liposomes. *Biochemistry 40*, 12552−12561.

DOI: 10.1021/acs.biochem.6b00425
Biochemistry 2016, 55, 3636−3649

(74) Liu, Z., Yan, H., Wang, K., Kuang, T., Zhang, J., Gui, L., An, X., and Chang, W. (2004) Crystal structure of spinach major light-harvesting complex at 2.72 A resolution. *Nature 428*, 287−292.
(75) Pan, X., Li, M., Wan, T., Wang, L., Jia, C., Hou, Z., Zhao, X., Zhang, J., and Chang, W. (2011) Structural insights into energy regulation of light-harvesting complex CP29 from spinach. *Nat. Struct. Mol. Biol. 18*, 309−315.
(76) Ballottari, M., Alcocer, M. J. P., D'Andrea, C., Viola, D., Ahn, T. K., Petrozza, A., Polli, D., Fleming, G. R., Cerullo, G., and Bassi, R. (2014) Regulation of photosystem I light harvesting by zeaxanthin. *Proc. Natl. Acad. Sci. U. S. A. 111*, E2431−E2438.
(77) Ferreira, K. N., Iverson, T. M., Maghlaoui, K., Barber, J., and Iwata, S. (2004) Architecture of the photosynthetic oxygen-evolving center. *Science 303*, 1831−1838.
(78) Andersson, B., Salter, A. H., Virgin, I., Vass, I., and Styring, S. (1992) Photodamage to Photosystem-II - Primary and Secondary Events. *J. Photochem. Photobiol., B 15*, 15−31.
(79) Rutherford, A. W., Osyczka, A., and Rappaport, F. (2012) Back-reactions, short-circuits, leaks and other energy wasteful reactions in biological electron transfer: redox tuning to survive life in O(2). *FEBS Lett. 586*, 603−616.
(80) Andreeva, A., Abarova, S., Stoitchkova, K., Picorel, R., and Velitchkova, M. (2007) Selective photobleaching of chlorophylls and carotenoids in Photosystem I particles under high-light treatment. *Photochem. Photobiol. 83*, 1301−1307.
(81) Sonoike, K., and Terashima, I. (1994) Mechanism of Photosystem-I Photoinhibition in Leaves of Cucumis-Sativus l. *Planta 194*, 287−293.
(82) Inoue, K., Sakurai, M., and Hiyama, T. (1986) Photoinactivation sites of photosystem I in isolated chloroplasts. *Plant Cell Physiol. 27*, 961−968.
(83) Tjus, S. E., and Andersson, B. (1993) Loss of the trans-thylakoid proton gradient is an early event during photoinhibitory illumination of chloroplast preparations. *Biochim. Biophys. Acta, Bioenerg. 1183*, 315−322.
(84) Amunts, A., Toporik, H., Borovikova, A., and Nelson, N. (2010) Structure determination and improved model of plant Photosystem I. *J. Biol. Chem. 285*, 3478−3486.
(85) Alboresi, A., Ballottari, M., Hienerwadel, R., Giacometti, G. M., and Morosinotto, T. (2009) Antenna complexes protect Photosystem I from photoinhibition. *BMC Plant Biol. 9*, 71.
(86) Morosinotto, T., Breton, J., Bassi, R., and Croce, R. (2003) The nature of a chlorophyll ligand in Lhca proteins determines the far red fluorescence emission typical of photosystem I. *J. Biol. Chem. 278*, 49223−49229.
(87) Croce, R., Zucchelli, G., Garlaschi, F. M., Bassi, R., and Jennings, R. C. (1996) Excited state equilibration in the photosystem I -light -harvesting I complex: P700 is almost isoenergetic with its antenna. *Biochemistry 35*, 8572−8579.

DOI: 10.1021/acs.biochem.6b00425
Biochemistry 2016, 55, 3636−3649

Supporting information

Figure S1. Purification of PSI-LHCI complexes. **S**ucrose gradient fractionation of thylakoid membranes, upon *in vitro* de-epoxidation of chloroplasts. Solubilization of membranes was performed with 0.8% β-DM. For each gradient, fractions harvested are indicated.

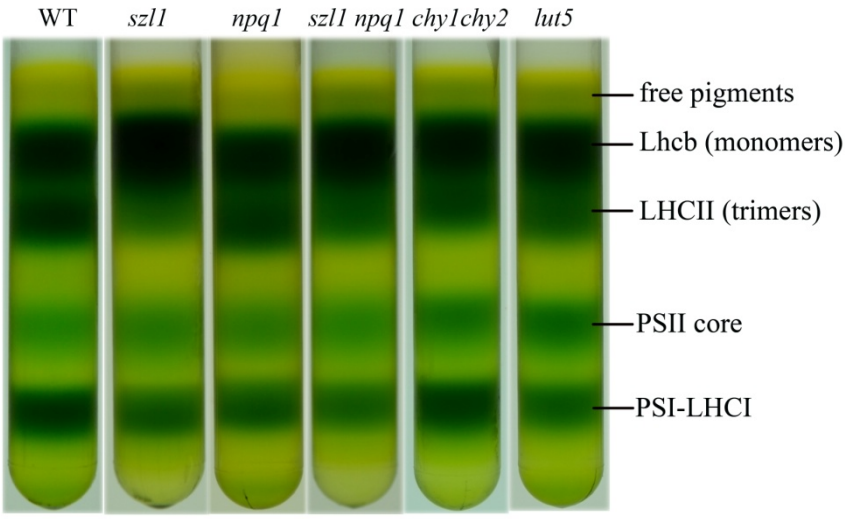

Figure S2. Characterization of PSI-LHCI complexes purified from WT and mutant genotypes. (A) Maximum photoxidizable P700 was measured at room temperature (RT) on PSI-LHCI complexes purified by sucrose gradient ultracentrifugation. $\Delta Abs_{705\ nm}$ has been expressed as percentage of the corresponding WT value. Chl concentration: 40 µg/ml. Data are expressed as mean ± SD, n = 7 (B) Electron transport from plastocyanin to $NADP^+$ was measured on thylakoids, continuously stirred and subjected to illumination (150 µmol photons m^{-2} s^{-1}, 600 nm < λ < 750 nm, RT). Chl concentration: 15 µg/ml. Electron transport rates were assayed by following $NADP^+$ reduction spectrophotometrically, as previously described (Casazza et al., 2001). Data are expressed as mean ± SD, n = 4. (C) SDS-PAGE of PSI-LHCI complexes. Main protein components are indicated. (D) Spectral deconvolution analysis of WT and mutant PSI-LHCI supercomplexes. (*upper panels*) Fitting of the red region absorption spectrum at RT of PSI-LHCI, with the spectra of individual Chl in a protein environment. (*lower panel*) Histogram of areas for the different sub-bands as obtained from deconvolution of the red region (645-735 nm) of the absorption spectra of complexes. Eight forms of Chl *a* and 2 of Chl *b* were the minimum number of forms in order to closely describe all the spectra. In our description of samples, the two Chl *b* forms peak at 640.5 and 652.5 nm, while the Chl *a* forms absorb at 663, 670, 677, 682.5, 689, 698, 708 and 716 nm. Amplitude of the different absorption forms were essentially the same in all complexes, indicating Chl organization in PSI-LHCI was unaffected by either *lut5*, *chy1 chy2* or *szl1* mutations.

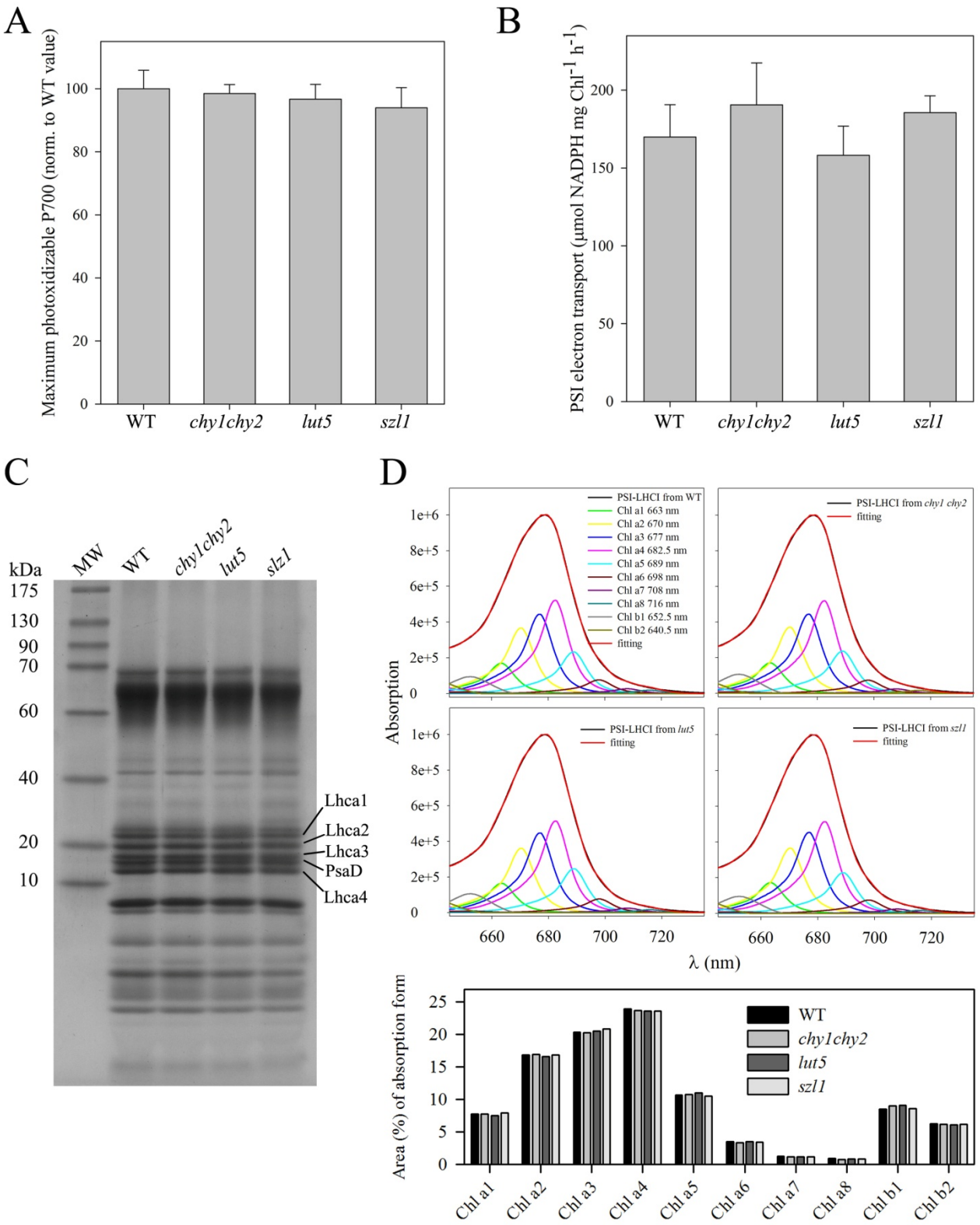
A
Maximum photoxidizable P700 (norm. to WT value)
0
20
40
60
80
100
WT
chy1chy2
lut5
szl1
B
PSI electron transport (µmol NADPH mg Chl-1 h-1)
0
50
100
150
200
WT
chy1chy2
lut5
szl1
C
kDa
MW
WT
chy1chy2
lut5
slz1
175
130
90
70
60
40
20
10
Lhca1
Lhca2
Lhca3
PsaD
Lhca4
D
PSI-LHCI from WT
Chl a1 663 nm
Chl a2 670 nm
Chl a3 677 nm
Chl a4 682.5 nm
Chl a5 689 nm
Chl a6 698 nm
Chl a7 708 nm
Chl a8 716 nm
Chl b1 652.5 nm
Chl b2 640.5 nm
fitting
PSI-LHCI from chy1 chy2
PSI-LHCI from lut5
PSI-LHCI from szl1
Absorption
1e+6
8e+5
6e+5
4e+5
2e+5
0
660
680
700
720
λ (nm)
Area (%) of absorption form
25
20
15
10
5
0
WT
chy1chy2
lut5
szl1
Chl a1
Chl a2
Chl a3
Chl a4
Chl a5
Chl a6
Chl a7
Chl a8
Chl b1
Chl b2

Figure S3. **Fluorescence detected magnetic resonance of the Chl and Car triplet states on isolated PSI-LHCI from dark adapted, WT plants.** FDMR signals of the ^{3}Chl* states (|D|-|E| and |D|+|E| transitions, panel A) and the ^{3}Car* states (2|E|, |D|-|E| and |D|+|E| transitions, panel B), observed in the PSI-LHCI complex purified from dark-adapted WT leaves, were detected at different wavelengths. Spectra have been vertically shifted for better comparison. Amplitude modulation frequency: 33 Hz (^{3}Chl* states) and 325 Hz (^{3}Car* states), tc 600 ms, number of scans 20, mw power 500 milliwatt, temperature 1.8 K.

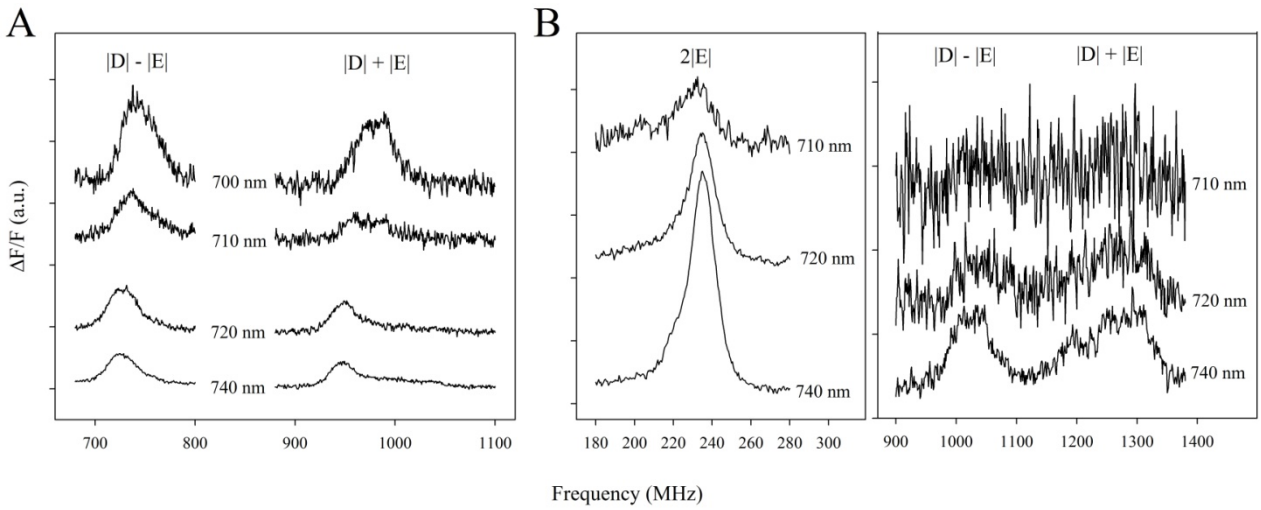

Figure S4. Reconstruction of the FDMR spectra of the ^{3}Chl* states on purified PSI-LHCI complexes, with Gaussians components. WT: left panels; *szl1:* right panels. *Upper panels*: FDMR spectra of the ^{3}Chl* states (|D|-|E| and |D|+|E| transitions, detected at different wavelengths - black traces). Spectra have been vertically shifted for better comparison. Fitting of the spectra are reported in green; single components are also shown in different colors. The constrains introduced for the fitting are the same used before for the same kind of spectral deconvolution (Santabarbara et al., 2002; Santabarbara et al., 2005a; Santabarbara et al., 2005b). Parameters used in the best fitting are reported in Table 1S. The fifth component (magenta) is observed only in the |D|+|E| transition and is assigned to a small contribution deriving from the |D|+|E| transition of the carotenoids. *Bottom panels*: amplitude of the main four gaussian components *vs.* detection wavelength (see Table 2S).

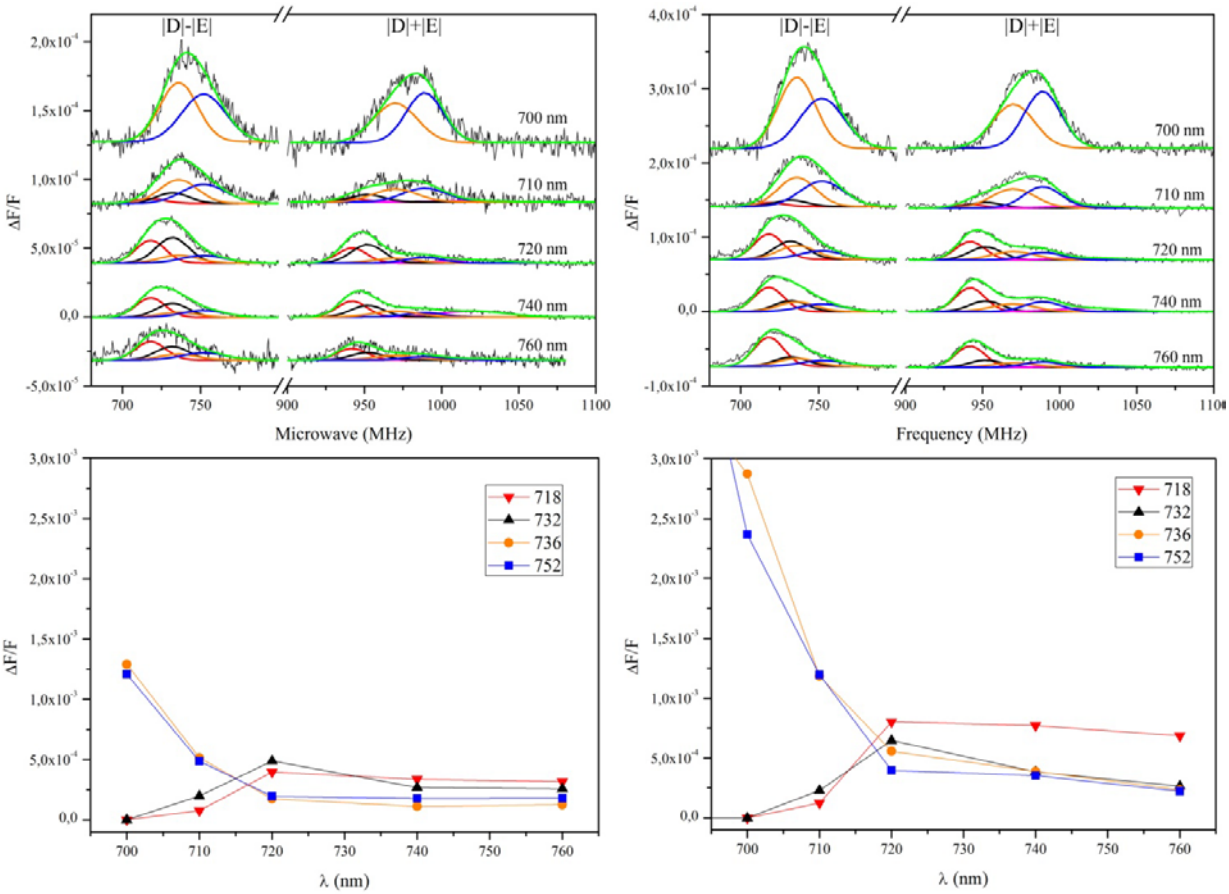

Figure S5. Fluorescence detected magnetic resonance of the ^{3}Car* and ^{3}Chl* on purified PSI-LHCI complexes. Comparison with Lhca4. FDMR signals of the ^{3}Car* states (2|E|, |D|-|E| and |D|+|E| transitions, panel A) and ^{3}Chl* states (|D|-|E| and |D|+|E| transitions, panel B) in the PSI-LHCI complex from WT (black lines) and *szl1* (green lines) in comparison with purified Lhca4 (red lines; modified from previously published data (Carbonera et al., 2005)). FDMR signals were detected at the wavelengths indicated in each panel.

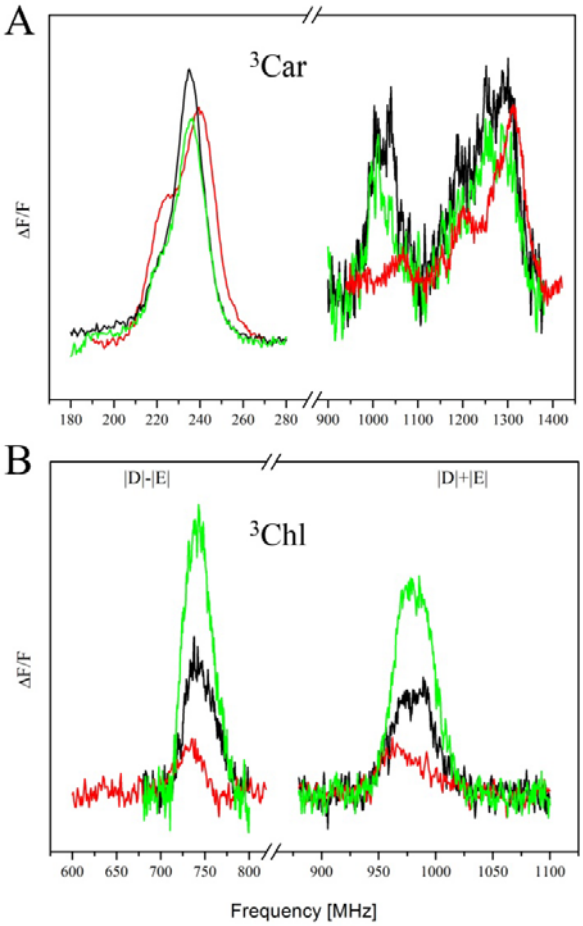

Figure S6. Purification of PSI core and LHCI complexes. Sucrose gradient fractionation of PSI core and LHCI complexes, upon solubilization of PSI-LHCI from WT, *npq1* and *szl1* with β-DM and Zwittergent (see Methods for details). For each gradient, fractions harvested are indicated.

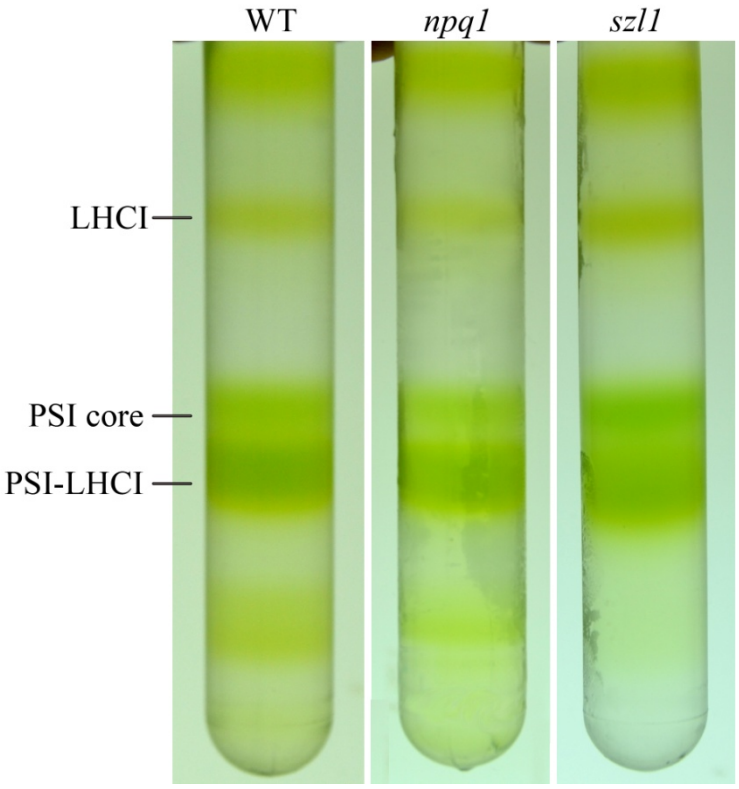

Table 1S. Parameters of the Global Gaussian Deconvolution of ^{3}Chl* states on purified PSI-LHCI complexes, with Gaussians components.

	|D|-|E|		**|D|+|E|**		**ZFS**	
	Center (MHz)	FWHM (MHz)	Center (MHz)	FWHM (MHz)	|D| (cm^{-1})	|E| (cm^{-1})
T_1	718	19	942	19	0.0277	0.0037
T_2	732	21	952	21	0.0281	0.0037
T_3	736	24	970	28	0.0284	0.0039
T_4	752	28	986	24	0.0290	0.0039
T_5	-	-	1020	42	-	-

Table 2S. Amplitude of the Gaussian components of ^{3}Chl* states used in the reconstruction of the FDMR spectra on purified PSI-LHCI complexes at different wavelengths.

|D|-|E|

WT	Center (MHz)	700 nm	710 nm	720 nm	740 nm	760 nm
T_1	718	-	$0.76*10^{-4}$	$3.96*10^{-4}$	$3.36*10^{-4}$	$3.17*10^{-4}$
T_2	732	-	$1.98*10^{-4}$	$4.88*10^{-4}$	$2.69*10^{-4}$	$2.57*10^{-4}$
T_3	736	$12.9*10^{-4}$	$5.15*10^{-4}$	$1.74*10^{-4}$	$1.11*10^{-4}$	$1.25*10^{-4}$
T_4	752	$12.1*10^{-4}$	$4.86*10^{-4}$	$1.95*10^{-4}$	$1.77*10^{-4}$	$1.78*10^{-4}$

szl1	Center (MHz)	700 nm	710 nm	720 nm	740 nm	760 nm
T_1	718	-	$1.25*10^{-4}$	$8.02*10^{-4}$	$7.71*10^{-4}$	$6.85*10^{-4}$
T_2	732	-	$2.28*10^{-4}$	$6.46*10^{-4}$	$3.84*10^{-4}$	$2.65*10^{-4}$
T_3	736	$28.7*10^{-4}$	$11.8*10^{-4}$	$5.57*10^{-4}$	$3.89*10^{-4}$	$2.34*10^{-4}$
T_4	752	$23.7*10^{-4}$	$12.0*10^{-4}$	$3.97*10^{-4}$	$3.54*10^{-4}$	$2.21*10^{-4}$

|D|+|E|

WT	Center (MHz)	700 nm	710 nm	720 nm	740 nm	760 nm
T_1	942	-	$0.52*10^{-4}$	$2.65*10^{-4}$	$2.76*10^{-4}$	$1.96*10^{-4}$
T_2	952	-	$1.34*10^{-4}$	$3.58*10^{-4}$	$2.30*10^{-4}$	$1.38*10^{-4}$
T_3	970	$10.8*10^{-4}$	$3.51*10^{-4}$	$1.22*10^{-4}$	$0.95*10^{-4}$	$0.73*10^{-4}$
T_4	989	$10.0*10^{-4}$	$3.31*10^{-4}$	$1.27*10^{-4}$	$1.54*10^{-4}$	$1.11*10^{-4}$
T_5	1020	-	$0.44*10^{-4}$	$1.36*10^{-4}$	$2.30*10^{-4}$	$0.54*10^{-4}$

szl1	Center (MHz)	700 nm	710 nm	720 nm	740 nm	760 nm
T_1	942	-	$1.10*10^{-4}$	$5.99*10^{-4}$	$7.62*10^{-4}$	$6.95*10^{-4}$
T_2	952	-	$2.00*10^{-4}$	$4.68*10^{-4}$	$3.62*10^{-4}$	$2.49*10^{-4}$
T_3	970	$20.1*10^{-4}$	$8.71*10^{-4}$	$3.13*10^{-4}$	$3.89*10^{-4}$	$2.24*10^{-4}$
T_4	989	$22.9*10^{-4}$	$9.03*10^{-4}$	$4.02*10^{-4}$	$3.98*10^{-4}$	$2.43*10^{-4}$
T_5	1020	-	$4.86*10^{-4}$	$1.95*10^{-4}$	$1.77*10^{-4}$	$1.78*10^{-4}$

References

Carbonera, D., Agostini, G., Morosinotto, T., and Bassi, R. (2005). Quenching of chlorophyll triplet states by carotenoids in reconstituted Lhca4 subunit of peripheral light-harvesting complex of photosystem I. Biochemistry **44**:8337-8346.

Casazza, A.P., Tarantino, D., and Soave, C. (2001). Preparation and functional characterization of thylakoids from Arabidopsis thaliana. Photosynth.Res. **68**:175-180.

Santabarbara, S., Agostini, G., Heathcote, P., and Carbonera, D. (2005a). A fluorescence detected magnetic resonance investigation of the carotenoid triplet states associated with photosystem II of isolated spinach thylakoid membranes. Photosynt.Res. **86**:283-296.

Santabarbara, S., Bordignon, E., Jennings, R.C., and Carbonera, D. (2002). Chlorophyll triplet states associated with photosystem II of thylakoids. Biochemistry **41**:8184-8194.

Santabarbara, S. and Carbonera, D. (2005b). Carotenoid triplet states associated with the long-wavelength-emitting chlorophyll forms of Photosystem I in isolated thylakoid membranes. J.Phys.Chem.B **109**:986-991.

Bryan Ferlez, Alessandro Agostini, Donatella Carbonera,
John H. Golbeck and Art van der Est*

Triplet Charge Recombination in Heliobacterial Reaction Centers Does Not Produce a Spin-Polarized EPR Spectrum

DOI 10.1515/zpch-2016-0825
Received June 13, 2016; accepted September 13, 2016

Abstract: In photosynthetic reaction centers, reduction of the secondary acceptors leads to triplet charge recombination of the primary radical pair (RP). This process is spin selective and in a magnetic field it populates only the T_0 state of the donor triplet state. As a result, the triplet state of the donor has a distinctive spin polarization pattern that can be measured by transient electron paramagnetic resonance (TREPR) spectroscopy. In heliobacterial reaction centers (HbRCs), the primary donor, P_{800}, is composed of two bacteriochlorophyll *g′* molecules and its triplet state has not been studied as extensively as those of other reaction centers. Here, we present TREPR and optically detected magnetic resonance (ODMR) data of $^3P_{800}$ and show that although it can be detected by ODMR it is not observed in the TREPR data. We demonstrate that the absence of the TREPR spectrum is a result of the fact that the zero-field splitting (ZFS) tensor of $^3P_{800}$ is maximally rhombic, which results in complete cancelation of the absorptive and emissive polarization in randomly oriented samples.

Keywords: chlorophyll *a*; P_{800} bacteriochlorophyll *g*; photosynthesis; type I reaction center.

***Corresponding author: Art van der Est,** Departments of Chemistry and Physics, Brock University, 1812 Sir Isaac Brock Way, St. Catharines, ON, Canada L2S 3A1; and Freiburg Institute of Advanced Studies (FRIAS), Albert-Ludwigs-Universität Freiburg, Albertstr.19, 79104 Freiburg, Germany, e-mail: avde@brocku.ca
Bryan Ferlez: Department of Biochemistry and Molecular Biology, The Pennsylvania State University, University Park, PA 16802, USA
Alessandro Agostini and Donatella Carbonera: Dipartimento di Scienze Chimiche, Università di Padova, Via Marzolo, 1, 35131 Padova, Italy
John H. Golbeck: Department of Biochemistry and Molecular Biology and Department of Chemistry, The Pennsylvania State University, University Park, PA 16802, USA; and Freiburg Institute of Advanced Studies (FRIAS), Albert-Ludwigs-Universität Freiburg, Albertstr.19 79104 Freiburg, Germany

1 Introduction

All known photosynthetic reaction centers (RCs) share a common structural motif with two branches of electron transfer co-factors extending across the complex from a pair of chlorophyll molecules, which act as an electron donor. The pair of chlorophylls is referred to as P_λ, where λ is the wavelength of their Q_y absorbance maximum. The components of the two branches and the acceptor sides of the complexes differ in the different classes. In type I RCs the two branches converge at an iron-sulfur cluster, while in type II RCs, two quinones flank a non-heme iron. In both cases, the absorption of light leads to electron transfer along the chain of acceptors. In type I RCs both branches are used, whereas in type II RCs the electron transfer is unidirectional in the L-branch. In both cases, if the secondary acceptors are either chemically reduced, removed or are otherwise inactivated, charge recombination occurs. The spin selectivity of this back reaction has been studied extensively [1–19] and despite differences in the midpoint potentials, structure and chemical properties of the donors and acceptors it is known that it is dominated by triplet recombination in all cases. The strongest evidence for the dominance of the triplet pathway is the characteristic spin-polarized transient EPR (TREPR) spectrum of the donor. This spectrum was first observed by Dutton, Leigh and co-workers [1–4] in purple bacteria. Thurnauer et al. [5] showed that the polarization pattern A/E/E/A/A/E (A = absorption, E = emission) occurs as a result of singlet-triplet mixing in the primary radical pair (RP). This pattern has also been observed in several artificial photosynthetic systems [20–23]. In the strong magnetic field of an EPR spectrometer, the spin-spin coupling in the RP is much weaker than the Zeeman interaction and the singlet state is mixed only with the T_0 triplet sublevel. As a result, only the T_0 sublevel of the donor triplet state is populated by recombination. In contrast, when a triplet state is generated by intersystem crossing (ISC), the population of the sublevels is determined by how strongly each of them is perturbed by spin-orbit coupling. This perturbation depends on the orientation of the molecule in the magnetic field and hence for some orientations, selective population of the T_0 sublevel occurs but for others T_+ and T_- are populated [15, 24].

The properties of the triplet state of the primary donor can be used to gain insight into its electronic structure. In the purple bacteria, for example, the zero-field splitting (ZFS) parameter D of the donor triplet states $^3P_{865}$ in *Rhodobacter sphaeroides* and $^3P_{960}$ in *Blastochloris viridis* is about 25% smaller than that of isolated bacteriochlorophyll *a* (BChl *a*) and BChl *b*, respectively [5, 8, 25–27]. This difference has been rationalized as resulting from delocalization of the triplet state and a possible charge-transfer contribution to the overall triplet wavefunction [15, 28]. ENDOR and Photo- CIDNP studies indicate that the delocalization of

$^3P_{865}$ and $^3P_{960}$ is asymmetric with higher spin density on the L-branch chlorophyll [25, 27, 29]. In Photosystem II, experiments on oriented membranes indicate that at 4 K, the triplet state formed by charge recombination does not reside on the chlorophyll dimer, P_{680}, but rather on an accessory chlorophyll, which is tilted at an angle of 30° to membrane plane [16]. At higher temperature, the spin polarized EPR spectra show evidence that the triplet state becomes delocalized onto one of the two chlorophylls of P_{680} [18, 19].

Of the triplet states in type I reaction centers, that of P_{700} in Photosystem I has been studied most extensively [10, 13, 17, 30]. The ZFS parameters of $^3P_{700}$ at 4 K are the same as those of isolated Chl *a*, indicating that the triplet excitation is localized on a single chlorophyll molecule [10, 13]. At room temperature, however, the ZFS parameter, *E*, becomes smaller. This change can be explained as a result of incoherent hopping of the excitation between the two chlorophylls of P_{700} [17]. In green sulfur bacteria, which have a homodimeric type I reaction center [31], the donor triplet state shows similar behavior to the purple bacteria with ZFS parameters consistent with delocalization [11, 32] over the special pair and a triplet wavefunction with charge-transfer character.

In contrast, the triplet state of P_{800} in heliobacterial reaction centers (HbRCs) has not been as well studied. P_{800} is of particular interest because it is the only donor that is composed of two BChl *g*′ molecules (the 13^2 epimer of BChl *g*) [33, 34] and the HbRC itself is composed of two identical proteins. Thus, as in green sulfur bacteria, a charge-transfer contribution to the triplet wavefunction would break the symmetry of the complex. Moreover, when HbRCs are exposed to oxygen, the BChl *g* (or BChl *g*′) is converted to Chl a_F (or Chl a_F') [35–37]. Hence different forms of the donor containing the different combinations of BChl *g*′ and Chl a_F' can be generated. We recently provided evidence that HbRCs containing a heterodimeric donor composed of a BChl *g*′ and a Chl a_F' molecule are photochemically active [37]. There are two early reports of the steady-state EPR spectra of triplet states in heliobacteria [38, 39] and a later, more extensive study using absorption-detected magnetic resonance (ADMR) [40]. In both of the EPR studies, only the two outermost features of the triplet spectrum were observed. It was suggested that these features contained two components with different *D* and *E* values, which were ascribed to $^3P_{800}$ and antenna triplets on the basis of their dependence on the reduction state of the acceptors. The *D* and *E* values obtained from the spectrum are in agreement with those observed by ADMR. However, the reported polarization pattern (A/E) of the spectrum is the same for both components, which is not consistent with two different mechanisms (ISC and charge recombination) for their formation. Moreover, the pattern (A/E) is opposite to the E/A pattern reported more recently for antenna triplet states in HbRCs under oxidizing conditions [37]. These discrepancies led us to re-investigate the spin polarized EPR

spectra of HbRCs and green-sulfur bacterial reaction centers (GsbRCs) under oxidizing and reducing conditions.

Here we demonstrate that under reducing conditions, the characteristic A/E/E/A/A/E polarization pattern of a triplet state formed by charge recombination is observed for GsbRCs but not for HbRCs, despite their structural similarity. This difference is explained as a result of differences in the ZFS parameters of BChl a' and BChl g'. We will show that when $D = 3E$, the intensity of the polarization pattern of the charge-recombination triplet becomes zero because of cancelation of the absorptive and emissive contributions. This means that for samples of HbRCs with a random distribution of orientations, the charge recombination triplet cannot be observed by TREPR and hence optical methods must be used to demonstrate whether it is present or not.

2 Materials and methods

2.1 Preparation and purification of heliobacterial reaction centers

HbRCs were isolated as previously described [41]. All manipulations were carried out under strict anoxic conditions under dim green light. For TREPR measurements, samples were prepared by incubating HbRCs at a BChl *g* concentration of 0.9 mM in 50 mM MOPS pH 7.0 with 0.02% dodecyl maltoside and 10% glycerol with 50 mM sodium ascorbate for 10 min in the dark for the oxidized sample or with 50 mM sodium dithionite at pH 10.0 for 10 min in the dark for the reduced sample prior to freezing in liquid nitrogen. BChl *g* concentrations were calculated using the absorbance at 788 nm and an extinction coefficient for BChl *g* of 110 mM^{-1} cm^{-1} [42].

2.2 Preparation and purification of membranes from green-sulfur bacteria

Chlorosome-depleted membranes were isolated from 2 L of *Chlorobium tepidum* cells grown to stationary phase as described in [43] with the exception that 10 mM potassium phosphate buffer at pH 7.2 with 150 mM NaCl was used to resuspend the *C. tepidum* whole cells and chlorosome depleted membranes. All manipulations were carried out under strict anoxic conditions under dim green light. For TREPR measurements, samples were prepared by incubating chlorosome

depleted membranes ($OD_{810\ nm}$ = 3.7) with 50 μM PMS and 50 mM sodium ascorbate for 10 min in the dark for the oxidized sample or with 50 mM sodium dithionite at pH 10.0 for 10 min in the dark for the reduced sample prior to freezing in liquid nitrogen.

2.3 Transient EPR spectroscopy

TREPR measurements were made using a modified Bruker E300 EPR spectrometer at X-band and 90 K as described in detail in [44]. To generate three dimensional time/field/amplitude data sets, 128 light induced EPR amplitude/time traces were collected and averaged at each magnetic field position spanning the region of interest at a resolution of 0.5 mT. The time traces are the EPR response to single-turnover flashes provided by a Vibrant 355II laser (Opotek, Inc., Carlsbad, CA, USA) running at 10 Hz with a single pulse energy of 20 mJ at 532 nm and a pulse width of 7 ns. For data analysis, boxcar spectra were extracted from the time/field/amplitude data sets by calculating the average EPR signal at each field point in a 1 μs long time window starting at 1 μs following the laser flash.

2.4 ODMR spectroscopy

The principle of the ODMR technique, reviewed in [45], will be briefly summarized. ODMR is a double resonance technique based on the principle that, when a steady-state population of a triplet state is generated under continuous illumination, the application of a resonant microwave electromagnetic field between a pair of spin sublevels of the triplet state generally induces a change of the steady-state population of the triplet state due to the anisotropy of the decay and population rates of the spin sublevels. The induced change of the triplet population may be detected as a corresponding change of the emission and/or absorption of the system. In particular, absorbance detected magnetic resonance (ADMR) detects the microwave-induced change in the steady state absorption of the chromophore carrying the triplet state, whereas fluorescence detected magnetic resonance (FDMR) detects the changes in the emission.

FDMR and ADMR experiments were performed using a home-built apparatus, described in detail in [46, 47]. Amplitude modulation of the applied microwave field is used to greatly increase the signal to noise ratio by means of a phase sensitive lock-in amplifier (EG&G 5220). In the FDMR experiments the fluorescence, excited by a halogen lamp (250 W) focused into the sample and filtered by a broadband 5 cm solution of $CuSO_4$ 1 M, was collected at 45 degrees, through a

780 nm cut-on filter and appropriate band-pass filters (10 nm FWHM), by a photodiode. The photodiode signal was demodulated after entering the lock-in amplifier. In ADMR, the same excitation lamp was used but without filters before the sample, except for 5 cm water and heat filters. The beam was focused into the monochromator after passing the sample and finally collected by the photodiode. The amplitude modulation frequency was 33 Hz and the microwave power 500 mW.

By fixing the microwave frequency at a resonant value and sweeping the detection wavelength, microwave-induced Triplet-minus-Singlet (T-S) spectra were collected. All of the ODMR experiments were performed at 1.8 K. At this temperature spin-lattice relaxation is inhibited and the ODMR signal is detectable.

The samples were diluted to give a final OD = 1.0 at 788 nm with a 1 mm light path (BChl *g* concentration of 91 μM). Degassed glycerol was added to the samples to a final concentration of 60% v/v, in order to obtain homogeneous and transparent matrices upon freezing. Reduced samples were prepared by adding a few microliters of a freshly prepared 500 mM sodium dithionite solution, to reach a final concentration of 50 mM. After 5 min of dark incubation, the samples were inserted into the cryostat at a temperature of 270 K and subsequently cooled to 1.8 K under illumination.

3 Results and discussion

A diagram of showing the electron transfer kinetics and pathways in HbRCs under oxidizing (left) and reducing (right) conditions is presented in Figure 1. In both cases, excitation of P_{800} results in rapid electron transfer to A_0. Under oxidizing conditions secondary electron transfer to F_X then occurs with a lifetime of 700 ps and at low temperature charge recombination to the ground state has a lifetime of 4 ms [37, 49]. If F_X is pre-reduced, electron transfer past A_0 is blocked (Figure 1, right) [44]. In this case, triplet recombination occurs and the triplet state of the donor relaxes to the ground state with a lifetime of ~500 μs at 5 K [49].

3.1 Transient EPR spectra

Figure 2 shows a comparison of transient EPR (TREPR) spectra of GsbRCs and HbRC obtained under oxidizing and strongly reducing conditions at 90 K. GsbRCs and HbRCs are both homodimeric type I RCs and their electron transfer kinetics are essentially the same [31, 50]. However, in HbRCs the primary

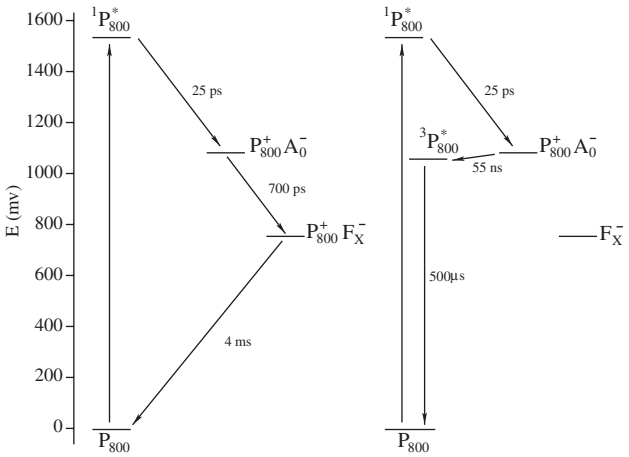

Fig. 1: Jablonski diagram of HbRCs showing the low temperature electron transfer pathways under oxidizing conditions (left) and reducing conditions (right). The energies of the charge separated states have been taken from reference [44]. The energy of $^3P_{800}$ has been estimated from the phosphorescence wavelength [48] of BChl *g* and the lifetime of P_{800} is the literature value at 5 K [49].

donor is composed of two BChl *g′* molecules, while in GsbRCs the donor is a BChl *a′* dimer. Under oxidizing conditions (spectra a and d) both types of RCs give TREPR spectra with a sharp emission/absorption (E/A) polarization pattern from the RP $P^+F_X^-$ and broad features on either side of the RP spectrum due to chlorophyll triplet states formed primarily by ISC. The shape of the triplet contribution is different for the two types of RCs because HbRCs contain BChl *g*, while GsbRCs contain BChl *a*.

When F_X is reduced by freezing in the presence of a reductant (Figure 2b and e), the contribution from $P^+F_X^-$ disappears. In GsbRCs (Figure 2b) this is accompanied by the appearance of a triplet spectrum with the AEEAAE polarization pattern characteristic of selective population of the T_0 state by charge recombination [11]. In contrast, in HbRCs (Figure 2e) the loss of $P^+F_X^-$ is not accompanied by any significant change in the triplet spectrum. This can be seen most clearly in the reduced minus oxidized difference spectra in Figure 2c and f.

The red curves in Figure 2 are simulations of the triplet component based on the ZFS parameters given in Table 1. For GsbRCs, the D and E values of $^3P_{840}$ obtained by fitting the triplet component in Figure 1c are in good agreement with those reported previously from TREPR and optically detected magnetic resonance (ODMR) measurements [11, 51]. Under oxidizing conditions, the triplet component of the GsbRC spectrum (Figure 1a) can be simulated as the

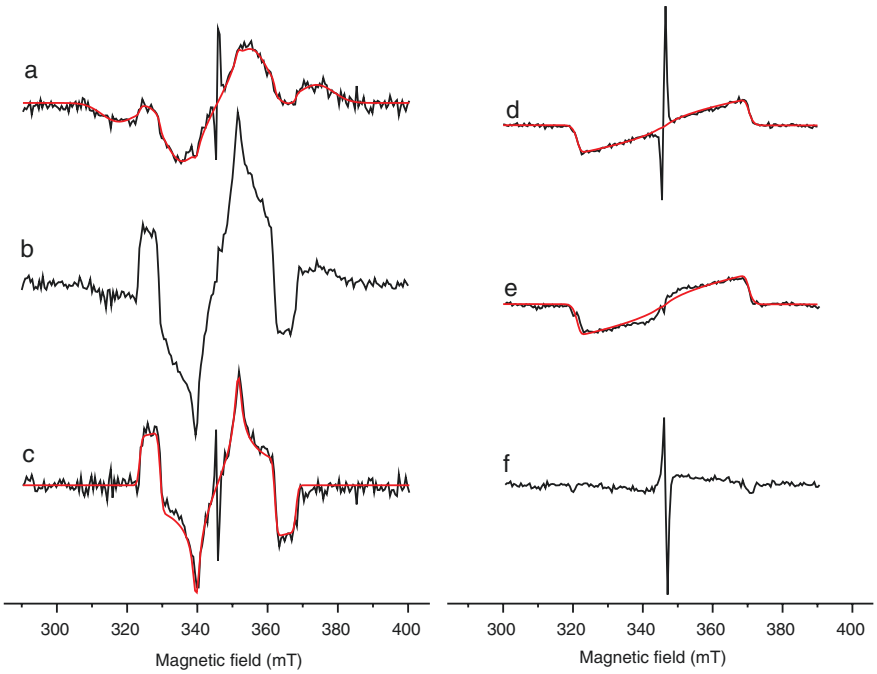

Fig. 2: TREPR spectra of GsbRCs (left) and HbRCs (right) under oxidizing and reducing conditions. (a) GsbRCs under oxidizing conditions; (b) GsbRCs frozen under reducing conditions; (c) Difference spectrum b-a; (d) HbRCs under oxidizing conditions; (e) HbRCs frozen under reducing conditions; (f) Difference spectrum e-d. The red spectra are simulations calculated using the parameters in Table 1.

Tab. 1: Simulation parameters for the TREPR spectra in Figure 2.

Component	|D| (10^{-4} cm^{-1})	|E| (10^{-4} cm^{-1})	Linewidth (mT)	Populations
GsbRC antenna	306	37	8.8	$p_x:p_y:p_z = 0.13:0.87:0$
GsbRC $^3P_{840}$	208	32	1.3	$p_{-1}:p_0:p_1 = 0:1:0$
HbRC antenna	227	77	2.0	$p_x:p_y:p_z = 0.62:0.38:0$
HbRC antenna	233	82	2.0	$p_x:p_y:p_z = 0.62:0.38:0$

sum of a triplet formed by ISC and a small contribution from $^3P_{840}$ in a ratio of 91:9. The minor contribution from $^3P_{840}$ is from a fraction of RCs in which electron transfer past A_0 is blocked, probably because of damage to F_X during the isolation procedure. The D value of the antenna triplet is larger than that of BChl *a* and the line width is large suggesting that this component is due to several different triplet species (chlorophylls and carotenoids) in a distribution

of environments. In contrast to GsbRCs, the triplet spectra observed for HbRCs contain only a contribution from ^{3}BChl *g* formed by ISC in the antenna and no contribution from $^3P_{800}$ is observed. The spectrum can be simulated using the D and E values of the two antenna triplets obtained from ODMR experiments, which will be discussed below.

3.2 Optically detected magnetic resonance

Because no contribution from $^3P_{800}$ was observed in the TREPR spectrum of HbRCs under reducing conditions, we performed ODMR experiments under similar conditions to determine whether $^3P_{800}$ is being formed. Figure 3 shows a comparison of the FDMR spectra of HbRCs frozen under oxidizing and reducing conditions (green and black spectra, respectively). The spectra are plots of the change in the fluorescence at $\lambda > 780$ nm as a function of the applied microwave frequency. In this wavelength range only fluorescence from BChl *g* is observed and the change in fluorescence occurs when the microwave frequency comes into resonance with a pair of triplet sublevels split by the ZFS. In general, peaks are observed at $|D|+|E|$, $|D|-|E|$ and $2|E|$. The peaks between 880 and 1000 MHz are the $|D|+|E|$ transitions from BChl *g* molecules in different environments. The peaks near 450 MHz are the corresponding $|D|-|E|$ and $2|E|$ transitions. For BChl *g*, $|D| \approx 3|E|$,

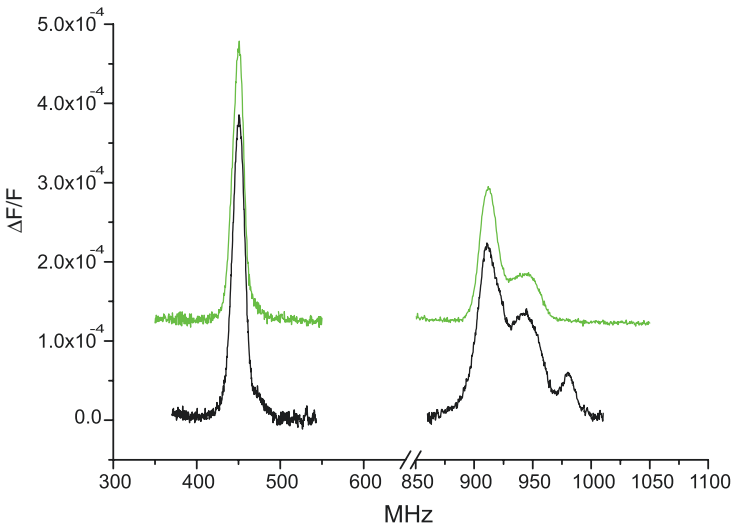

Fig. 3: Fluorescence detected magnetic resonance spectra of HbRCs frozen under oxidizing conditions (green) and under reducing conditions (black).

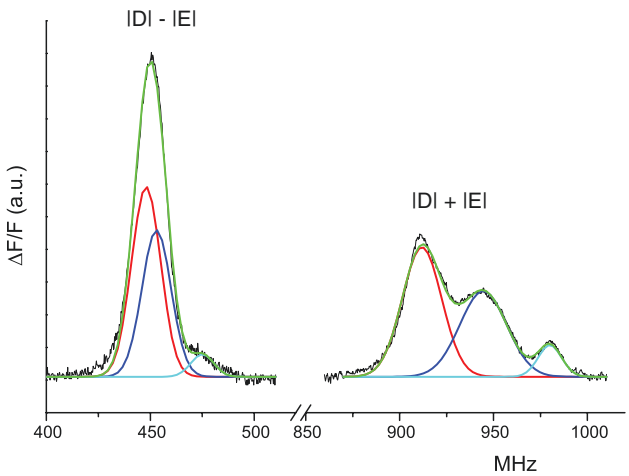

Fig. 4: Reconstruction of the experimental FDMR spectrum of HbRCs under strongly reducing conditions as the sum of three Gaussian components. The black trace is the experimental spectrum. The red, blue and cyan spectra are the three components and the green spectrum is their sum. The red and blue components are present in oxidized HbRCs but the cyan component due to $^3P_{800}$ only appears when F_X is reduced.

which means the 2|E| and |D| – |E| transitions occur at approximately the same frequency. However, as discussed by Vrieze et al. [40], the contribution from the 2|E| transition is weak because decay and population rates of the *x*- and *y*-sublevels of the triplet are similar.

Figure 4 shows a reconstruction of the FDMR spectra of the reduced sample by a sum of three Gaussian components corresponding to three different types of BChl *g*. As can be seen in Figure 3, the peak at 980 MHz is not present in the oxidized sample but appears when F_X is reduced. Careful comparison of the FDMR spectra and their detection wavelength dependence (not shown) reveal that there is also a peak at 475 MHz that appears only when F_X is reduced. The peaks at 980 MHz and 475 MHz agree well with the position of the |D| + |E| peak of $^3P_{800}$ in ADMR spectra reported previously [40]. The FDMR spectra measured with different detection wavelengths and microwave-induced triplet-minus-singlet absorption difference spectra (T-S) collected at different microwave frequencies (not shown) reveal three different types of BChl *g* molecules with different Q_y absorbance maxima and |D| and |E| values. As shown in Figure 4, the FDMR spectrum can be decomposed into three components corresponding to these three different types of BChl *g*. The values of the ZFS parameters and absorbance maxima are summarized in Table 2 and are in very good agreement with previously reported values [40]. Importantly the values of D and E obtained from the FDMR spectrum

Tab. 2: Zero-field splitting parameters of HbRCs from FDMR data and Q_y absorbance maxima from microwave induced T-S spectra[a].

Component	|D| – |E| (MHz)	Width (MHz)	|D| + |E| (MHz)	Width (MHz)	|D| (10^{-4}cm^{-1})	|E| (10^{-4} cm^{-1})	Q_y (nm)
Antenna	448	14	912	21	226.8	77.4	815
Antenna	453	14	944	25	233.0	81.9	798
$^3P_{800}$	475	11	980	13	242.7	84.2	792

[a]Estimated error ± 0.5%.

of the oxidized sample, reproduce the TREPR spectra of both the oxidized and reduced samples as can be seen in Figure 2 (spectra d and e).

3.3 Charge recombination triplet state polarization

The ODMR data show that under reducing conditions $^3P_{800}$ is formed. However, in the TREPR data there is no evidence of a spin-polarization pattern from this species. To investigate why this is, we have calculated the expected spin polarization pattern for $^3P_{800}$. From Tables 1 and 2 we see that an important difference in the ZFS parameters of the triplet states of the two donors is that $^3P_{800}$ has a much larger E-value because it is composed of BChl *g*′ while P_{840} is BChl *a*′. This difference is related to the difference in the arrangement of the conjugated double bonds in the porphyrin ring in the two chlorophylls. Thus, we have calculated a series of chlorophyll triplet spectra for different values of E and for formation of the triplet by ISC and by RP recombination. These spectra are shown in Figure 5. On the left of Figure 5, the spectra of ISC triplets are shown and those formed by RP recombination are displayed on the right. For the ISC triplets, the polarization pattern is E/E/E/A/A/A, while for RP recombination an A/E/E/A/A/E pattern is obtained. With E = 0, the ZFS tensor is axial and the splitting is the same for molecules oriented with any axis in the *xy* plane oriented along the magnetic field. This results in the strong inner peaks in both the ISC and RP recombination triplet spectra. As the value of E increases, the rhombicity of the ZFS tensor increases and the features from the *x*- and *y*-orientations no longer appear at the same position in the spectrum. The maximum rhombicity is attained when |E| = |D|/3. Under these conditions the splitting for the *x*-orientation is zero and is equal and opposite for the *y* and *z*-orientations. Here we have chosen the convention that the direction with the smallest ZFS is labeled *x*. In Chl *a* this direction corresponds to the direction of the Q_y optical transition dipole. For the RP recombination triplet spectra on the right of Figure 5, it can be seen that the intensity of the spectrum decreases

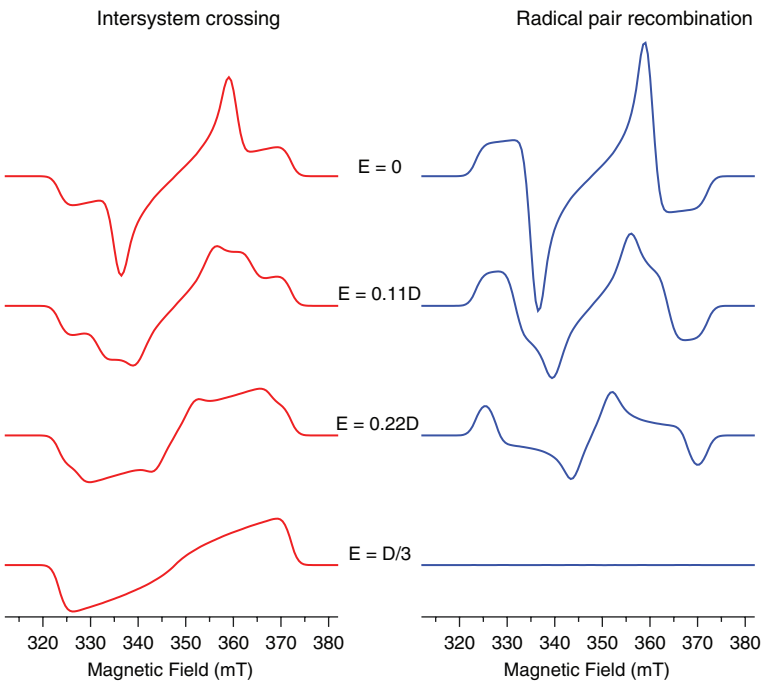

Fig. 5: Dependence of the spin polarization pattern of a triplet state on the value of the zero-field splitting parameter E, for ISC (left) and RP recombination (right). For all spectra $D = 211 \times 10^{-4}$ cm^{-1}. For the ISC spectra the triplet sublevels are populated according to their *x*, *y* and *z* character with the population ratios: $p_x:p_y:p_z = 0.5:0.5:0$. For the RP recombination triplets the high-field states are populated with the ratio $p_{-1}:p_0:p_1 = 0:1:0$.

as E increases and with $E = D/3$ no spectrum is obtained. For $^3P_{800}$, the ODMR data show that $E = 84.2 \times 10^{-4}$ cm^{-1} and $D/3 = 80.9 \times 10^{-4}$ cm^{-1}. Hence, the intensity of the spin-polarized TREPR spectrum of $^3P_{800}$ should be very close to zero.

To illustrate why the intensity of the RP recombination triplet is zero when $D/E = 3$, a comparison of the calculated the spectra of $^3P_{840}$ in GsbRCs and $^3P_{800}$ in HbRCs is shown in Figure 6. In the top part of the figure, contributions of the absorptive $T_0 \rightarrow T_+$ and emissive $T_0 \rightarrow T_-$ transitions to the overall spectrum are plotted separately. The total spectrum, which is the sum of the two contributions, is shown at the bottom of Figure 6. For $^3P_{840}$, $D/E = 6.5$ and the absorptive and emissive patterns are strongly shifted relative to one another. Their sum is the characteristic A/E/E/A/A/E pattern. In $^3P_{800}$, $D/E = 2.9$, and the absorptive and emissive transitions cancel one another giving no overall spectrum.

An important consequence of the cancelation of the emissive and absorptive contributions to the RP-recombination TREPR spectrum is that the intensity of

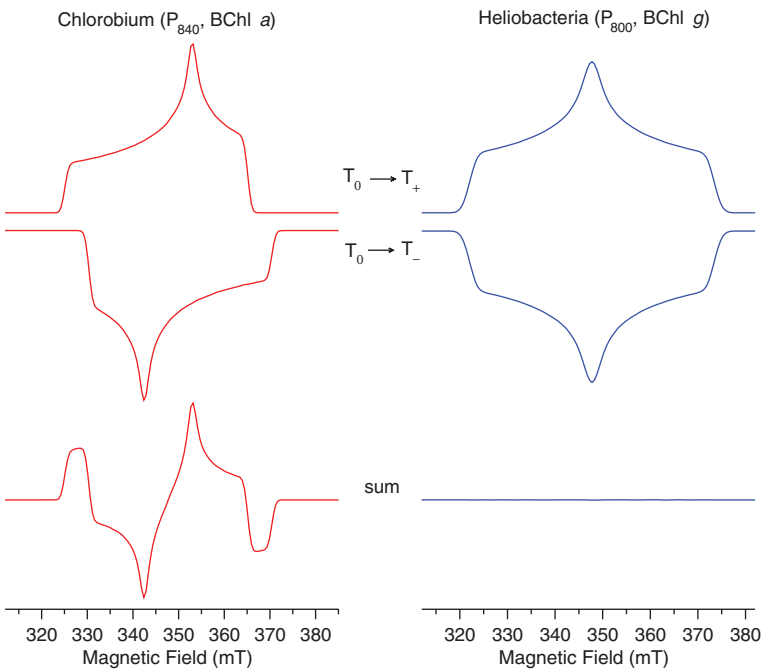

Fig. 6: Calculation of the contributions to the polarization pattern generated by RP recombination to the triplet state of P_{840} in GsbRCs and P_{800} in HbRCs. The spectra have been calculated using the values of D and E given in Tables 1 and 2.

the spectrum can be misleading as a measure of concentration. In HbRCs the fact that the intensity of the RP-recombination triplet spectrum is close to zero means that it cannot be used as a marker for recombination of the primary RP. However, because the cancelation of the polarization arises as a result of the overlap of signal contributions from different orientations it will not be complete in oriented samples. For example, the contributions to the spectrum from molecules with their molecular *y*- and *z*-axes parallel to the field cancel each other in a randomly oriented sample. If the molecules can be oriented such that one of these orientations has a higher probability then the cancelation will not be complete and the spectrum should become observable.

3.4 Concluding remarks

The data presented here, reveal that when the ZFS tensor of a triplet state is highly rhombic, cancelation of the absorptive and emissive polarization occurs when

the T_0 level is selectively populated by charge recombination. A similar situation can also arise for triplets populated by ISC. For a triplet state with $|D| = 3|E|$ nearly complete cancelation of the polarization also occurs if the high field sublevels are populated according to their *y*-character and D and E have the same sign or if they are populated according to their *x*-character and D and E have opposite sign. However, such a situation is unlikely to arise in practice since for most molecules, the rates of ISC associated with the *x*- and *y*-directions are usually fairly similar and either significantly larger or significantly smaller than the *z*-component.

Acknowledgements: The work was supported by NSERC in the form of a Discovery Grant to AvdE and by a grant from the Photosynthetic Systems Program, Chemical Sciences, Geosciences, & Biosciences (CSGB) Division, US Department of Energy (DE-FG02-98ER20314) to JHG. BF, JHG and AvdE thank Stefan Weber and his group for their great hospitality during our stay in Freiburg. We also thank Donald Bryant for providing the culture of *C. tepidum*.

References

1. P. L. Dutton, J. S. Leigh, M. Seibert, Biochem. Biophys. Res. Commun. **46** (1972) 406.
2. P. L. Dutton, J. S. Leigh, D. W. Reed, Biochim. Biophys. Acta **292** (1973) 654.
3. J. S. Leigh, P. L. Dutton, Biochim. Biophys. Acta **357** (1974) 67.
4. C. Wraight, J. Leigh, P. Dutton, R. Clayton, Biochim. Biophys. Acta **333** (1974) 401.
5. M. C. Thurnauer, J. J. Katz, J. R. Norris, Proc. Natl. Acad. Sci. USA. **72** (1975) 3270.
6. A. J. Hoff, H. Rademaker, R. Van Grondelle, L. N. Duysens, Biochim. Biophys. Acta **460** (1977) 547.
7. A. Hoff, H. G. De Vries, Biochim. Biophys. Acta **503** (1978) 94.
8. M. C. Thurnauer, Res. Chem. Intermed. **3** (1979) 197.
9. H. Rademaker, A. J. Hoff, R. Van Grondelle, L. N. Duysens, Biochim. Biophys. Acta **592** (1980) 240.
10. A. Rutherford, J. Mullet, Biochim. Biophys. Acta **635** (1981) 225.
11. T. Swarthoff, P. Gast, A. Hoff, FEBS Lett. **127** (1981) 83.
12. H. Den Blanken, A. Hoff, Biochim. Biophys. Acta **681** (1982) 365.
13. P. Gast, T. Swarthoff, F. Ebskamp, A. Hoff, Biochim. Biophys. Acta **722** (1983) 163.
14. A. Hoff, I. Proskuryakov, Chem. Phys. Lett. **115** (1985) 303.
15. D. E. Budil, M. C. Thurnauer, Biochim. Biophys. Acta **1057** (1991) 1.
16. F. Van Mieghem, K. Satoh, A. Rutherford, Biochim. Biophys. Acta **1058** (1991) 379.
17. I. Sieckmann, K. Brettel, C. Bock, A. van der Est, D. Stehlik, Biochemistry **32** (1993) 4842.
18. M. K. Bosch, I. I. Proskuryakov, P. Gast, A. J. Hoff, J. Phys. Chem. **100** (1996) 2384.
19. A. Kamlowski, L. Frankemöller, A. van der Est, D. Stehlik, A. Holzwart, Ber. Bunsen. Phys. Chem. **100** (1996) 2045.
20. G. P. Wiederrecht, W. A. Svec, M. R. Wasielewski, T. Galili, H. Levanon, J. Amer. Chem. Soc. **121** (1999) 7726.

21. Y. Kandrashkin, P. Poddutoori, A. van der Est, Appl. Magn. Reson. **30** (2006) 605.
22. Z. E. Dance, Q. Mi, D. W. McCamant, M. J. Ahrens, M. A. Ratner, M. R. Wasielewski, J. Phys. Chem. B **110** (2006) 25163.
23. D. J. Weinberg, S. M. Dyar, Z. Khademi, M. Malicki, S. R. Marder, M. R. Wasielewski, E. A. Weiss, J. Amer. Chem. Soc. **136** (2014) 14513.
24. S. P. McGlynn, T. Azumi, M. Kinoshita, Molecular Spectroscopy of the Triplet State, Englewood Cliffs: Prentice-Hall, 1969.
25. F. Lendzian, R. Bittl, W. Lubitz, Photosynth. Res. **55** (1998) 189.
26. A. Marchanka, M. Paddock, W. Lubitz, M. van Gastel, Biochemistry **46** (2007) 14782.
27. A. Marchanka, W. Lubitz, M. Plato, M. van Gastel, Photosynth. Res. **120** (2014) 99.
28. J. Norris, D. Budil, P. Gast, C. Chang, O. El-Kabbani, M. Schiffer, Proc. Natl. Acad. Sci. USA. **86** (1989) 4335.
29. S. S. Thamarath, B. E. Bode, S. Prakash, K. B. Sai Sankar Gupta, A. Alia, G. Jeschke, J. Matysik, J. Amer. Chem. Soc. **134** (2012) 5921.
30. H. A. Frank, M. B. McLean, K. Sauer, Proc. Natl. Acad. Sci. USA. **76** (1979) 5124.
31. G. Hauska, T. Schoedl, H. Remigy, G. Tsiotis, Biochim. Biophys. Acta **1507** (2001) 260.
32. W. Nitschke, U. Feiler, A. W. Rutherford, Biochemistry **29** (1990) 3834.
33. M. Kobayashi, E. J. van de Meent, C. Erkelens, J. Amesz, I. Ikegami, T. Watanabe, Biochim. Biophys. Acta **1057** (1991) 89.
34. I. Sarrou, Z. Khan, J. Cowgill, S. Lin, D. Brune, S. Romberger, J. H. Golbeck, K. E. Redding, Photosynth. Res. **111** (2012) 291.
35. P. Beer-Romero, J. L. Favinger, H. Gest, FEMS Microbiol. Lett. **49** (1988) 451.
36. M. Kobayashi, T. Hamano, M. Akiyama, T. Watanabe, K. Inoue, H. Oh-oka, J. Amesz, M. Yamamura, H. Kise, Anal. Chim. Acta **365** (1998) 199.
37. B. Ferlez, W. Dong, R. Siavashi, K. Redding, H. J. Hou, J. H. Golbeck, A. van der Est, J. Phys. Chem. B **119** (2015) 13714.
38. M. R. Fischer, Biochim. Biophys. Acta **1015** (1990) 471.
39. W. Nitschke, P. Setif, U. Liebl, U. Feiler, A. W. Rutherford, Biochemistry **29** (1990) 11079.
40. J. Vrieze, E. Van de Meent, A. Hoff, Biochemistry **37** (1998) 14900.
41. M. Heinnickel, R. Agalarov, N. Svensen, C. Krebs, J. H. Golbeck, Biochemistry **45** (2006) 6756.
42. F. Kleinherenbrink, J. Amesz, Biochim. Biophys. Acta **1143** (1993) 77.
43. C. Klughammer, C. Hager, E. Padan, M. Schütz, U. Schreiber, Y. Shahak, G. Hauska, Photosynth. Res. **43** (1995) 27.
44. B. Ferlez, J. B. Cowgill, W. Dong, C. Gisriel, S. Lin, M. Flores, K. Walters, D. Cetnar, K. E. Redding, J. H. Golbeck, Biochemistry **55** (2016) 2358.
45. D. Carbonera, Photosynth. Res. **102** (2009) 403.
46. D. Carbonera, G. Giacometti, G. Agostini, Appl. Magn. Reson. **3** (1992) 859.
47. S. Santabarbara, E. Bordignon, R. C. Jennings, D. Carbonera, Biochemistry **41** (2002) 8184.
48. D. A. Hartzler, D. M. Niedzwiedzki, D. A. Bryant, R. E. Blankenship, Y. Pushkar, S. Savikhin, J. Phys. Chem. B **118** (2014) 7221.
49. F. A. Kleinherenbrink, T. J. Aartsma, J. Amesz, Biochim. Biophys. Acta **1057** (1991) 346.
50. S. Neerken, J. Amesz, Biochim. Biophys. Acta **1507** (2001) 278.
51. H. Vasmel, H. J. Den Blanken, J. T. Dijkman, A. J. Hoff, J. Amesz, Biochim. Biophys. Acta **767** (1984) 200.

Part III

Water Soluble Chlorophyll-binding Protein

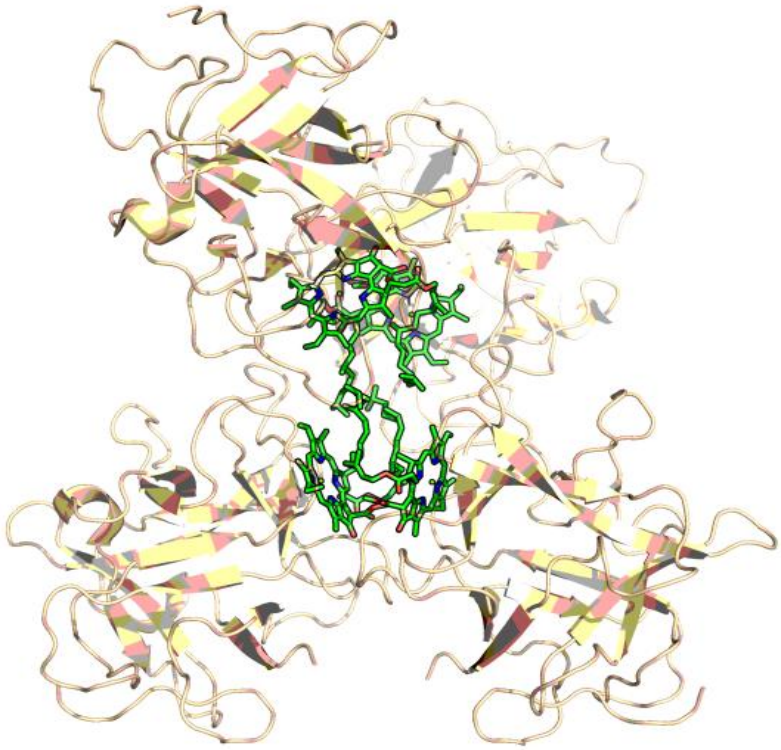

Water-Soluble Chlorophyll Protein (WSCP) Stably Binds 2 or 4 Chlorophylls

Daniel M. Palm[§‡], Alessandro Agostini[§†‡], Stefan Tenzer[‖], Barbara M. Gloeckle[§], Mara Werwie[§], Donatella Carbonera[†], and Harald Paulsen[§*]

[§]Institute of General Botany, Johannes-Gutenberg University Mainz, Johannes-von-Müller-Weg 6, 55128 Mainz, Germany,

[†]Department of Chemical Sciences, University of Padova, Via Marzolo 1, 35131 Padova, Italy,

[‖] Institute for Immunology, University Medical Center Mainz, Langenbeckstr. 1, 55131 Mainz, Germany.

[‡] These authors contributed equally

[*] Author to whom correspondence should be addressed.

HP Telephone: E-mail: paulsen@uni-mainz.de

ABSTRACT

Water-soluble chlorophyll proteins (WSCP) of class-IIa from *Brassicaceae* form tetrameric complexes containing one chlorophyll (Chl) per apoprotein but no carotenoids. The complexes are remarkably stable towards dissociation and protein denaturation even at 100 °C and extreme pH values, and the Chls are partially protected against photooxidation. There are several hypotheses for the biological role of WSCPs, one of them proposing them to function as a scavenger of Chls set free upon plant senescence or pathogen attack. The biochemical WSCP properties described in this paper are consistent with the protein acting as an efficient and flexible Chl scavenger. Under limiting Chl concentrations, the recombinant WSCP apoprotein binds substoichiometric amounts of Chl (2 Chls/tetramer) to form complexes that are as stable towards thermal dissociation, denaturation, and photodamage as the fully pigmented ones. If more Chl is added, these 2-Chl complexes can bind another 2 Chls to reach the fully pigmented state. The protection of WSCP Chls against photodamage has been attributed to the apoprotein serving as a diffusion barrier for oxygen, preventing its access to triplet-excited Chls and thus,

the formation of singlet oxygen. By contrast, the sequential binding of Chls by WSCP suggests a partially open or at least flexible structure, raising the question of how WSCP photoprotects its Chls without the help of carotenoids.

INTRODUCTION

Water-soluble chlorophyll protein (WSCP) is an unusual protein in several respects. Whereas all other chlorophyll (Chl) proteins in higher plants are membrane-bound, WSCP is not. WSCP contains no carotenoids and even so, is able to protect its Chl to some extent against photooxidation.[1] And finally, WSCP is extremely stable towards thermal dissociation and denaturation.[1–5] This latter property is particularly intriguing as the biological function of WSCP is unclear. In this paper, we show that the stability of WSCP extends to a version with a substoichiometric number of Chls bound.

All WSCPs are tetrameric with four subunits of roughly 20 kDa.[6–8] Two classes of WSCPs have been described. Class-I WSCPs isolated from *Amaranthaceae* (including *Chenopodiaceae*) and *Polygonaceae* have in common that they shift their absorption spectra upon illumination.[9] Class-II WSCPs, dealt with in this paper, show no such photoconvertibility[10] and have been found so far only in *Brassicaceae*. The class-II WSCPs can be further subdivided into class-IIa (including *Arabidopsis*, *Brassica*, *Raphanus*) with a Chl *a/b* ratio >6, and class-IIb (so far only found in *Lepidium virginicum*) with Chl *a/b* <3.5 (for a review see Satoh *et al.*[11]). Another difference between the two WSCP tetramer classes is the lowest energy Q_y absorption band of bound Chls. *Brassica oleracea* var. *Botrytis* (from here on referred to as *B. oleracea*) Chl *a* WSCP (class-IIa) exhibits a Q_y peak at 673 nm, whereas Chl *a* WSCP from *L. virginicum* WSCP (class-IIb) is characterized by a Q_y peak at 663 nm.[11]

Class-II WSCPs can be over-expressed in *E. coli* and purified as a monomeric apoprotein, which is water soluble and can be reconstituted *in vitro* with Chls to a tetrameric complex that biochemically and spectroscopically is very similar to native WSCP.[1,4,6,7,12,13] The crystal structure of *L. virginicum* (class-IIb) WSCP has been known since 2007.[14] Recently, the structure of recombinant WSCP from *B. oleracea* was added at 1.9 Å resolution.[15] In both structures, each of the four protein subunits binds one Chl.[14,15] The pigments are β-ligated (i.e. from their *syn*-side,[14] following the previous nomenclature of Balaban *et al.*[16]). This is an uncommon feature in Chl-binding proteins where chlorophylls are prevalently α-ligated.[16-18] The four Chls in each WSCP tetramer are organized into two open-sandwich structures each constituted by a Chl dimer forming an angle of approximately 27°. The phytol tails of each dimer are sandwiched by

the two tetrapyrrole planes and protrude from the tetrapyrrole dimer at one end facing each other, thereby creating a hydrophobic cavity center.[14,15] This is consistent with an earlier report that the phytol chains stabilize the tetrameric structure.[1] Also the structures of the two protein dimers, each binding one Chl dimer, are highly homologous between the *L. virginicum* and *B. oleracea* structures.[14,15] The main difference is a 60° rotation of one of the two dimeric units against the other one within the tetramer.[15] The recently resolved class-IIa (*B. oleracea*) structure also gave a partial explanation for the red shift of the Q_y absorption peak in class-IIa WSCPs in comparison to *L. virginicum* by a deformation of the planar Chl macrocycle in the former due to the steric clash with a tryptophan side chain nearby.[15]

The biological function of WSCP remains an unsolved matter. The chlorophyll-protein complex does not seem to be involved in photosynthesis, as class-II WSCPs are not located in the chloroplast[19] and the gene of *L. virginicum* WSCP is transcribed in roots.[19] All class-II WSCPs isolated so far possess a Künitz-type protease inhibitor sequence.[4,6,13,19–21] In accordance with this, there are, on one hand, different examples for a suggested protease inhibitor activity of WSCP, for instance the *Brassica napus* WSCP against trypsin during nitrogen starvation[22,23] and *Arabidopsis thaliana* WSCP against the cysteine protease papain.[24] On the other hand, some WSCPs were reported to fail as a trypsin inhibitor,[20,25] which of course does not exclude an inhibitor function of these towards other proteases. Künitz-type protease inhibitors have been described to be directed against a broad spectrum of serine and cysteine proteases and even against other enzymes like amylase, with each individual Künitz protease inhibitor being highly specific for one or few proteases. Likewise, different WSCPs may be involved in different functions. Recently it was suggested that *A. thaliana* WSCP plays a role in herbivore resistance activation during greening and in programmed cell death at least during flower development.[26,27] Due to its ability to extract and bind Chls from thylakoid membranes[6] WSCP has been proposed to function as a scavenger of Chls which are set free upon cellular breakdown or disruption[13,19] for instance under stress conditions.[23] WSCPs from *B. oleracea, Raphanus sativus, A. thaliana* and *L. virginicum* were shown to be localized in the endoplasmic reticulum body,[13,19,28] a cell compartment contributing to the *Brassicaceae* defense system (for a review see Nakano *et al.*[29]).

The biochemical data on *B. oleracea* WSCP reported on in this paper are consistent with its proposed function as a chlorophyll scavenger. At low Chl concentrations the protein tetramer can bind 2 Chl molecules instead of 4. Irrespective of the number of Chls bound, the protein is stable towards thermal dissociation or denaturation or extreme pH values, and it protects its

Chls against photooxidation. Moreover, 2-Chl WSCP can scavenge additional Chls to fill the vacant binding sites.

MATERIALS AND METHODS

Proteins. Recombinant WSCP apoprotein from *B. oleracea* (recWSCP) possessing an N-terminal hexahistidyl (His_6)-tag[1] was overexpressed as described earlier[30] with a few variations. Cell lysis was conducted by lysozyme treatment (0.5 mg/ml, 30 min at 37 °C) in lysis buffer (20 mM sodium phosphate pH 7.8, 300 mM NaCl, 15 mM imidazole, 1 mM EDTA) followed by three freeze-thaw cycles. After adding 3.3 µg/ml DNase I and 5 mM $MgCl_2$ and incubating for 20 min at 37 °C, the lysed bacteria cells were centrifuged (10,000 ×*g*, 4 °C, 25 min). The supernatant containing the soluble WSCP was applied to a Chelating Sepharose™ Fast Flow (GE Healthcare) column loaded with Ni^{2+} ions and equilibrated with 2 column volumes (CV) of 20 mM sodium phosphate pH 7.8. After washing (2 CV each) the column with increasing imidazole concentrations (25 mM, 50 mM and 60 mM in 20 mM sodium phosphate pH 7.8), WSCP was eluted with 2 CV of elution buffer (300 mM imidazole, 20 mM sodium phosphate pH 7.8). Desalting of the protein solution was performed by using Zeba™ spin desalting columns (Thermo Fisher Scientific) with a 7 kDa molecular weight cut off (MWCO) according to the manufacturer`s instructions. Protein concentrations were determined via absorption spectroscopy using extinction coefficient (ε_{280nm}) and molecular weight of 25,440 cm^{-1} M^{-1} and 21,734 g/mol, respectively, calculated from the amino acid sequence using the software ExPASy-ProtParam.[31] Protein purity and accuracy of protein quantification were verified by denaturing SDS polyacrylamide (PAA) gel electrophoresis (SDS PAGE) on a 15 % PAA-gel.[32] Native WSCP (natWSCP) was isolated and purified from *B. oleracea* leaves as previously described[20] with a few variations of the protocol. For homogenization, 100 mM sodium phosphate pH 7.4 buffer containing 850 mM NaCl, 26 mM ascorbate and 0.6 % (w/v) polyvinylpyrrolidon was used. After ammonium sulfate precipitation, the pellet was resuspended in 10 ml of 5 mM sodium phosphate pH 7.4 and centrifuged for 10 min at 27,200 ×*g* (4 °C). The supernatant was collected and boiled for 6 min followed by another centrifugation step (same conditions as above). The supernatant was dialyzed against 5 mM sodium phosphate pH 7.4 and subsequently applied on a DEAE Sepharose column equilibrated with the same buffer. The column then was washed with 2 CV each of 5 mM, 10 mM and 20 mM sodium phosphate pH 7.4, before the WSCP was eluted with 2 CV of 50 mM sodium phosphate pH 7.4. The eluate was concentrated (Amicon Ultra-4 Filter, 30 kDa MWCO, Millipore) and

subjected to an 8 % PAA-gel for separation via detergent-free PAGE. WSCP was recovered by excising and thoroughly crushing the greenish gel bands and soaking them in 10 mM sodium phosphate pH 7.4 at 4 °C for 16 h. The eluted WSCP fraction was purified by size-exclusion chromatography (SEC) on a Sephacryl S-200 HR column equilibrated with 20 mM sodium phosphate pH 7.8. Elution of the green WSCP fraction was conducted with the same buffer. For further purification, the eluate was applied to a Superdex 200 10/300 GL prepacked column (GE Healthcare) operated by a BioRad HR system at 4 °C.

Pigments. Chl *a* and Chl *b* were isolated and purified from pea plants (*Pisum sativum*) according to Booth and Paulsen.[33] After quantification via analytical HPLC, pigments were dried and stored under inert atmosphere (N_2) at -20 °C. Thylakoid membrane preparation from pea leaves was done as described in Nakayama *et al.*[34] using 75 ml of extraction buffer (330 mM sorbitol, 1 mM dithiothreitol, 25 mM Tris-HCl pH 7.8) per 100 grams of plant material. After homogenizing (Heavy Duty Blender CB62T, Bachofer GmbH), the suspension was filtered through three layers of cotton gaze and one layer of nylon gaze (mesh size 20 µm). The filtrate was collected and subsequently centrifuged (9,000 ×*g*, 4 °C, 10 min). After discarding the supernatant, the pelleted thylakoid membranes were resuspended in 20 mM sodium phosphate pH 7.8 (75 ml per 100 grams of plant material). Chl concentration and Chl *a/b* ratio were determined as described elsewhere.[35]

Reconstitution of recWSCP with purified Chls. For reconstitution of recWSCP to yield 4 Chls per tetramer, a five-fold molar excess of Chl over protein was used. The Chls were dissolved in ethanol (EtOH) and added dropwise under stirring to the protein solution containing sodium phosphate pH 7.8 and β-mercaptoethanol (final concentrations of 20 mM and 5 mM, respectively). The final concentration of EtOH was 20 % (v/v). The reconstitution mixture was incubated for 30 min at 23°C and 1,000 rpm (Thermomixer comfort, Eppendorf). After boiling treatment (5 min) and centrifugation (10 min, 15,000 ×*g* at room temperature, RT), the supernatant was collected and applied to a Superose 12 10/300 GL prepacked column (GE Healthcare) for purification via SEC. The column was equilibrated with 20 mM sodium phosphate pH 7.8 at RT. After the first SEC, peak fractions were pooled and subjected to a second SEC run. In order to yield 2 Chls per WSCP tetramer, a four-fold molar excess of protein over Chls was chosen and octyl β-D-glucopyranoside (OG) was added to the protein solution yielding a final concentration of 2.5 % (w/v). Incubation was carried out over night at 4 °C without shaking, boiling treatment was omitted. After centrifugation (10 min, 15,000 ×*g*, RT), the supernatant was purified twice via SEC in order to get rid of non-reconstituted recWSCP.

Finally, after SEC, peak fractions containing reconstituted WSCP were pooled and characterized spectroscopically.

Spectroscopy. UV-Vis absorption spectra of WSCPs were measured between 750 and 250 nm in a quartz cuvette (10 mm path length) with a scan speed of 200 nm/min and a bandwidth of 2 nm at RT using a V-550 UV/VIS spectrophotometer (Jasco). Circular dichroism (CD) was measured in a J-810 spectropolarimeter (Jasco) equipped with a Jasco CDF-426S peltier element for temperature control. Vis-CD spectra were taken between 750 and 350 nm at 23 °C (2 mm path length, data pitch 1 nm, 100 nm/min scan speed, response time 4 s, 4 × accumulation). UV-CD spectra were recorded in a range from 300 to 180 nm at 23 °C (0.5 mm path length, data pitch 0.5 nm, 50 nm/min scan speed, response time 4 s, 9 × accumulation). Steady-state fluorescence emission was monitored between 650 and 850 nm after excitation at 410 nm on a FluoroMax-2 (Jobin Yvon-Spex). Spectra were taken at RT in a cuvette with dimensions of 5×5 mm (slits 1 nm, increment 1 nm, integration time 1 s).

Determination of secondary structure elements. To estimate secondary structure contents, measured UV-CD spectra were analyzed by the BeStSel method, specifically optimized for β-strand rich proteins.[36] This algorithm distinguishes between parallel and antiparallel β-structures, and further differentiates between the more widespread antiparallel β-strands depending on the twist angle between relaxed and left- or right-hand twisted.

Determination of extinction coefficients for Chl *a* and Chl *b* bound to recWSCP. Pigments were dissolved in EtOH and added dropwise to a protein solution containing a ten-fold molar excess of recWSCP in 20 mM sodium phosphate pH 7.8 and 5 mM β-mercaptoethanol. The final concentration of EtOH was 20 % (v/v). After incubation for 30 min at 23°C and 1,000 rpm (Thermomixer comfort, Eppendorf), the reaction mixture was centrifuged (10 min, 15,000 ×*g* at RT) and the supernatant characterized via absorption spectroscopy. For a comparison of the spectroscopic properties of recWSCP bound Chls with that of unbound ones, the same amount of pigments was added to EtOH. By comparing the Q_y absorption maxima (average of five) of recWSCP bound Chls and EtOH dissolved Chls and taking into account the molar extinction coefficients in EtOH (74,400 cm^{-1} M^{-1} for Chl *a* and 40,000 cm^{-1} M^{-1} for Chl *b*),[37] effective extinction coefficients for Chls bound to recWSCP were determined.

Determination of Chl/protein stoichiometries. Molar Chl to protein ratios were determined from absorption spectra. Based on the Q_y absorption maximum, the Chl concentration was calculated taking into account the different extinction coefficients for Chl *a* (74,400 cm^{-1} M^{-1}) and Chl *b* (52,450 cm^{-1} M^{-1}) bound to recWSCP determined as described

above. The protein concentration was determined from the absorption value at 280 nm ($A_{280;}$ $WSCP_{measured}$). To take into account that Chls also absorb at 280 nm, spectra of pure Chl *a* or Chl *b* or mixtures thereof in EtOH were normalized to the Q_y absorption maximum in the measured WSCP spectrum to yield the Chl contribution ($A_{280}(Chl_{fit})$). Following the equation

$$A_{280}\ (\text{protein}) = A_{280}(WSCP_{measured}) - A_{280}(Chl_{fit})$$

and applying the extinction coefficients of 25,440 cm^{-1} M^{-1} for a WSCP protein binding Chl *a* and 18,900 cm^{-1} M^{-1} for a WSCP protein binding Chl *b*, the concentration of the protein was calculated.

Intact protein electrospray ionization mass spectrometry (ESI-MS). WSCP was dialyzed overnight against 10 mM ammonium acetate pH 4 and adjusted to 1 mg/ml in either 10 mM ammonium acetate pH 4 or 10 mM ammonium formate pH 3 + 20 % acetonitrile. Intact protein ESI-MS was performed on a Waters Synapt G2-S instrument operated in positive ionization mode at a resolution of 25,000 full width at half maximum (FWHM). WSCP solution was infused using a low-flow ESI probe at 5 µl/min using the following instrument parameters: capillary voltage 2.6 kV, source temperature 100 °C, sampling cone voltage: 35 V, source offset voltage 80 V, desolvation gas temperature 350 °C, cone gas flow 0 ml/min, nebulizer gas pressure 3.5 bar. Mass spectra were acquired over a mass range of 50 - 5000 *m/z* using a spectrum integration time of 1 s. Data were analyzed and processed in MassLynx 4.1 (Waters). Spectra were smoothed using a Savitzky-Golay filter with 20 bin width.

RESULTS

Tetrameric WSCP binds 2 or 4 Chls. As shown before, class-IIa recombinant WSCP can be reconstituted with Chl *in vitro* to yield tetrameric pigmented complexes that are very similar to the corresponding native complexes.[1,4,6,7,13] In earlier publications we[1] and others[6] reported a Chl/protein stoichiometry of both native and recombinant WSCP of 2 Chl per tetramer for this class. This has been doubted by Noy and coworkers,[7] and in fact, we confirm that both versions contain 4 Chls per protein tetramer. At the same time, we present a reconstitution protocol leading to complexes with only 2 Chls per tetramer. To characterize these complexes with different stoichiometries a reliable analysis of pigment and protein amounts in WSCP is essential. To this end, we improved our absorption analyses and verified the results by using total amino acid analysis and mass spectrometry.

The Chl amount in WSCP is quantitated by measuring the absorption at the Q_y maxima of Chl *a* and Chl *b* at 673 nm and 657 nm, respectively. The protein amount is calculated from the

absorption at 280 nm, taking into account the contributions of Chl *a* and/or Chl *b* to the absorption at this wavelength, as reported in the Material and Methods section. To determine the effective extinction coefficient of Chls at their Q_y maxima in the WSCP complex, whose absorption spectrum is influenced by the exciton coupling of the Chls, the ethanol-dissolved pigments were quantitatively bound to an excess amount of recWSCP. The results showed that the recWSCP-bound Chl *a* exhibits the same extinction coefficient as the one in ethanol (74,400 cm^{-1} M^{-1}),[37] whereas recWSCP-bound Chl *b* has a 24 % higher extinction coefficient (52,450 cm^{-1} M^{-1}) compared to that in ethanol (40,000 cm^{-1} M^{-1})[37] (see Figure S1).

The protein quantification, routinely performed by exploiting the absorption bands of aromatic residues in the near-UV, in pigmented protein is affected by the concomitant absorption of the chromophores in this spectral region. In WSCP there is also the additional complication of the close contact of two of the three tryptophans with the bound Chls, as revealed by the crystallographic structure,[15] that could affect their spectral properties. Therefore, we tested whether the spectroscopic protein quantification at 280 nm, subtracting the Chl contribution, is satisfactory for pigmented WSCP. We did this by quantitative total amino acid analysis of recWSCP reconstituted with pure Chl *a* or Chl *b* and comparing the results with the amounts calculated from the absorption at 280 nm (see Table S1 and S2). In the case of WSCP reconstituted with Chl *a*, both values are the same within 5 % deviation; thus, the extinction coefficient of the recWSCP in aqueous solution, 25,440 cm^{-1} M^{-1}, can also be applied to the protein moiety in the pigmented complex. Upon reconstituting recWSCP with Chl *b*, the protein concentration determined by amino acid analysis was 26 % higher than what was expected from the A_{280} value. Consequently, in order to have a precise stoichiometry determination, an extinction coefficient of the protein in Chl *b*-containing WSCP of 18,900 cm^{-1} M^{-1} has to be employed.

When recWSCP was reconstituted with a five-fold molar excess of Chl *a*, the Chl/protein ratio calculated from absorption data as detailed above was 1.02 (± 10 %), thus exhibiting a binding stoichiometry of four Chl molecules per WSCP tetramer. The same is true for natWSCP with its Chl *a*/*b* ratio of 9.5. The Chl *a*/*b* ratio was determined by fitting the measured absorption spectrum of natWSCP with an appropriate mixture of the spectra of recWSCP reconstituted with pure Chl *a* or pure Chl *b.* The absorption spectra of recWSCP reconstituted with Chl *a* and natWSCP are nearly superimposable (Figure 1). The small differences seen, e. g. the shoulder at 460 nm or the slightly higher absorption at 440 nm of natWSCP, can be attributed to the presence of the Soret absorption of Chl *b*.

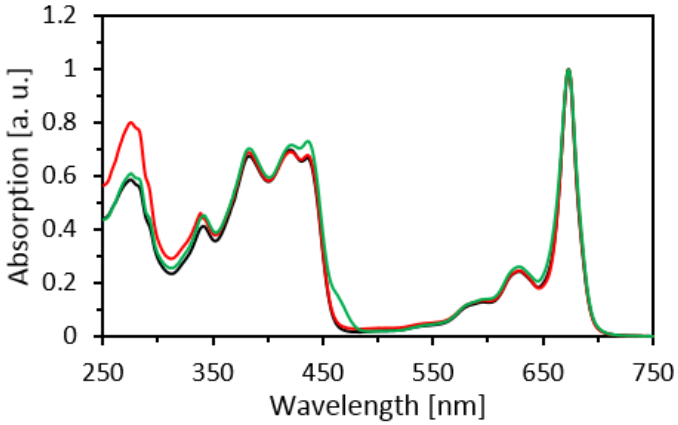

FIGURE 1: Absorption spectra of natWSCP (green) and recWSCP reconstituted with a five-fold molar excess of Chl *a* (black). The red spectrum displays absorption of recWSCP reconstituted with a four-fold excess of apoprotein over Chl *a* in presence of 2.5 % OG. The spectra were normalized to 1 at their Q_y maxima.

When a four-fold molar excess of recWSCP over Chl *a* was reconstituted in the presence of 2.5 % OG, the resulting absorption spectrum (red in Figure 1), normalized to the other spectra at 673 nm, exhibited a distinctly higher A_{280} value compared to those of natWSCP and of recWSCP reconstituted with a five-fold molar excess of Chl *a*. Calculation of the Chl/protein ratio yielded a value of 0.64 (± 10 %). Identical retention times in the SEC purification step as well as a separation via native PAGE of the complexes reconstituted by the two procedures (see Figure S2), indicate that both complexes adopt the same tetrameric oligomerization state. Hence, most of the complexes reconstituted under limiting Chl *a* conditions presumably contain only two Chl *a* molecules per WSCP tetramer. To validate this stoichiometry, an intact protein ESI-MS was performed (Figure 2). This technique has proven to be a powerful tool for investigating pigment-protein complexes under almost native conditions and thus allowing not only the determination of molecular weights (MW) but also the assessment of Chl/protein stoichiometries (for a detailed review see Zhang *et al.*[38]).

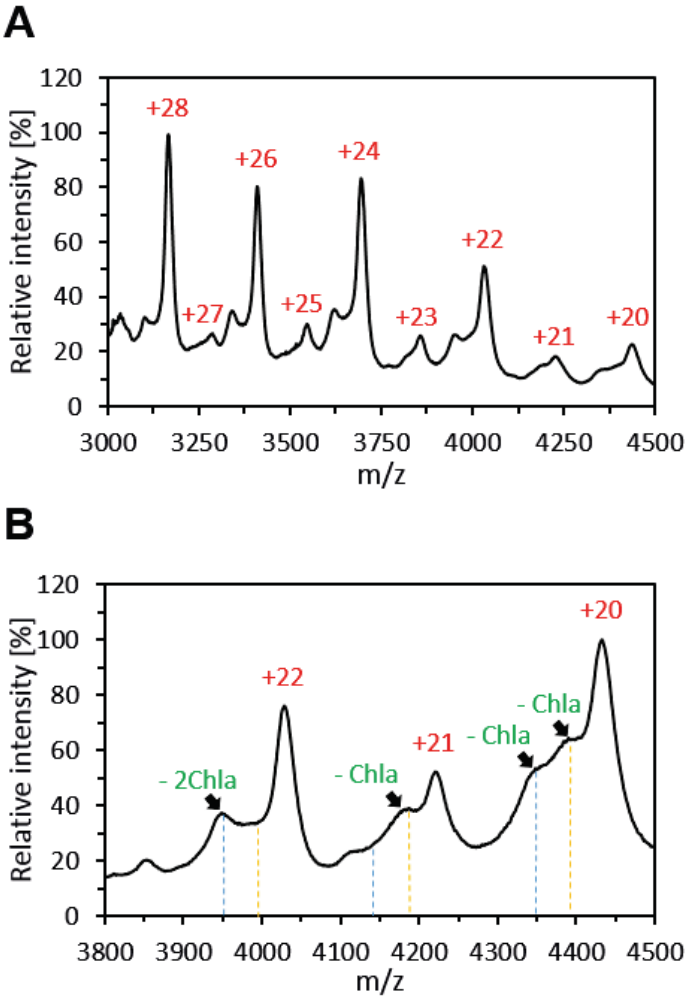

FIGURE 2: Intact protein ESI-MS spectra of recWSCP reconstituted with a four-fold excess of apoprotein over Chl *a* in presence of 2.5 % OG. After purification of the complex via SEC the sample was adjusted to either 10 mM ammonium formate (pH 3) + 20 % acetonitrile (A) or 10 mM ammonium acetate pH 4 (B) before performing native intact protein ESI-MS analysis. Charge states are given in red. Black arrows indicate the loss of Chl *a* molecules. The vertical blue lines are theoretical *m/z* values for a recWSCP tetramer without any Chls bound; the orange lines display a theoretical *m/z* value for a recWSCP tetramer binding one Chl *a* molecule.

The chosen intact ESI conditions at pH 3 lead to an ionization pattern (Figure 2A) consisting of nine charge states (from +20 to +28) in the high mass range (*m/z* 3000 – 5000). This relatively low number of charge states is a good indicator of intact and compact structures maintained in the gas phase.[39]

Our reported data reveal well resolved peaks with narrow widths and clear separated shoulder peaks leading to an easy assignment of charge states and hence to an optimum assignment of the oligomeric state of the WSCP and its number of Chls bound. Taking into account the MW of recWSCP (21,734 Da) and Chl *a* (893.5 Da) the MW of a tetrameric WSCP complex binding two Chl *a* molecules can be determined to be 88,723 Da. A theoretical calculation of *m/z* values for charge states from +20 to +28 for a protein assembly consisting out of four recWSCP apoproteins and two Chl *a* molecules is given in Table 1 in comparison to the values calculated for a recWSCP tetramer binding four Chl *a* molecules (MW of 90,510 Da) and to our experimental data obtained.

TABLE 1: Comparison of theoretical *m/z* values at charge states +20 to +28 between a recWSCP tetramer binding either two (2ChlaWSCP) or four Chl *a* molecules (4ChlaWSCP) and the experimental data.

experimental *m/z* values	**charge state**	**theoretical *m/z* values**	
		2ChlaWSCP	**4ChlaWSCP**
4438	+20	4437	4527
4228	+21	4226	4311
4031	+22	4034	4115
3857	+23	3859	3936
3694	+24	3698	3772
3545	+25	3550	3621
3409	+26	3413	3482
3287	+27	3287	3353
3165	+28	3170	3234

As evident from Figure 2 all calculated *m/z* values corresponding to a recWSCP tetramer binding two Chl *a* molecules are represented by our experimental data. Calculation of the experimental mass yields a MW of 88,692 ± 60 Da, a value in good agreement with the theoretical MW of a recWSCP tetramer carrying two Chl *a* molecules. Moreover there is no evidence for the presence of recWSCP tetramers binding four Chl *a* molecules since no peaks are observed at the corresponding charge states. Shoulder peaks at even charge states can be assigned to *m/z* values representing recWSCP tetramer binding four Chl *a* molecules; however, they show no good agreement with the theoretical *m/z* values. The shoulder peaks can better be explained by a loss of two Chl *a* molecules from protein ions representing a recWSCP tetramer

binding two pigments since the mass differences between the major and minor peaks are ≈ 1800 Da. This MW can be determined by calculating the mass difference between the two neighboring peaks at each charge state. For example the two resolved signals at charge state +24 exhibit an *m/z* difference of ≈ 74, which corresponds to a mass difference of 24 × 74 ≈ 1800 Da. Subsequent ESI-MS analysis at pH 4 in the absence of acetonitrile (Figure 2B) resulted in a charge state reduction (only charge states +20 to +22 are shown for a better comparison) exhibiting narrow peak widths and well resolved shoulder peaks. The shoulder peaks at each charge state indicate the loss of one or two Chl *a* molecules, respectively, which is in good agreement with the theoretical charge state distribution of a tetrameric recWSCP without any Chls bound (blue lines Figure 2B) and a tetrameric recWSCP carrying one Chl *a* molecule (orange lines Figure 2B). Especially the two shoulder peaks at charge state +20 indicate a consecutive loss of two Chl *a* molecules from a recWSCP tetramer giving a strong indication for the presence of a recWSCP tetramer binding two Chl *a* molecules.

In Figure 2A, the larger intensities of peaks representing even charge states compared to the low-intensity odd charge states is intriguing. In principle, this could be interpreted to indicate the presence of mostly recWSCP dimers with only one Chl *a* molecule bound that can give rise only to even charge states, and only small amounts of tetrameric WSCP with 2 Chls bound that can give rise to either even or odd charge states. However, we can exclude dimeric WSCP in the samples applied to ESI analysis since no dimers were detectable in SEC profiles or native PAGE (see Figure S2). Therefore, the dimers presumably form by dissociation of tetramers during the relatively harsh conditions in the electrospray ionization process required to obtain a good signal. Notably, under less denaturing conditions (pH 4, no acetonitrile) the differences are smaller between the peak intensities of even and odd charge states. If the assumption of tetramers dissociating into dimers during ionization is correct then this dimerization must result in two dimers each carrying 1 Chl. Given the strong coupling between the two Chls in 2ChlaWSCP (see below) one would expect a dissociation into a protein dimer carrying 2 Chls and 2 recWSCP monomers. However we do not see any indication of a dimer with 2 Chls. This point needs further inspection. Taken together, there is no indication in the 2ChlaWSCP ESI-MS data of protein tetramers with 4 Chls or protein dimers with 2 Chls. Therefore, the ESI-MS data are consistent with the 2ChlaWSCP stoichiometry deduced from the absorption data (see above) and confirmed by the ability of 2ChlaWSCP to bind more Chl if exposed to thylakoids (see Figure 8 below).

Tetrameric WSCP binds 1 or 2 pairs of tightly coupled Chls. In principle the two pigments bound by this substoichiometric complex (2ChlaWSCP) could occupy any of the four binding sites, which would lead to a mixture of strongly and weakly interacting Chls in the complex. To determine the arrangement of the two Chls in 2ChlaWSCP, Vis-CD spectra were measured, which reflect the excitonic Chl-Chl interactions. Native and both recombinant WSCPs with 2 or 4 Chls per tetramer give rise to spectra that are nearly identical in shape (Figure 3), in particular at the Q_y position where the CD signals have been attributed to the characteristic open sandwich arrangement of the Chls bound.[12,40] To evaluate the percentage of Chls undergoing strong excitonic interactions in 2ChlaWSCP, all Vis-CD spectra shown in Figure 3 have been normalized to their corresponding Q_y absorption band. The three spectra show virtually the same signal intensities (less than 10% difference).

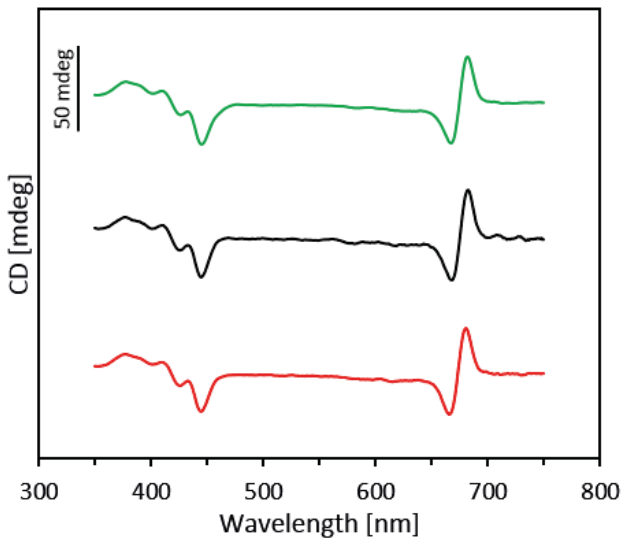

FIGURE 3: Vis-CD spectra of natWSCP (green), 4ChlaWSCP (black) and 2ChlaWSCP (red). The spectra were normalized to the maximum of the Chl Q_y absorption band and vertically shifted for ease of comparison.

In natWSCP and 4ChlaWSCP all the Chls have to be in the open sandwich conformation due to the 1:1 Chl/protein ratio. Because of the very similar CD signals, therefore, the same has to be true for 2ChlaWSCP. Consequently, in the substoichiometric complexes two tightly coupled adjacent Chl binding sites are occupied and the other two are open. This conclusion is also in agreement with the unchanged Q_y maximum at 673 nm observed in the 2ChlWSCP absorption spectrum reported in Figure 1, which in case of weakly interacting Chls would be red-shifted to values closer to the site energy of Chl *a*. The latter has been reported to be 677 nm in Class IIa WSCP by T. Renger and coworkers.[40]

CD spectra have been collected also in the UV in order to assess the secondary protein structure in dependence on the number of Chls bound. In this spectral region the dichroism of the Chls has a low intensity and can be neglected in comparison to the strong signal arising from the peptide bonds, allowing to assign the observed differences to variations in the secondary structure.[41] To ease the comparison of the rather similar signals, normalized CD spectra are shown in Figure 4A. The most intense signal is a negative band between 190 and 220 nm, in good agreement with the high content in β-strands[42] seen in the X-ray structure.[15]

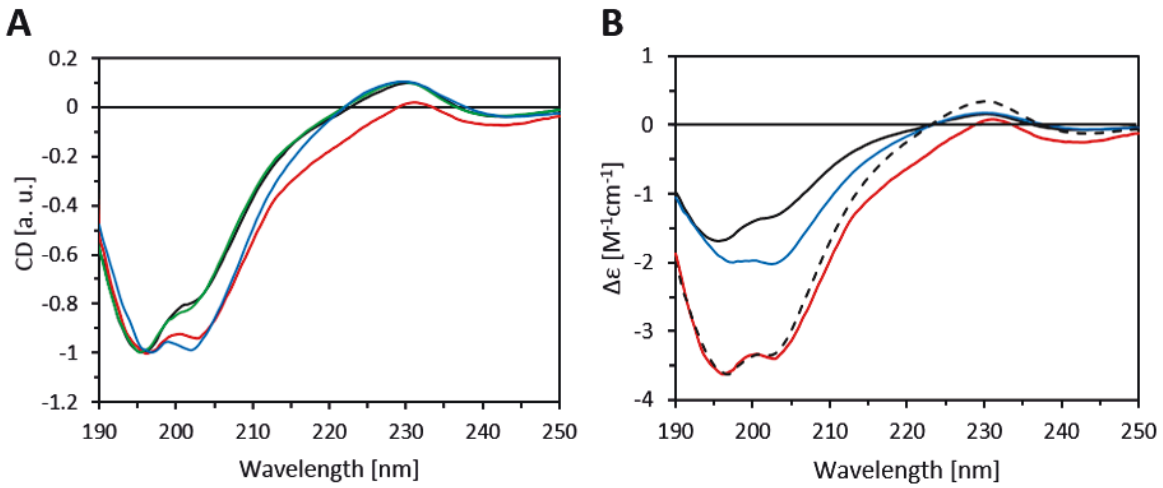

FIGURE 4: (A) UV-CD spectra of natWSCP (green), 4ChlaWSCP (black), 2ChlaWSCP (red) and recWSCP (cyan). The spectra were normalized to -1 at the minima. (B) Comparison of the UV-CD spectrum of 2ChlaWSCP (red) with a sum of the spectra of 4ChlaWSCP (black) and recWSCP (cyan) at a ratio of 1:1.2 (black dash).

In this band two negative peaks are seen at 196 nm and 203 nm, whose relative intensities depend on the Chl content. The 196 nm peak is predominant in the complexes containing 4 Chls; in this case, only a weak shoulder appears at 203 nm. By contrast, the UV-CD of recWSCP exhibits comparable intensities of the 196 and 203 nm peaks. Intriguingly the 2ChlaWSCP UV-CD spectrum appears to be an intermediate between these two profiles with regard to the negative maxima at 196 nm and 203 nm and can be simulated with a sum of the 4ChlaWSCP and recWSCP spectra in a 1:1.2 ratio (Figure 4B).

The UV-CD spectra without normalization (see Figure S3) were used to estimate the secondary structure contents by using the BeStSel algorithm, specifically optimized for β-strand rich proteins.[36] The fittings of the experimental spectra are satisfactory (see Figure S3) and

indicate a prevalence of antiparallel β-strands (34 % in the 4ChlaWSCP and 31 % in recWSCP). As expected from the X-ray structure[15] the prevailing twisting angles of the β-strands are positive, leading to right-hand twisted structures. The majority of the β-strands are predicted to have an intense twist (with a twisting angle larger than +23°), while a minor fraction (6 % in 4ChlaWSCP and 7 % in recWSCP) is assigned to the more common relaxed structures (hence with twisting angles between +3° and +23°).

Since the spectroscopic comparison of native and both recombinant WSCP versions showed a close similarity with regard to their absorption and Vis-CD spectra but differences in UV-CD spectra, the question arose of whether these alterations of the secondary structure affect the stability of the substoichiometric WSCP. We compared recombinant 4ChlaWSCP and 2ChlaWSCP with regard to heat resistance, tolerance against extreme pH values and the ability to protect the bound Chls against photodynamic processes.

Tetrameric WSCP with only 2 Chls is highly stable. As previously reported, class-II WSCPs are heat stable.[3–5] Schmidt *et al.*[1] have shown that this is also true for recombinant 4ChlaWSCP. As shown in Figure 5, 2ChlaWSCP is as resistant to heat treatment as its counterparts containing 4 Chls. After boiling treatment (5 min) in aqueous buffer solution (20 mM sodium phosphate pH 7.8), neither the absorption nor the Vis-CD spectrum of 2ChlaWSCP show significant changes. Also, the elution behavior in size-exclusion chromatography remains unchanged after boiling treatment (see Figure S4). We cannot exclude that (some of) the tetrameric complexes dissociate at 100 °C but if they do the dissociation is reversible and upon cooling all the 2ChlaWSCP material is tetrameric again.

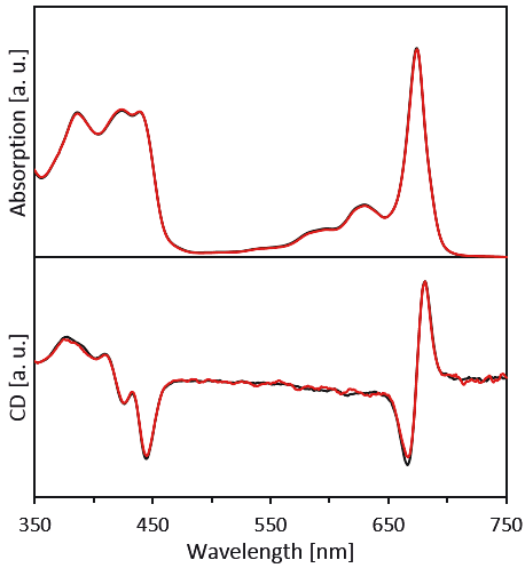

FIGURE 5: Heat stability of 2ChlaWSCP. Absorption (top) and Vis-CD (bottom) spectra of 2ChlaWSCP before (black) and after (red) a 5 min boiling treatment. The spectra were normalized to 1 at the Q_y maxima.

To further characterize the stability of the complex, both recombinant WSCPs have been treated for 1 h under extreme pH conditions, namely pH 0 and 14. Also in these cases, the complexes seemed to be unaffected in their optical properties (Figure 6), regardless of whether 2 or 4 Chls are bound. Only slight alterations in absorption and Vis-CD are visible, particularly upon incubation at pH 14. We conclude that both 4ChlaWSCP and 2ChlaWSCP tolerate extreme pH values.

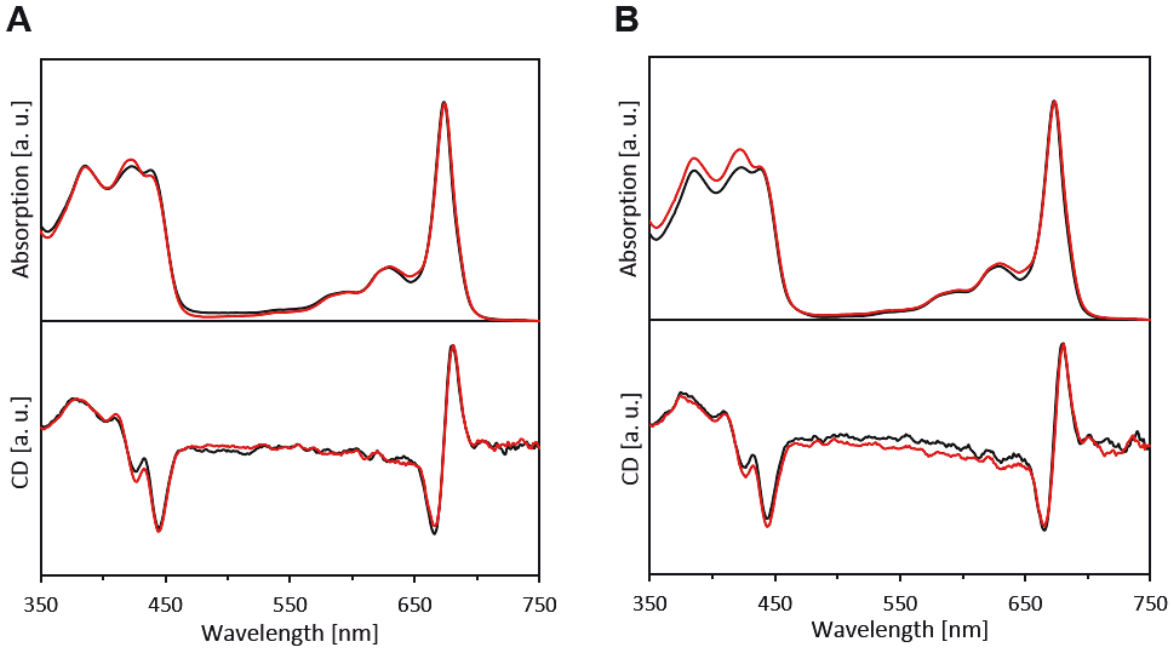

FIGURE 6: pH stability of 4ChlaWSCP (A) and 2ChlaWSCP (B). Absorption (top) and Vis-CD (bottom) spectra at pH 0 (black) and pH 14 (red). Both recombinant WSCPs were incubated for 1 h at 23 °C and 500 rpm (Thermomix comfort, Eppendorf). pH was adjusted by adding 1 N HCl or 1 N NaOH. The spectra were normalized to 1 at the Q_y maxima.

The results so far on heat and pH treatments demonstrate that 2ChlaWSCP, although lacking two additional Chls, possesses the same extraordinary stability as 4ChlaWSCP. Even though WSCP does not contain any carotenoids, it was previously shown[1] that 4ChlaWSCP is also able to protect its bound Chls to some extent against photodynamic damage. We asked the question whether WSCP is also able to protect its Chls if only 2 binding sites are occupied. Since Schmidt *et al.*[1] used a different procedure for preparing WSCP (refolding the protein from a guanidinium hydrochloride solution followed by a sucrose gradient purification), we repeated the photostability measurements with both 4Chla- and 2ChlaWSCP. Both recombinant WSCP complexes and detergent-dissolved (2 % OG) Chl *a* as a control in 20 mM sodium phosphate pH 7.8 at the same Chl concentrations were illuminated with white light at 500 µmol m^{-2} s^{-1} of photons. Photodynamic damage was monitored by measuring the decrease of fluorescence intensity upon photooxidation of the Chls. After 1 h of light exposure 4ChlaWSCP and 2ChlaWSCP exhibited a loss of roughly 40 % and 32 %, respectively, of their Chl fluorescence (Figure 7) whereas the fluorescence of the detergent-dissolved Chl *a* was almost completely (96

%) gone. This shows that under the chosen conditions in both recombinant WSCP complexes the Chls are protected from photodynamic damage to a similar extent.

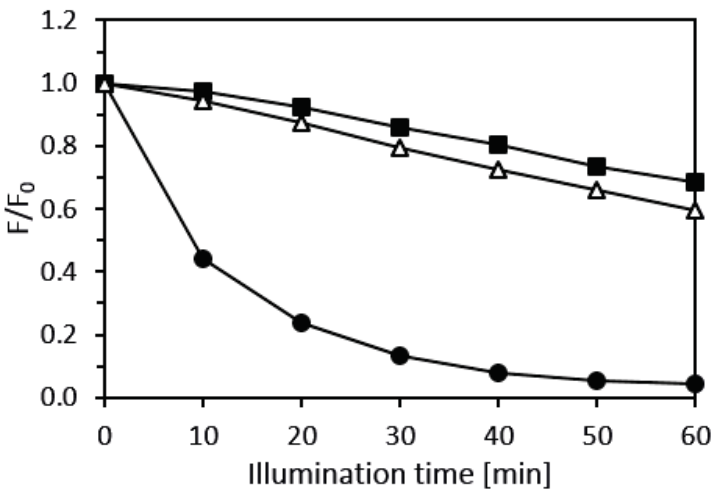

FIGURE 7: Photostability of 4ChlaWSCP (open triangles) and 2ChlaWSCP (filled squares). Both recombinant WSCPs as well as Chl *a* dissolved in 2 % OG (filled circle) were illuminated under medium-strong light conditions (500 µmol of photons m^{-2} s^{-1}) for 0-60 min. Emission maxima were measured upon excitation at 410 nm (F) and compared to the initial maximum before illumination (F_0). F/F_0 was plotted against illumination time.

2ChlaWSCP extracts 2 additional Chls from thylakoids. Satoh *et al.*[6] demonstrated for the first time that WSCP apoprotein is capable to extract Chls from thylakoid membranes to form native-like complexes. Various recombinant class-II WSCPs have been reconstituted by incubating their apoproteins with thylakoids.[5,12,13,19,21] As 2ChlaWSCP lacks two Chls, hence possesses two free Chl binding sites, the question arose whether the substoichiometric complex is still able to extract Chls from a thylakoid membrane suspension and fill its free binding sites. To address this question, 2ChlaWSCP was incubated with thylakoids and the absorption spectra were compared before and after incubation (Figure 8).

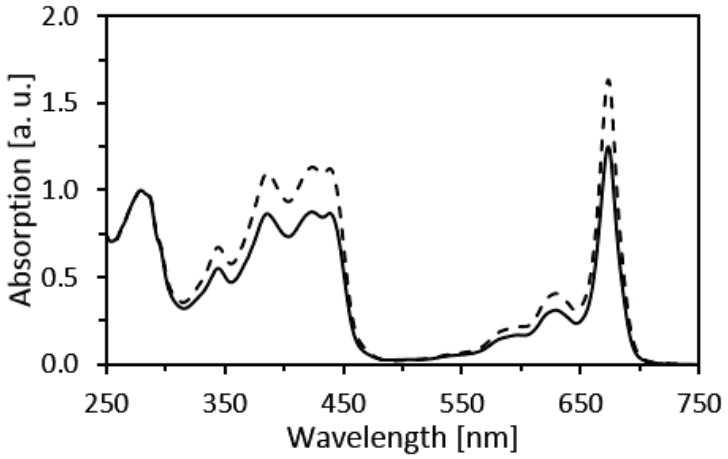

FIGURE 8: Chl extraction capability of 2ChlaWSCP from thylakoid membranes. Absorption spectra measured before (solid line) and after incubation (dashed line) with thylakoid membranes. The spectra were normalized at 280 nm. Incubation was carried out by adding thylakoid suspension (Chl *a/b* = 2.3) to 2ChlaWSCP in aqueous buffer solution (20 mM sodium phosphate pH 7.8) at a three-fold molar excess of Chls over the free Chl binding sites. After 1 h of incubation at 23 °C and 1000 rpm (Thermomix comfort, Eppendorf), the reaction mixture was centrifuged (5 min, 14,000 ×*g*, RT) and the supernatant purified via SEC.

The absorption spectrum after thylakoid incubation exhibits distinctly higher Q_y and Soret absorption bands compared to that of the 2ChlaWSCP before incubation, indicating Chl uptake by the substoichiometric WSCP. The Chl/protein ratio rose from 0.62 before incubation with thylakoids to 0.93 afterwards, demonstrating that most of the 2ChlaWSCP complexes were able to fill their two open Chl binding sites with Chls extracted from thylakoids.

DISCUSSION

Chl stoichiometries. In the present work we have confirmed the findings of Bednarczyk *et al.*[7] that class-IIa recombinant WSCP binds four Chls per tetramer like class-IIb, by contrast to previous reports.[1,6] Furthermore, for the first time we have shown by means of absorption analysis that this is indeed the binding stoichiometry of native class-IIa WSCP. Earlier calculations of Chl binding stoichiometries in WSCP relied on a comparison of the amounts of Chls and WSCP apoproteins after extracting the pigments from WSCP complexes with organic solvents and/or detergents. Since the Chls are tightly bound to the WSCP complexes, we assume that in previous studies by others and us on Chl to protein stoichiometries, the extraction of the Chls was not quantitative, leading to imprecise Chl/protein ratios. Another explanation is that

the purification of WSCP complexes prior to Chl extraction was not sufficient leading to an over-estimation of the protein content. With our spectroscopic approach based on highly purified WSCP complexes, a separate quantification of Chl and protein after Chl extraction is obsolete. By determining the modified extinction coefficients of both Chls and protein present in WSCP complexes, we were able to calculate Chl/protein binding stoichiometries directly and precisely from absorption spectra. The extinction coefficient of Chl *a* in WSCP resulted to be very close to the value of Chl *a* dissolved in ethanol. This is consistent with the highly asymmetric oscillatory strength distribution in the exciton states of the WSCP[30,40] and is likely due to compensative effects of the protein environment. A more significant difference was found between the extinction coefficients of Chl *b* in WSCP and in ethanol, which may be due to the different exciton coupling and/or to specific protein interactions. Since WSCP, native or recombinant, of both classes (IIa and IIb) contains 4 Chl per apoprotein tetramer, the differences between the two classes are limited to the optical properties of the bound Chls[15] as well as to their different affinities to Chl *a* and *b*.[13,19]

Substoichiometric Chl binding. By modifying the reconstitution procedure, we were able to obtain substoichiometric complexes, in which only 2 Chls are bound per protein tetramer as verified by intact protein ESI-MS. Vis-CD spectra clearly show that all the Chls in the 2ChlaWSCP complex are involved in strong excitonic coupling and thus, in the open sandwich configuration. So, if we consider the tetrameric WSCP as a dimer of protein dimers,[15] the 2ChlaWSCP would contain one dimer binding a tightly coupled Chl pair and the other dimer would contain two empty Chl binding sites (Figure 9).

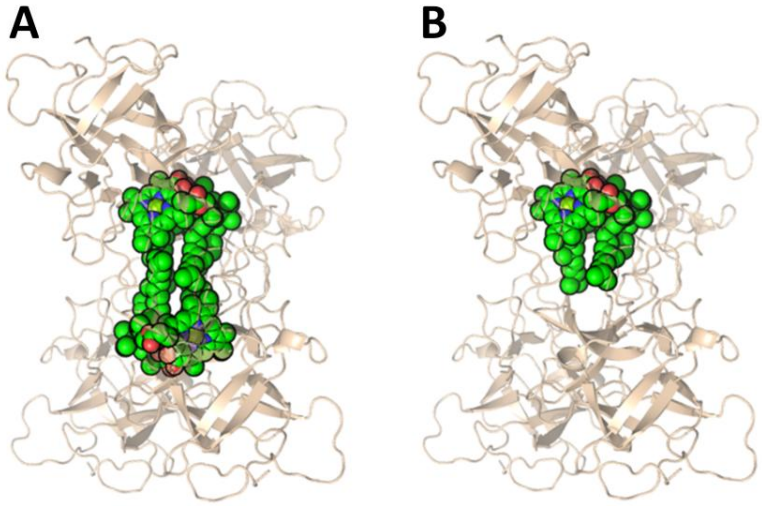

FIGURE 9: Structure of 4ChlaWSCP (A) and 2ChlaWSCP (B). *Brassica oleracea* WSCP (PDB entry 5HPZ)[15] is shown with Chls *a* in green spheres and the polypeptide secondary structure in wheat cartoon.

Remarkably we were unable to obtain a binding ratio lower than 2 Chls per tetramer, hence it seems that one Chl dimer is a minimum requirement for the stabilization of the tetrameric complex. Moreover, we never observed substantial amounts of dimeric WSCP composed of 2 apoproteins with 2 Chls. The WSCP apoproteins form no stable tetramers in the absence of bound Chls, as evident from the size exclusion chromatography (Figure S2). Consequently, Chl binding is a key step in the formation of stable tetramers. Two different paths can be envisioned for tetramer formation: either labile pigmented monomers form first and then assemble into tetramers containing 2 or 4 Chls, or labile apoprotein tetramers form and are then stabilized by binding at least 2 Chls. As a matter of statistics, one would expect that in reconstitutions with a four-fold molar excess of WSCP apoprotein over Chl most of the protein will stay non-pigmented (as seen in Figure S2A) and the rest will form pigment-protein complexes with the smallest possible Chl/protein ratio that would lead to stable complexes. This ratio appears to be 2 Chl per protein tetramer. Statistically, it is unlikely that significant amounts of tetrameric complexes containing 4 Chls will form under these conditions.

Both of the hypothetical pathways mentioned above are in agreement with the finding that upon Chl binding there is a detectable change in the protein secondary structure, as highlighted by the UV-CD spectra (Figure 4). Roughly half of this spectral change is seen upon the binding of 2 Chls compared to the binding of 4 Chls. This cannot be explained by a mixture of apoprotein and fully pigmented tetramers in the 2ChlaWSCP preparation, as this is ruled out by size exclusion chromatography (Figure S2) and ESI-MS analysis (Figure 2). The gradual change in protein structure upon the binding of 2 or 4 Chls suggests that each Chl pair modifies the secondary structure of its local protein dimer that it is bound to but not the other one. This may strengthen protein-protein interactions and, thus, contribute to the stability of WSCP.

The finding that one Chl dimer seems to be necessary for the stabilization of the tetrameric complex points in the direction of the hypothesis according to which the pre-formation of this Chl dimer between two labile pigmented monomers is necessary prior to the closure of the WSCP tetramer and is probably the initial step that triggers the oligomerization process. From inspecting the crystallographic structure of WSCP[15] it clearly appears that the Chl dimers contribute directly to the stabilization of the subunit dimers that compose the tetrameric complex. A calculation done with the PISA software[43] on the crystal structure of *B. oleracea* WSCP[15] indicates that each Chl pair contributes to more than 40 % of the surface interaction area of the two protein subunits binding this Chl dimer. The close distance and the reciprocal orientation of the two Chls constituting the open sandwich, in addition to giving rise to this

consistent interaction surface, have been shown to generate a strong attractive Coulomb coupling in the closely related *L. virginicum* WSCP structure.[44]

Moreover, every Chl interacts with both protein subunits within each dimer. In particular the C-13[1] oxo group of the isocyclic ring of each Chl forms a hydrogen bond with a water molecule that is also hydrogen bonded to a highly conserved glutamine residue (Q53 in *B. oleracea*) of the other protein subunit of the dimer. This kind of hydrogen bonding has been proven to be critical for the assembly of the accessory light harvesting complex (LH2) from *Rhodobacter sphaeroides*[45] and proposed to be equally fundamental for the stabilization of the inner core light harvesting complex (LH1)[46] and of photosystem I[45] (see Figure S5). For sterical reasons, this structural feature has been shown[45] to be more frequent for Chls ligated from the thermodynamically unfavorable β-side.[18] We propose that in WSCP the [illegible]-ligated Chls help to stabilize the complex in a similar way. As proposed by Horigome *et al.,*[14] this unusual Chl ligation mode may also be a prerequisite for the remarkable ability of WSCP to extract Chls from thylakoid membranes.

All the considerations above suggest that the protein dimers, each with their Chl pair, represent the "functional units" of WSCP. This notion is corroborated by the comparison of the structure of class-IIa and class-IIb WSCPs, in which the principal dimers are perfectly superimposable, while the organization of the two dimers leading to the tetramer is not homologous.[15] This fact indicates a less conserved interaction between the two dimers, making their relative orientation less pivotal in the stabilization of the complex.

Although protein dimers may be the "functional units" of WSCP, such dimers have never been observed experimentally in substantial amounts. Fluorescent protein bands migrating between WSCP tetramer and apoprotein bands have been seen under mildly denaturing conditions in PAGE containing 0.15 % (w/v) Deriphat[4] but not under detergent free conditions.[6] Thus, tetrameric WSCP must be more stable than a dimeric form, even if only one of the two dimers contains Chls. This is corroborated by the fact that 2ChlaWSCP virtually is as stable as 4ChlaWSCP. Thus, each Chl pair must also contribute to the stable binding of the opposing protein dimer, which in the case of 2ChlaWSCP contains two empty Chl binding sites. In fact, the phytol moieties of the Chls are in van der Waals contacts with a cluster of hydrophobic side chains constituted by W151 and L152 of the subunit binding the Chl and I37, L38, and F40 of the opposing subunit of the other dimer. Presumably, these hydrophobic interactions in the WSCP core suffice to stabilize the complex with either 2 or 4 phytol moieties present.

Stability and flexibility of 2ChlaWSCP. Even though 2ChlaWSCP appears to be as stable as 4ChlaWSCP towards thermal dissociation, protein denaturation at extreme pH, or photodamage of the Chls, it is flexible enough to allow two more Chls into the empty binding sites in its hydrophobic interior cavity upon mere contact with Chl-containing membranes or detergent micelles. One possible scenario for this binding step is a movement of the two dimers away from one another, creating an opening for the passage of the Chls to be bound. Such a "breathing" movement may be highly unfavorable as long as the WSCP is in aqueous solution because it would expose part of the hydrophobic interior of the complex to the aqueous environment. However, such a movement may be facilitated if WSCP comes into contact with the hydrophobic interior of a membrane or a micelle, forming at the same time a hydrophobic path for the Chls to be extracted from the membrane or micelle into the WSCP complex. Whatever the mechanism is for the uptake of another two Chls by 2ChlaWSCP, this process requires the complex to open up temporarily to allow access to its interior. This indicates that WSCP, at least the 2ChlaWSCP form, is less rigid than one would anticipate with regard to its extreme biochemical stability. This notion does not support the "diffusion barrier" model[1,14] used to explain the photostability of WSCP. In all other Chl-containing protein complexes in plants, the Chls are protected against photodynamic damage by the presence of carotenoids acting as quenchers of triplet-excited Chl or singlet-excited oxygen. WSCP does not contain any carotenoids. It has been hypothesized that instead the WSCP apoproteins form a diffusion barrier around the Chls blocking the access of oxygen and thus preventing the formation of highly reactive singlet oxygen. However, if even Chls are allowed into the hydrophobic interior of 2ChlaWSCP it is hard to imagine that oxygen is kept out. Consequently, a new explanation is needed for the protection of WSCP towards photodamage. In a forthcoming paper we will propose a different mechanism protecting WSCP-bound Chls against photooxidative degradation.

Biological function. Both the stability of WSCP towards photodamage and thermal dissociation and its ability to bind different numbers of Chls are consistent with the proposed WSCP function as a Chl scavenger.[13,19] As shown in this work, WSCP apoproteins are able to bind Chls to form a substoichiometric but still fully photoprotected and stable complex. Thus, WSCP is a useful scavenger even if only small, substoichiometric amounts of Chl are to be bound. These 2ChlaWSCP tetramers are able consecutively to bind another two Chls per tetramer, making WSCP a more efficient scavenger when larger amounts of Chl are around. This plasticity in the Chl-apoprotein stoichiometry without compromising Chl photoprotection or

complex stability may help to protect plant cells or tissues threatened by photooxidative damage due to unbound Chls. However, how WSCP apoproteins meet their Chls (for instance in the organisms in which the protein has been localized in the roots[19]), and the mechanism by which the water-soluble protein extracts Chls that presumably are confined to membranes has yet to be explained. Also, the presumed Künitz protease inhibitor function of WSCP is likely to play a role. Although our data are consistent with the proposed role of WSCP as an efficient Chl scavenger, this can only be a partial answer to the question of its biological function. The fact that class-II WSCPs in different species are found in different plant organs and tissues and are expressed during different developmental stages supports the notion that individual WSCPs may be involved in different functions.

ACKNOWLEDGMENT

A.A. gratefully acknowledges the *Ing. Aldo Gini* foundation for supporting his stay in Germany with a travel grant.

ABBREVIATIONS

Chl, chlorophyll; CD, circular dichroism; ESI-MS, electrospray ionization mass spectrometry; OG, octyl-β-D-glucopyranoside; RT, room temperature; PAGE, polyacrylamide-gel-electrophoresis; SEC, size-exclusion-chromatography; WSCP, water soluble chlorophyll protein; natWSCP, native WSCP; recWSCP, recombinant WSCP apoprotein; 2ChlaWSCP, substoichiometric WSCP complex binding two Chls *a*; 4ChlaWSCP, WSCP complex binding four Chls *a*.

REFERENCES

(1) Schmidt, K., Fufezan, C., Krieger-Liszkay, A., Satoh, H., and Paulsen, H. (2003) Recombinant water-soluble chlorophyll protein from *Brassica oleracea* var. *botrys* binds various chlorophyll derivatives. *Biochemistry 42*, 7427–7433.

(2) Oku, T., Yoshida, M., and Tomita, G. (1972) Heat stability of the phototransforming activity of *Chenopodium* chlorophyll protein. *Plant Cell Physiol. 13*, 183–186.

(3) Kamimura, Y., Mori, T., Yamasaki, T., and Katoh, S. (1997) Isolation, properties and a possible function of a water-soluble chlorophyll *a/b*-protein from Brussels sprouts. *Plant Cell Physiol. 38*, 133–138.

(4) Bektas, I., Fellenberg, C., and Paulsen, H. (2012) Water-soluble chlorophyll protein (WSCP) of Arabidopsis is expressed in the gynoecium and developing silique. *Planta 236*, 251–259.

(5) Takahashi, S., Uchida, A., Nakayama, K., and Satoh, H. (2014) The C-terminal extension peptide of non-photoconvertible water-soluble chlorophyll-binding proteins (class II WSCPs) affects their solubility and stability: Comparative analyses of the biochemical and chlorophyll-binding properties of recombinant *Brassica*, *Raphanus* and *Lepidium* WSCPs with or without their C-terminal extension peptides. *Protein J. 33*, 75–84.

(6) Satoh, H., Nakayama, K., and Okada, M. (1998) Molecular cloning and functional expression of a water-soluble chlorophyll protein, a putative carrier of chlorophyll molecules in cauliflower. *J. Biol. Chem. 273*, 30568–30575.

(7) Bednarczyk, D., Takahashi, S., Satoh, H., and Noy, D. (2015) Assembly of water-soluble chlorophyll-binding proteins with native hydrophobic chlorophylls in water-in-oil emulsions. *Biochim. Biophys. Acta - Bioenerg. 1847*, 307–313.

(8) Hirabayashi, H., Amakawa, M., Kamimura, Y., Shino, Y., Satoh, H., Itoh, S., and Tamiaki, H. (2006) Analysis of photooxidized pigments in water-soluble chlorophyll protein complex isolated from *Chenopodium album*. *J. Photochem. Photobiol. A Chem. 183*, 121–125.

(9) Yakushiji, E., Uchino, K., Sugimura, Y., Shiratori, I., and Takamiya, F. (1963) Isolation of water-soluble chlorophyll protein from the leaves of *Chenopodium album*. *Biochim. Biophys. Acta 75*, 293–298.

(10) Murata, T., Toda, F., Uchino, K., and Yakushiji, E. (1971) Water-soluble chlorophyll protein of *Brassica oleracea* var. *botrys* (cauliflower). *Biochim. Biophys. Acta 245*, 208–215.

(11) Satoh, H., Uchida, A., Nakayama, K., and Okada, M., (2001) Water-soluble chlorophyll protein in Brassicaceae plants is a stress-induced chlorophyll-binding protein. *Plant Cell Physiol. 42*, 906–911.

(12) Hughes, J. L., Razeghifard, R., Logue, M., Oakley, A., Wydrzynski, T., and Krausz, E. (2006) Magneto-optic spectroscopy of a protein tetramer binding two exciton-coupled chlorophylls. *J. Am. Chem. Soc. 128*, 3649–3658.

(13) Takahashi, S., Yanai, H., Nakamaru, Y., Uchida, A., Nakayama, K., and Satoh, H. (2012) Molecular cloning, characterization and analysis of the intracellular localization of a water-soluble chl-binding protein from Brussels sprouts (*Brassica oleracea* var. *gemmifera*). *Plant Cell Physiol. 53*, 879–891.

(14) Horigome, D., Satoh, H., Itoh, N., Mitsunaga, K., Oonishi, I., Nakagawa, A., and Uchida, A. (2007) Structural mechanism and photoprotective function of water-soluble chlorophyll-binding protein. *J. Biol. Chem. 282*, 6525–6531.

(15) Bednarczyk, D., Dym, O., Prabahar, V., Peleg, Y., Pike, D. H., and Noy, D. (2016) Fine tuning of chlorophyll spectra by protein-induced ring deformation. *Angew. Chemie Int. Ed. 55,* 6901–6905.

(16) Balaban, T. S., Fromme, P., Holzwarth, A. R., Krauß, N., and Prokhorenko, V. I. (2002) Relevance of the diastereotopic ligation of magnesium atoms of chlorophylls in Photosystem I. *Biochim. Biophys. Acta - Bioenerg. 1556*, 197–207.

(17) Balaban T. S. (2005) Relevance of the diastereotopic ligation of magnesium atoms of chlorophylls in the major light-harvesting complex II (LHC II) of green plants. *Photosynth. Res. 86,* 251-262.

(18) Oba, T., and Tamiaki, H. (2002) Which side of the π-macrocycle plane of (bacterio)chlorophylls is favored for binding of the fifth ligand? *Photosynth. Res. 74*, 1–10.

(19) Takahashi, S., Yanai, H., Oka-Takayama, Y., Zanma-Sohtome, A., Fujiyama, K., Uchida, A., Nakayama, K., and Satoh, H. (2013) Molecular cloning, characterization and analysis of the intracellular localization of a water-soluble chlorophyll-binding protein (WSCP) from Virginia pepperweed (*Lepidium virginicum*), a unique WSCP that preferentially binds chlorophyll *b* in vitro. *Planta 238*, 1065–1080.

(20) Nishio, N., and Satoh, H. (1997) A water-soluble chlorophyll protein in cauliflower may be identical to BnD22, a drought-induced, 22-kilodalton protein in rapeseed. *Plant Physiol. 115*, 841–846.

(21) Takahashi, S., Ono, M., Uchida, A., Nakayama, K., and Satoh, H. (2013) Molecular cloning and functional expression of a water-soluble chlorophyll-binding protein from Japanese wild radish. *J. Plant Physiol. 170*, 406–412.

(22) Etienne, P., Desclos, M., Le Gou, L., Gombert, J., Bonnefoy, J., Maurel, K., Le Dily, F., Ourry, A., and Avice, J.-C. (2007) N-protein mobilisation associated with the leaf senescence process in oilseed rape is concomitant with the disappearance of trypsin inhibitor activity. *Funct. Plant Biol. 34*, 895–906.

(23) Desclos, M., Dubousset, L., Etienne, P., Le Caherec, F., Satoh, H., Bonnefoy, J., Ourry, A., and Avice, J.-C. (2008) A proteomic profiling approach to reveal a novel role of *Brassica napus* drought 22 kD/water-soluble chlorophyll-binding protein in young leaves during nitrogen remobilization induced by stressful conditions. *Plant Physiol. 147*, 1830–1844.

(24) Halls, C. E., Rogers, S. W., Oufattole, M., Østergard, O., Svensson, B., and Rogers, J. C. (2006) A Kunitz-type cysteine protease inhibitor from cauliflower and Arabidopsis. *Plant Sci. 170*, 1102–1110.

(25) Ilami, G., Nespoulous, C., Huet, J.-C., Vartanian, N., and Pernollet, J.-C. (1997) Characterization of BnD22, a drought-induced protein expressed in *Brassica napus* leaves. *Phytochemistry 45*, 1–8.

(26) Boex-Fontvieille, E., Rustgi, S., von Wettstein, D., Reinbothe, S., and Reinbothe, C. (2015) Water-soluble chlorophyll protein is involved in herbivore resistance activation during greening of *Arabidopsis thaliana. Proc. Natl. Acad. Sci. U. S. A. 112*, 7303–7308.

(27) Boex-Fontvieille, E., Rustgi, S., Reinbothe, S., and Reinbothe, C. (2015) A Kunitz-type protease inhibitor regulates programmed cell death during flower development in *Arabidopsis thaliana*. *J. Exp. Bot. 66*, 6119–6135.

(28) Takahashi, S., Aizawa, K., Nakayama, K., and Satoh, H. (2015) Water-soluble chlorophyll-binding proteins from *Arabidopsis thaliana* and *Raphanus sativus* target the endoplasmic reticulum body. *BMC Res. Notes 8*, 365.

(29) Nakano, R. T., Yamada, K., Bednarek, P., Nishimura, M., and Hara-Nishimura, I. (2014) ER bodies in plants of the *Brassicales* order: biogenesis and association with innate immunity. *Front. Plant Sci. 5*, 73.

(30) Theiss, C., Trostmann, I., Andree, S., Schmitt, F.-J., Renger, T., Eichler, H. J., Paulsen, H., and Renger, G. (2007) Pigment-pigment and pigment-protein interactions in recombinant water-soluble chlorophyll proteins (WSCP) from cauliflower. *J. Phys. Chem. B 111*, 13325–13335.

(31) Gasteiger E., Hoogland C., Gattiker A., Duvaud S., Wilkins M. R., Appel R. D., and Bairoch, A. (2005) Protein identification and analysis tools on the ExPASy server. (In) John M. Walker (ed) The proteomics protoc. handbook, *Humana Press*, 571–607.

(32) Laemmli, U. K. (1970) Cleavage of structural proteins during the assembly of the head of Bacteriophage T4. *Nature 227*. 680–685.

(33) Booth, P. J., and Paulsen, H. (1996) Assembly of light-harvesting chlorophyll *a/b* complex in vitro. Time-resolved fluorescence measurements. *Biochemistry 35*, 5103–5108.

(34) Nakayama, K., Itagaki, T., and Okada, M. (1986) Pigment composition of chlorophyll-protein complexes isolated from the green alga *Bryopsis maxima. Plant Cell Physiol. 27*, 311–317.

(35) Porra, R. J., Thompson, W. A., and Kriedemann, P. E. (1989) Determination of accurate extinction coefficients and simultaneous equations for assaying chlorophylls *a* and *b* extracted with four different solvents: verification of the concentration of chlorophyll standards by atomic absorption spectroscopy. *Biochim. Biophys. Acta - Bioenerg. 975*, 384–394.

(36) Micsonai, A., Wien, F., Kernya, L., Lee, Y.-H., Goto, Y., Réfrégiers, M., and Kardos, J. (2015) Accurate secondary structure prediction and fold recognition for circular dichroism

spectroscopy. *Proc. Natl. Acad. Sci. U. S. A. 112*, E3095–E3103.
(37) Wintermans, J. F. G. M., and De Mots, A. (1965) Spectrophotometric characteristics of chlorophylls *a* and *b* and their pheophytins in ethanol. *Biochim. Biophys. Acta 109*, 448–453.
(38) Zhang, H., Cui, W., Gross, M. L., and Blankenship, R. E. (2013) Native mass spectrometry of photosynthetic pigment-protein complexes. *FEBS Lett. 587*, 1012–1020.
(39) Wen, J., Zhang, H., Gross, M. L., and Blankenship, R. E. (2011) Native electrospray mass spectrometry reveals the nature and stoichiometry of pigments in the FMO photosynthetic antenna protein. *Biochemistry 50*, 3502–3511.
(40) Renger, T., Trostmann, I., Theiss, C., Madjet, M. E., Richter, M., Paulsen, H., Eichler, H. J., Knorr, A., and Renger, G. (2007) Refinement of a structural model of a pigment-protein complex by accurate optical line shape theory and experiments. *J. Phys. Chem. B 111*, 10487–10501.
(41) Olszówka, D., Maksymiec, W., Krupa, Z., and Krawczyk, S. (2003) Spectral analysis of pigment photobleaching in photosynthetic antenna complex LHCIIb. *J. Photochem. Photobiol. B Biol. 70*, 21–30.
(42) Greenfield, N., Davidson, B., and Fasman, G. D. (1967) The use of computed optical rotatory dispersion curves for the evaluation of protein conformation. *Biochemistry 6*, 1630–1637.
(43) Krissinel, E., and Henrick, K. (2007) Inference of macromolecular assemblies from crystalline state. *J. Mol. Biol. 372*, 774–797.
(44) Renger, T., Madjet, M. E., Müh, F., Trostmann, I., Schmitt, F.-J., Theiss, C., Paulsen, H., Eichler, H. J., Knorr, A., and Renger, G. (2009) Thermally activated superradiance and intersystem crossing in the water-soluble chlorophyll binding protein. *J. Phys. Chem. B 113*, 9948–9957.
(45) Garcia-Martin, A., Kwa, L. G., Strohmann, B., Robert, B., Holzwarth, A. R., and Braun, P. (2006) Structural role of (bacterio)chlorophyll ligated in the energetically unfavorable *β*-position. *J. Biol. Chem. 281*, 10626–10634.
(46) Parkes-Loach, P. S., Majeed, A. P., Law, C. J., and Loach, P. A. (2004) Interactions stabilizing the structure of the core light-harvesting complex (LH1) of photosynthetic bacteria and its subunit (B820). *Biochemistry 43*, 7003–7016.

Supporting Information

Water-Soluble Chlorophyll Protein (WSCP) Stably Binds 2 or 4 Chlorophylls

Daniel M. Palm[§‡], Alessandro Agostini[§†‡], Stefan Tenzer[‖], Barbara M. Gloeckle[§], Mara Werwie[§], Donatella Carbonera[†], and Harald Paulsen[§*]

[§]Institute of General Botany, Johannes-Gutenberg University Mainz, Johannes-von-Müller-Weg 6, 55128 Mainz, Germany,

[†]Department of Chemical Sciences, University of Padova, Via Marzolo 1, 35131 Padova, Italy,

[‖] Institute for Immunology, University Medical Center Mainz, Langenbeckstr. 1, 55131 Mainz, Germany.

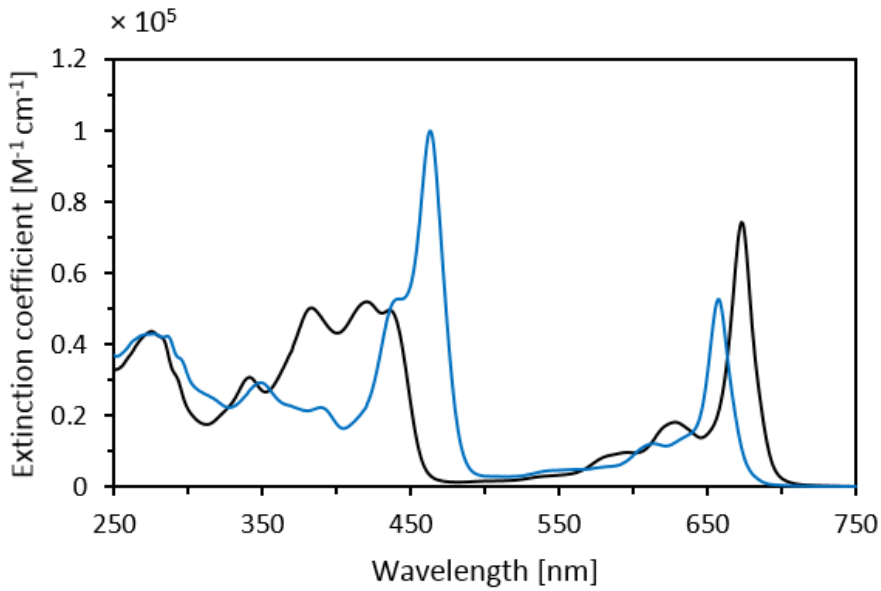

FIGURE S1: Absorption spectra of recWSCP reconstituted with a five-fold molar excess of Chl *a* (black) and Chl *b* (blue).

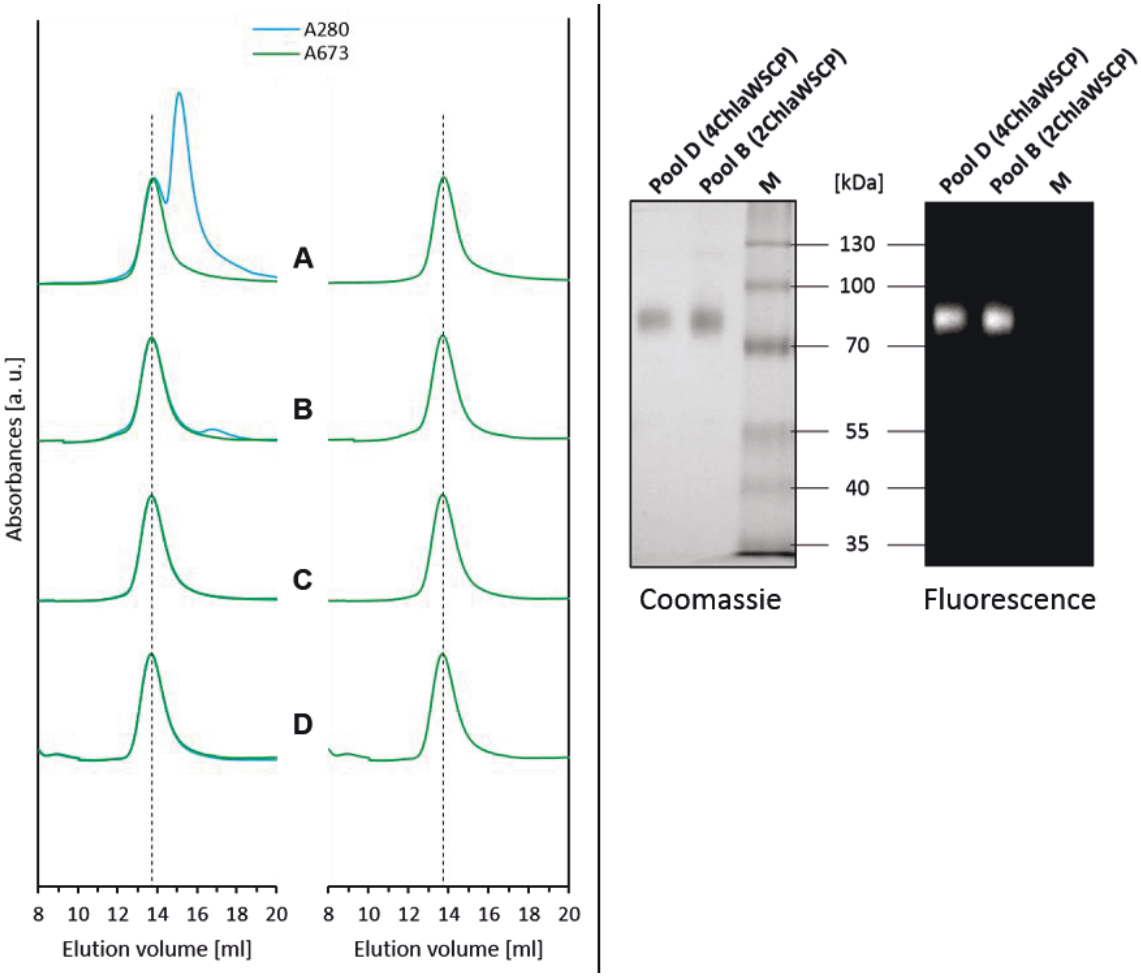

FIGURE S2: Size-exclusion chromatograms of the 2ChlaWSCP purification steps (A-C) and a 4ChlaWSCP (D) purification (left panel). Protein absorption and Chl *a* absorption were monitored at 280 nm and 673 nm, respectively. Left traces show an overlay of both recorded wavelengths; right traces show the recorded Chl *a* absorption exclusively. Dashed lines are centered to the elution volume corresponding to the maximum of Chl *a* absorption of recWSWCP reconstituted with a five-fold molar excess of Chl *a* yielding a Chl *a*/protein ratio of 1:1 (4ChlaWSCP). The SEC was performed on a Superose 12 10/300 GL prepacked column (GE Healthcare) equilibrated with 20 mM sodium phosphate pH 7.8 and operated on a BioRad NGC system at RT.
After incubation, the reaction mixture containing a four-fold molar excess of recWSCP apoprotein over Chl *a*, 2.5 % OG and 20 mM sodium phosphate pH 7.8 was purified via SEC (elution profile A). Fractions corresponding to an elution volume of 12.45 – 14.25 ml were pooled and subjected to a second purification step via SEC (elution profile B) to get rid of not reconstituted recWSCP apoprotein (second peak in (A) corresponding to an elution volume of 15.2 ml). After SEC, fractions corresponding to an elution volume of 13.05 – 14.85 ml were pooled (→ pool B) and analyzed spectroscopically. To validate its purity pool B was applied to a third SEC run (elution profile C).
To further characterize the purity and oligomerization state, pool B and as a comparison pooled WSCP fractions from SEC run (D) were subjected to a 10 % PAA-gel for separation via native PAGE (right-hand panel) using a detergent-free buffer (25 mM Tris, 192 mM Glycin). The samples were adjusted to the same Chl *a* concentration. Protein bands were stained with Coomassie and Chl *a* fluorescence was detected under UV radiation.

TABLE S1: Total amino acid analysis of 4ChlaWSCP. The complex was hydrolyzed in 6 M HCl. After incubation (24 h at 110 °C) amino acids were separated by cation exchange chromatography followed by a post-column derivatization with ninhydrin for photometric quantification. Since Genaxxon bioscience GmbH states that 1 to 10 % deviation from the expected number of amino acids is generally acceptable in the experimental set-up, only amino acids with less than 10 % deviation (bold type) were taken into account for concentration determination.
Determination of the protein concentration was done by calculating the total concentration of each amino acid divided by its theoretical number in sequence. In order to minimize the error of determination, the results of all amino acids taken into account for calculation were averaged. The protein concentration of 4ChlaWSCP calculated from the absorption at 280 nm was 16 µM, total amino acid analysis found 15.18 µM.

Amino acid	**number in sequence**	**number found**	**relative deviation in %**		**Calculated concentration per amino acid [µM]**
Asp/Asn (D/N)	**17**	**17.3**	**1.9**		**15.47**
Thr (T)	19	14.6	-23.1		11.67
Ser (S)	14	9.6	-31.7		10.37
Glu/Gln (E/Q)	**16**	**15.6**	**-2.5**		**14.80**
Pro (P)	**15**	**15.9**	**5.9**		**16.08**
Gly (G)	**16**	**16.2**	**1.1**		**15.36**
Ala (A)	**16**	**16.6**	**3.9**		**15.78**
Cys (C), (Cys(O3H); Cys2)	2	0.0	-100		----
Val (V)	**14**	**12.8**	**-8.2**		**13.94**
Met (M)	1	0.0	-100		----
Ile (I)(+ allo-Ile)	**15**	**14.4**	**-4.2**		**14.55**
Leu (L)	**13**	**13.8**	**6.3**		**16.14**
Tyr (Y)	6	5.2	-13.7		13.10
Phe (F)	**8**	**7.7**	**-3.4**		**14.66**
His (H)	7	2.1	-69.4		4.65
Lys (K)	**12**	**11.9**	**-0.8**		**15.06**
Trp (W)	3	0.0	-100		----
Arg (R)	6	4.7	-21.8		11.87
		Mean absolute deviation	**3.8 %**		
		calculated concentration			**15.18**

TABLE S2: Total amino acid analysis of 4ChlbWSCP. The complex was hydrolyzed in 6 M HCl. After incubation (24 h at 110 °C) amino acids were separated by cation exchange chromatography followed by a post-column derivatization with ninhydrin for photometric quantification. Since Genaxxon bioscience GmbH states that 1 to 10 % deviation from the expected number of amino acids is generally acceptable in the experimental set-up, only amino acids with less than 10 % deviation (bold type) were taken into account for concentration determination.
Determination of the protein concentration was done by calculating the total concentration of each amino acid divided by its theoretical number in sequence. In order to minimize the error of determination, the results of all amino acids taken into account for calculation were averaged. The protein concentration of 4ChlbWSCP calculated from the absorption at 280 nm was 12.5 µM, total amino acid analysis found 16.82 µM.

Amino acid	**number in sequence**	**number found**	**relative deviation in %**		**Calculated concentration per amino acid [µM]**
Asp/Asn (D/N)	**17**	**17.3**	**1.9**		**17.39**
Thr (T)	19	12.8	-32.4		11.37
Ser (S)	14	6.3	-54.9		7.59
Glu/Gln (E/Q)	**16**	**15.9**	**-0.3**		**16.77**
Pro (P)	**15**	**15.8**	**5.5**		**17.75**
Gly (G)	**16**	**16.2**	**1.1**		**17.03**
Ala (A)	**16**	**16.8**	**4.9**		**17.65**
Cys (C), (Cys(O3H); Cys2)	2	0.5	-74.7		4.25
Val (V)	**14**	**12.8**	**-8.3**		**15.43**
Met (M)	1	0.3	-70.2		5.01
Ile (I)(+ allo-Ile)	**15**	**14.5**	**-3.2**		**16.29**
Leu (L)	**13**	**13.3**	**2.6**		**17.25**
Tyr (Y)	**6**	**5.7**	**-4.3**		**16.11**
Phe (F)	**8**	**7.9**	**-0.8**		**16.70**
His (H)	7	1.2	-83.6		2.77
Lys (K)	**12**	**11.9**	**-0.7**		**16.69**
Trp (W)	3	1.2	-60.2		6.69
Arg (R)	6	4.3	-27.8		12.14
		Mean absolute deviation	**3.19 %**		
		calculated concentration			**16.82**

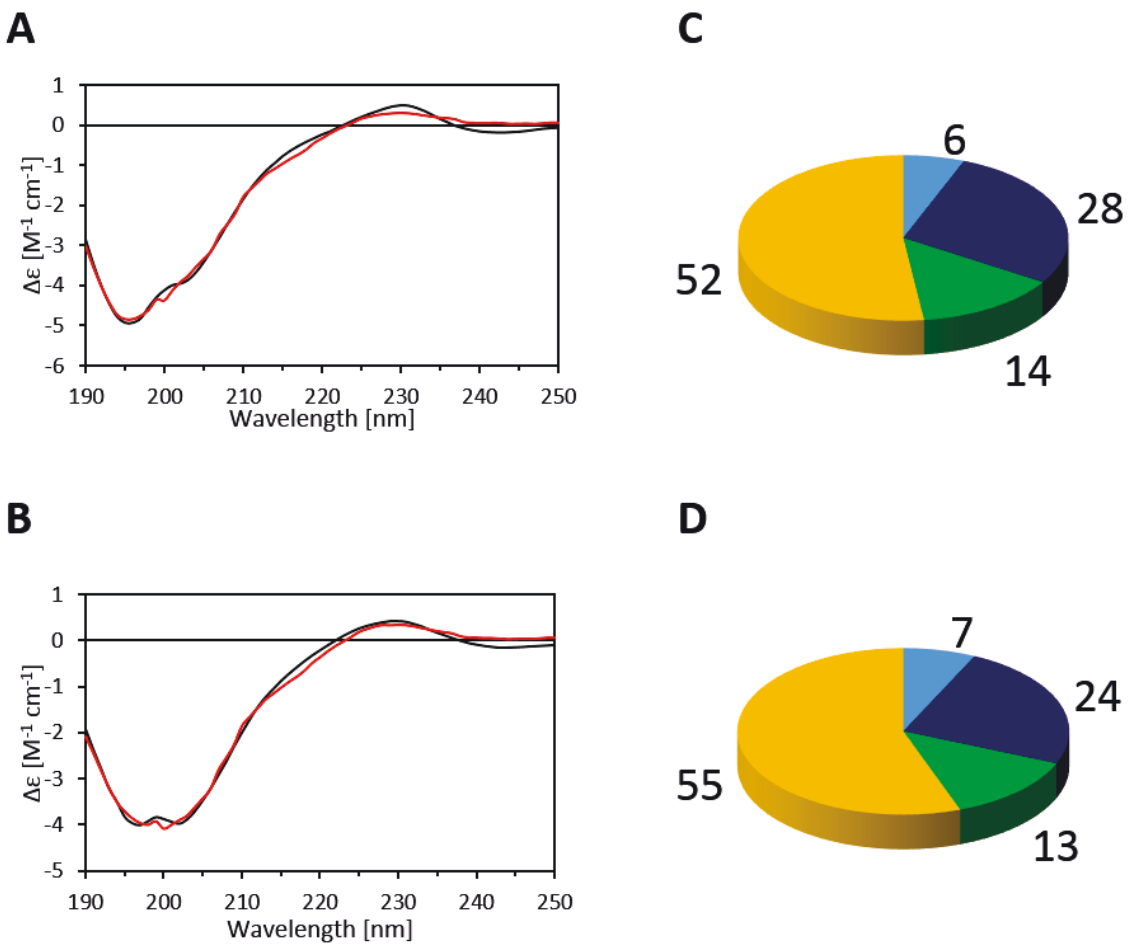

FIGURE S3: UV-CD spectra (left) and corresponding secondary structure determination (right) of 4ChlaWSCP (A and C) and recWSCP (B and D). Measured spectra (black) were analyzed and fitted (red) with the BeStSel algorithm[1] to calculate secondary structure elements. Light blue: Anti 2 (relaxed); dark blue: Anti 3 (right-hand-twisted); green: Turn; yellow: Others. Values are given in percent.

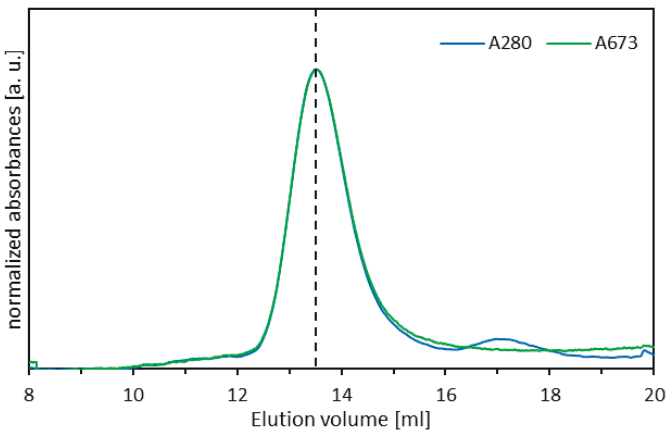

FIGURE S4: Size-exclusion chromatogram of 2ChlaWSCP after boiling treatment. Protein absorption and Chl *a* absorption were monitored at 280 nm and 673 nm, respectively.

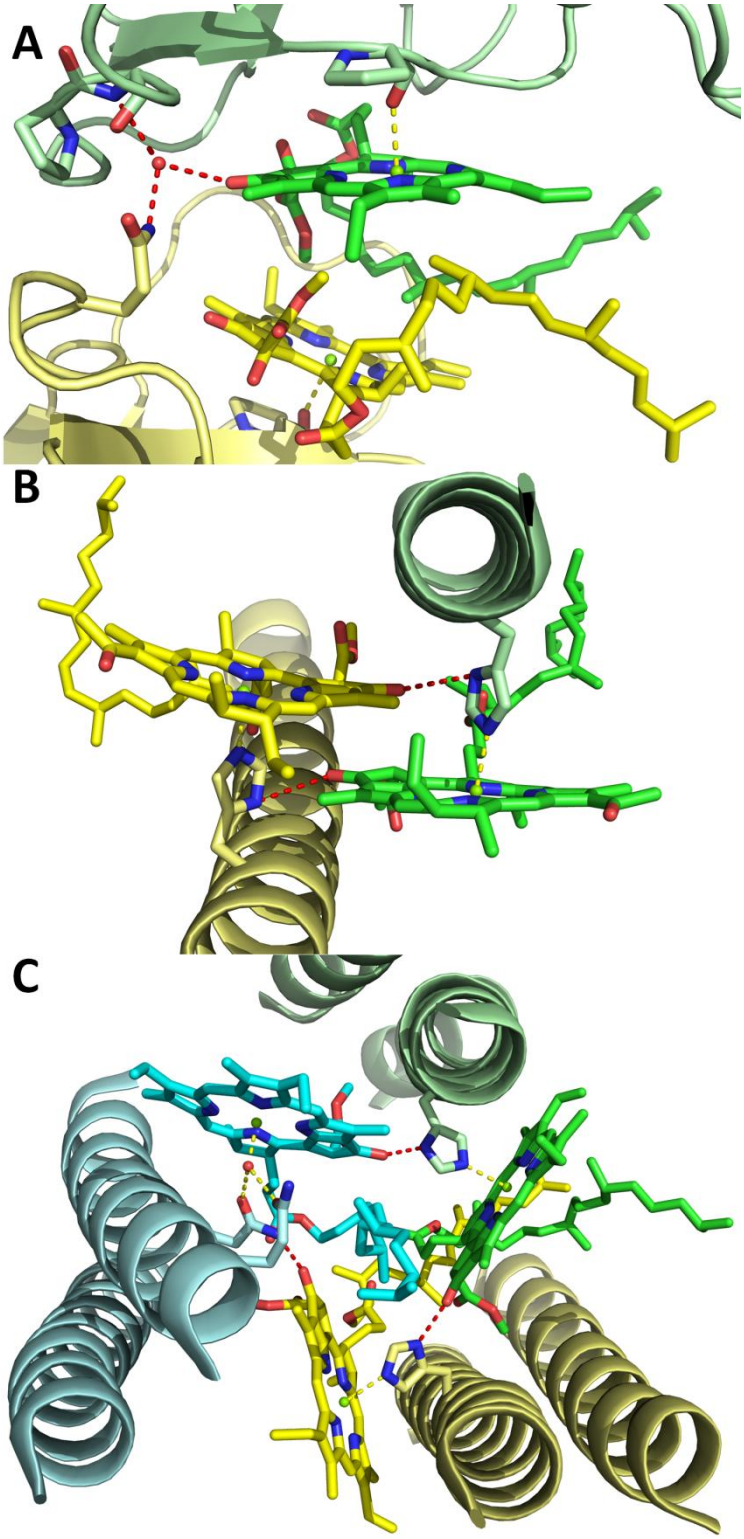

FIGURE S5: View of the hydrogen-bonding network of β-ligated (Bacterio)Chls *a* in the crystallographic structure of (A) *Brassica oleracea* WSCP (PDB entry 5HPZ)[2] (B) *Rhodoblastus acidophilus* LH2 complex (PDB entry 1NKZ)[3], and (C) *Pisum sativum* PSI-LHCI supercomplex (in particular the six N-terminal helices of the A subunit) (PDB entry 3LW5)[4]. The ligation to the central magnesium and the hydrogen-bonds involving the C-13[1] oxo are indicated by dashed lines (yellow and red, respectively). The (Bacterio)Chls *a* are colored according to the chain to which they are ligated, in order to highlight their hydrogen-bonds to residues belonging to adjacent loops (A) and helixes (B and C) differently colored.

An unusual role for the phytyl chains in the photoprotection of the chlorophylls bound to Water-Soluble Chlorophyll-binding Proteins.

Alessandro Agostini[1,2‡], Daniel M. Palm[2‡], Franz-Josef Schmitt[3], Marco Albertini[1], Marilena Di Valentin[1], Harald Paulsen[2*], and Donatella Carbonera[1*]

[1]Department of Chemical Sciences, University of Padova, via Marzolo 1, 35131 Padova, Italy

[2]Institute of General Botany, Johannes Gutenberg-University, Johannes-von-Müller-Weg 6, 55128 Mainz, Germany

[3]Institute of Chemistry, Technische Universität Berlin, Straße des 17. Juni 135, 10623 Berlin, Germany

[‡] These authors contributed equally

[*] Author to whom correspondence should be addressed.

DC Telephone: E-mail: donatella.carbonera@unipd.it

HP Telephone: E-mail: paulsen@uni-mainz.de

Abstract

Water Soluble Chlorophyll Proteins (WSCPs) from *Brassicaceae* are non-photosynthetic proteins which form a tetramer upon binding of chlorophyll (Chl) molecules. Although the physiological function of WSCPs is still unclear, it is likely to be related to their unusual biochemical stability and their resistance to photodegradation. WSCP-bound Chls are highly photostable, despite the lack of bound carotenoids known, in Chl containing photosynthetic proteins, to act as singlet oxygen and Chl triplet (^{3}Chl) quenchers. In order to get insight into the origin of this photo-resistance, the properties of the ^{3}Chl generated in WSCPs under excitation were investigated.

We found that, unlike the excited singlet states, which are excitonic states, the triplet state is localized on a single Chl molecule, as proven by the values of the hyperfine coupling constants measured by triplet ENDOR spectroscopy. Moreover, flash photolysis measurements revealed that the lifetime of the ^{3}Chl generated in WSCPs is comparable to that observed in other Chl-containing systems and is reduced in the presence of oxygen. In contrast to previous observations, we found that WSCP actually photosensitizes singlet oxygen with an efficiency comparable to that of Chl in organic solvent.

In this work we demonstrate that the observed resistance of the protein to singlet oxygen damage depends on the conformation of the phytyl moieties, which are interposed between the rings of the Chl dimers in WSCP, hindering the access of singlet oxygen to the oxidizable sites of the pigments.

1. Introduction

An unusual chlorophyll (Chl) binding protein in plants belonging to the *Brassicaceae* family was identified by Murata *et al.*(Murata et al. 1971; Murata & Murata 1971) This protein, called Water-Soluble Chlorophyll Protein (WSCP), strikingly differs from most (bacterio)Chl-containing proteins in that it is water-soluble rather than being inserted into membranes. The only other two water-soluble (bacterio)Chl-binding proteins known so far are the Fenna-Matthews-Olson (FMO) complex (Olson & Romano 1962) and the Peridinin-Chlorophyll *a*–Protein (PCP) complex (Song et al. 1976). However, unlike WSCP, both are involved in photosynthesis.

Recombinant WSCP have been successfully reconstituted in vitro with Chls to a tetrameric complex that biochemically and spectroscopically is equivalent to native WSCP.(Schmidt et al. 2003; Bektas et al. 2012; Satoh et al. 1998; Bednarczyk et al. 2015; Hughes et al. 2006; Takahashi et al. 2012) WSCP binds 4 molecules of Chl *a* (or *b*) per protein tetramer, as indicated by X-ray structures (Horigome et al. 2007; Bednarczyk et al. 2016)(figure 1). The induction of WSCP synthesis under stress conditions (Downing et al. 1992; Reviron et al. 1992; Nishio & Satoh 1997; Annamalai & Yanagihara 1999) and its ability to protect the bound Chls against photodynamic damage (Schmidt et al. 2003), led to the hypothesis of its functional role as Chl scavenger.(Takahashi et al. 2012; Takahashi et al. 2013) Alternatively, Boeux-Fontvieille *et al.*(Boex-fontvieille, Rustgi, Wettstein, et al. 2015; Boex-fontvieille, Rustgi, Reinbothe, et al. 2015) proposed that WSCP from *Arabidopsis thaliana* plays a role in herbivore resistance activation during greening and in programmed cell death at least during flower development. WSCP has been shown to have proteinase inhibitor activity,(Halls et al. 2006; Desclos et al. 2008) inhibiting for instance RD21 (Responsive to Desiccation),(Boex-fontvieille, Rustgi, Reinbothe, et al. 2015) a papain-like protease.(van der Hoorn et al. 2004; Koizumi et al. 1993)

The homotetrameric structure, showing a strict 222 symmetry in the X-Ray structure of *Lepidium virginicum* WSCP,(Horigome et al. 2007) forms a hydrophobic cavity in the center, occupied by four Chls. Unusually,(Balaban et al. 2002; Oba & Tamiaki 2002; Balaban 2005) these are bound from their β-side, a feature that could play a role in the stabilization of the tetramer(Palm et al. n.d.) as well as in the capability of the apo-protein to extract Chls directly from the thylakoid proteins(Satoh et al. 1998) where Chls are bound mostly from their α-side. The Chls share the same symmetric relationship of the homotetramer, with 2 Chls at a close distance (10 Å center to center) constituting an excitonic dimer, weakly coupled to the other dimer (ca. 20 Å center to center distance) (figure 1).

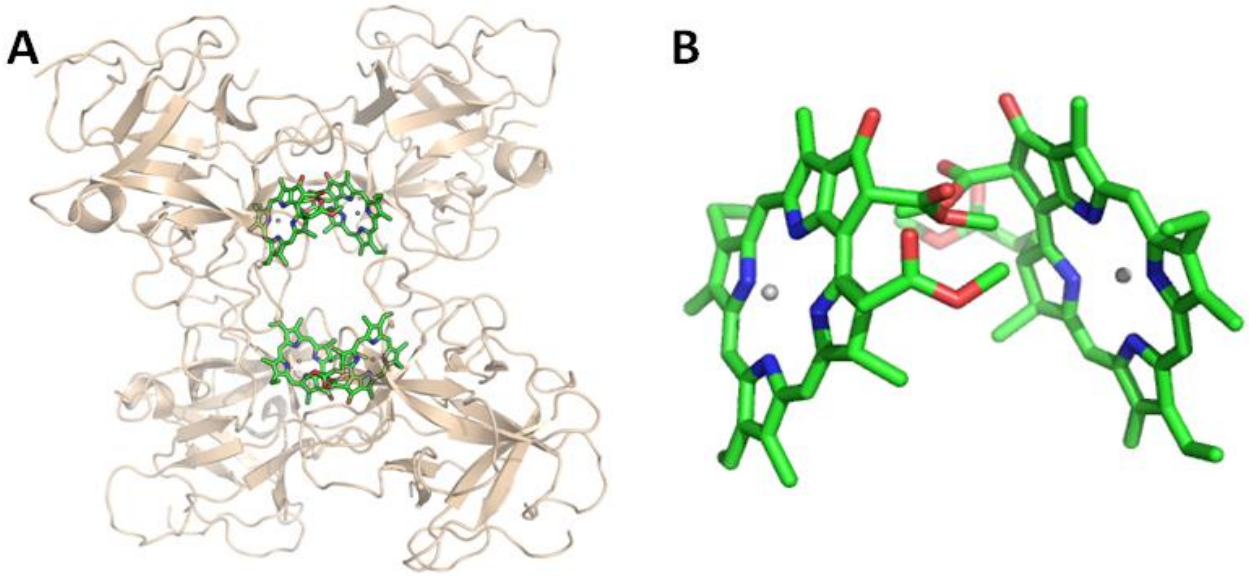

Figure 1: A Structure of *Lepidium virginicum* tetrameric WSCP (Horigome et al. 2007) with Chls *a* in sticks. **B** "Open sandwich" structure of Chl dimer. The phytyl chains have been omitted for clarity.

In the configuration adopted by the Chls in the protein, the excitation of the upper energy exciton band has a transition dipole moment that exceeds that of the lower energy band by almost one order of magnitude. (Theiss et al. 2007) This feature strikingly contrasts the properties of the excitons in strongly coupled pigments of light harvesting complexes and RCs, having most of the oscillator strength in the lower energy exciton state (van Amerongen et al. 2000). The "open sandwich" geometry of the dimer (Hughes et al. 2006) leads to an increase of the lifetime of the excited singlet state,(Schmitt et al. 2008) with a concomitant increase of the ISC probability and triplet yield. (Renger et al. 2009). In aerobic media, Chls are known to transfer the photoexcited triplet state energy to oxygen in less than 1 µs,(Küpper et al. 2002) resulting in the formation of highly reactive singlet oxygen ($^1O_2$). The quantum yield of such an energy transfer in solution approaches 100%,(Krasnovskii jr. 1994) because the natural lifetime of the Chl triplet state (^{3}Chl) is about 1.5 ms in most solvents.(Krasnovskii jr. & Kovalev 2014) In most chlorophyll-binding proteins, the formation of $^1O_2$ is prevented by carotenoids located close to the Chls. These carotenoids quench ^{3}Chl through triplet-triplet energy transfer.(Foote 1976; Siefermann-Harms 1987; Di Valentin, Salvadori, et al. 2013). In addition, carotenoids are also able to deactivate $^1O_2$ directly. (Di Mascio et al. 1991; Osto et al. 2007) Although WSCP does not contain any carotenoid, the bound Chls have been shown to be effectively resistant to photobleaching.(Schmidt et al. 2003)

So far, the unexpected photostability of WSCP-bound Chls has not been satisfactorily explained. A shielding of the Chls from oxygen by the protein scaffold forming an efficient diffusion barrier been proposed by Schmidt *et al.* (Schmidt et al. 2003), however no clear evidence for this has been provided. In

principle, the presence of strongly excitonically coupled dimers could lead to triplet states unable to photosensitize $^1O_2$, as observed in some photosynthetic systems. This mechanism has been suggested to occur in chlorosomes.(Kim et al. 2007) where bacteriochlorophylls (BChls) form aggregated states resulting in strong π-π interactions allowing the formation of triplet excitons sufficient to lower the triplet excited state energy below that of $^1O_2$. It is known that also the solvent or the local pigment environment may shift the triplet state energies of several chlorin-type molecules by up to 0.11 eV(Hartzler et al. 2014), possibly below the energy of $^1O_2$. This latter effect has been proposed to underlie the photostability of the Fenna-Matthews-Olson (FMO) complex.(Kihara et al. 2015)

In order to get insight into the mechanism responsible for the photostability of WSCP, we performed a systematic study using electron paramagnetic resonance (EPR) techniques to determine the properties of the photoexcited ^{3}Chl, flash photolysis to measure the ^{3}Chl *a* lifetime, and trapping experiments to evaluate the $^1O_2$ yield.

2. Material and methods

2.1. Sample preparation

Chl *a* was isolated and purified from pea plants (*Pisum sativum*) according to Booth and Paulsen.(Booth & Paulsen 1996) Chlorophyllide *a* (Chlide *a*) was obtained using recombinant chlorophyllase from wheat (*Triticum aestivum*). Expression and purification of recombinant chlorophyllase was carried out following the protocol described earlier(Arkus et al. 2005). Chlorophyllase assay used for obtaining Chlide *a* is based on the method of Fang *et al.* (Fang et al. 1998) with a few variations of the protocol. The reaction mixture containing 20 mM sodium phosphate pH 7.8, 0.5 mg/ml chlorophyllase, 1 mM ascorbate, 5 mM $MgCl_2$, 50 % (v/v) acetone and 1.25 mg/ml Chl *a* was incubated for 4 h at 37 °C and 80 rpm. After adjusting to 70 % acetone, the reaction mixture was centrifuged (10 min, 4 °C, 10,000 ×*g*) and the supernatant subjected to Sep-Pak® cartridges (Plus tC18, Waters) for purification via reversed phase chromatography. Chlide *a* was eluted by washing the cartridges with 4 ml of 70 % acetone. After quantification via analytical HPLC, pigments were dried and stored under N_2 atmosphere at -20 °C. Pet24b plasmid with a gene encoding for a recombinant WSCP protein from Virginia pepperweed (*Lepidium virginicum*) possessing a C-terminal hexahistidyl tag (Takahashi et al. 2013) was kindly provided by the group of Prof. Satoh (Toho University, Japan). The plasmid was transformed in *Escherichia coli* (BL21). Recombinant apo-protein expression and purification was carried out as described previously(Palm et al. n.d.) except the bacteria growth was carried out at 37 °C and kanamycin was used as the selection antibiotics. The purified apoprotein was reconstituted with a three-fold molar excess of either Chl *a* or Chlide *a*. Pigments were dissolved in Triton™ X-114 (TX-114) and added dropwise to the protein solution

containing 20 mM sodium phosphate pH 7.8 and 5 mM β-mercaptoethanol yielding a final concentration of TX-114 of 2 % (v/v). After incubation for 30 min at 4 °C and 30 rpm, phase separation was induced by increasing the temperature to 40 °C followed by a 5 min incubation step. The aqueous phase harboring the reconstituted WSCP complexes was collected after centrifugation (2 min, at room temperature, RT, 14,000 ×*g*) and applied to a Superose™ 12 10/300 GL prepacked column (GE Healthcare) equilibrated with 20 mM sodium phosphate pH 7.8 and operated by a BioRad NGC system at RT for further purification via size-exclusion chromatography (SEC). Peak fractions containing tetrameric WSCP were analyzed via absorption and circular dichroism (CD) spectroscopy. Recombinant LHCII was reconstituted and purified as described earlier.(Roeder et al. 2014) After sucrose density gradient purification, trimeric LHCII was collected and adjusted to 20 mM sodium phosphate pH 7.8 + 0.2 % (w/v) *n*-dodecyl-β-maltoside. LHCII complex integrity and functionality was verified by applying absorption, CD and fluorescence spectroscopy.

2.2 Time resolved (TR) and pulse EPR

Samples were concentrated to a Chl concentration of 700 µg/ml. Oxygen was removed by flushing nitrogen in the EPR sample tube before freezing. Residual oxygen was removed exploiting the glucose/glucose oxidase/catalase system.(Yruela et al. 1994) Glycerol, previously degassed by several cycles of freezing and pumping, was added (60 % v/v) just before freezing to obtain a transparent matrix.

TR-EPR experiments were performed on a modified Bruker ER200D spectrometer with an extended detection bandwidth (6 MHz). Laser excitation at 532 nm (5 mJ per pulse and repetition rate of 50 Hz) was provided by the second harmonic of a Nd:YAG laser (Quantel Brilliant) in a dielectric cavity. The temperature was controlled with a nitrogen flow cryostat. The signal was recorded with a LeCroy LT344 digital oscilloscope, triggered by the laser pulse. Transient signal rise time was about 150 ns. The experiments were carried out with a microwave power in the cavity of 2 mW. To eliminate the laser background signal, transients accumulated under off-resonance field conditions were subtracted from those on resonance.

Pulse EPR experiments were performed on a Bruker Elexsys E580 spectrometer. Laser excitation at 532 nm (10 mJ per pulse and repetition rate of 10 Hz) was provided by the second harmonic of a Nd:YAG laser (Quantel Brilliant) in a dielectric cavity. The temperature was controlled with a Helium cryostat (Oxford CF935) driven by a temperature controller (Oxford ITC503).

Field-swept Electron spin echo (ESE) spectra were recorded using a 2-pulse ESE sequence according to the scheme: flash-DAF-π/2-τ-π-τ-echo. ESE-detected kinetics at the triplet canonical orientations were recorded using a 2-pulse (flash-π/2-τ-π-τ-echo) ESE sequence. The π/2-pulse was of 16 ns and the delay τ was set at 200 ns for the field-swept ESE experiment and to 120 ns for the ESE-detected kinetics.

Davies-ENDOR experiments were performed using the microwave pulse sequence (flash-π-T-π/2-τ-π-τ-echo) with an inversion π pulse of 200 ns, T of 8 μs and a RF pulse of 6 μs. The detection sequence was similar to the field-swept ESE experiment but with τ of 300 ns.

Mims ENDOR experiments were recorded using the microwave pulse sequence (flash-π/2-τ-π/2-T-π/2-echo), with 16 ns pulse duration, in conjunction with an RF pulse of 6 μs duration, starting 0.8 μs after the second microwave pulse. The delay τ was variable, and the time T was 8 μs to accommodate the RF pulse. Mims ENDOR spectra were recorded at different τ values (from 160 to 240 ns) and added together to eliminate τ-dependent blind spots. Pulse ENDOR spectra were accumulated for ≈15 h.

2.3 TR-EPR spectra simulation

Simulations of the powder spin-polarized triplet spectra were performed using a program written in MatLab®, with the aid of the Easyspin routine (ver. 5.1.9),(Stoll & Schweiger 2006) based on the full diagonalization of the triplet state spin Hamiltonian, including the Zeeman and magnetic dipole–dipole interactions, considering a powder distribution of molecular orientations with respect to the magnetic field direction.(Di Valentin et al. 2008) Input parameters are the triplet state sublevel populations, the zero-field splitting (ZFS) parameters, the linewidth, and the isotropic g value.

2.4 Flash photolysis

To measure the bleaching of the Chl ground state absorption upon excitation, the sample was excited by a flash lamp with a saturating μs flash centered at 680 nm. The ground state absorption change was then measured at 405 nm with low intensity. In the anoxic condition, oxygen was removed with the glucose/glucose oxidase/catalase system,(Yruela et al. 1994) then the cuvette was closed with a tap.

2.5 Photobleaching

Photobleaching was measured by quantitating the loss in fluorescence intensity upon illumination with white light at 500 μmol of photons m^{-2} s^{-1}. As a control, free Chl *a* was dissolved in a 20 mM sodium phosphate pH 7.8 buffer with 2 % (w/v) octyl-β-D-glucopyranoside (OG).

After excitation at 410 nm, Chl *a* emission detected at the maximum of the emission spectrum (at 667, 674, 678 and 674 nm for Chl *a* WSCP, Chlide *a* WSCP, LHCII and Chl *a* in 2 % OG, respectively) was compared to the initial emission before illumination (F/F_0) and plotted against illumination time. The measurements were performed on a FluoroMax-2 (Jobin Yvon-Spex) at RT using a cuvette with the dimensions of 5×5 mm and the following parameters: slits 1 nm, increment 1 nm, integration time 1 s.

2.6 Singlet oxygen quantification

Quantification of singlet oxygen ($^1O_2$) production were performed with singlet oxygen sensor green (SOSG; Molecular Probes, Eugene). SOSG is a fluorescent probe highly selective for $^1O_2$ that increases its 530 nm emission band upon reaction with this species (Flors et al. 2006). The different samples were diluted to the same integrated absorption area in the wavelength range 590–750 nm (around 2.5 μg Chls/ml) in the presence of 2 μM SOSG and 2 % methanol, and illuminated with red light (λ ≥ 590 nm) at 500 μmol of photons m^{-2} s^{-1} under stirring. Fluorescence yield of SOSG (λ_{ex} 480 nm, λ_{em} 530 nm, slits 0.5 nm, increment 1 nm, integration time 1 s, cuvette 1×1 cm) was determined after light treatment in order to quantify $^1O_2$-dependent fluorescence increase.

Spin-trapping assays of $^1O_2$ were also performed following the procedure described in Schmidt *et al.*(Schmidt et al. 2003) All the samples were prepared in 20 mM sodium phosphate pH 7.8 with a Chl concentration of 1 μg/mL, 100 mM TEMP (2,2,6,6-Tetra-methyl-piperidine), and 3.5% methanol (v/v). Samples were illuminated for one hour with white light at 150 μmol of photons m^{-2} s^{-1} on a water bath at 20 °C. Continuous-Wave (CW) EPR spectra of the samples were measured before and after exposure to light with a Bruker Elexsys E580 spectrometer. X-band spectra were recorded at 298 K with modulation frequency of 100 kHz, modulation amplitude of 0.2 mT, microwave frequency 9.6 GHz, and a microwave power of 3.76 mW.

3. Results

3.1 TR- EPR and pulse ENDOR

Illumination of WSCP reconstituted with Chl *a* leads to formation of ^{3}Chl, which can be easily detected by TR-EPR at low temperature (figure 2). The polarization pattern of the spectrum is EAEAEA (A = absorption, E = emission), similar to that reported for ^{3}Chl *a* in MTHF (Di Valentin et al. 2007), rather than for ^{3}Chl *a* in light-harvesting proteins(Di Valentin et al. 2008; Di Valentin et al. 2009; Di Valentin et al. 2010; Di Valentin, Meneghin, et al. 2013; Carbonera et al. 2014).

Simulation of the spectrum (figure 2) was obtained with the values reported in table 1. The zero-field splitting (ZFS) parameters used in the simulation to reproduce the TR-EPR spectrum were similar to those reported for ^{3}Chl *a* in MTHF and ^{3}P680 in photosystem II particles. (Lendzian et al. 2003). The scheme of the Zeeman splitting of the triplet sublevels typical of chlorines, at the three canonical orientations of the triplet state (i.e. magnetic field parallel to the ZFS tensor axes X, Y, or Z) (van Mieghem et al. 1991), is reported in figure S1

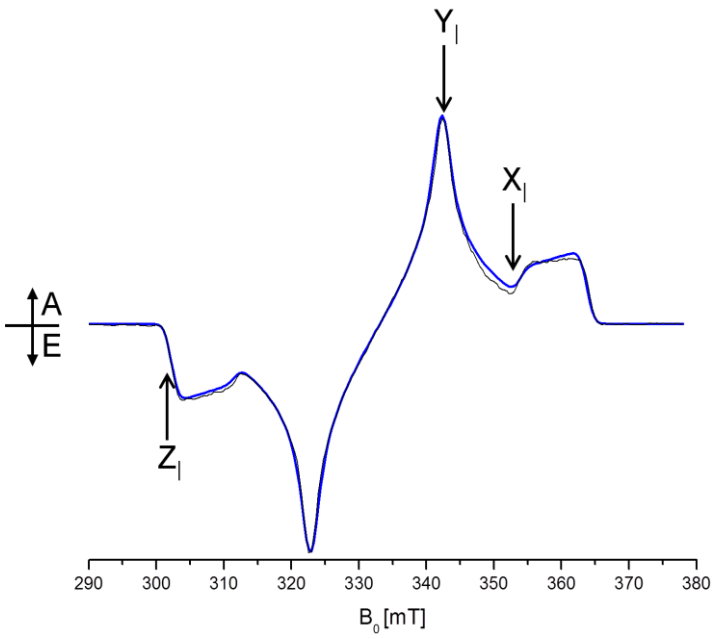

Figure 2: TR-EPR spectrum of Chl *a* WSCP (black line), taken 150 ns after the laser pulse, at 130 K. Calculated spectrum (blue line) according to the parameters reported in table 1. X, Y and Z represent the ZFS canonical orientations, only the ms = 0 to ms = +1 transitions are highlighted.

The similarity of the D values of ^{3}Chl *a* in WSCP with those measured in MTHF,(Lendzian et al. 2003) suggests a localization of the triplet state on only one of the two Chls constituting the Chl dimers bound to the protein, as observed for other Chl dimers in photosynthetic reaction centers of plants (Di Valentin et al. 1996; Lendzian et al. 2003). However, a triplet state delocalization among Chls could still occur even in the absence of significant changes in the ZFS parameters with respect to those of the corresponding monomer, as recently observed in synthetic conjugated multimeric porphyrin systems.(Tait et al. 2015) On the contrary, electron-nucleus hyperfine coupling constants (hfcs), being directly related to the spin density distribution, strictly depend on the triplet delocalization. Thus we measured the proton hyperfine couplings on ^{3}Chl *a* the by means of pulse ENDOR spectroscopy.

Table 1: ZFS parameters and Zero-field populations ($p_{x,y,z}$) of the ^{3}Chl used in simulations of the TR-EPR spectrum. Other parameters: linewidth = 2 mT, g_{iso} =2.0023.

	|D|		**|E|**		
	[mT]	[cm^{-1}]	[mT]	[cm^{-1}]	(p_x,p_y,p_z)
WSCP Chl *a*	30.7	0.0287	3.8	0.0036	(0.12,0.36,0.52)
MTHF Chl *a* (Lendzian et al. 2003)	30.5	0.0285	4.5	0.0042	(0.33,0.56,0.11)

Davies ENDOR spectra of WSCP were collected at field positions corresponding to orientations of ZFS axes of ^{3}Chl parallel to the static field B_0, yielding single crystal-like ENDOR spectra, from which it is possible to extract the projections of the hfc tensors on the ZFS axis system. Transitions connecting the $m_s = 0$ and $m_s = +1$ levels of protons with positive hfcs give rise to signals at frequencies lower than proton Larmor frequency (ν_H), while those of protons with negative hfcs are visible at higher frequencies with respect to ν_H (see black lines in figure 3A).

It is known that Davies pulse sequence does not allow resolving signals with small hfcs. On the other hand, Mims ENDOR is particularly suitable for measuring small hfcs, but, since the spectra are intrinsically affected by blind spots, averaging at different τ values is required, making the experiment time consuming. Therefore, we performed Mims experiments only in a narrow frequency interval around ν_H (purple line in figure 3A) sufficient to obtain a complete set of the smaller hfcs.

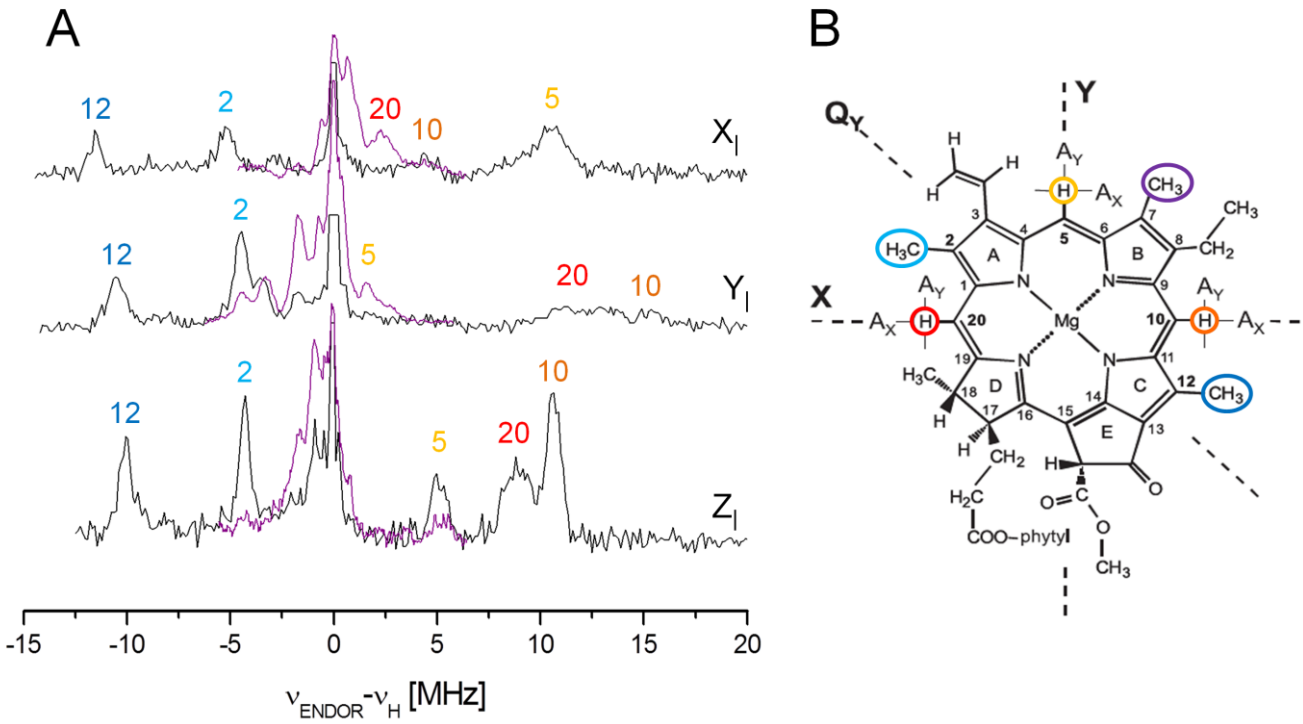

Figure 3: A) Pulse ENDOR spectra of WSCP ^{3}Chl *a* for the X_I, Y_I and Z_I EPR field positions (363.0 mT, 356.1 mT and 315.3 mT, respectively). Davies (black) and Mims (purple) spectra. Temperature 20K. The frequency scale gives the deviation from ν_H. The intense central ν_H lines in the Davies spectra have been cropped for better comparison. The assignments are labeled according to numbering and color code reported in B. **B)** Scheme of Chl *a* structure with the orientation of the ZFS axes (**Z** not shown, perpendicular to the molecular plane). The protons corresponding to the ENDOR peaks in A) are highlighted by circles.

The spectra were highly structured and well resolved, showing sharper peaks compared to the pulse ENDOR spectra of ^{3}Chl *a* in MTHF reported before (Lendzian et al. 2003). This is likely due to the lower inhomogeneous broadening experienced in the protein medium compared to the frozen glassy organic solution (MTHF). A similar effect was previously observed for the ENDOR spectrum of the primary donor ^{3}P680. (Lendzian et al. 2003)

In the negative region of the spectra two main narrow peaks are distinguishable at each orientation selected by the field position, which can be attributed to protons belonging to rotating methyl groups, on the basis of the sign of the hfcs and on their small anisotropy. In particular, the highest hfc (A_{iso} +10.7 MHz) is almost coincident with the value observed in the ENDOR spectrum of ^{3}P680 (A_{iso} +10.6 MHz), a monomeric ^{3}Chl *a* (Lendzian et al. 2003), and assigned to methyl 12 (nomenclature as reported in figure 3B).

Table 2: hfcs of ^{3}Chl a protons from the Davies and Mims ENDOR spectra shown in figure 4A.

hfc component[a]		**Assignment[b] (Proton position)**					
		12	**2**	**7**	**5**	**10**	**20**
WSCP	A_X [MHz]	+11.6	+5.3	+0.6	-10.5	-4.4	-2.3
	A_Y [MHz]	+10.4	+4.5	+1.7	-1.6	-15.6	-12
	A_Z [MHz]	+10.1	+4.3	+0.9	-5.0	-10.7	-8.8
	A_{iso} [MHz]	+10.7	+4.7	+1.1	-5.7	-10.2	-7.7
MTHF[b]	A_Z [MHz]	+7.4	n.d.	n.d.	(-6.2)	-11.4	-7.2
^{3}P680[b]	A_X [MHz]	+11.4	n.d.	n.d.	-7.1	-4.7	-3.3
	A_Y [MHz]	+10.0	n.d.	n.d.	-1.8	-14.8	-11.8
	A_Z [MHz]	+10.3	n.d.	n.d.	-5.5	-10.4	-8.4
	A_{iso} [MHz]	+10.6	n.d.	n.d.	-4.8	-10.0	-7.8
Chl $a^{+\bullet}$[c]	A_{iso} [MHz]	+7.1	+3.0	+3.0	≤ |0.6|	≤ |0.6|	≤ |0.6|
Chl $a^{-\bullet}$[d]	A_{iso} [MHz]	+10.6	+5.3	-1.5	-4.7	-11.7	-4.4

[a]Principal components of the hyperfine tensor, axes collinear with the ZFS axes X,Y,Z
[b] based on (Lendzian et al. 2003)
[c] based on (Huber et al. 1986)
[d] based on (Hoff et al. 1982)

The other intense peak, with lower hfc values (A_{iso} +4.7 MHz), may be assigned to methyl 2 on the basis of the hfcs reported for the Chl *a* anion (Hoff et al. 1982) and cation (Huber et al. 1986) at this proton position, taking into account that, in the Huckel approximation, the hfc for a nucleus of a triplet state is expected to be the average of those observed in the respective cation (singly occupied HOMO) and anion (singly occupied LUMO) radicals, since in the triplet state the HOMO and LUMO are both singly

occupied.(Lendzian et al. 2003) It is worth noting that this is the first time that the transition belonging to proton 2 is clearly detected in a ^{3}Chl *a* ENDOR spectrum. Methyl at position 7 is expected to give smaller hfcs, on the basis of the corresponding values measured for the cation and the anion radicals, which likely correspond to the less intense transitions visible in the Mims spectra (A_{iso} +1.1 MHz), as reported in table 2.

In the positive part of the spectra three signals are present which can be assigned to three α protons, due to their sign and large anisotropy. Comparison with the previously published couplings relative to ^{3}P680 and ^{3}Chl *a* in frozen organic solvent, allows us to assign the observed transitions to the specific protons in the structure (table 2).(Lendzian et al. 2003) The small hfcs, which are well resolved in our Mims spectra, were neither assigned nor detected in previous pulse ENDOR studies, and will require a further computational analysis to reach a reliable and complete assignment.

The ^{3}Chl *a* Z-axis is perpendicular to the molecular plane, and is expected to be also a principal axis of the observed hfc tensors for the -CH_3 and α protons. Hence, changes on the spin density distribution of due to delocalization of the triplet state between different Chls, should be directly reflected in the A_Z hfc values of the protons. Therefore the high values of the hfcs observed clearly indicate that in WSCP the triplet state is localized on a single Chl molecule without any significant delocalization on the other Chls bound to the protein.

3.2 Flash photolysis

The characterization of the triplet state with EPR techniques ruled out the possibility of a photoprotective mechanism based on delocalization of the triplet state. Another important property of the triplet state that could be related to the slow photobleaching is the triplet lifetime. Since the intensity of the EPR signal depends mainly on spin relaxation processes and the ^{3}Chl lifetime is usually not directly accessible by TR-EPR measurements.(Fessmann et al. 1988), we measured the ^{3}Chl *a* lifetime by means of flash photolysis.

From the inspection of the flash photolysis spectra reported in figure 4, it is clear that the Chl ground state is depleted in the ms time range under anoxic conditions, while, in oxic conditions, this time shortens to less than 10 μs (the limit of the time response of the setup). From a deconvolution of the lamp profile of the anoxic time trace, a lifetime of 1.4 ms for recovery of the ground state and then for the ^{3}Chl *a* in WSCP was obtained, a value which is typical for ^{3}Chl *a* in both organic solvent and proteins.(Krasnovskii jr. & Kovalev 2014) Hence a shortening of the lifetime of the triplet state is not observed and cannot be invoked for explaining the photostability of WSCP. On the other hand the lifetime resulted to be very sensitive to the presence of O_2, ruling out the hypothesis that the protein scaffold is shielding ^{3}Chl *a* from interaction with oxygen, in agreement with our recent findings on *Brassica oleracea* WSCP.(Palm et al. n.d.)

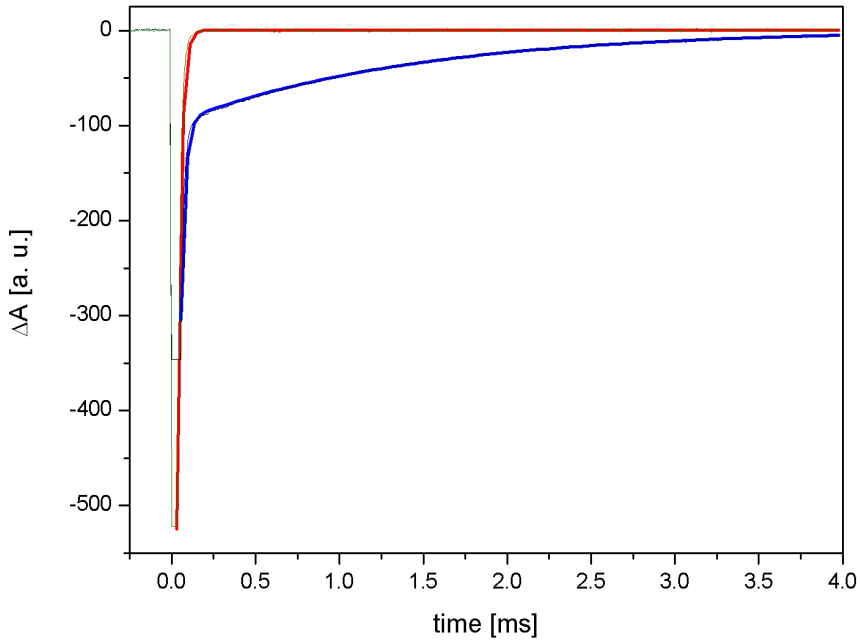

Figure 4: Recovery of the ground state absorption bleaching upon saturating excitation of WSCP Chl *a* in oxic (green) and anoxic (black) conditions. Saturating µs flash centered at the Q_y. Low intensity probing light beam centered at the Soret band. Fitting of time traces in red (oxic) and blue (anoxic), respectively.

Schmidt *et al.*(Schmidt et al. 2003) previously reported that light-induced $^1O_2$ formation in WSCP was significantly reduced compared to that of free Chls in solution. This would imply that the shortening of the lifetime of ^{3}Chl that we observed in the presence of O_2 should take place without generating the oxidative species $^1O_2$. In order to verify this possibility, we measured the photo-induced $^1O_2$ yield in our system.

3.3 $^1O_2$ and photobleaching quantification

The photoproduction of $^1O_2$ was measured using the fluorescent probe Single Oxygen Sensor Green® (SOSG). This sensor selectively reacts with $^1O_2$, leading to an epoxidized product with a highly increased fluorescence quantum yield. The measurements of $^1O_2$ were accompanied by photobleaching measurements, performed on the same samples, by means of Chl fluorescence detection.

A remarkable photo-stability of WSCP was observed, as highlighted by the comparison with the major light harvesting complex (LHCII) of the photosynthetic apparatus in plants (figure 5A). The two Chl-binding complexes display a comparable photobleaching, largely reduced in comparison to a reference sample containing free Chl *a* in DM micelles. Thus, WSCP and LHCII exhibit a similar light tolerance although WSCP does not contain any carotenoids whereas LHCII binds four.(Mozzo et al. 2008)

Surprisingly and in marked contrast to the previous work of Schmidt *et al.* (Schmidt et al. 2003) mentioned above, we detected an intense $^1O_2$ production in case of WSCP (figure 5B), that achieved a

plateau only due to the consumption of the SOSG as highlighted by a control experiment in which upon addition of fresh SOSG, the fluorescence signal started again to grow upon illumination (data not shown). In comparison, LHCII exhibited a far smaller $^1O_2$ production. A free Chl reference sample displayed, under the same experimental conditions, an unexpectedly low $^1O_2$ evolution. However, the reason for this behavior can be attributed to the concomitant high degree of photobleaching: due to the fast reaction with $^1O_2$, the number of excitable Chls quickly decreases, and therefore less and less $^1O_2$ is photosensitized at increasing time intervals.

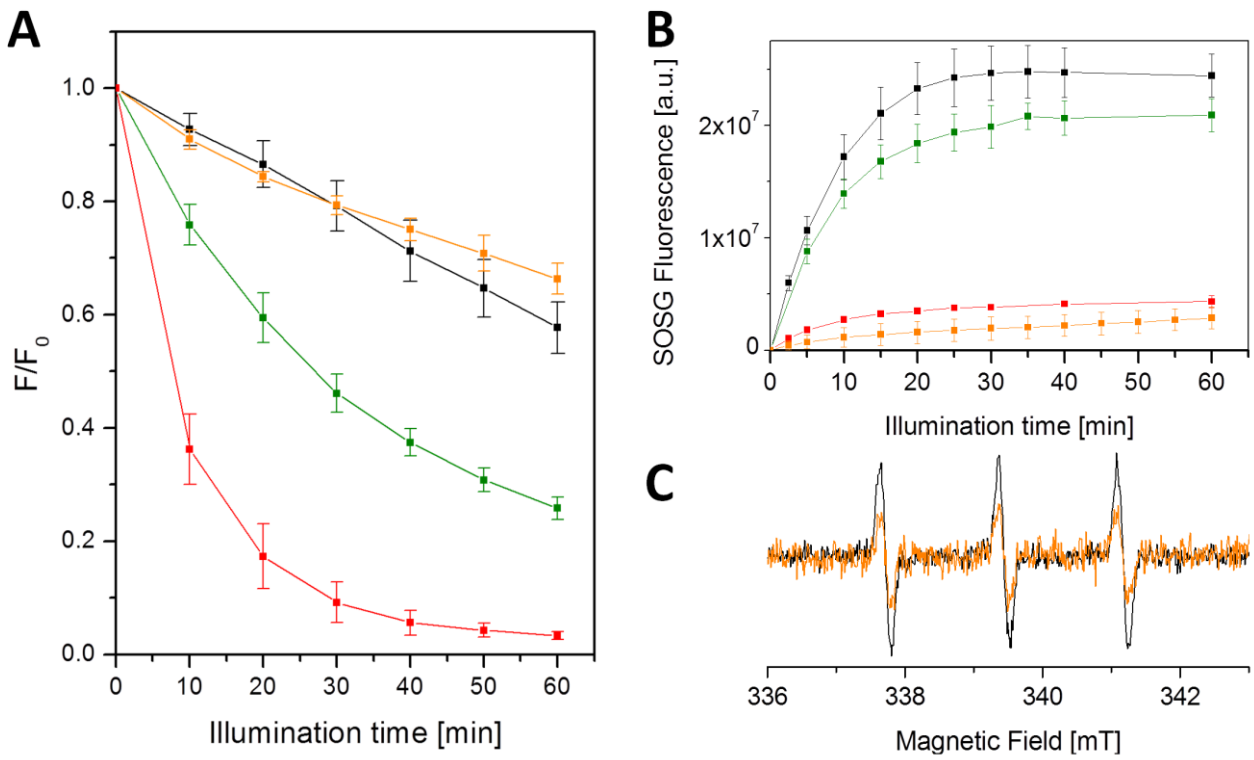

Figure 5: A) Photostability of Chl *a* (black) or Chlide *a* (green) reconstituted WSCP and LHCII (orange) in comparison to Chl *a* in 2 % OG (red). The samples were illuminated with 500 µmol of photons m^{-2} s^{-1} for 0-60 min. before fluorescence measurements (excitation at 410 nm, emission F detected at the maximum of the emission spectrum). Emission before illumination: F_0. Data are expressed as means (n = 3) **B)** Singlet oxygen production of Chl *a* (black) or Chlide *a* (green) reconstituted WSCP and LHCII (orange) in comparison to Chl *a* in 2 % OG (red). The samples were illuminated with 500 µmol red (λ> 590 nm) photons m^{-2} s^{-1} for 0-60 min before SOSG emission detection (excitation 480 nm, emission 530 nm). Data are expressed as means (n = 3) **C)** Spin-trap EPR measurements of $^1O_2$ production in Chl *a* reconstituted WSCP complexes (black) and LHCII (orange). TEMPO-formation detected after illumination at 150 µmol of photons m^{-2} s^{-1} for 60 min. Background signals were subtracted.

Since these results, showing a high $^1O_2$ yield in WSCP, were in contrast with those previously published, we performed also control spin-trapping experiments. When working in the same experimental

conditions adopted by Schmidt *et al.* (Schmidt et al. 2003), that is in the presence of *n*-dodecyl-β-maltoside (figure S2A), we also measured a low $^1O_2$ yield. The different quantification of $^1O_2$ measured by SOSG and spin probe methods may be related to the different repartition coefficients of the probes between the micellar and the aqueous phases. SOSG which is a hydrophilic molecule, efficiently reacts with the $^1O_2$ photosensitized by WSCP, whereas TEMP (2,2,6,6-Tetra-methyl-piperidine) is expected to be more concentrated in the micellar phase, in analogy with TEMPO (2,2,6,6-Tetra-methyl-piperidin-1-oxyl).(Pyter et al. 1982). Accordingly, we obtained a strong increase of the EPR signal of the trap upon removal of the *n*-dodecyl-β-maltoside from the WSCP solution (figure S2A), confirming that TEMP is sequestered away from the aqueous phase in the presence of the micelles. Therefore an underestimate of the $^1O_2$ photosensitization (Schmidt et al. 2003) derived from the interfering presence of *n*-dodecyl-β-maltoside micelles.

Control experiments with free Chl *a* dissolved in an organic phase (ethanol) rather than in a micellar phase showed a 20% lowering (as estimated by double integration of the EPR signal) of the signal of the $^1O_2$ spin trap (figure S2B). The decrease of the signal under this condition can be attributed to the fact that in homogeneous solution the increase in the local concentration, generated in micelles by the confinement of Chls and TEMP, is lost, and the probability of encounter between TEMP and $^1O_2$ is consequently diminished.

In conclusion, our experimental approach based on two different methods for determining the $^1O_2$ production led to the conclusion that $^1O_2$ production in WSCP is not suppressed but is of the same order as that of free Chl and larger than that observed in LHCII (figure 5B and 5C), although a quantitative comparison between the two proteins is difficult, due to the fact that LHCII is a membrane protein while WSCP is water-soluble.

In summary, the extensive spectroscopic characterization of the triplet state of the Chls bound to WSCP did not reveal any specific characteristic that could explain their resistance towards the reaction with $^1O_2$, which is formed during illumination.

Prompted by these results we looked at the protein environment of the Chls, searching for a possible explanation of the scarce reactivity of the pigments towards $^1O_2$. From the inspection of the crystallographic structure,(Horigome et al. 2007) it appears that two tryptophans are in close contact to the macrocycle (namely W90 and W154). A possible role of tryptophans in photoprotection of photosynthetic proteins has already been hypothesized,(Dreaden Kasson et al. 2012) because of their high reactivity with $^1O_2$.(Berlett & Stadtman 1997; Rinalducci et al. 2005) W90 and W154 are important residues in the binding of the Chls in WSCP, as suggested by the fact that their exchange with alanine leads to a loss of the capability to bind Chls (personal communication from Professor Satoh). We mutated both of them to phenylalanine residues, chosen because of the similarity of the side chains but the reduced

reactivity with $^1O_2$ reported for Phe.(Michaeli & Feitelson 1994) The mutants were successfully reconstituted with Chl *a*, obtaining complexes with unchanged absorption and dichroism spectra in comparison to the wild type (see figure S3). Photobleaching of the mutants was very similar to that of the wild type, with a comparable loss of Chl *a* fluorescence (see figure S4) clearly indicating that neither of the Trp is involved in the photoprotection of the bound Chls, at least not by reaction with $^1O_2$.

In order to study a possible photo-protective role of the phytyl chains of the bound Chls, which are interposed between the Chl planes, WSCP was reconstituted with chlorophyllide *a* (Chlide *a*), i.e. the phytyl-free analog of Chl *a*. The reconstituted pigment-protein complex was obtained in high yield and the purification via size exclusion chromatography showed that it was comparable in the size of the oligomers to the Chl *a* analog (see figure S5). Thus, although Chlide-containing WSCP is less stable than the Chl complex, the phytyls are not strictly required for the tetramerization of WSCP, by contrast to previous report.(Schmidt et al. 2003).

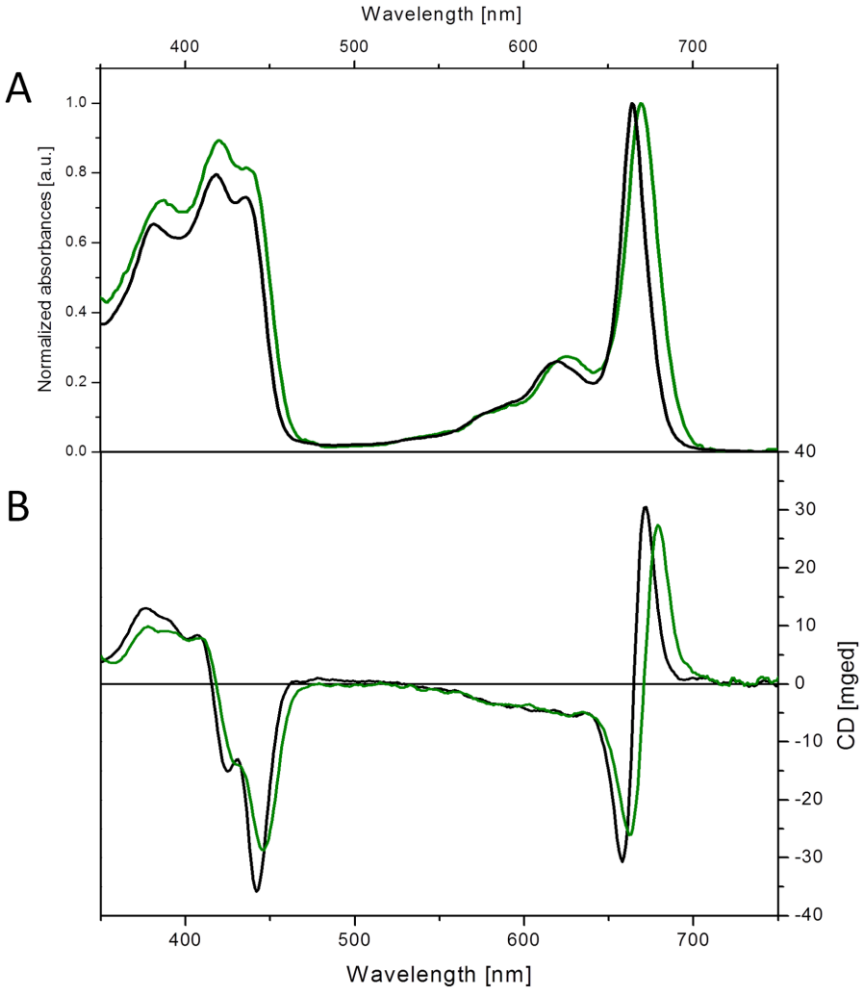

Figure 6: A) Absorption spectra of WSCP reconstituted with either Chl *a* (black) or Chlide *a* (green). The spectra were normalized to their Q_y maxima. **B)** Vis-CD spectra of WSCP reconstituted with either Chl *a* (black) or Chlide *a* (green). The spectra were normalized to the Q_y absorption band.

The Chl *a* and Chlide *a* reconstituted complexes exhibited similar optical properties, as evident from the absorption and CD spectra (figure 6A and 6B). Both Chl *a* and Chlide *a* upon binding to WSCP undergo a change in their absorption spectra compared to that of the pigments in organic solvents (see figure S5). The small differences in the CD spectra of Chl *a* and Chlide *a* containing WSCPs (figure 6B) are mainly attributable to the shifts observed in the absorption spectra of the free pigments themselves (see figure S6). The spectral similarity strongly suggests that the Chlides bound to WSCP are excitonically coupled in the same open sandwich configuration adopted by Chls. Interestingly, Chlide *a* WSCP showed a severe photobleaching (figure 5A), with an 80% loss of fluorescence after 1 h illumination. This is much higher than the photodegradation of Chl *a* WSCP under the same conditions (figure 5A) despite the similar spectral properties and although the $^1O_2$ production was comparable between Chl *a*- and Chlide *a*-containing WSCP, as revealed by SOSG quantification (figure 5B).

4. Discussion

In the present study, we used magnetic resonance techniques to characterize the ^{3}Chl *a* populated in WSCPs under illumination. Our experimental results provide clear evidence for the triplet state to be localized on a single Chl molecule among the four interacting pigments belonging to one protein tetramer. This was demonstrated by the large values of the hfcs determined by ENDOR spectroscopy, which were very similar to those reported for monomeric ^{3}Chl *a* in frozen organic solution.(Lendzian et al. 2003) On the basis of these results we conclude that the photoprotective properties of the WSCP complex cannot be derived from a delocalization of the triplet state.

In marked contrast to previous findings,(Schmidt et al. 2003) we measured an intense photoproduction of $^1O_2$ in WSCP complexes. The method used in the study of Schmidt *et al.*, (Schmidt et al. 2003) performed on *Brassica oleracea* WSCP, led to a underestimation of the $^1O_2$ due to the presence of detergent in the solution and to the limited solubility in water of the TEMP spin-trap. By modifying the experimental conditions we obtained spin-trapping results in agreement with SOSG quantification. Thus, the remarkable photostability of WSCP (Schmidt et al. 2003) (Palm et al. n.d.), which is comparable to the one displayed by systems in which the $^1O_2$ production is efficiently avoided by the photoprotective role of carotenoids, has to rely on the capability of the system to resist to bleaching <u>after</u> $^1O_2$ production. We have ruled out a possible involvement of two conserved tryptophans which are in van der Waals contact with the chlorine planes of the Chls. Indeed a sacrificial role of the protein matrix is unlikely to occur, since the protein scaffold is very resistant to prolonged light exposure.

The experiments performed on WSCP reconstituted with Chlide *a* clearly indicate that the presence of the Chl phytyls is required for the photostability of the system. A photoprotective action of the phytyls through a direct reaction with $^1O_2$, i.e. acting as oxidizable species,(Rontani & Aubert 1994) can be

excluded, as this would have led to a photobleaching curve characterized by a change in slope, with a faster loss in fluorescence once all the phytyls would have been consumed by the reaction. Instead the profile of the Chl fluorescence keeps its decay rate constant for long illumination times. (see figure S7) The phytyls are intertwined between the Chl pairs constituting the open sandwich dimers (see figure 7). Interestingly this configuration brings them in van der Waals contact with the methine carbon atom of the Chl ring (number 20 in figure 3B) that is known to be the most susceptible site for reaction with $^1O_2$ in the photobleaching of Chls.(Troxler et al. 1980; Iturraspe & Gossauer 1991) Also methine 5, that was observed to be a preferential site of oxidation in a Cd(II) derivative of Chl *a*, (Iturraspe & Gossauer 1991) appears to be effectively shielded by the phytyl chains (see figure S8)

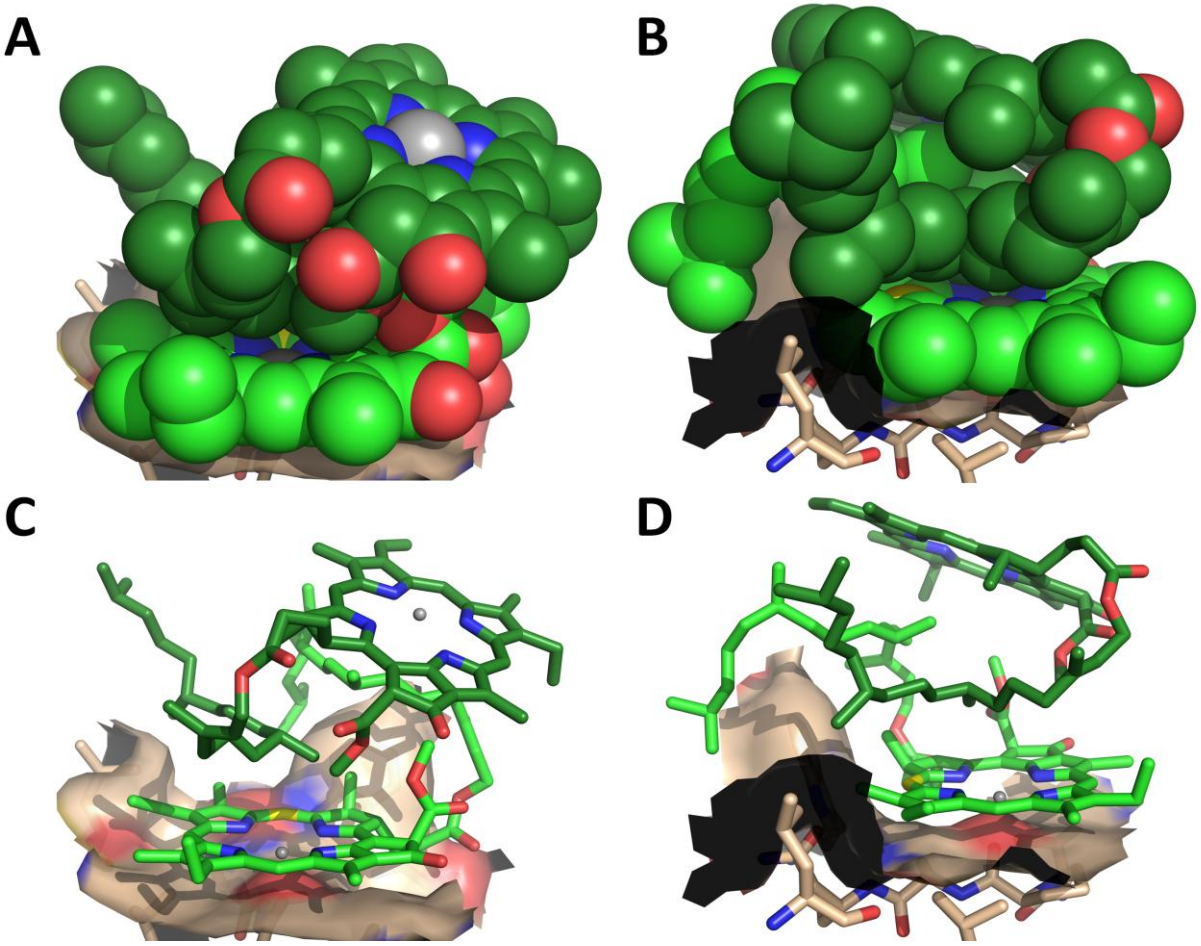

Figure 7: Structure of *Lepidium virginicum* WSCP (Horigome et al. 2007) with the Chls *a* in green. Only the surface of the WSCP monomer binding one of the four Chls is shown. The methine carbon 20 is colored in yellow. Two different views are reported (**A**, **C** and **B**, **D**), with the Chls constituting a dimer either in spheres (**A** and **B**) or in sticks (**C** and **D**).

At the same time a small portion of the ring remains accessible, explaining why the molecular oxygen can exchange triplet energy with ^{3}Chl populating the $^1O_2$.

It is worth noting that a photoprotective mechanism like this, with the reactive portions of the Chl macrocycle sterically shielded from the detrimental interaction with $^1O_2$, has never been reported before in a protein system, but it is similar to that found by Bonchio *et al.*(Bonchio et al. 2002) in a porphyrin-cyclodextrin supramolecular complex.(Manka & Lawrence 1990; Carofiglio et al. 1996) These authors found that the encapsulation of the porphyrins inside a cyclodextrin matrix efficiently photoprotects the porphyrins from photobleaching, while preserving the capability of $^1O_2$ sensitization . The available structural data of that system(Manka & Lawrence 1990; Ribó et al. 1995; Carofiglio et al. 1996) suggested that two cyclodextrins shield the methine carbon atoms avoiding their reaction with the photoproduced $^1O_2$. A similar mechanism of protection of the bound Chls, likely takes place in WSCP, thanks to the hindering effect of the phytyl chains.

The discovery that WSCP does not have, as previously reported, a reduced production yield of $^1O_2$ upon illumination, undermines its possible role as a Chl scavenger as proposed by Takahashi *et al.*(Takahashi et al. 2012; Takahashi et al. 2013) The remarkable photostability of the complex would be even detrimental to the photoprotection of the cell, due to the fact that the elongated lifespan of the Chls, once that they are bound to WSCP, may lead to an even increased production of $^1O_2$ over time.

The localization of WSCP in the ER bodies,(Takahashi et al. 2012; Takahashi et al. 2013; Takahashi et al. 2015) its ability to extract Chls from the thylakoids(Satoh et al. 1998) and the presence of a Künitz-type protease inhibitor sequence(Nishio & Satoh 1997; Satoh et al. 1998; Bektas et al. 2012; Takahashi et al. 2012; Takahashi et al. 2013) is more compatible with a role of this complex in sensing breakage or disruption of plant cells or organelles. Indeed, breakage of green plant cells or damage of their organelles, due to herbivore attack, senescence, stress conditions, or during programmed cell death, all destroy the separation of cell compartments. Under such conditions, WSCP apoprotein would be set free (or released) from the ER bodies, bind Chls upon contact with thylakoids as proposed by Takahashi *et al.* (Takahashi et al. 2012), and concomitantly form tetramers. The change in oligomerization of the protein may be then the way to "sense" the breaking conditions.

A possible role of WSCP discussed in the literature is its function as a Künitz-type protease inhibitor. Different WSCPs have been reported to show inhibitory activity against some proteases(Etienne et al. 2007; Desclos et al. 2008), while others fail in protease inhibition(Nishio & Satoh 1997; Ilami et al. 1997). Interestingly, Boex-Fontvieille *et al.* (Boex-fontvieille, Rustgi, Reinbothe, et al. 2015) have recently identified a complex consisting of WSCP apoprotein and RD21, a papain-like cystein protease (van der Hoorn et al. 2004; Koizumi et al. 1993) located in the ER bodies of *Arabidopsis thaliana*. Since ER bodies are part of the *Brassicaceae* defense system(Matsushima et al. 2003; Nakano et al. 2014) and RD21 has been shown to be involved in stress response and defense(Takayuki et al. 2012; Koizumi et al. 1993;

Gepstein et al. 2003; Yamaguchi-Shinozaki et al. 1992) it is likely that the RD21-WSCP complex and its localization plays a major role in stress response or in sensing cell or organelle disruption. This complex, released from the ER bodies upon cell or organelle disruption, could undergo a loss of interaction between WSCP and RD21 as a consequence of the tetramerization of the WSCP due to interaction with free Chls. This in turn would activate the protease activity. Such a mechanism would rely on highly stable WSCP complexes once they were formed. Since bound Chls are required to promote and mantain the tetramerization of WSCP(Palm et al. n.d.) the stability to photobleaching is important for the protein function. In fact a Chl ring opening, resulting from reaction with $^1O_2$, (Troxler et al. 1980; Iturraspe & Gossauer 1991) would disrupt the WSCP complex itself and, as a consequence, the WSCP apoprotein would act as protease inhibitor again.

Other possible functions of WSCP based on the tetramerization upon Chl binding might be suggested. For instance, WSCP might be involved into signaling of cell or organelle disruption to the nucleus or surrounding tissue cells once the tetramer is formed. Also in this case the system would need a remarkable photostability, in order to allow the complex to live long enough to transfer the signal to the next step in the signaling pathway.

5. Conclusion

We have shown that Chls in WSCP efficiently produce $^1O_2$ upon illumination but even so undergo little photooxidation. Our study solves the riddle of this photostability. We demonstrated that photoprotection requires the presence of the phytyl moieties of the bound Chls, sterically protecting the sites of the Chl macrocycle which are most susceptible to the $^1O_2$ attack.

We suggest that the photostability of the Chls bound to WSCP is required to allow playing the cell function, since Chls are needed to initially form, and then maintain, the tetrameric structure of the protein which in turn is instrumental for “sensing” and signaling the change in cellular conditions which leads to Chl release.

As a final remark, it is worth noting that, due to its simplicity, the mechanism of photoprotection of the bound Chls adopted by WSCP, could be mimicked to inspire molecular design in the fields of photodynamic therapy and photocatalysis.

Acknowledgments

A.A. gratefully acknowledges the *Ing. Aldo Gini* foundation for supporting his stay in Germany with a travel grant.

6. References

Annamalai, P. & Yanagihara, S., 1999. Identification and characterization of a heat-stress induced gene in cabbage encodes a kunitz type protease inhibitor. *Journal of Plant Physiology*, 155, pp.226–233.

Arkus, K.A.J., Cahoon, E.B. & Jez, J.M., 2005. Mechanistic analysis of wheat chlorophyllase. *Archives of Biochemistry and Biophysics*, 438, pp.146–155.

Balaban, T.S., 2005. Relevance of the diastereotopic ligation of magnesium atoms of chlorophylls in the major light-harvesting complex II (LHC II) of green plants. *Photosynthesis Research*, 86, pp.251–262.

Balaban, T.S. et al., 2002. Relevance of the diasteretopic ligation of magnesium atoms of chlorophylls in photosystem I. *Biochimica et biophysica acta*, 1556, pp.197–207.

Bednarczyk, D. et al., 2015. Assembly of water-soluble chlorophyll-binding proteins with native hydrophobic chlorophylls in water-in-oil emulsions. *BBA - Bioenergetics*, 1847(3), pp.307–313.

Bednarczyk, D. et al., 2016. Chlorophyll Fine Tuning of Chlorophyll Spectra by Protein-Induced Ring Deformation. *Angewandte Chemie International Edition*, 55, pp.1–6.

Bektas, I., Fellenberg, C. & Paulsen, H., 2012. Water-soluble chlorophyll protein (WSCP) of Arabidopsis is expressed in the gynoecium and developing silique. *Planta*, 236, pp.251–259.

Berlett, B.S. & Stadtman, E.R., 1997. Protein Oxidation in Aging , Disease , and Oxidative Stress. *Journal of Biological Chemistry*, 272(33), pp.20313–20316.

Boex-fontvieille, E., Rustgi, S., Reinbothe, S., et al., 2015. A Kunitz-type protease inhibitor regulates programmed cell death during flower development in Arabidopsis thaliana. *Journal of Experimental Botany*, 66(20), pp.6119–6135.

Boex-fontvieille, E., Rustgi, S., Wettstein, D. Von, et al., 2015. Water-soluble chlorophyll protein is involved in herbivore resistance activation during greening of Arabidopsis thaliana. *Proceedings of the National Academy of Sciences*, 112(23), pp.7303–7308.

Bonchio, M. et al., 2002. Efficient Sensitized Photooxygenation in Water by a Porphyrin−Cyclodextrin Supramolecular Complex. *Organic Letters*, 4(26), pp.4635–4637.

Booth, P.J. & Paulsen, H., 1996. Assembly of Light-Harvesting Chlorophyll a / b Complex in Vitro . Time-Resolved Fluorescence Measurements †. *Biochemistry*, 35(16), pp.5103–5108.

Carbonera, D. et al., 2014. Photoprotective sites in the violaxanthin-chlorophyll a binding Protein (VCP) from Nannochloropsis gaditana. *Biochimica et Biophysica Acta - Bioenergetics*, 1837(8), pp.1235–1246.

Carofiglio, T. et al., 1996. Very Strong Binding and Mode of Complexation of Water-Soluble Porphyrins with a Permethylated β-Cyclodextrin. *Tetrahedron Letters*, 37(44), pp.8019–8022.

Desclos, M. et al., 2008. A proteomic profiling approach to reveal a novel role of Brassica napus drought 22 kD/water-soluble chlorophyll-binding protein in young leaves during nitrogen remobilization induced by stressful conditions. *Plant physiology*, 147, pp.1830–1844.

Di Valentin, M. et al., 1996. A time-resolved electron nuclear double resonance study of the photoexcited triplet state of P680 in isolated reaction centers of photosystem II. *Chemical Physics Letters*, 248, pp.434–441.

Di Valentin, M. et al., 2008. Identification by time-resolved EPR of the peridinins directly involved in chlorophyll triplet quenching in the peridinin-chlorophyll a-protein from Amphidinium carterae. *Biochimica et Biophysica Acta - Bioenergetics*, 1777, pp.186–195.

Di Valentin, M. et al., 2009. Identification of the sites of chlorophyll triplet quenching in relation to the structure of LHC-II from higher plants. Evidence from EPR spectroscopy. *Journal of Physical*

Chemistry B, 113, pp.13071–13078.

Di Valentin, M. et al., 2007. The photo-excited triplet state of chlorophyll d in methyl-tetrahydrofuran studied by optically detected magnetic resonance and time-resolved EPR. *Molecular Physics*, 105, pp.2109–2117.

Di Valentin, M., Meneghin, E., et al., 2013. Triplet-triplet energy transfer in fucoxanthin-chlorophyll protein from diatom Cyclotella meneghiniana: Insights into the structure of the complex. *Biochimica et Biophysica Acta - Bioenergetics*, 1827(10), pp.1226–1234.

Di Valentin, M. et al., 2010. Triplet-triplet energy transfer in the major intrinsic light-harvesting complex of Amphidinium carterae as revealed by ODMR and EPR spectroscopies. *Biochimica et Biophysica Acta - Bioenergetics*, 1797(10), pp.1759–1767.

Di Valentin, M., Salvadori, E., et al., 2013. Unravelling electronic and structural requisites of triplet–triplet energy transfer by advanced electron paramagnetic resonance and density functional theory. *Molecular Physics*, 111, pp.2914–2932.

Downing, W.L. et al., 1992. A Brassica napus ranscript encoding a protein related to the Kunitz protease inhibitor family accumulates upon water stress in leaves, not in seeds. *The Plant Journal*, 2(5), pp.685–693.

Dreaden Kasson, T.M., Rexroth, S. & Barry, B.A., 2012. Light-Induced Oxidative Stress, N-Formylkynurenine and Oxygenic Photosynthesis. *Plos One*, 7(7), p.e42220.

Etienne, P. et al., 2007. N-protein mobilisation associated with the leaf senescence process in oilseed rape is concomitant with the disappearance of trypsin inhibitor activity. *Functional Plant Biology*, 34, pp.895–906.

Fang, Z., Bouwkamp, J.C. & Solomos, T., 1998. Chlorophyllase activities and chlorophyll degradation during leaf senescence in non-yellowing mutant and wild type of Phaseolus vulgaris L . *Journal of Experimental Botany*, 49(320), pp.503–510.

Fessmann, J. et al., 1988. Molecular dynamics studied by transient esr nutation spectroscopy of photoexcited triplet states: Chlorophyll a in liquid crystalline matrix. *Chemical Physics*, 152(6), pp.491–496.

Flors, C. et al., 2006. Imaging the production of singlet oxygen in vivo using a new fluorescent sensor , Singlet Oxygen Sensor Green â. *Journal of experimental botany*, 57(8), pp.1725–1734.

Foote, C.S., 1976. Photosensitized oxidation and singlet oxygen: consequences in biological systems. In W. A. Pryor, ed. *Free radicals in biology vol. 2*. Academic Press.

Gepstein, S. et al., 2003. Large-scale identification of leaf senescence-associated genes. *The Plant Journal*, 36, pp.629–642.

Halls, C.E. et al., 2006. A Kunitz-type cysteine protease inhibitor from cauliflower and Arabidopsis. *Plant Science*, 170, pp.1102–1110.

Hartzler, D.A. et al., 2014. Triplet Excited State Energies and Phosphorescence Spectra of (Bacterio)Chlorophylls. *The Journal of Physical Chemistry B*, 118, pp.7221–7232.

Hoff, A.J. et al., 1982. Proton and nitrogen electron nuclear double and triple resonance of the chlorophyll a anion in liquid solution. *Chemical Physics Letters*, 85, pp.3–8.

van der Hoorn, R.A.L. et al., 2004. Activity Profiling of Papain-Like Cysteine Proteases in Plants. *Plant Physiology*, 135, pp.1170–1178.

Horigome, D. et al., 2007. Structural mechanism and photoprotective function of water-soluble chlorophyll-binding protein. *Journal of Biological Chemistry*, 282(9), pp.6525–6531.

Huber, M. et al., 1986. ENDOR and triplet resonance in solutions of the chlorophyll a and

bis(chlorophyll)cyclopentane radical cations. *Chemical Physics Letters*, 132, pp.467–473.

Hughes, J.L. et al., 2006. Magneto-optic spectroscopy of a protein tetramer binding two exciton-coupled chlorophylls. *Journal of the American Chemical Society*, 128(5), pp.3649–3658.

Ilami, G. et al., 1997. Characterization of BnD22, a drought-induced protein expressed in Brassica napus leaves. *Phytochemistry*, 45(1), pp.1–8.

Iturraspe, J. & Gossauer, A., 1991. Dependence of the Regioselectivity of Photo-oxidative Ring Opening of the Chlorophyll Macrocycle on the Complexed Metal Ion. *Helvetica Chimica Acta*, 74, pp.1713–1717.

Kihara, S. et al., 2015. The Fate of the Triplet Excitations in the Fenna − Matthews − Olson Complex. *The Journal of Physical Chemistry B*, 119, pp.5765–5772.

Kim, H. et al., 2007. Triplet Exciton Formation as a Novel Photoprotection Mechanism in Chlorosomes of Chlorobium tepidum. *Biophysical journal*, 93, pp.192–201.

Koizumi, M. et al., 1993. Structure and expression of two genes that encode distinct drought- inducible cysteine proteinases in Arabidopsis thaliana. *Gene*, 129(2), pp.175–182.

Krasnovskii jr., A.A., 1994. Singlet molecular oxygen: mechanisms of formation and paths of deactivation in photosynthetic systems. *Biofizika*, 39(2), pp.236–250.

Krasnovskii jr., A.A. & Kovalev, Y. V, 2014. Spectral and Kinetic Parameters of Phosphorescence of Triplet Chlorophyll a in the Photosynthetic Apparatus of Plants. *Biochemistry (Moscow)*, 79(4), pp.349–361.

Küpper, H. et al., 2002. Kinetics and efficiency of excitation energy transfer from chlorophylls , their heavy metal-substituted derivatives , and pheophytins to singlet oxygen. *Biochimica et Biophysica Acta (BBA) - General Subjects*, 1572(1), pp.107–113.

Lendzian, F. et al., 2003. Hyperfine structure of the photoexcited triplet state 3P680 in plant PS II reaction centres as determined by pulse ENDOR spectroscopy. *Biochimica et Biophysica Acta - Bioenergetics*, 1605, pp.35–46.

Manka, J.S. & Lawrence, D.S., 1990. Template-Driven Self-Assembly of a Porphyrin-Containing Supramolecular Complex. *J. Am. Chem. Soc.*, 112, pp.2440–2442.

Di Mascio, P., Murphy, M.E. & Sies, H., 1991. Antioxidant defense systems: the role of carotenoids, tocopherols, and thiols. *The American Journal of Clinical Nutrition*, 53, pp.194–200.

Matsushima, R. et al., 2003. The ER body, a novel endoplasmic reticulum-derived structure in Arabidopsis. *Plant and Cell Physiology*, 44(7), pp.661–666.

Michaeli, A. & Feitelson, J., 1994. Reactivity of singlet oxygen toward amino acids and peptides. *Photochemistry and Photobiology*, 59(3), pp.284–289.

van Mieghem, F.J.E., Satoh, K. & Rutherford, a. W., 1991. A chlorophyll tilted 30° relative to the membrane in the Photosystem II reaction centre. *BBA - Bioenergetics*, 1058, pp.379–385.

Mozzo, M. et al., 2008. Photoprotection in the antenna complexes of photosystem II: Role of individual xanthophylls in chlorophyll triplet quenching. *Journal of Biological Chemistry*, 283(10), pp.6184–6192.

Murata, T. et al., 1971. Water-Soluble Chlorophyll Protein of Brassica oleracea var. botrys (cauliflower). *Biochimica et biophysica acta*, 245, pp.208–215.

Murata, T. & Murata, N., 1971. Water-soluble chlorophyll-proteins from Brassica nigra and Lepidium virginicum. *Carnegie Inst Wash Yearb*, 90, pp.504–507.

Nakano, R.T. et al., 2014. ER bodies in plants of the Brassicales order : biogenesis and association with innate immunity. *frontiers in Plant Science*, 5, pp.1–17.

Nishio, N. & Satoh, H., 1997. A water-soluble chlorophyll protein in cauliflower may be identical to BnD22,

a drought-induced, 22-kilodalton protein in rapeseed. *Plant physiology*, 115, pp.841–846.

Oba, T. & Tamiaki, H., 2002. Which side of the π-macrocycle plane of (bacterio)chlorophylls is favored for binding of the fifth ligand? *Photosynthesis Research*, 74(1), pp.1–10.

Olson, J.M. & Romano, C.A., 1962. A new chlorophyll from green bacteria. *Biochimica et biophysica acta*, 59(3), pp.726–728.

Osto, L.D. et al., 2007. Different Roles of α- and β-Branch Xanthophylls in Photosystem Assembly and Photoprotection. *Journal of Biological Chemistry*, 282(48), pp.35056–35068.

Palm, D.M. et al., Water-Soluble Chlorophyll Protein (WSCP) Stably Binds 2 or 4 Chlorophylls. *submitted to Biochemistry*.

Pyter, R.A., Ramachandran, C. & Mukerjee, P., 1982. Micelle-Water Distribution Coefficients of Nitroxides. Correlation with Dodecane-Water Distributions and Interfacial Activity. *Journal of Physical Chemistry*, 86, pp.3206–3210.

Renger, T. et al., 2009. Thermally activated superradiance and intersystem crossing in the water-soluble chlorophyll binding protein. *Journal of Physical Chemistry B*, 113, pp.9948–9957.

Reviron, M.P. et al., 1992. Characterization of a Novel Protein-Induced By Progressive or Rapid Drought and Salinity in Brassica-Napus Leaves. *Plant Physiology*, 100, pp.1486–1493.

Ribó, J.M. et al., 1995. Self-Assembly of Cyclodextrins with meso-Tetrakis(4-sulfonatophenyl)porphyrin in Aqueous Solution. *Tetrahedron*, 51(12), pp.3705–3712.

Rinalducci, S. et al., 2005. Formation of Truncated Proteins and High-Molecular-Mass Aggregates upon Soft Illumination of Photosynthetic Proteins research articles. *Journal of proteome research*, 4, pp.2327–2337.

Roeder, S., Hobe, S. & Paulsen, H., 2014. Silica Entrapment for Significantly Stabilized , Energy-Conducting Light-Harvesting Complex (LHCII). *Langmuir*, 30(47), pp.14234–14240.

Rontani, J.-F. & Aubert, C., 1994. Effect of oxy-free radicals upon the phytyl chain during chlorophyll a photodegradation. *J. Photochem. Photobiol. A:Chem.*, 79, pp.167–172.

Satoh, H., Nakayama, K. & Okada, M., 1998. Molecular cloning and functional expression of a water-soluble chlorophyll protein, a putative carrier of chlorophyll molecules in cauliflower. *Journal of Biological Chemistry*, 273(46), pp.30568–30575.

Schmidt, K. et al., 2003. Recombinant water-soluble chlorophyll protein from Brassica oleracea var. Botrys binds various chlorophyll derivatives. *Biochemistry*, 42, pp.7427–7433.

Schmitt, F.J. et al., 2008. Excited state dynamics in recombinant water-soluble chlorophyll proteins (WSCP) from cauliflower investigated by transient fluorescence spectroscopy. *Journal of Physical Chemistry B*, 112, pp.13951–13961.

Siefermann-Harms, D., 1987. The light-harvesting and protective functions of carotenoids in photosynthetic membranes. *Physiologia Plantarum*, 69(3), pp.561–568.

Song, P.-S. et al., 1976. Molecular Topology of the Photosynthetic Light-Harvesting Pigment Complex, Peridinin-Chlorophyll a-Protein, from Marine Dinoflagellates. *Biochemistry*, 15(20), pp.4422–4427.

Stoll, S. & Schweiger, A., 2006. EasySpin, a comprehensive software package for spectral simulation and analysis in EPR. *Journal of Magnetic Resonance*, 178, pp.42–55.

Tait, C.E. et al., 2015. Triplet State Delocalization in a Conjugated Porphyrin Dimer Probed by Transient Electron Paramagnetic Resonance Techniques. *Journal of the American Chemical Society*, 137, pp.6670–6679.

Takahashi, S. et al., 2012. Molecular cloning, characterization and analysis of the intracellular localization

of a water-soluble chl-binding protein from brussels sprouts (brassica oleracea var. gemmifera). *Plant and Cell Physiology*, 53(5), pp.879–891.

Takahashi, S. et al., 2013. Molecular cloning, characterization and analysis of the intracellular localization of a water-soluble chlorophyll-binding protein (WSCP) from Virginia pepperweed (Lepidium virginicum), a unique WSCP that preferentially binds chlorophyll b in vitro. *Planta*, 238, pp.1065–1080.

Takahashi, S. et al., 2015. Water‐soluble chlorophyll‐binding proteins from Arabidopsis thaliana and Raphanus sativus target the endoplasmic reticulum body. *BMC Research Notes*, 8(365), pp.1–5.

Takayuki, S. et al., 2012. A Role in Immunity for Arabidopsis Cysteine Protease RD21, the Ortholog of the Tomato Immune Protease C14. *Plos One*, 7(1), p.e29317.

Theiss, C. et al., 2007. Pigment - Pigment and pigment - Protein interactions in recombinant Water-Soluble Chlorophyll Proteins (WSCP) from cauliflower. *Journal of Physical Chemistry B*, 111, pp.13325–13335.

Troxler, R.F., Smith, K.M. & Brownc, S.B., 1980. Mechanism of photo-oxidation of bacteriochloropyhll-c derivatives. *Tetrahedron Letters*, 21, pp.491–494.

Yamaguchi-Shinozaki, K. et al., 1992. Molecular Cloning and Characterization of 9 cDNAs for Genes That Are Responsive to Desiccation in Arabidopsis thaliana: Sequence Analysis of One cDNA Clone That Encodes a Putative Transmembrane Channel Protein. *Plant and Cell Physiology*, 33(3), pp.217–224.

Yruela, I. et al., 1994. Characterization of a D1-D2-cyt b-559 complex containing 4 chlorophyll a/2 pheophytin a isolated with the use of MgSO4. *FEBS Letters*, 339, pp.25–30.

van Amerongen, H., van Grondelle, R. & Valkunas, L., 2000. *Photosynthetic excitons*.

Supporting Information

An unusual role for the phytyl chains in the photoprotection of the chlorophylls bound to Water-Soluble Chlorophyll-binding Proteins.

Alessandro Agostini[1,2‡], Daniel M. Palm[2‡], Franz-Josef Schmitt[3], Marco Albertini[1], Marilena Di Valentin[1], Harald Paulsen[2*], and Donatella Carbonera[1*]

[1]Department of Chemical Sciences, University of Padova, via Marzolo 1, 35131 Padova, Italy
[2]Institute of General Botany, Johannes Gutenberg-University, Johannes-von-Müller-Weg 6, 55128 Mainz, Germany
[3]Institute of Chemistry, Technische Universität Berlin, Straße des 17. Juni 135, 10623 Berlin, Germany

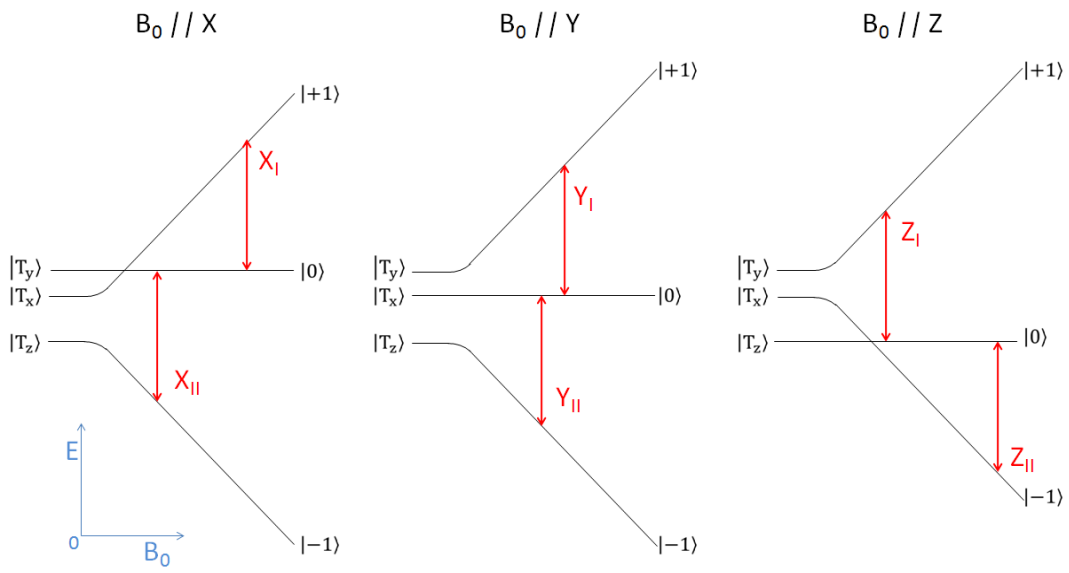

Figure S1: Scheme of electron spin energy levels of a chloryne triplet state in a magnetic field, with D>0 and E<0, for the canonical orientations as function of the magnetic field.

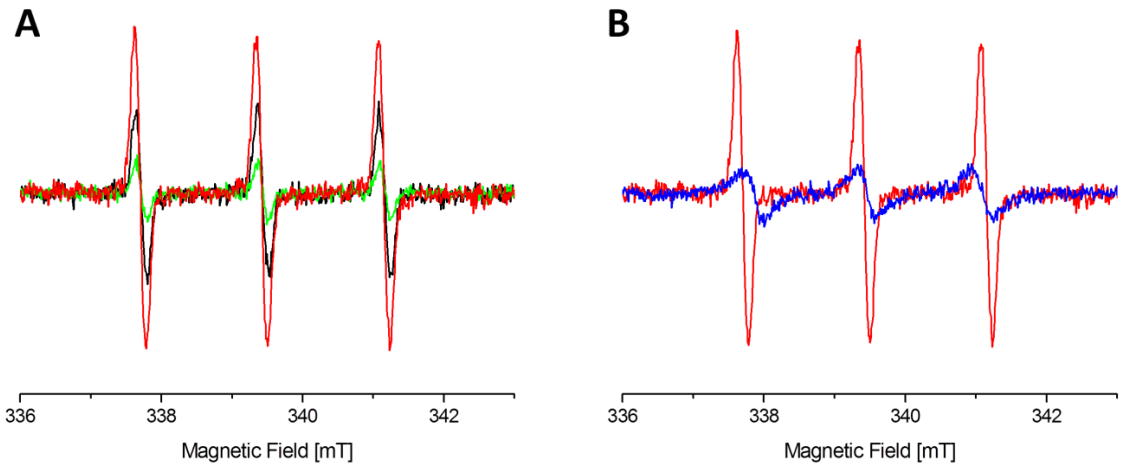

Figure S2: Spin-trap EPR measurements of singlet oxygen via TEMPO-formation after illumination at 150 µmol of photons m^{-2} s^{-1} for 60 min. Background signals were detected prior to illumination and subtracted. **A)** Spin-trap EPR measurements on Chl *a* reconstituted WSCP complexes in 20 mM sodium phosphate pH 7.8 (black) and in the same buffer with the addition of 0.1% *n*-dodecyl-β-maltoside (green), in comparison to Chl *a* in 0.1% *n*-dodecyl-β-maltoside (red). **B)** Comparison of spin-trap EPR measurements on Chl *a* (1 µg/mL) in 0.1% n-dodecyl-β-maltoside (red) and in ethanol (blue).

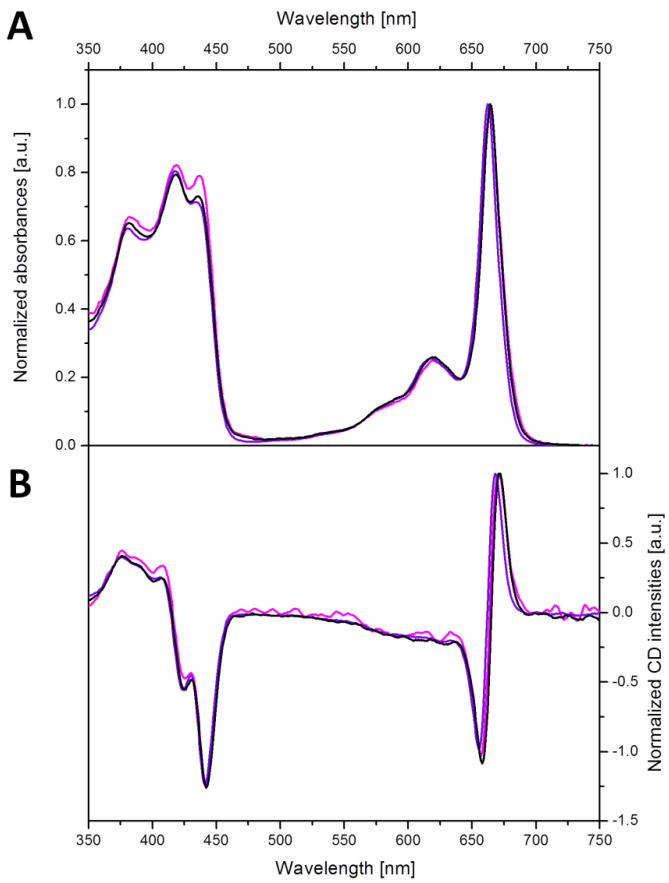

Figure S3: Absorption **(A)** and Vis-CD **(B)** spectra of Chl *a* reconstituted WSCP (WT in black, W90F in magenta and W154F in violet). The spectra were normalized to their Q_y absorption maxima.

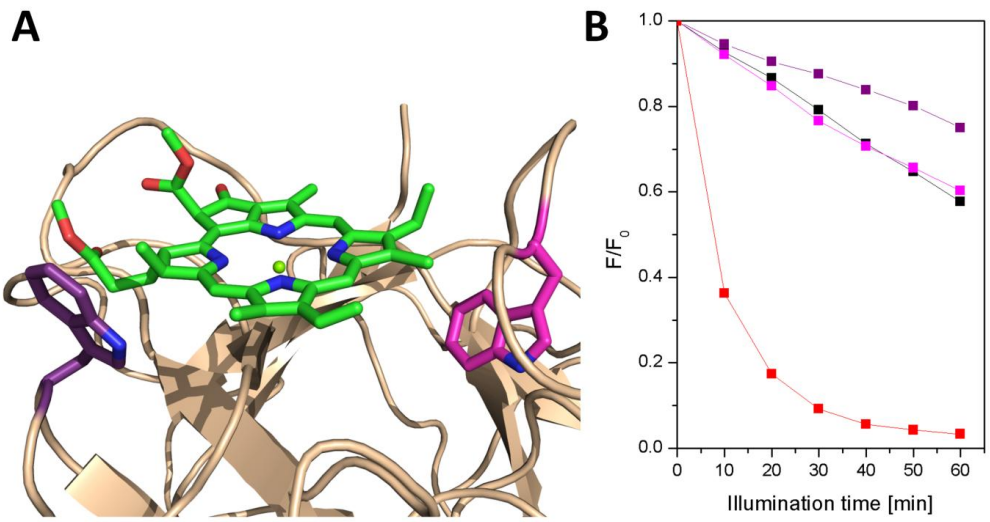

Figure S4: **(A)** Structure of *L. virginicum* WSCP (PDB entry 2DRE) with the Chl *a* in green (phytyl omitted for clarity) and the secondary structure in wheat. Only a detail of the surrounding (within 10 Å)of the bound Chl is shown. Tryptophans W90 (magenta) and W154 (violet), in van der Waals contact with the Chl, are shown in stick. **(B)** Photostability of Chl *a* reconstituted WSCP (WT,black;W90F, magenta; W154F, violet) in comparison to Chl *a* in 2 % OG (red). The samples were illuminated with 500 µmol of photons m^{-2} s^{-1} for 0-60 min. Emission detected at the maximum of the emission spectrum, excitation at 410 nm. Ratio (F/F_0) of emission after (F) and before illumination is plotted against illumination time.

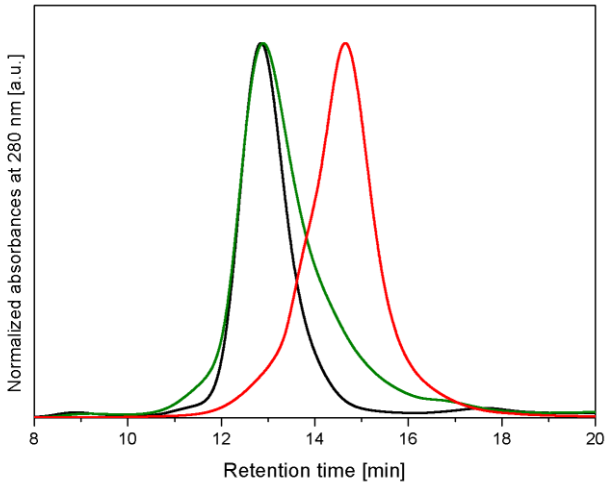

Figure S5: Size-exclusion chromatograms of apo-WSCP (red) and WSCP reconstituted with either Chl *a* (black) or Chlide *a* (dark green).

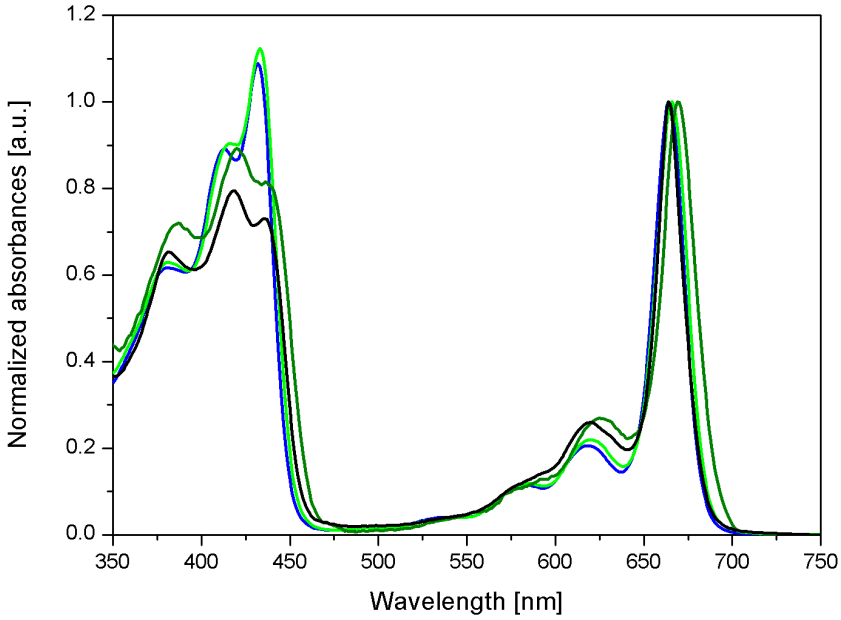

Figure S6: Comparison of absorption spectra of Chl *a* (blue) and Chlide *a* (light green) in 80 % acetone with the spectra, reported also in figure 7 of the main text, of WSCP reconstituted with either Chl *a* (black) or Chlide *a* (dark green). The spectra were normalized to the Q_y maxima.

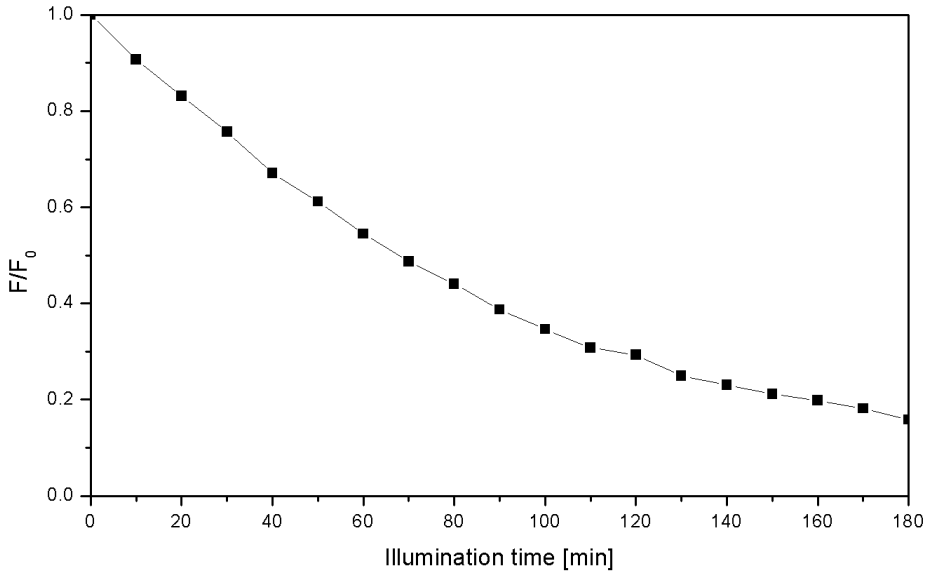

Figure S7: Photostability of Chl *a* reconstituted WSCP for long illumination times. The samples were illuminated with 500 µmol of photons m^{-2} s^{-1} for 0-60 min. Emission detected at the maximum of the emission spectrum, excitation at 410 nm. Ratio (F/F_0) of emission after (F) and before illumination is plotted against illumination time.

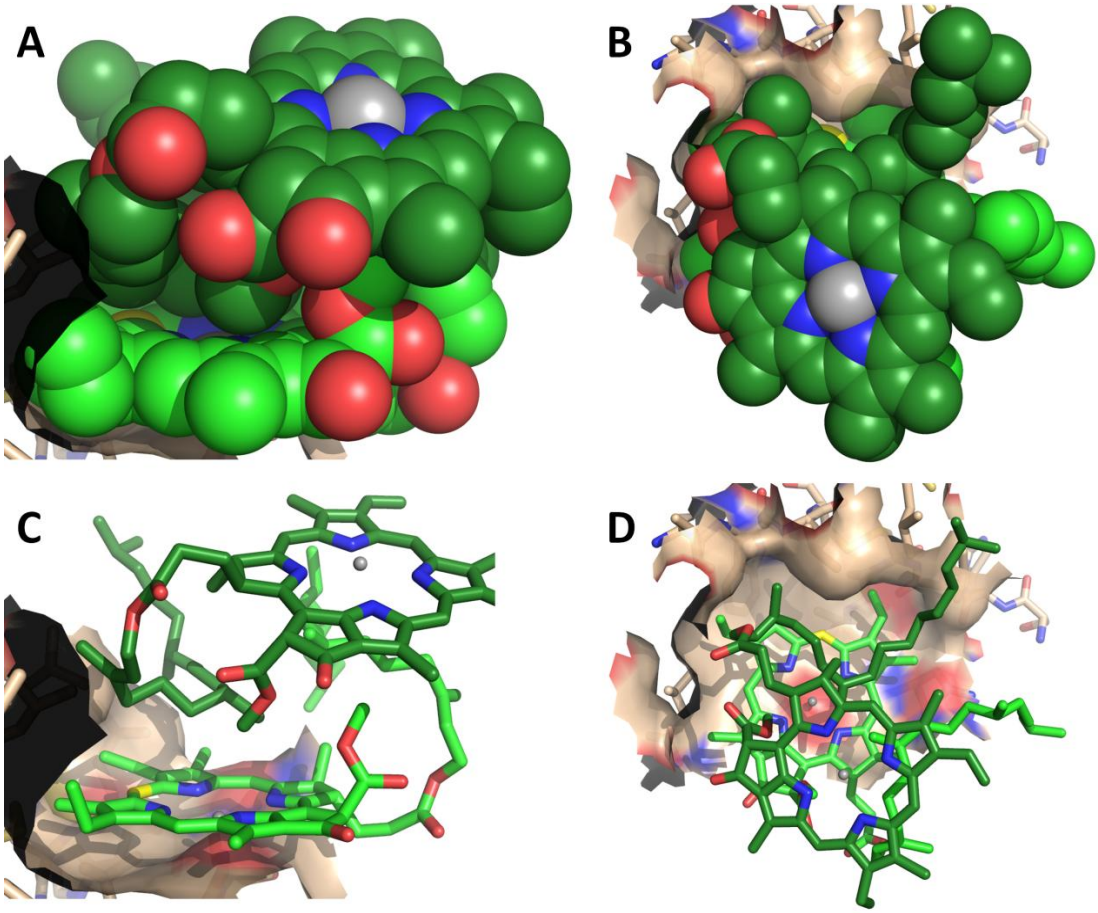

Figure S8: Structure of *Lepidium virginicum* WSCP (Horigome et al. 2007) with the chlorophylls Chls *a* in green. Only the surface of the WSCP monomer binding one of the four Chls is shown. The methine carbon 5 is colored in yellow. Two different views are reported (**A, C** and **B, D**), with the Chls constituting a dimer either in spheres (**A** and **B**) or in sticks (**C** and **D**).

Appendix

Author contributions

This dissertation was written on the basis of laboratory data which were produced in the framework of a joint project between the research group of professor Donatella Carbonera within the department of Chemical Sciences of the University of Padova, and the research group of professor Paulsen within the Institute of General Botany of the Johannes Gutenberg University Mainz.

The first half of the results of my thesis is based on ODMR data that I collected and analyzed in the laboratory of professor Carbonera, in Padova, thanks to the collaboration with several research groups. The PSI–LHCI complex isolated from various *Arabidopsis thaliana* mutants were provided from Dr. Stefano Cazzaniga, Mauro Bressan, and professor Luca Dall'Osto (University of Verona, Italy). The *Heliobacterium modesticaldum* reaction centers were provided from professor Art van der Est (Brock University, Canada), Bryan Ferlez and professor John H. Goldbeck (Pennsylvania University, USA). The data collection and analysis on the PSII core complex isolated from*Spinacia oleracea* were conducted working with Dr. Stefano Santabarbara, Dr. Anna Paola Casazza, and Dr. Giuseppe Zucchelli (Institute of Biophysic of the Consiglio Nazionale delle Ricerche, Italy). The resulting publications, that I contributed to write, are attached.

The second half of the results of my thesis, dealing with the characterization of WSCP, have been conducted jointly in Padova and in Mainz. I over-expressed, reconstituted and purified the WSCP complexes in the laboratory of professor Paulsen, in Mainz, working along with Daniel Palm, Philippe Girr, Dr. Mara Werwie, and Dr. Barbara Glöckle. I analyzed the samples in Mainz by means of circular dichroism and fluorescence working with Daniel Palm, and in Padova with CW and pulsed EPR methodologies. ESI-MS data have been provided from professor Stefan Tenzer (University Medical Center Mainz, Germany), and the flash photolysis measurements have been performed from professor Franz-Joseph Shmitt (Technische Universität Berlin, Germany).

Statuary declaration

I hereby declare that I wrote the dissertation submitted without any unauthorized external assistance and used only sources acknowledged in the work. All textual passages which are appropriated verbatim or paraphrased from published and unpublished texts as well as all information obtained from oral sources are duly indicated and listed in accordance with bibliographical rules. In carrying out this research, I complied with the rules of standard scientific practice as formulated in the statutes of Johannes Gutenberg-University Mainz to insure standard scientific practice.

Padova, 31.01.2017

CURRICULUM VITAE

PERSONAL INFORMATION

Name: **Alessandro Agostini**
E-mail: alessandro.agostini.3@gmail.com
Nationality: Italian
Date of birth: 26th October 1989

EDUCATION

January 2014 – January 2017
Cotutelle graduate program between the **Doctoral School in Molecular Sciences** of the University of Padova (Italy) and the **Doctoral School in Biology** of the University of Mainz (Germany)
Research activity focused on the biochemical and biophysical characterization of photoprotective mechanisms in photosynthetic organisms via Optically Detected Magnetic Resonance and advanced Electron Paramagnetic Resonance spectroscopy techniques (Time-resolved EPR, Pulsed EPR and ENDOR).
Italian Supervisor: Prof. Donatella Carbonera.
German Supervisor: Prof. Harald Paulsen.

11st July 2013
Master Degree in Chemistry (Final mark 110/110 *cum laude*), University of Padova.
One year practical thesis work about the characterization by means of Optically Detected Magnetic Resonance and Time-Resolved EPR of the triplet states present in antenna proteins extracted from the microalga *Nannochloropsis gaditana.*

"Photoprotection mechanism in the major light harvesting complex of *Nannochloropsis gaditana* as revealed by ODMR and TR-EPR spectroscopies"
Supervisor: Prof. Donatella Carbonera.

21st July 2011
Bachelor in Chemistry (Final mark 107/110), University of Padova.
Three months practical thesis work dealing with the study of chlorosomes extracted from *Chlorobaculum tepidum* via Time-Resolved EPR and Pulsed EPR.

"A time-resolved EPR study of the photoprotection mechanism in the chlorosomes of *Chlorobaculum tepidum*"
Supervisor: Prof. Donatella Carbonera.

TEACHING AND SCIENTIFIC DISSEMINATION ACTIVITIES

January 2016 and 2017
Assistance to undergraduate Industrial Biotechnologies students in laboratory activities of Physical Chemistry courses (UV-Vis absorption and fluorescence spectroscopies). University of Padova.

September 2015 and 2016
Laboratory demonstration open to the public in scientific dissemination events promoted by the Chemistry Department, University of Padova.

SELECTED CONFERENCES AND MEETINGS

4th - 8th September 2016
Participation to the **Xth EF-EPR Conference,** Turin, Italy.
Presented poster: "Chlorophyll triplet state in the Water Soluble Chlorophyll Protein: a combined ODMR and EPR investigation."

7th - 12th August 2016
Participation to the **17th International Conference on Photosynthetic Research.** Maastricht, Netherlands.
Presented poster: "Water-Soluble Chlorophyll Protein (WSCP): insight into its photoprotective mechanism from a combined EPR and ODMR characterization"

25th - 29th January 2016
Participation to the **20th School of pure and applied biophysics on 'Molecular and biophysical aspects of photosynthesis'** Venice, Italy.
Presented poster: "A spectroscopic study of the Water-Soluble Chlorophyll Protein: insight into its photoprotective mechanism"
The poster was selected for an oral presentation.

11th – 15th October 2015
Participation to the **International Conference on Tetrapyrrole Photoreceptors of Photosynthetic Organism,** Hagoshrim, Israel.
Presented poster: "Triplet state population in the Water-Soluble Chlorophyll Protein as revealed by EPR and ODMR spectroscopies"

7th – 11th September 2014
Participation to the **IXth EF-EPR Conference,** Marseille, France.
Presented poster: " Triplet state population in the oligomeric states of Fucoxanthin-Chlorophyll Protein from *Cyclotella meneghiniana* as revealed by EPR and ODMR spectroscopies"

2nd - 4th April 2014
Participation to the **PhD Spring School on Computational Biology,** Padova, Italy

28th January - 1st February 2013
Participation to the **17th School of pure and applied biophysics on 'Renewable energy and biofuels: a biophysical and biochemical approach'** Venice, Italy.
Presented poster: "Chlorophyll and carotenoid triplet states in FCP of the diatom *Cyclotella meneghiniana* and VCP of the microalga *Nannochloropsis gaditana* revealed by ZF-FDMR spectroscopy"

12th - 18th January 2013
Participation to the **6th European EPR Federation School in 'Advanced Techniques in EPR'**, Rehovot, Israel

Ferlez B., Agostini A., Carbonera D., Goldbeck J., van der Est A.* *Triplet Charge Recombination in Heliobacterial Reaction Centers Does Not Produce a Spin-Polarized EPR Spectrum* **(2016)** *Zeitschrift für Physikalische Chemie*, **Ahead of print**: 10.1515/zpch-2016-0825

Cazzaniga S., Bressan M., Carbonera D., Agostini A., Dall'Osto L.* *Differential roles of carotenes and xanthophylls in Photosystem I photoprotection* **(2016)** *Biochemistry*, *55,* 3636–3649

Santabarbara S.,* Agostini A., Casazza A.P., Zucchelli G., Carbonera D.* *Carotenoid Triplet States in Photosystem II: Coupling With Low-Energy States of the Core Complex.* **(2015)** *BBA-Bioenergetics*, *1847,* 262–275

Carbonera D.,* Agostini A., Di Valentin M., Gerotto C., Basso S., Giacometti G.M., Morosinotto T. *Photoprotective sites in the Violaxanthin-Chlorophyll a binding Protein (VCP) from Nannochloropsis gaditana.* **(2014)** *BBA-Bioenergetics*, *1837,* 1235–1246

Acknowledgments

"I have stolen ideas from every book I have ever read. My principle in researching a novel is 'Read like a butterfly, write like a bee', and if this story contains any honey, it is entirely because of the quality of the nectar I found in the work of better writers."

The Amber Spyglass, Philippe Pulmann

Paraphrasing words from a better writer, if this thesis contains any honey, it is entirely because of the quality of the mentors, colleagues, and friends that I had the opportunity to work with, and I want to catch this opportunity to express my gratitude to the many individuals who allowed me to achieve this result.

First of all I want to thank my Doktormutter, Donatella Carbonera. In the past six years I had the opportunity to study under her supervision, as she has instructed me throughout all my formal education, from the bachelor thesis to the doctoral degree. Her scientific passion, her vast knowledge of the field, and her instrumental insight are the best model for a student. She always sets the bar higher, and I am glad that she did it with me.

Harald Paulsen, my Doktorvater, welcomed me in his laboratory in Mainz making me feel at home, and I will also be grateful for this. His commitment to students is admirable, and I am thankful to him for all the support and scientific guidance that he gave me all over my doctorate.

It was a rewarding experience to have worked together with Stefano Santabarbara. His interest in all the aspects of the biophysical inquiry and his willingness to tackle some of the hardest topics in photosynthesis are aspects of Stefano that I admire.

Daniel Palm strongly influenced my graduate career. It was his insights and hard work in the lab that made possible to start with the WSCP project that blossomed into amazing results in these three years. We made a great team. The second half of this thesis is not mine—it is ours.

The biophysical group in Padova is the place in which I spent the majority of my time in the past years, and I have had the privilege of working alongside amazing colleagues that both academically inspired me and relieved me with their congeniality and funniness. In particular I

want to thank Marilena Di Valentin, Enrico Salvadori and Marco Albertini, who taught me essentially how to run an EPR experiment from the beginning to the end; Bianca Posocco, who gave me seminal suggestions regarding ODMR data analysis; MariaGiulia Dal Farra, who was always there to help me with Matlab; Chiara De Santi, who enthusiastically joined me in the ODMR investigation of WSCPs and with which I really enjoyed to work. Laura Galazzo and me have never worked on the same subject, but I am sure that my life in the lab would have been miserable without her friendship.

All the members of the Arbeitsgruppe-Paulsen in Mainz were fantastic lab mates and made the Institut für Allgemeine Botanik a great place to call home with their warmth, contrarily to what is said about Germans. I am grateful to everyone, but I shall thank in particular Christian Zefraß, who is an amazing scientist whose views about science are views I share; Philippe Girr, who taught me everything I know about *Brassicaceae* and plants physiology; Dennis Seiwert, who enthusiastically contributed to improve my "German experience"; Fabian Jung, who has the ability to piece together really interesting sides of a project; Liv Krämer, who tutored me in my first microscopic investigation of algae; Oliver Dautermann, who is a fantastic experimentalist and a lot of fun when he is "downstairs"; Mara Werwie and Barbara Glöckle, who shaped the Arbeitsgruppe-WSCP and coordinated us all.

Outside of my (bio)chemical life, I want to express my deep gratitude to my friends and family. My parents always accepted me the way I am and supported me in every decision I ever take, and for this I will always be grateful to them. My friends makes the best part of my life, and their deep friendships means a lot to me.